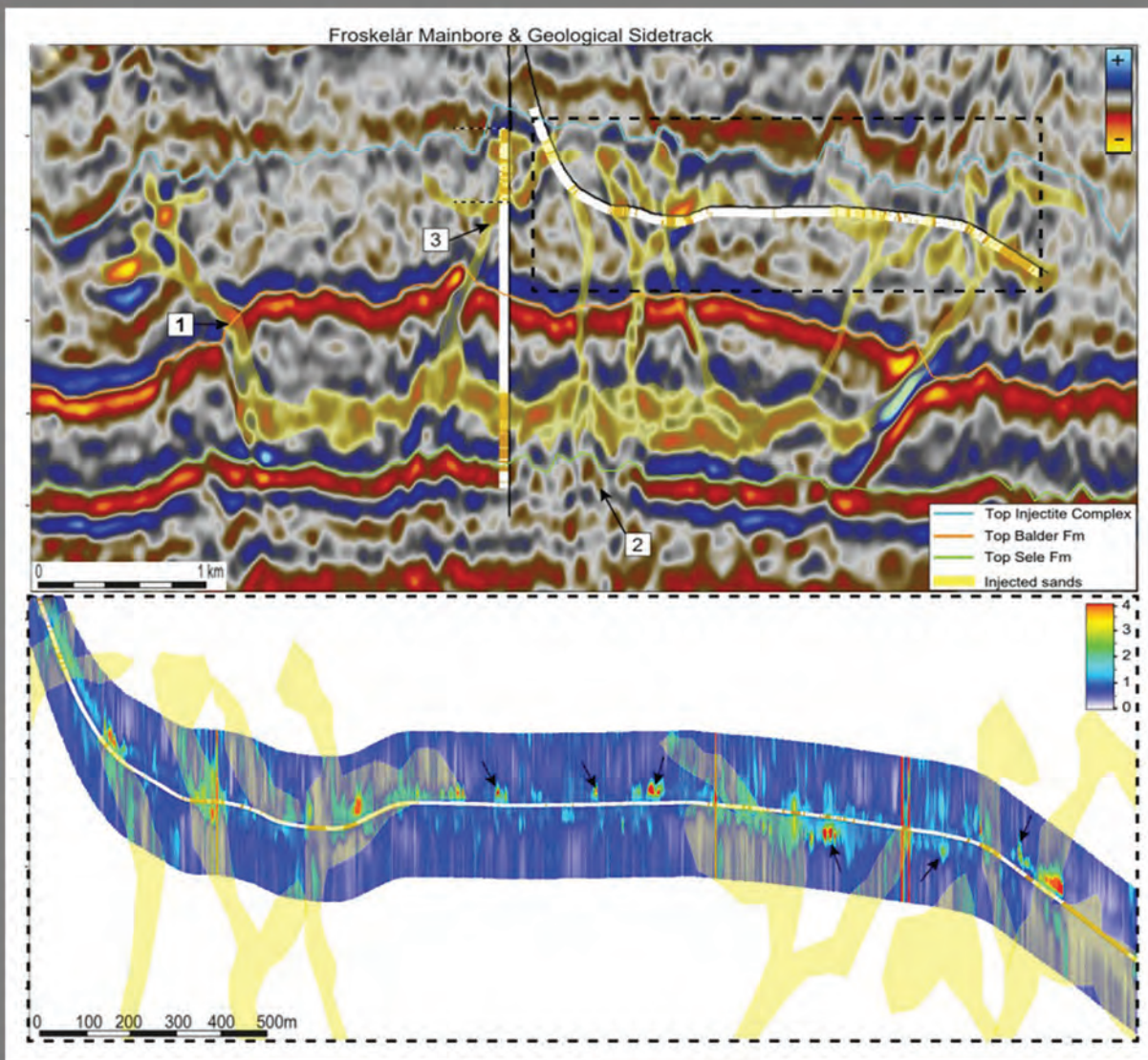


Petrophysics

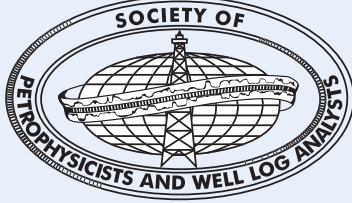
The SPWLA Journal of Formation Evaluation and Reservoir Description



Vol. 63, No. 1

February 2022





The Society of Petrophysicists and Well Log Analysts

8866 Gulf Freeway, Suite 320
Houston, TX 77017, USA
P: +1-713-947-8727
F: +1-713-947-7181
Email: Sharon@spwla.org
Membership@spwla.org
www.SPWLA.org

SPWLA Foundation. This fund supports scholarships in higher education and research in formation evaluation. Please send donations to: SPWLA, 8866 Gulf Freeway, Suite 320, Houston, TX 77017, USA

ISSN 1529-9074

PETROPHYSICS is published bimonthly by the Society of Petrophysicists and Well Log Analysts (SPWLA). Subscription is included in annual dues for members. Library Subscription cost is \$250 (6-issues, Feb, April, June, Aug, Oct, Dec) Send Subscription and member address changes to the SPWLA business office. Back issues if available are \$35 each to members and \$45 each to library subscribers.

ADVERTISING RATES: (based on one-time, full color) Full Page: \$1500, Half Page: \$1200, Quarter Page: \$1000. Additional fee for printing on covers. Media kits are available by contacting the SPWLA business office or by visiting the SPWLA website www.spwla.org. Responsibility: The statements and opinions expressed in PETROPHYSICS are those of the authors and should not be construed as an official action or opinion of the Society of Petrophysicists and Well Log Analysts, Inc. © Copyright 2022 by the Society of Petrophysicists and Well Log Analysts, Inc.

About the Cover

In this issue, Kotwicki et al. explain how integration of all logging technologies is key to defining sand content and hydrocarbon potential. It is important that all techniques show some indication of sand or hydrocarbon potential at a given depth. Over or underestimation from the various techniques should be understood and adequately dealt with in the final interpretation. In this image, the authors show an ultradeep resistivity inversion along a Froskelår geological sidetrack with seismic interpretation. The black arrows indicate near-wellbore sands not captured in the seismic interpretation.

PRINTED IN THE USA ON ACID-FREE PAPER

PETROPHYSICS

February Vol. 63, No. 1

Contents

- 3 From the Editor

ARTICLES

- 4 **New Logging Tool for Enhanced Oil Recovery and Gas Storage Monitoring Applications**
A. Ballard Andrews and Andrew J. Speck
- 12 **Automated Well-Log Depth Matching – 1D Convolutional Neural Networks vs. Classic Cross Correlation**
Veronica Alejandra Torres Caceres, Kenneth Duffaut, Anis Yazidi, Frank O. Westad, and Yngve Bolstad Johansen
- 35 **Automated Log Data Analytics Workflow – The Value of Data Access and Management to Reduced Turnaround Time for Log Analysis**
Veronica Alejandra Torres Caceres, Kenneth Duffaut, Frank Ove Westad, Alexey Stovas, Yngve Bolstad Johansen, and Arne Jenssen
- 61 **Ultrasonic Logging of Creeping Shale**
Anja Diez, Tonni F. Johansen, and Idar Larsen
- 82 **Evaluating Petrophysical Properties and Volumetrics Uncertainties of Sand Injectite Reservoirs – Norwegian North Sea**
Artur Kotwicki, Mirza Hassan Baig, Yngve Bolstad Johansen, Guro Leirdal, Brage Vikauane Aftret, Odd Arne Sandstad, Anne Mette Anthonsen, Bruis Gianotten, Tor Arne Hansen, and Mauro Firinu
- 104 **Investigating Delaware Basin Bone Spring and Wolfcamp Observations Through Core-Based Quantification: Case Study in the Integrated Workflow, Including Closed Retort Comparisons**
Stephanie E. Perry, J. Alex Zumberge, and Kai Cheng

Full-color versions of all technical articles are available in the digital edition of PETROPHYSICS, which is free to SPWLA members and can be found at https://www.spwla.org/SPWLA/Publications/Journals/Recent_Petrophysics_Journals.aspx.

The Society of Petrophysicists and Well Log Analysts is dedicated to the advancement of the science of formation evaluation through well logging and other formation evaluation techniques. SPWLA is dedicated to the application of these techniques, to the exploration and exploitation of gas, oil and other minerals. PETROPHYSICS publishes original contributions on theoretical and applied aspects of formation evaluation; particularly well logging and petrophysics.

As of Vol. 46 (1) 2005,
PETROPHYSICS [ISSN: 1529-9074]
is indexed and abstracted in
Thomson Reuters:
Scientific Citation Index Expanded
Journal Citation Report–Science
Current Contents—Physical, Chemical,
and Earth Sciences

PETROPHYSICS Editor



Songhua Chen
Halliburton
VP-Publications@spwla.org
(+1) 281-871-7253

Associate Editors



Acoustics and Rock Physics
Alexei Bolshakov, *Chevron*



Carbon Capture, Utilization, and Storage
Robert Laronga, *Schlumberger*



Core Analysis and Laboratory Petrophysics
Josephina Schembre, *Chevron*
S. Mark Ma, *Saudi Aramco*



Electromagnetics
Hui Xie, *Schlumberger*



Formation Testing
Melton Hows, *Shell*



Integrated Formation Evaluation
Chengbing Liu, *Saudi Aramco*
Haijing Wang, *Chevron*



Integrated Formation Evaluation and Case Studies
Hesham El-Sobky, *ConocoPhillips*



Magnetic Resonance
Lalitha Venkataraman, *Schlumberger*
Wim Looyestijn, *Shell*



Mud Logging and Surface Logging
Jinhong Chen, *Aramco Americas*



Nuclear
Pingjun Guo, *ExxonMobil*



Petroleum Geochemistry
Drew Pomerantz, *Schlumberger*



Well and Reservoir Surveillance
Michael Ehiwario, *Shell*



Data-Driven Analytics
Chicheng Xu, *Aramco Services*
Radompon Sungkorn, *Halliburton*

The Society of Petrophysicists and Well Log Analysts Board of Directors 2021–2022



President
Katerina Yared
SM Energy
Highlands Ranch, CO, USA
(+1) 720-431-7482
President@spwla.org



**VP Finance, Secretary,
and Administration**
Adam Haecker
Continental
OKC, OK USA
(+1) 979-587-1061
VP-Finance@spwla.org



President Elect
Tegwyn Perkins
Lloyd's Register
Houston, TX, USA
(+1) 713-670-4976
President-Elect@spwla.org



VP Publications
Songhua Chen
Halliburton
Houston, TX, USA
(+1) 281-871-7253
VP-Publications@spwla.org



VP Technology
Carlos Torres-Verdin
University of Texas at Austin
Austin, TX, USA
(+1) 512-471-4216
VP-Technology@spwla.org



VP Information Technology
Harry Xie
CoreLab
Houston, TX USA
(+1) 713-328-2768
VP-InfoTech@spwla.org



VP Education
Fransiska Goenawan
Halliburton
Houston, TX, USA
(+1) 346-401-8201
VP-Education@spwla.org



VP Social Media
Mathilde Luyckx
ExxonMobil
Houston, TX USA
VP-SocialMedia@spwla.org

REGIONAL DIRECTORS



N. America 1
Robin Slocombe
Schlumberger
Houston, TX, USA
(+1) 281-690-0837
Director-NA1@spwla.org



Middle East/Africa
Nelson Suarez
Roccia Energy
Mexico City, Mexico
(+1) 786-458-7130
Director-ME@spwla.org



North America 2
Matthew Blyth
Schlumberger
Houston, TX USA
(+1) 832-444-4206
Director-NA2@spwla.org



Asia Pacific/Australia
Ryan Lafferty
Consultant
Bangkok, Thailand
Director-Asiapacific@spwla.org



Latin America
Bruno Menchio Faria
Rio de Janeiro, Brazil
(+55) 219-9140-150
Director-LA@spwla.org



Executive Director
Sharon Johnson
SPWLA
Houston, TX 77017
(+1) 713-947-8727
sharon@spwla.org



Europe
Eva Gerick
Neptune Energy
Aberdeen, United Kingdom
(+44) 799 958 0218
Director-Europe@spwla.org



Managing Editor
Elizabeth Naggar
(+1) 713-444-3495
editor@spwla.org

Publication Manager
Anna Tarlton
InkSpot Printing
2301 S. Shaver
Pasadena, TX 77502, USA
(+1) 713-472-1100
orders@inkspotprinting.com

FROM THE EDITOR

Welcome to the February 2022 issue of *Petrophysics*.

Recently, we have updated the *Petrophysics* journal technical classifications and aligned these classifications with our Associate Editors (AEs). A few new classifications, such as CCUS, have been added to reflect the increased interest of the petrophysics community's involvement in this environmental science and technology advancement. We also welcomed three new technical experts in their respective fields, Jinhong Chen, Robert Laronga, and Radompon Sungkorn, to join our AE team. These additions certainly will strengthen our peer-review capability.

Entering 2022, we have reviewed our editorial process for the past year. While all AEs and Elizabeth have done a great job of making the process hum along very well, we also recognized that, occasionally, the turnaround time of the reviewing feedback for a few submissions was a bit longer than anticipated. We made a new year's resolution to improve the reviewing turnaround time. I would like to also thank the authors who gave us timely feedback when any issue came up. Your feedback certainly motivates us to make improvements.

The current issue includes six papers on a variety of topics, including production logging, data analytics workflow and applications, and petrophysical analysis of unconventional reservoirs and sand injectites, as well as a plug and abandonment (P&A) application. Andrews and Speck describe a new production logging tool that introduces downhole zonal gas composition analysis to the production logging tool string. The tool unlocks key applications related to gas reservoir management, including enhanced oil recovery applications such as injection monitoring, pressure maintenance, and identification of layers that contain low-calorific-value gas.

Two papers by Torres et al. are related. The first one presents the application of deep-learning techniques to tackle the common problem of well-log depth mismatch and well coordination. In their work, seven CNN models were trained corresponding to the seven logging measurements used. The CNN models identify patterns between well logs acquired in the same depth section at different times, e.g., logging while drilling (LWD) and electrical wireline logging (EWL), and suggest depth shifts to improve their alignment. The results are compared and evaluated against a classical cross-correlation method.

The second Torres et al. paper presents a prototype well-log database built using Python programming and based on raw well-log data files such as DLIS. They propose that a single well consisting of several DLIS files is converted into a unique HDF5 format, which supports a variety of data types and can allocate the information in different folders or group levels with their corresponding metadata. In addition, the database is integrated with a semi-automatic well-log depth matching workflow by using two different methods, such as cross correlation and dynamic time warping (DTW). A complete depth-matching workflow is developed to synchronize a suite of LWD and EWL logs simultaneously using these two methods. The pros and cons of the cross-correlation method and DTW method are discussed.

Diez et al.'s paper presents a P&A application that is quite unique for petrophysical application. For P&A processes, the possibility of shale bonding to the well casing that forms a natural barrier is explored. This paper presents a unique laboratory experiment of creeping shale in a pressure cell, which is monitored during the creep and bonding processes using the ultrasound measurement techniques: pulse echo (PE) and pitch catch (PC). An improved understanding of the bonding process is gained by combining high-resolution measurements over time in one direction and regular measurements with high azimuthal resolution using PE and PC ultrasound measurements.

Kotwicki et al. describe the petrophysical properties of sand injectite facies, dykes, sills, and brecciated sands, along with their identification from seismic data. A perception that volumetrics of sand injectite reservoirs cannot be reliably evaluated from petrophysical logs is assessed. Their result confirmed that the Thomas-Stieber method could be used for brecciated rocks and sand injectite reservoirs, which leads to some useful recommendations on how to best log and perform a petrophysical evaluation in such reservoirs.

Perry et al.'s paper focuses on five Delaware Basin wells spatially covering Loving, Ward, and Reeves counties in West Texas, where whole core samples were acquired and investigated to compare variations in the Bone Spring and Wolfcamp Formations across varying geological contexts. Integration of geological context with measured laboratory data constraints and petrophysical wireline-log-based interpretation links predictive trends from the defined rock and fluid property distributions and may aid in predicting hydrocarbon vs. water production.

Reading such diverse topics certainly is inspiring. That is why I like to read *Petrophysics*—it is never boring.

Best,
Songhua Chen

New Logging Tool for Enhanced Oil Recovery and Gas Storage Monitoring Applications

A. Ballard Andrews¹ and Andrew J. Speck¹

ABSTRACT

There is currently no production logging tool that can analyze in-situ gas composition in wells that intersect more than one pay zone. In high-value gas wells, zonal isolation is useful for enhanced oil recovery (EOR) applications such as injection monitoring, pressure maintenance, and identification of layers that contain low-calorific-value gas. To unlock these key applications related to gas reservoir management, a new production logging tool was developed that introduces downhole gas composition analysis to the

production logging tool string. The tool does not require a formation seal and so can log continuously or at a station. For gas field applications with pressures above 3,000 psi, the estimated mole fraction errors in continuous logging mode are ~2% for methane and ~1% for ethane, propane, nitrogen, and carbon dioxide. In formations with lower pressures, station logs can achieve mole fraction errors < 1% for all components.

INTRODUCTION

Formation testing tools determine composition by measuring the infrared vibrational bands of hetero-atomic species such as CH, CO, and OH in the visible to near-infrared using absorption spectroscopy (Mullins, 2008). Raman scattering excites modes of hetero-atomic and mono-atomic species in the fingerprint region (900 to 3,400 cm⁻¹) and can meet the needs of EOR and gas storage applications. Moreover, it is ideal for casedhole logging: the scattered photons can be detected using a backscattering geometry, obviating the need for an internal flowline and/or mechanical pumps, which are not easily accommodated through the surface trees of producing wellheads.

A novel high-temperature laser and spectrometer were developed for Raman spectroscopy. The prototype has been tested in a gas storage well and a producing well with good results. For high-value multizone vertical producing gas wells, the tool enables a suite of applications that can be part of a larger strategy of increasing the recovery factor of the entire asset. For hydrogen storage in depleted reservoirs, the tool could enable in-situ monitoring of chemical, microbial, and loss mechanisms which, at present, are not fully understood.

METHODOLOGY

Methane has a CH stretch band at 2,916 cm⁻¹, ethane has a unique CC stretch mode at 992 cm⁻¹, and propane at 869 cm⁻¹ (Fig. 1). Carbon dioxide has CO stretch bands at 1,386 and 1,281 cm⁻¹, and nitrogen has an NN stretch at 2,329 cm⁻¹. Hydrogen has rotational S branches at 584.5 cm⁻¹ and 1,035 cm⁻¹. From the Raman intensities of these bands, the mole fractions of H₂, CO₂, CH₄, N₂, and H₂S can be determined.

The main steps of the algorithm are illustrated in the flow chart in Fig. 2. The pure gases are measured in the laboratory, and a calibration file records the Raman intensity vs. molar density. During a logging run, the calibration file is used in conjunction with the inversion algorithm (below) to calculate the gas composition on a zone-by-zone basis in the borehole. To first order, the Raman intensity is linearly proportional to the molar density. An additional linear response term $1 + 3r_m\rho_m$, where the molar refractivity $r_m = 1/\rho_m (n^2 - 1)/(n^2 + 2)$, ρ_m is the number density, and n is the index of refraction of the gas, is included to account for index variations with gas density that affect the sample excitation volume.

Manuscript received by the Editor August 26, 2021; revised manuscript received November 11, 2021; manuscript accepted November 11, 2021.
¹Schlumberger-Doll Research, bandrews@slb.com; aspeck@slb.com

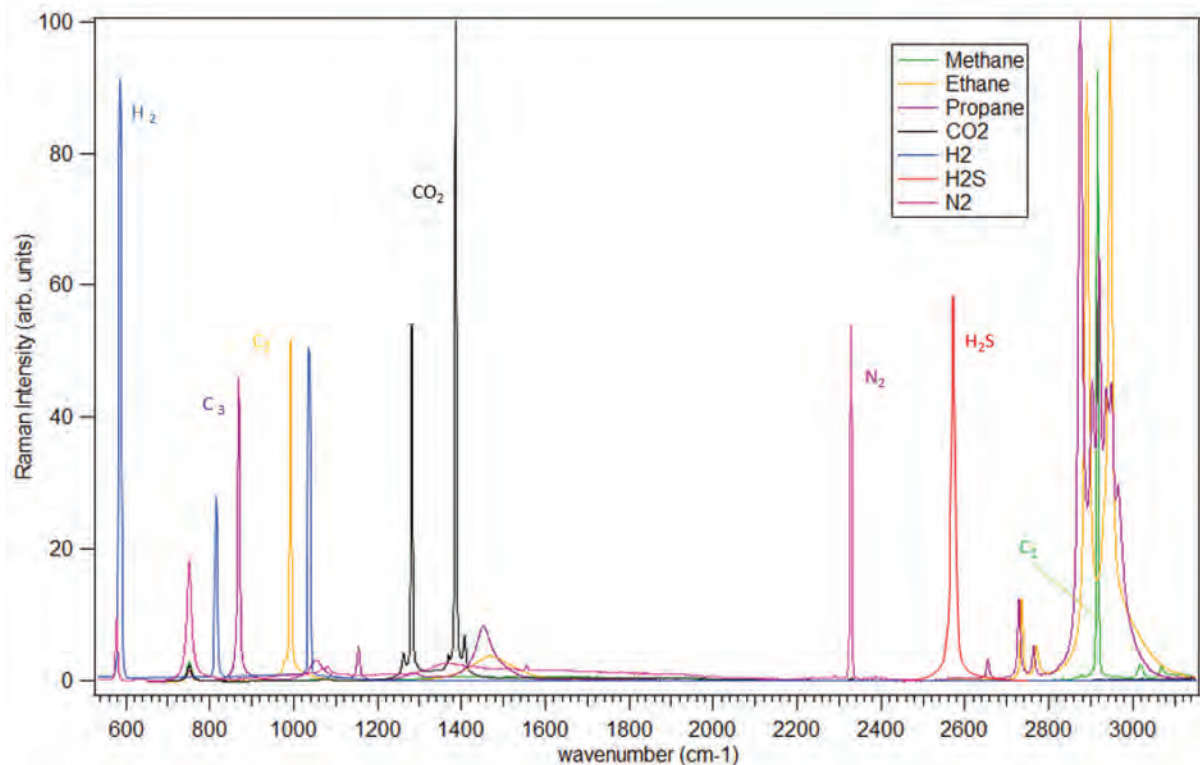


Fig. 1—Raman stretch modes of pure components for H₂, N₂, CO₂, H₂S, and C₁ through C₃ (arbitrary units). H₂ has prominent rotational S branches at 584.5 cm⁻¹ and 1,035 cm⁻¹. Methane has a CH stretch band at 2,916 cm⁻¹, and CO₂ has two CO stretch bands at 1,386 and 1,281 cm⁻¹.

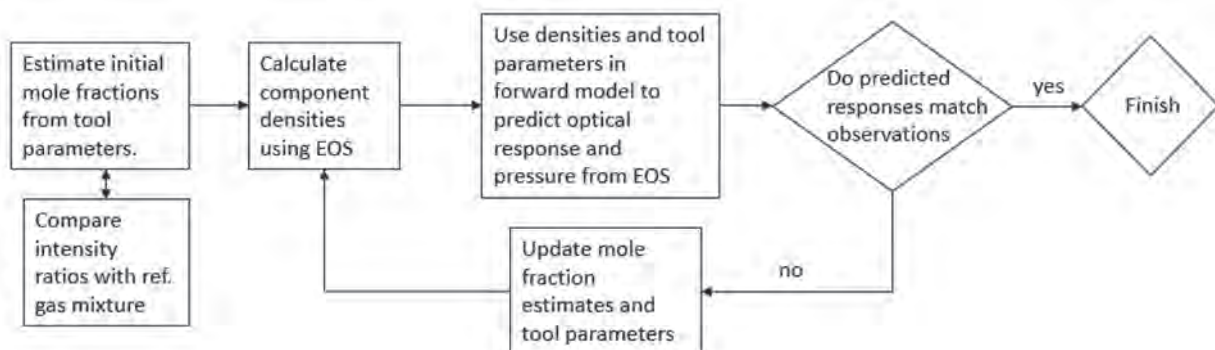


Fig. 2—Algorithm to determine composition from the molar densities of measured gases as described in the text.

To determine the composition of each reservoir zone, a conventional production logging tool on the string measures the total volumetric flow rate Q_n above each layer using standard production logging techniques. The Raman spectrometer returns a signal proportional to the mass fractions of each component, measured at the same depths

as Q_n . If the number of compositional components is y and f_{n_x} is the mole fraction of the x^{th} compositional component to the n^{th} zone, it can be shown using the ideal gas law that the production fluid flow rates (of each component) are given by

$$Q_{n_x} = \frac{f_{n_x}}{f_{n_1} + f_{n_2} + f_{n_3} + \dots + f_{n_y}} Q_n \frac{P_n T_{ref} Z_{ref}}{P_{ref} T_n Z_n} \quad (1)$$

The mole fractions f_{n_x} are measured by the spectrometer, which obtains a signal proportional to the number density of each component at each of the zones. In Eq. 1, the pressure P_n at each of the zone-associated depths has been normalized by a factor P_n/P_{ref} to account for borehole pressure changes between zones that might appear as changes in flow rate, due to the corresponding volumetric changes. Changes in temperature and compression factor resulting from departures from the ideal gas law are accounted for by factors T_{ref}/T_n and z_{ref}/z_n , where the reference conditions are standard conditions. It follows then that the zonal contribution to the n^{th} zone of the x^{th} compositional component is given by

$$q_{n_x} = Q_{n_x} - Q_{n-1_x} \quad (2)$$

Most optical measurements provide a response that is proportional to the number density, ρ_m , of the analyte. For gases, this scales with both pressure and temperature [e.g., for ideal gases $\rho_m = P/(k_b T)$] and thus depends on both the well conditions and the fluid composition. To convert this to mole fractions, a knowledge of the total density of all molecules in the sample volume is needed. In typical measurements, to calculate mole fractions, the assumption is thus made that only the analytes capable of being measured optically are present, which leads to errors due to the unobserved fraction. The method described below allows us to infer the concentration of unobserved species. Additionally, to convert the measured optical response into an absolute number density, an overall system calibration factor is needed to remove the effect of optical losses throughout the signal path. This is typically done by measuring a reference fluid at surface prior to a job, but for many measurements, this factor can change over time due to optical misalignment or contamination of the windows. In many configurations, it is impossible to account for this factor in real time, and thus it increases the error of a measurement.

A core principle of our methodology is that, for gases, knowing the pressure and temperature provides an additional constraint to optical responses proportional to absolute densities. This allows one to infer the mole fractions of the sample gas along with either additional components unresolved by the optical measurement or the overall system gain factors. The basic method is to develop the forward model of the tool response as a function of absolute densities of the measured analytes. To provide these inputs, an equation of state is used to predict the absolute densities as a function of pressure, temperature, and mole fractions of the sample gas. By adjusting the inputs so that the predicted

optical response matches the measured responses, the best-fit mole fractions can be inferred by the optimization method of choice (e.g., nonlinear fitting, Bayesian inference, etc.).

To demonstrate these methods, we can first consider a trivial model comprising Raman scattered signals for l gases and o measurement channels, X_m that are linearly proportional to the absolute densities of the analytes, ρ_m , through a response matrix, and M of size o rows by l columns. As such

$$\vec{X} = M\vec{\rho} \quad (3)$$

Similarly, we can assume the ideal gas law holds for all the analytes so that

$$\vec{\rho} = \vec{f} \frac{P}{k_b T} \quad (4)$$

where f_m is the mole fraction for analyte, m . Combining these equations and also adding the relationship that the sum of the mole fractions must equal 1, we find

$$\begin{aligned} \vec{X} &= M\vec{f} \frac{P}{k_b T} \\ \Sigma \vec{f} &= 1 \end{aligned} \quad (5)$$

The system is thus overdetermined, and it is possible to infer one more parameter of interest. This can be either the overall system calibration factor, G , such that

$$\vec{X} = G(M\vec{\rho}) \quad (6)$$

or it can be an additional gas that has small overlapping optical responses to the tool. In this case, the response matrix is enlarged by one column to include the responses of the unresolved measurements (M of size o rows by $l + 1$ columns). In either case, for a well-defined response matrix, M , we have enough independent measurements to determine all the components of \vec{f} .

In a real-world system, the response function is likely not to be a simple linear matrix. For example, in a Raman measurement, there could be additional linear response terms due to the densities of the gas (due to index variations with density that affect the sample volume) and an exponential dependence on the concentrations of other gases from cross absorption such that the signal for a single channel is approximately

$$X_i = (M_{ij} \rho_j)(1 + 3n_k r_k)(10^{-\alpha_{io} n_o l}) \quad (7)$$

where r_k is the molar refractivity of gas k , α_{io} is the absorption coefficient of gas o at measurement channel i , and l is the optical path length within the sample volume. For other measurements, such as transmission optical spectroscopy, the response function might be given by Beer's law:

$$X_i = (10^{-\alpha_{io} n_o l}) \quad (8)$$

In many of these nonlinear cases, Bayesian inference allows us to cleanly define through prior knowledge the region of allowed mole fractions and thus ensure the inversion occurs in a unique region. In a case where the ideal gas law is not accurate enough, an equation of state that accounts for interactions between molecules may be used.

INSTRUMENTATION

Raman scattering is highly inefficient: only approximately 1 in 10^8 photons are scattered. Approximately one-hundred quadrillion photons/pulse are required to detect a million photons/pulse for pure methane at 5,000 psi, considering the Raman cross section, collection, and detection efficiencies. As such, a laser is the only suitable light source.

Semiconductor laser diodes (LD) suffer from fundamental physics limitations and catastrophic packaging flaws that preclude use in a logging tool. Above about 100°C, LD do not typically lase as the cavity losses exceed the optical gain; moreover, the output wavelength is unstable due to shifts from thermal effects. In such a harsh environment, a laser must provide adequate optical power at high temperature and stable center wavelength along with withstanding high shock and vibration without cavity misalignment.

A high-temperature, high-energy pulsed solid-state laser (SSL) capable of withstanding shock and vibration was developed. A combination of modeling using the rate equation with a saturable absorber (Bass et al., 2003; Koechner, 2006) and discrete component testing was employed to evaluate the optimal combination of key laser parameters to produce the requisite pulse energy: the high reflector (HR), output coupler (OC) coatings, and Q-switch transmission. A simplified mockup prototype was tested in an oven cycling between 25°C and 200°C and showed excellent results. The output center wavelength was stable with a shift of less than 1 nm (Fig. 3), and the pulse energy increases with temperature due to a reduction in the stimulated emission cross section that allows more energy to be stored prior to reaching Q-switch saturation.

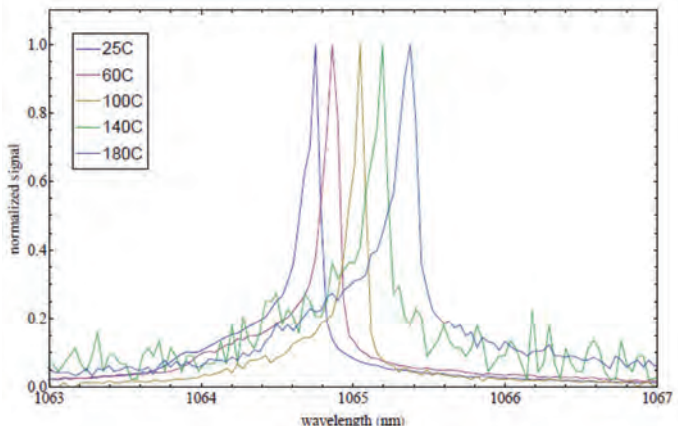


Fig. 3—Wavelength shift vs. temperature.

To circumvent the risk of cavity misalignment from shock and vibration during logging operations, a monolithic laser rod was fabricated. In particular, the Nd:YAG gain medium and Cr:YAG passive Q-switch were diffusion bonded into a monolithic structure, and the end facets were polished and coated with dielectric films. The gain medium is optically pumped by an uncooled flashlamp with a trigger wire, powered by a pulse-forming network comprising a capacitor bank, inductor, and high-voltage power supply. With an OC reflectivity of 50% and Q-switch T0 also at 50%, the laser produces 10-ns-long, 40-mJ pulses supplying 4-MW peak power.

The laser excitation is free space coupled through a sapphire viewport, which seals the tool body from the well pressure. To further minimize the risk of ablation and plasma formation, which would risk tool flooding, an imaging system using crossed microlenses was developed, which spreads out the beam energy without sacrificing photon count rate or collection efficiency, producing a homogeneously illuminated distribution in the focal plane. Collection optics include a multileg fiber bundle, which splits the Raman signal into channels for each analyte, including two baselines to compensate for background drift and a crystal to act as a reference. A normalization channel compensates for pulse-to-pulse variations in the laser power. The spectrometer incorporates integrating charge-sensitive amplifiers with response times that match the short laser pulses and produce output voltages proportional to the integral of the current or total number of photons (Fig. 4). The tool outer diameter is 1.6875-in., and the tool can access the majority of multizone vertical gas-condensate-producing wells and gas storage wells.



Fig. 4—The Raman spectrometer has five analyte channels that can be configured for any combination of methane, ethane, propane, carbon dioxide, nitrogen, water, or hydrogen. The pulse-forming network comprises a capacitor bank, inductor, and high-voltage power supply.

APPLICATIONS

In high-value gas wells, zonal isolation is useful for EOR applications such as injection monitoring, pressure maintenance, and identification of layers that contain low-calorific-value gas (Andrews et al., 2020). In the example illustrated in Fig. 5, a lean gas (e.g., mostly methane) is pumped into an injector well by surface equipment to sweep gas condensate from zones of a formation to a producing well. In one of the zones, the sweeping fluid from the injector well has broken through into the producing well. The breakthrough is detected using the surface equipment, but the location of the breakthrough is unknown because the flow is commingled. By measuring the ratios of compositional components at depths associated with each of the zones, the tool can identify in which zone the breakthrough has occurred. The zone can then be shut in by wireline or slickline remediation and/or other means. Because of the shut-in, less compressed gas, water, and/or other sweeping agent are returned to the surface through the production well, and condensate swept from the other zones is thus increased.

In Fig. 6, a well is depicted extending through the formation, including intersecting sand bodies and/or other zones having variable CO₂ content. The net caloric content of the commingled production fluid flow is lowered because of the contribution of zones with the higher CO₂ content. The tool can measure the CO₂ proportion of the zonal fluid flow from each of the sand bodies. For example, the CO₂ proportion of the sand bodies may be less than 10%, whereas the CO₂ proportion of another sand body may be greater than 20%. Accordingly, the sand body with the higher CO₂ proportion may be shut in. As a result, more CO₂ may be sequestered downhole instead of being separated and/or otherwise handled by the surface equipment.

Hydrogen is generated through electrolysis of water and can be injected and recovered from underground salt caverns. However, salt caverns are limited in size and geographical distribution, and cannot meet the anticipated global demand for hydrogen storage. Depleted oil and/or gas reservoirs can be exploited for hydrogen storage, but there are many technical uncertainties that must be addressed before widespread commercial adoption is feasible. In depleted reservoirs, compositional changes can occur due

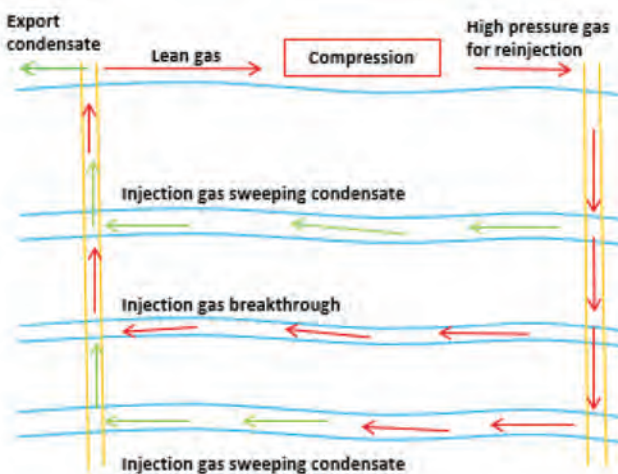


Fig. 5—Brownfield in which an injection gas, such as methane or nitrogen, is used for drainage. The tool can identify the breakthrough zone(s).

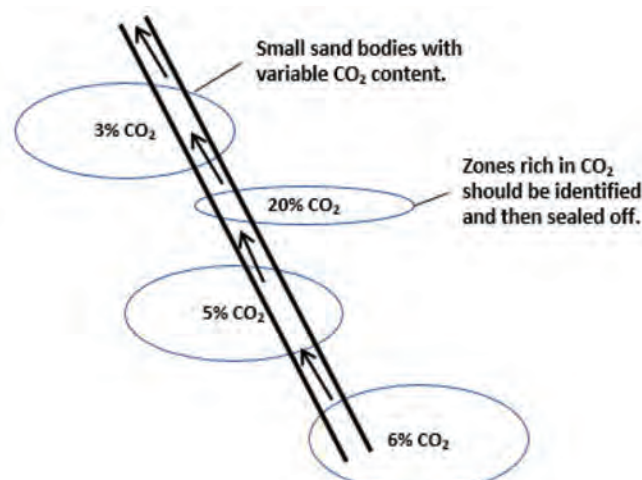


Fig. 6—A well intersects multiple sand bodies, with variable CO₂ concentrations. The tool identifies the sand bodies with higher CO₂ content.

to chemical reactivity, microbial activity, and differential leakage, resulting in irrecoverable loss. These processes are complex and difficult to model on the reservoir scale. Surface measurements can analyze the composition of the recovered commingled gases. However, gas mixing on a reservoir scale is slow relative to the cycle times for injection and withdrawal from storage. Therefore, compositional changes can be localized. Zonal isolation is necessary to identify the subsurface regions in which these processes occur, and in-situ compositional measurements are key (Fig. 7).

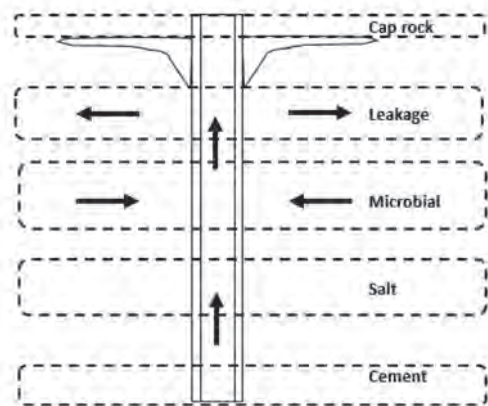


Fig. 7—There may be reactions with subsurface minerals in a depleted reservoir used for hydrogen storage. A microbial layer containing methanogens may consume either CO_2 or H_2 and produce CH_4 and/or H_2S as an unwanted byproduct. A cement layer may react with H_2 . A porous layer may lead to irrecoverable loss of hydrogen to the formation.

RESULTS

Figure 8 shows a plot of the CH stretch intensity vs. molar density for methane and propane recorded in the laboratory. Figure 9 shows data from a producing well with a single zone logged continuously at 3,600 ft/hr with gas phase composition 100% methane and liquid phase composition 100% water.

After a baseline calibration using only pure components, natural gas mixtures were measured, and mole fraction errors (MFE) were calculated over a range of pressures. Molar concentration errors were averaged from all mixtures and converted into errors in partial pressures assuming an ideal gas law and a temperature of 25°C. From the known temperatures and pressures of several exemplary gas fields, we can predict the MFE accuracies we expect to achieve for the instantaneous signal if the tool is run in the fields (Fig. 10). For gas field applications with pressures above 3,000 psi, the MFE in continuous logging mode are ~2% for methane and ~1% for ethane, propane, nitrogen, and carbon dioxide. For lower pressures, from 1,500 to 3,000 psi, the MFE are larger, but with station logs, statistical averaging can achieve errors of less than 1% for all components after 1 hour (Fig. 11).

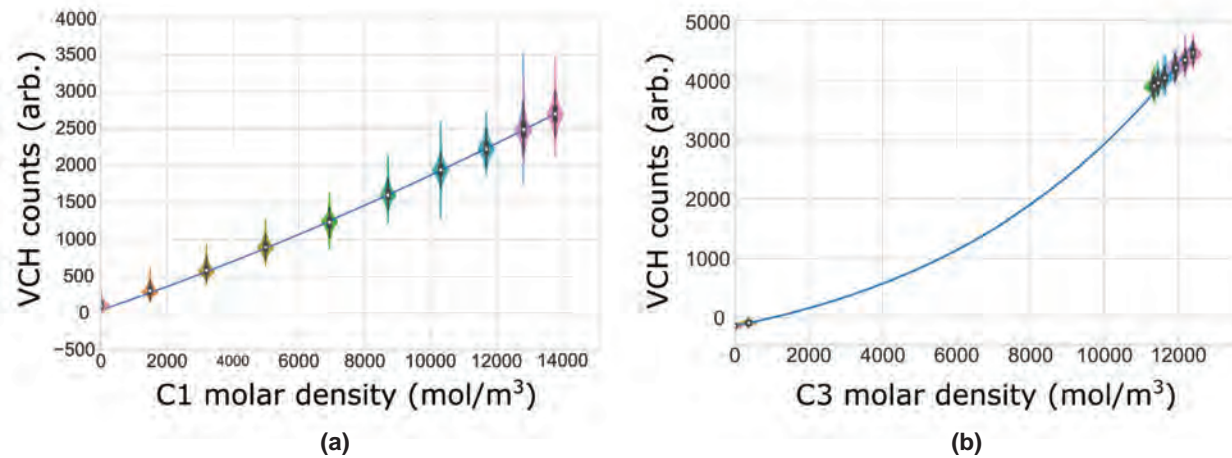


Fig. 8—(a) Methane CH stretch intensity vs. molar density and (b) propane CH stretch intensity vs. molar density across phase transition. The solid lines are fits to the data, and the violin plots show the raw data distribution.

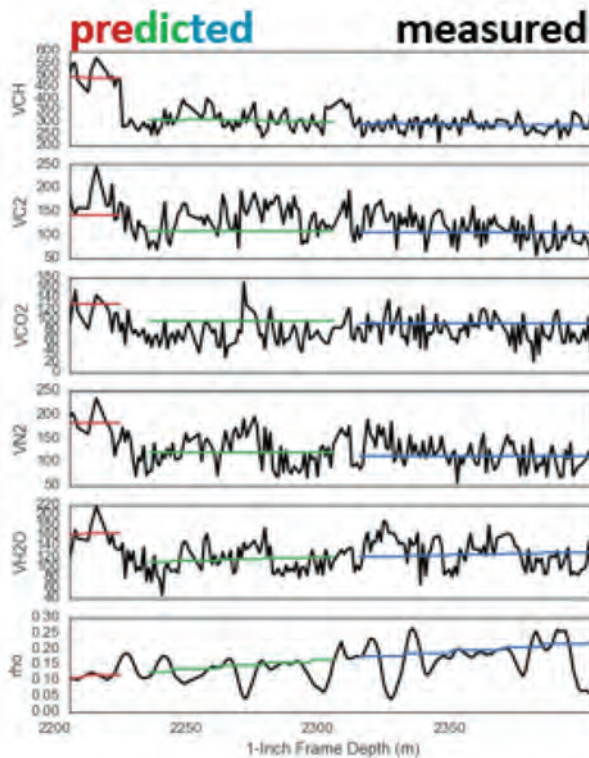


Fig. 9—Measured data (black) vs. predictions (red/blue/green) for the signals assuming multiple zones, each with fixed composition. Gas (liquid) phase composition was 100% methane (water). The producing well was logged continuously at 3,600 ft/hr.

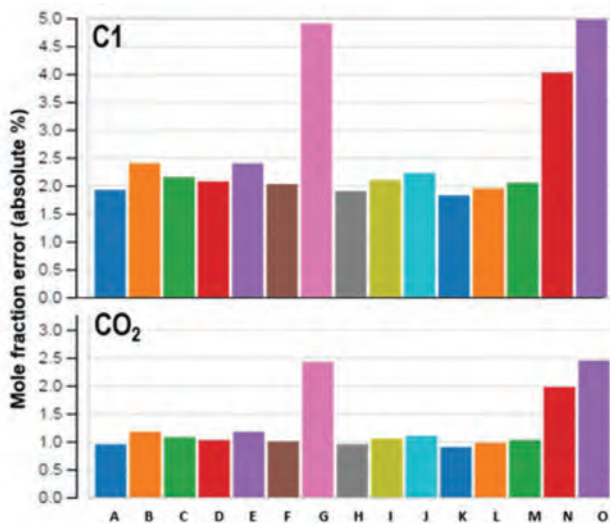


Fig. 10—Instantaneous C₁ and CO₂ mole fraction errors for exemplary Gas Fields A through O. For gas fields with pressures above 3,000 psi, the estimated MFE in continuous logging mode are ~2% for methane and ~1% for ethane, propane, nitrogen, and carbon dioxide. Fields with pressures from 1,500 to 3,000 psi (G, N, and O) can achieve lower MFE with station logs (Fig. 11).

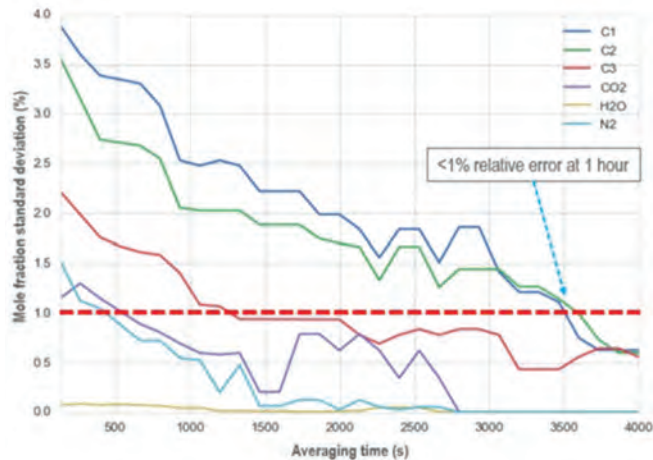


Fig. 11—For fields with higher MFE in continuous logging mode resulting from the lower pressures (G, N, and O in Fig. 10), station logs can achieve errors less than 1% for all components.

CONCLUSIONS

The development of a high-powered pulsed laser that can operate at high temperature provides significant noise reduction compared to continuous noise sources and, furthermore, enables applications related to gas reservoir management (EOR) as well as the potential to be used for gas storage monitoring, such as carbon capture and sequestration/storage (CCS) and hydrogen storage.

Raman spectroscopy probes the fingerprint region where the pattern of peaks for each molecule is unique and excites modes of homonuclear diatomic molecules such as nitrogen and hydrogen, which are not infrared active. To our knowledge, no downhole tool has both these capabilities—features that are key for some of the applications described above.

More broadly, the laser opens up the possibility of new downhole measurements. For example, by coupling with nonlinear optical materials and performing wavelength conversion, absorption spectroscopy at wavelengths from the UV to the far-infrared is feasible. Thus, it is a key enabler for multiple downhole measurements not limited to Raman spectroscopy.

NOMENCLATURE

Abbreviations

CC = carbon-carbon	Kingdom of Saudi Arabia, 13–15 January. DOI: 10.2523/IPTC-19990-Abstract.
CCS = carbon capture sequestration/storage	Bass, M., Weichman, L.S., Vigil, S., and Brickeen, B.K., 2003, The Temperature Dependence of Nd ³⁺ Doped Solid-State Lasers, <i>IEEE Journal of Quantum Electronics</i> , 39 (6), 741–748. DOI: 10.1109/JQE.2003.810773.
CH = carbon-hydrogen	Mullins, O.C., 2008, <i>The Physics of Reservoir Fluids; Discovery Through Downhole Fluid Analysis</i> , Schlumberger, Houston, Texas. ISBN: 978-0978853020.
CH ₄ = methane	Koechner, W., 2006, <i>Solid-State Laser Engineering</i> , sixth edition, Springer. DOI: 10.1007/0-387-29338-8. ISBN: 978-0-387-29338-7.
CO ₂ = carbon dioxide	
Cr:YAG = chromium: yttrium aluminum garnet	
EOR = enhanced oil recovery	
H ₂ = hydrogen	
H ₂ S = hydrogen disulfide	
HR = high reflector	
LD = semiconductor laser diode	
MFE = mole fraction error	
mJ = millijoule	
MW = mega-watts	
N ₂ = nitrogen	
Nd:YAG = neodymium: yttrium aluminum garnet	
ns = nanosecond	
OC = output coupler	
OH = oxygen-hydrogen	
ref = standard conditions	
SSL = solid-state laser	
UV = ultraviolet	

Symbols

cm^{-1} = wavenumber	
f_{n_x} = mole fraction of gas x at n^{th} zone	
G = system calibration factor	
k_b = Boltzmann constant	
M = response matrix	
n = index of refraction	
P_n = pressure at depth of n^{th} zone	
Q_n = total volumetric flow rate	
q_{n_x} = contribution to n^{th} zone of x^{th} compositional component	
r_m = molar refractivity	
T_n = temperature at depth of n^{th} zone	
X_i = response function	
α_{io} = absorption coefficient	
ρ_m = number density of analyte m	

REFERENCES

Andrews, A.B., Speck, A., McCowan, D., and Mukerji, P., 2020, Real-Time Downhole Zonal Gas Composition Tool for Production Logging, Paper IPTC-19990 presented at the International Petroleum Technology Conference, Dhahran,

Kingdom of Saudi Arabia, 13–15 January. DOI: 10.2523/IPTC-19990-Abstract.

Bass, M., Weichman, L.S., Vigil, S., and Brickeen, B.K., 2003, The Temperature Dependence of Nd³⁺ Doped Solid-State Lasers, *IEEE Journal of Quantum Electronics*, **39**(6), 741–748. DOI: 10.1109/JQE.2003.810773.

Mullins, O.C., 2008, *The Physics of Reservoir Fluids; Discovery Through Downhole Fluid Analysis*, Schlumberger, Houston, Texas. ISBN: 978-0978853020.

Koechner, W., 2006, *Solid-State Laser Engineering*, sixth edition, Springer. DOI: 10.1007/0-387-29338-8. ISBN: 978-0-387-29338-7.

ABOUT THE AUTHORS



A. Ballard Andrews is a scientific advisor in the Perception and Sensing program at Schlumberger-Doll Research Center in Cambridge MA, USA. His current research focuses on high-pressure, high-temperature Raman and infrared spectroscopies and emissions monitoring. He graduated from the University of Texas at Austin with a PhD degree in condensed matter physics in 1991. His doctoral and post-doctoral research was conducted at the National Synchrotron Light Source at Brookhaven National Laboratory. He has more than 50 peer-reviewed publications, has coauthored book chapters in the *Handbook of Physics and Chemistry of the Rare Earths* and the *Springer Handbook of Petroleum Technology*, and has 20 granted patents.



Andrew J. Speck is a principal scientist and program manager of the Perception and Sensing program at Schlumberger-Doll Research Center in Cambridge, MA, USA. His research focuses on a wide range of sensing methodologies, including the development of novel downhole optical sensors, emissions monitoring, and undersea autonomous vehicles. He graduated from Harvard University with a PhD in physics in 2005. He is a recipient of the Henri Doll Prize for Innovation and the Maurice and Gertrude Goldhaber Prize for outstanding graduate achievement in experimental physics. He has coauthored 19 peer-reviewed publications and has seven granted patents.

Automated Well-Log Depth Matching – 1D Convolutional Neural Networks vs. Classic Cross Correlation

Veronica Alejandra Torres Caceres¹, Kenneth Duffaut¹, Anis Yazidi¹, Frank O. Westad¹, and Yngve Bolstad Johansen²

ABSTRACT

During drilling and logging, depth alignment of well logs acquired in the same borehole section at different times is a vital preprocessing step before any petrophysical analysis. Depth alignment requires high precision as depth misalignment between different log curve measurements can substantially suppress possible correlations between formation properties, leading to imprecise interpretation or even misinterpretation. Standard depth alignment involves cross correlation, which typically requires user intervention for reliability. To improve the depth alignment process, we apply deep-learning techniques and propose a simple and practical implementation of a one-dimensional (1D) supervised convolutional neural network (1D CNN). We train seven CNN models using different log measurements, such as gamma ray, resistivity, P- and S-wave sonic, density, neutron, and photoelectric factor (PEF), to estimate depth mismatches between the corresponding raw logging-while-drilling (LWD) and electrical-wireline-logging (EWL) logs of each measurement type. Our deep-learning approach avoids manual feature extraction; hence, no high-level petrophysical knowledge is needed by our algorithms. We use log data from six wells from

the Ivar Aasen Field in the Norwegian North Sea. Four of the six wells constitute the entire data set for training and model selection, in which we compare three search algorithms during the hyperparameter tuning. Only two wells have both LWD and EWL log suites. These wells are used for depth-shift inference. We focus on estimating bulk shifts, and we assume the existence of small pattern differences. We assess our results by visual inspection and quantitative metrics such as the Pearson correlation and Euclidean distance. We also compare the CNN depth shifts with depth shifts obtained using the classical cross-correlation method. The CNN performs well and is competitive with cross correlation. CNN performs better for some log types—resistivity, for instance—than others. Several factors influence our results, including the quality of the input data, borehole conditions, pattern differences between LWD and EWL, and significant stretch/squeeze effects. Differences between the mean Pearson correlation computed after CNN and the cross-correlation depth-matching process are of the order of 10^{-1} and 10^{-2} . Our CNN approach is, therefore, a potential alternative to current depth-matching methods, which may reduce the amount of user intervention required from the petrophysicist.

INTRODUCTION

In the oil and gas industry, the value of well-log data is well recognized as they yield insights into the subsurface as a function of depth. Real-time well-log measurements of the subsurface are typically available to geoscientists, petrophysicists, and rock physics practitioners at all stages in exploration and production settings. Well logs provide valuable information about petrophysical properties, including porosity, permeability, fluid saturation, and geomechanics-related properties, which can be used

for reserves estimation, well completion, and reservoir modeling. However, these measurements are imperfect, as they are prone to systematic and random errors and noise during acquisition. Although most of these problems can be mitigated using advanced acquisition techniques or sophisticated processing algorithms, other fundamental problems still pose major challenges in well logging. One clear example is the mismatches in depth between well logs acquired within the same run or different runs (repeated logging passes along the same borehole). The reasons for such mismatches usually depend on the logging system,

Manuscript received by the Editor April 12, 2021; revised manuscript received September 1, 2021; manuscript accepted September 2, 2021.

¹Norwegian University of Science and Technology (NTNU), veronica.a.t.caceres@ntnu.no; kenneth.duffaut@ntnu.no; anis.yazidi@ntnu.no; frank.westad@ntnu.no

²Aker BP ASA, yngve.b.johansen@akerbp.com

e.g., LWD or EWL. Furthermore, borehole conditions and environment play a role in magnifying misalignment during acquisition. For example, for LWD measurements, noise generated by the drill bit and circulating fluids can pollute the logging data. There are also other factors that increase the uncertainty of LWD measurements, such as the changes undergone by the drilling pipes due to the increase in temperature and pressure with depth, changes in drilling parameters, e.g., the weight on the bit, the torque on the pipe, as well as all inherent interactions between the pressure and fluids in the formation and the pressure and drilling fluids along the annulus, inside or outside the tubing strings, etc. The combination of all these factors can lead to variable depth errors ranging from approximately 1 to 10 m (Theys, 1999; Wilson et al., 2004; Chia et al., 2006; Bolt, 2016) in the LWD measurements. On the other hand, the corresponding EWL measurements are very prone to tool sticking and slipping caused by variations in borehole rugosity (mudcake buildup or large changes in the borehole dimensions). This leads to depth errors of up to 12 m (Theys, 1999) and significantly compressed and expanded data sections (squeeze/stretch). Due to the elasticity of the cable, its length is also affected by increasing temperature and pressure, as well as by twisting effects. However, these are considered minor effects, which are usually neglected (Sollie and Rodgers, 1994; Theys, 1999).

Depth alignment of log data is an early stage in petrophysical preprocessing workflows. If log measurements are not properly aligned, all possible correlations across different measurements will be partially or completely suppressed (Zangwill, 1982). For instance, density-neutron porosity crossplots are a well-established tool for lithology identification and gas detection and can be significantly affected by log misalignments, thus leading to suboptimal or incorrect interpretations (Zangwill, 1982; Torres et al., 2020). To avoid this, repeated measurements are taken with the gamma ray log, which is selected as a depth reference. This allows all other log types to be aligned since the gamma ray captures the general geological patterns very well. This task has been researched for many years. Kerzner (1984), for example, proposed an automatic depth matching across wells via cross correlation and dynamic programming. However, most current methods, which are in theory automatic, are not in reality fully automatic, as they require significant user intervention. Too much user intervention in depth matching is often regarded by petrophysicists as a time-consuming and cumbersome process. Hence, they would prefer to focus their time and attention on the analysis of the massive

amounts of data becoming available through the digitization of the oil industry. Such analysis may demand high-level knowledge and expertise.

Zimmerman et al. (2018) presented a compact artificial neural network (ANN) architecture to perform automated depth matching between gamma ray logs from different runs or logging passes. Their work was inspired by the previous application of ANNs for log pattern recognition, which aimed to perform automatic well-to-well correlation within the same field, based on geological datums and relevant markers (Luthi and Bryant, 1997). Two neural networks were proposed. They work in a sequential manner providing geologists with a tool that allows them to speed up the process interactively, assisted by a neural network that recognizes a pattern in a well and searches for similar patterns in neighboring wells. Zimmermann et al. (2018) and Le et al. (2019) implemented an ANN that mimics the manual procedures carried out by expert petrophysicists for depth matching of well logs. In that sense, they designed a neural network that takes two input depth series: one synchronized (reference) and one desynchronized, with the aim of identifying anchor points in the reference and their corresponding position in the desynchronized signal to be matched. The neural network performs a classification task with 121 classes representing all possible shifts. The class assigned the highest probability by the network corresponds to the shift. The authors emphasized that one major bias in their approach is due to the selection of anchor points. These correspond to peaks, typically suggested by experts. However, not all peaks necessarily yield the best accuracy for depth matching (Zimmermann et al., 2018).

To reduce the problems related to limited data and improve the robustness and accuracy of the machine-learning model, Le et al. (2019) further developed the approach originally presented by Zimmermann et al. (2018). They used a continuously self-evolving depth-matching framework with a depth-matching service in which the user reviews the output matching from the algorithm and performs the necessary adjustments. This feedback is sent back into the algorithm to retrain and improve it over time. The shift suggested by the algorithm passes through an automatic quality control designed by a combination of different metrics before reaching the user. In that way, they assure that the machine outputs high-quality results. The inclusion of such anchor filtering into the pipeline circumvents the peak bias effect mentioned previously as now the point selection task is automatically performed by the engine, allowing for generalization when it comes to the log type. However,

this approach has only been tested on gamma ray logs. For different log types, a new training step needs to be performed because other log types have different distributions from gamma ray logs, and their patterns might differ. Wang et al. (2020) presented a dynamic depth-matching method for geological correlation using a deep neural network with a multitask-learning technique. The deep neural network uses a 1D CNN architecture that recognizes patterns from a reference gamma ray log to find the corresponding depth of this pattern in gamma ray logs from another well in the field. The multitask problem is implemented by finding the best matching pattern between a query (a pattern in the reference log) and a target gamma ray log (sliding window along the target gamma ray log) considering global and local information. They proved the power of a CNN to recognize geological patterns across different wells within a field and to accommodate both larger depth shifts than those typically observed between logs from the same well and the absence and distortion of the patterns due to lateral lithofacies variations between wells.

As an alternative solution to the depth-matching problem, we propose a proof-of-concept, machine-learning algorithm using a 1D CNN algorithm capable of estimating depth shifts between logs from different runs, specifically between LWD and EWL logs. The main challenge here is the differences between the signals due to significant changes in borehole conditions, formation properties due to invasion effects, depth sampling, log resolution, different tool design and technologies, and different companies' algorithms and procedures. However, the feature extraction power of the CNN allows the extraction of relevant invariant characteristics of the signals that can retain the important patterns for depth matching, regardless of the aforementioned factors. This provides our workflow with more flexibility and generalization capacity. First, we explain the theory behind the CNN machine-learning algorithm. Second, we describe the practical implementation of the CNN from data preparation and splitting into train, validation, and test sets. The training process, hyperparameter tuning, model selection, and assessment of results uses well data from the Ivar Aasen Field in the Norwegian North Sea. Third, we evaluate and discuss the results of the depth-shift inference via qualitative visual inspection and comparison of quantitative metrics such as Pearson correlation coefficient and Euclidean distance. We also compare the CNN depth shifts with those obtained using cross correlation. Finally, we emphasize the main contribution of this work in automating and speeding up potentially time-consuming interactive

processes, as well as the remaining scope for improvements through further work.

TRADITIONAL METHODS

Cross Correlation

The cross correlation is a well-known and widely used technique in signal processing to detect and match signals. In other words, the cross correlation is a measure of similarity between two series (e.g., in time or depth) with respect to the displacement of one relative to the other. We use the cross correlation as a depth-matching benchmark between LWD and EWL logs in this work because it is easy to implement and works well when the shape of the patterns is fixed (Wang et al., 2020). The mathematical definition of the cross correlation is given in Eq. 1. In formal terms, given a reference depth series, e.g., an EWL log $X = (x_1, \dots, x_N)$, and a test depth series, e.g., an LWD log, $Y = (y_1, \dots, y_M)$, the cross correlation (c) between them at depth lag $L = 0, 1, \dots, (\|X\| + \|Y\| - 2)$ is:

$$c(L) = \frac{1}{\sqrt{\|X\|\|Y\|}} \sum_{i=1}^N x_i y_{i+L}, \quad (1)$$

where $\|X\|$ and $\|Y\|$ are the lengths of X and Y , respectively, and $N = \max(\|X\|, \|Y\|)$ (Anderson and Gaby, 1983).

Even though it is an easy method to be implemented, the cross correlation needs some user intervention to assess the reliability of its solution in the presence of excessive noise and distortion of the signal (Zimmerman et al., 2019). Similarly, some drawbacks can arise when the patterns of the signal differ considerably, which can occur when depth matching LWD and EWL logs within the same depth interval due to changes in the borehole environment and conditions through time, leading the cross correlation to choose a wrong time/depth lag or fail to make a detection (Wang et al., 2020). Cycle skipping is another possible problem that cross correlation might run into whenever borehole depth intervals have low property contrast, suggesting wrong peaks to be matched. An additional limitation of the cross correlation is that it works well only if a constant time/depth shift characterizes both signals. In other words, the problem is reduced to the correction of the time/depth lag detected by the cross correlation. In contrast, it will fail to find the best match between signals when the time/depth shift is not stationary or if a dynamic shift exists, which cannot be properly addressed by a linear metric (Herrera and van der

Baan, 2014). In those cases, additional user intervention is needed to ensure optimal signal alignments, for instance, manual stretching-squeezing adjustments and the definition of relevant patterns to be synchronized. These issues do not allow having a fully automated workflow (without interaction of the petrophysicist at any stage of the process) for well-log depth matching based on cross correlation.

MACHINE-LEARNING IMPLEMENTATION

1D CNN

Building invariance properties into the structure of neural networks is the basis for CNNs (LeCun et al., 1989; LeCun et al., 1998). The CNN's capability of extracting local features that depend on small subregions of an image is adopted by modern computer vision approaches and other disciplines. These capabilities of CNNs can be obtained using three different mechanisms: (i) local receptive fields, (ii) sharing weights, and (iii) subsampling (Bishop, 2006).

In general, a convolutional neural network can be divided into three different types of layers or blocks: convolutional layers, pooling, and fully connected (FC) layers. The first two perform the feature extraction process, while the latter are like ANNs and do the mapping between the extracted features and output based, for example, on feedforward propagation. Feature extraction is a sequential process, i.e., the output of one layer is fed into the next such that the extracted features can hierarchically become more complex as we move deeper into the network. The optimization of all learnable parameters is performed during the training process, which can be highly computationally demanding, and is based on minimizing a loss function through an optimization algorithm such as backpropagation and gradient descent (Yamashita et al., 2018).

The mechanism behind 1D CNN is similar to ANN. The main difference is the input preprocessing stage; 1D CNN inputs raw data that is processed through convolutional trainable layers to learn an adequate representation of the input. The neurons in a layer are connected to small regions of the previous layer. These small regions are called receptive fields. The input of the 1D CNN is an array representing a segment of the well logs as X . The network is trained to learn a set of parameters θ to map the input to the output prediction S , following a hierarchical feature extraction process given as:

$$S = F(X | \theta) = f_L(f_{L-1}(\dots f_1(X | \theta_1) | \theta_2) | \theta_L), \quad (2)$$

where L is the number of hidden layers in the network. The

operation of the l_{th} layer in the convolutional layers is given by:

$$\begin{aligned} S_l &= f_l(X_l | \theta_l) = h(W \otimes X_l + b), \\ \theta &= [W, b], \end{aligned} \quad (3)$$

and \otimes represents the convolutional operation, X_l is the two-dimensional (2D) input of N feature maps, W is a set of N 1D weights or kernels (receptive fields), b is the bias vectors, and $h(.)$ is the activation function, which introduces the nonlinearity. The output of the final convolutional layer is transformed into a vector and input of several stacked FC layers that are described in Eq. 4 (Abdoli et al., 2019).

$$\begin{aligned} S_l &= f_l(X_l | \theta_l) = h(WX_l + b), \\ \theta &= [W, b]. \end{aligned} \quad (4)$$

CNNs are very popular in 2D and three-dimensional (3D) settings; however, it is also possible to use them with 1D data types such as time series, e.g., accelerometers, speech, audio, text data, automatic music tagging, speaker identification, and environmental sound classification, among others. Their ability to use the raw data instead of using handcrafted features, which require a high level of expertise in the field, makes them very popular (Abdoli et al., 2019). However, the limitations of 2D CNNs lie in the larger amount of data that is needed for training. In the case of environmental sound recognition, there is a huge scarcity in the data; therefore, other techniques such as data augmentation, like time stretching, pitch shifting, adding background noise, and dynamic range compression, must be carried out, as shown by Salamon and Bello (2017). All these additional processes also imply higher levels of expertise and uncertainty. We find in the literature studies implementing 2D CNNs for depth series, for example, well logs. Zhu et al. (2018) used the discrete wavelet transform (DWT) as a low-pass filter based on cascade frequency bands of the different log types like gamma ray, resistivity, density, and acoustic to generate their 2D representation as maps (spectrograms) with different frequency levels as a function of depth. This serves as input maps for a 2D CNN supervised lithology classification task. A 1D CNN has been successfully implemented for a well-log task as lithology classification (Imamverdiyev and Sukhostat, 2019), well to well correlation (Wang et al., 2020, Brazell et al., 2019), and vug facies identification and vug-size classification (Deng et al., 2021). Hoshen et al. (2015) found that time differences between channels in an end-to-end multichannel 1D CNN

for speech recognition are indicators of the spatial locations of the inputs. This is an important characteristic that we would like to exploit to synchronize depth series.

1D CNN Architecture

Abdoli et al. (2019) showed a compact network representation that extracts both low- and high-level features capturing the most interesting patterns in a signal. In other words, the lower-level features are the starting point of a CNN, which is the raw data moving toward a more complex or abstract representation of the data known as a higher-level representation (LeCun et al., 2015). We adopt their architecture as an initial model while enjoying the advantage of an implementation to be used on limited amounts of data. There is no need for exhaustive preprocessing, and we can divide the logs into windows of fixed length. The chosen network topology is based on the following principles: i) the first convolutional layer must have a large kernel size or receptive fields in such a way that it can capture the global features of the log signals (long-wavelength content). The successive filters increase in number and decrease in size as we move deeper into the network, extracting the local features (short-wavelength content). ii) The pooling layers are set in a way that reduces the dimensionality of the feature maps and speeds up the training. Max pooling layers are the most common form of pooling layers, which extract patches of the feature maps and output the maximum value discarding the rest (Yamashita et al., 2018). iii) The output of the last max pooling layer is transformed into a single vector or 1D array of numbers (flattened). It is passed through two FC layers or dense layers, in which every input is connected to every output by a learnable weight. The activation function ($h(\cdot)$) for all the convolutional layers and the fully connected layers are rectified linear unit (ReLU) as defined in Eq. 5, whereas the output layer has one single unit that estimates the depth shift:

$$\text{ReLU} = f(x) = \max(0, x). \quad (5)$$

To reduce overfitting and speed up the training process, Abdoli et al. (2019) used batch normalization layers after each activation function of the convolutional layers and added a dropout after each FC layer with a probability of 0.25. The batch normalization layers apply a transformation to keep the mean and standard deviation of the convolutional layers' outputs close to 0 and 1, respectively. By doing so, it accelerates the training process, enabling the use of high-learning rates, avoiding the risk of divergence during optimization, and acting as regularization, reducing overfitting of the networks (Ioffe and Szegedy, 2015).

Machine-Learning Algorithm Deployment

We proposed a machine-learning algorithm based on 1D CNN to depth match LWD and EWL logs, focusing on the correlated depth concept, in which the main goal is to correlate one log measurement LWD with a reference EWL that is assumed to be in the correct position in depth (Theys, 1999). We assume that the depth shift is no larger than 10 ft (≈ 3 m) within a window; therefore, the maximum number of data points ranges between -20 and 20. The sampling interval between data points is 0.5 ft (≈ 0.1524 m). This assumption is based on the observed shifts present in the data, which do not reach values larger than 4.5 m. Additionally, this range allows us to test our proposed approach faster since it limits the number of simulated shifts without compromising the results, acting just as a soft constrain. The main idea is to define segments or windows of limited length (256 data points ≈ 39 m) for different pairs of log measurements, e.g., gamma ray pairs, resistivity pairs, density pairs, etc., where distinctive log patterns present in both (reference and shifted logs) are identified and matched by the network to improve the alignment between the two signals automatically.

The problem setup can be described as follows. First, we select a pair of logs that measure the same property within a specific depth window, which are used as input to the CNN algorithm. Second, the CNN algorithm finds the distinctive patterns in the reference log (EWL) and identifies the same patterns in the corresponding shifted log (LWD). Finally, we synchronize or align the logs by estimating the number of samples, either positive or negative, that the LWD log needs to be shifted to best match the EWL log. By using the feature extraction capacity of the CNN, the identification of the patterns is performed automatically by the algorithm. We start from an initial model consisting of three convolutional layers with ReLU as their activation function and their associated pooling layers, specifically max pooling. In between each convolution-pooling layer block, we place a batch normalization layer. These provide the feature extraction components of the network. Then, we perform the estimation of the depth shift with two FC layers with ReLU activation functions, with batch normalization and dropout layers in between each FC layer. The batch normalization and dropout act as a regularization method. The output layer has a single unit with the identity function to estimate the depth shift in the number of data points, solving a regression task. The best architecture of the network and hyperparameters for each individual pair of logs is determined by testing three different search algorithms: random search, Hyperband, and Bayesian optimization.

This framework is tested on two wells from the Ivar Aasen Field in the Norwegian sector of the North Sea, which have available separated LWD and EWL suites of logs. The training of the network is carried out with final petrophysical composite logs (depth matched, spliced, and edited logs) from four wells in the same field. Therefore, semisynthetic data must be generated considering the absence of LWD and EWL logs and ground truth labels in the training wells. To generate the training data, we take each log measurement from the four wells and produce copies that are bulk shifted by a range of numbers of data points up or down (positive or negative). Thus, the output labels for each semisynthetic log will correspond to the signed magnitude of the shift in data points. During training, model selection, and preliminary model assessment, we use the mean squared error (MSE) as a metric to evaluate the algorithm on the semisynthetic data.

However, for depth inference with real data, the absence of ground truth labels requires the use of signal analysis metrics like Pearson correlation and Euclidean distance on the reference and the shifted log before and after depth matching. We also use the values of the same metrics after depth matching using cross correlation for comparison with the CNN results.

Our initial network structure is shown in Fig. 1. The input of the CNN consists of two channels. The first channel is a window of the reference log (EWL) with a fixed length equal to 256 data points, and the second channel is a copy of the reference bulk shifted by a given number of samples. These two channels of the same length represent a single depth window and a single input sample into the network, which extracts the relevant features and determines the depth shift needed to align the two logs.

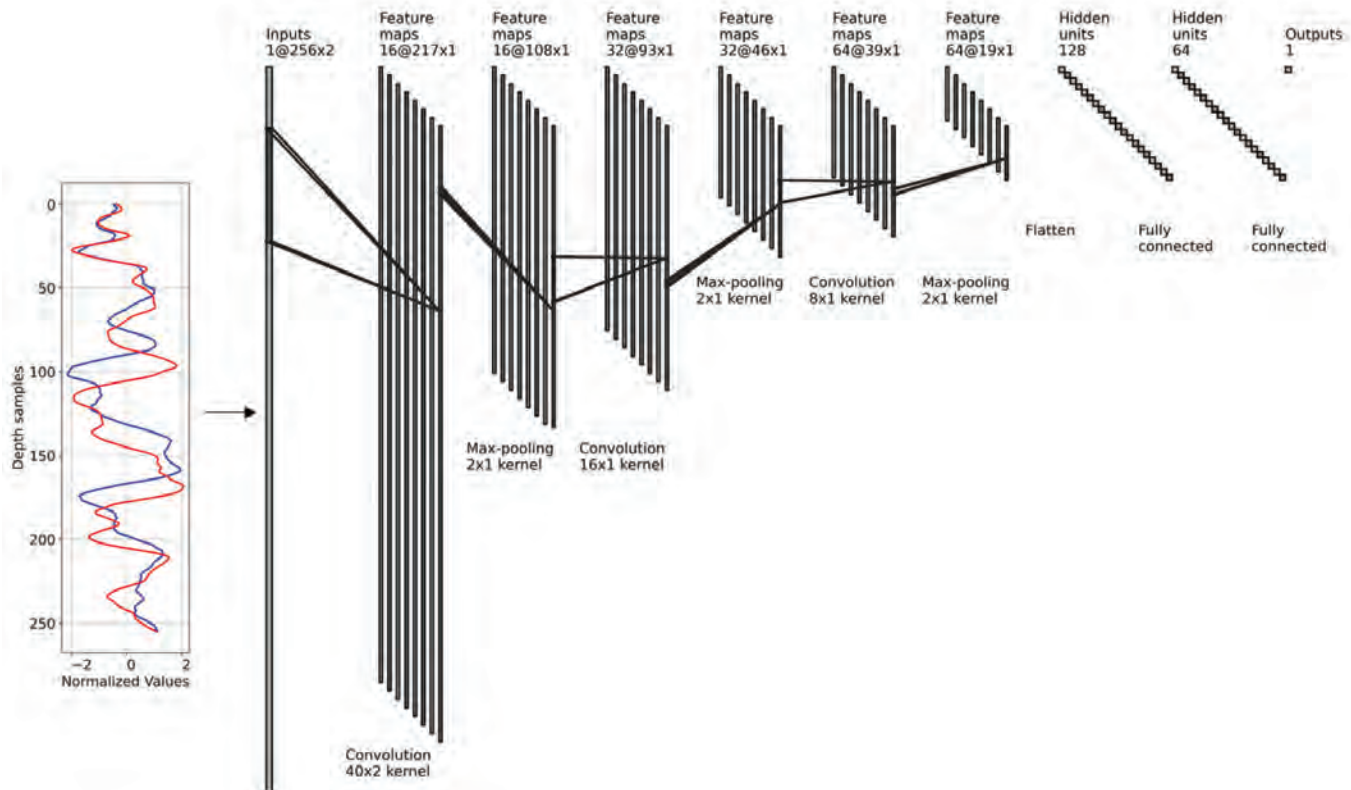


Fig. 1—Sketch of a 1D CNN base model architecture. The input layer is a double channel corresponding to the reference EWL log (solid red) and the misaligned LWD log (solid blue). After each convolution layer, we introduce batch normalization layers (not shown), and after each fully connected layer, we introduce batch normalization and apply a dropout (not shown). This figure is generated by adapting the code from https://github.com/gwding/draw_convnet.

Data Set and Data Preparation Method

Our data set consists of six well logs acquired in the Ivar Aasen Field in the Norwegian sector of the North Sea. The wells are a mixture of exploration and appraisal wells, and most of them are considered vertical with maximum deviations of between 0° and 13°. However, two of them are slightly deviated with maximum values of 20° to 25° (Wells 16/1-22S and 16/1-21S, respectively). Four out of six are introduced as a part of the training data set, while the other two (Wells 16/1-9 and 16/1-21S) are kept as a test set (unseen LWD and EWL logs) for depth-shift inference. The training set consists of logs that have already been depth shifted and spliced. They are the final petrophysical composite log suite contained in Log ASCII Standard (LAS) files. This means that no distinction is made between EWL and LWD. For training purposes, this is not a problem since we are interested in identifying the shifts needed to depth align the signals. Another important aspect of our approach is removing the need for ground truth labeling by a petrophysicist. We achieve this by training the network using semisynthetic for the supervised-learning process. To generate ground truth labeled data, we artificially simulate an acceptable range of depth shifts expected for all the log types by copying the logs and applying all possible shifts within the range to them. This limits the type of shift applied to be a constant value (bulk shift) for the whole log. An additional augmentation technique is the generation of overlapping windows, which means that each depth window will have an overlap of 50% with the previous one, doubling the number of training samples.

Data preparation consists first of a gentle smoothing with filter parameters chosen after testing. Second, we make multiple copies of each log type equal to the number of bulk depth shifts we want to simulate, setting a maximum depth shift of ± 3 m. This implies the generation of 41 copies for each log type, ranging from -20 to 20 data point shifts, including the zero shift. Thus, we ensure that all depths along the well log can experience all likely shifts. This avoids skewness in the training set. Third, we divide the shifted logs into windows of 256 data points, and we apply a local normalization and standardization of the data in each window. The number of windows depends on the length of each log type (see Table 1). We store the depth shifts applied to each log copy in a depth-shift vector as ground truth labels for the training and model selection process. From now on,

we will refer to the number of windows into which each log has been divided as the number of samples when we talk about the machine-learning implementation. The input samples for the CNN are the log windows consisting of 256 data points.

Training, Tuning, and Model Selection

We use the whole synthetically shifted data derive from only four out of the six wells available (Wells 16/1-2, 16/1-11, 16/1-16, and 16/1-22S) to train and optimize the model and get a first test assessment of the method. Fig. 2 shows the splitting of the data at each stage and the general workflow. After preparing the data set for a single log type, e.g., gamma ray (GR), we have a total of 21,320 samples. We split these into a training set (70%), a validation set (18%), and a test set (12%). The validation set is used to monitor the training and model selection process. For this set, our samples have ground truth labels (signed depth shifts) that allow us to track the training process and evaluate the models. Table 1 summarizes the size of the data sets per log type, and their corresponding splits into training, validation, and test sets. Notice that the number of samples per log type varies depending on how the logging plan was designed for each well. For example, usually, gamma ray and resistivity logs are acquired along the full depth range logged, while density, neutron, and PEF are mostly acquired only over the reservoir/target depth interval. This strategy is very common for appraisal and development wells. It is worth noticing that the models for each log type are trained and tuned individually.

We train our initial model using an Adam optimizer, which is a stochastic gradient descent method based on adaptive estimates of first- and second-order moments (Kingma and Ba, 2015). We use the default parameter settings from Tensorflow Keras banked (Chollet, 2015). The learning rate was constant at 0.001. We set the batch size to 128 and the number of epochs to 100. The objective function to be minimized during training is the mean squared error (MSE). We use the MSE to monitor the training and hyperparameter tuning process at each epoch.

From the learning curves (see Fig. 3), we can see that the MSE in the validation set decreases rapidly and reaches stability quite fast, at MSE even lower than those of the training set. This suggests that 50 to 100 epochs are sufficient to train the model without overfitting.

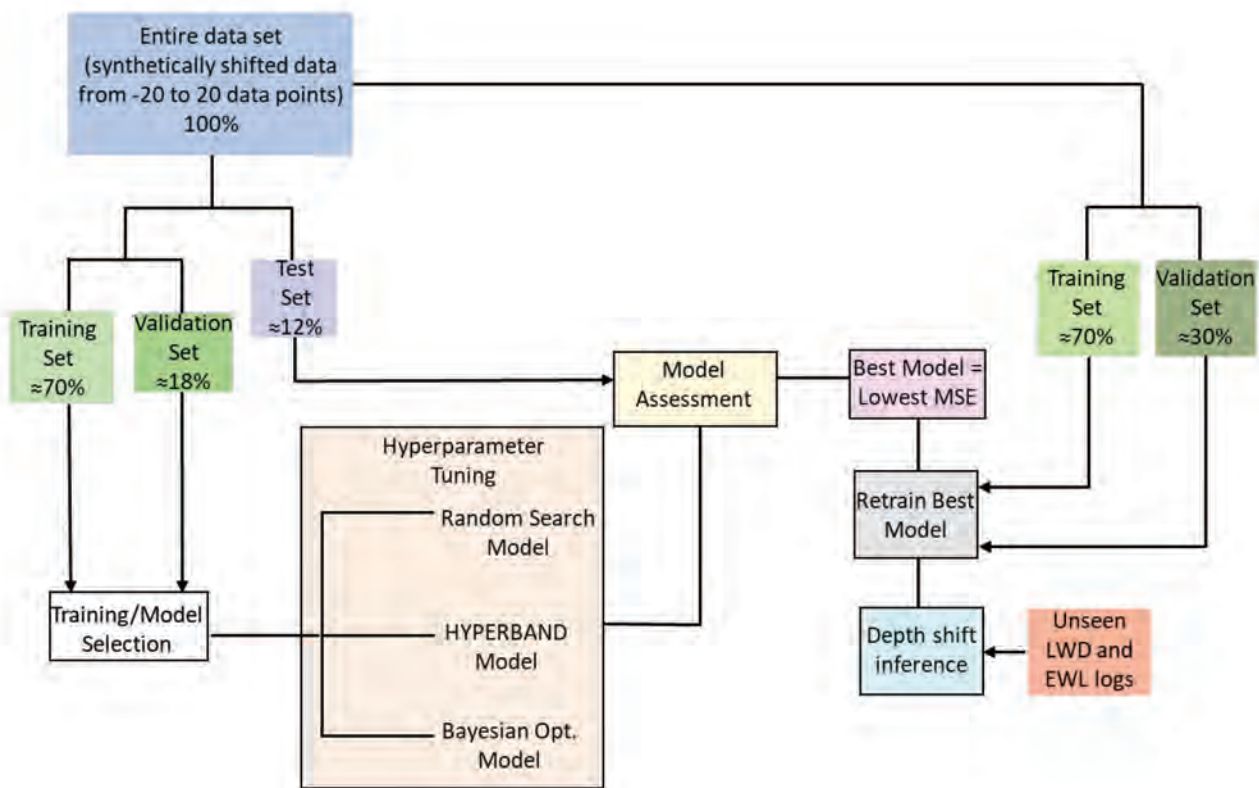


Fig. 2—Sketch of the data splitting, training-model selection workflow, and final depth-shift inference on the completely unseen data from the other two wells (Wells 16/1-9 and 16/1-21S) kept outside of the training and model selection process.

Table 1—Data Set Size in Samples for Training and Model Selection From Four Wells for Each Log Type

Log Type	Complete Data Set Size (Synthetically Bulk Shifted)	Training Set Size	Validation Set Size	Test Set Size
Gamma Ray	21,320	14,924	3,895	2,501
Resistivity	20,664	14,596	3,608	2,460
P-Wave Sonic	16,564	12,013	2,829	1,722
S-Wave Sonic	7,093	5,084	1,148	861
Density	7,995	5,617	1,394	984
Neutron	8,159	5,658	1,435	1,066
PEF	7,380	5,166	1,394	820

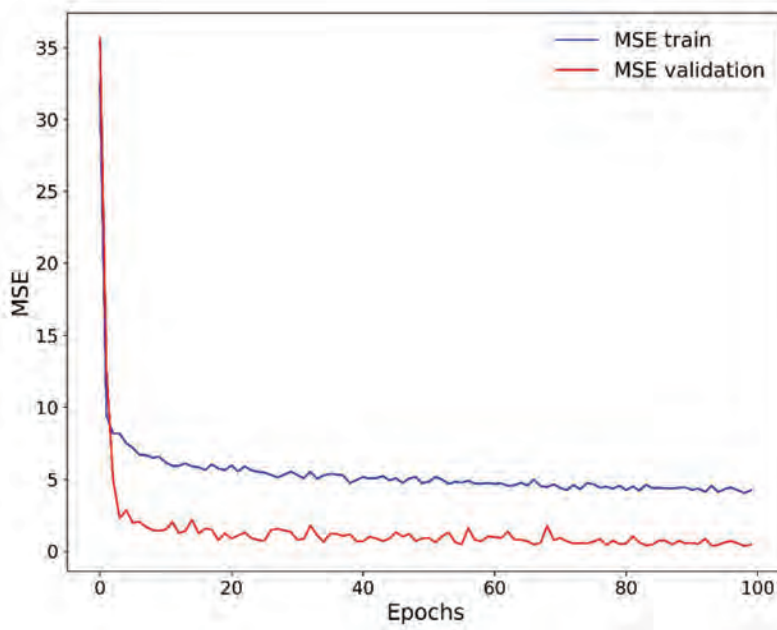


Fig. 3—Training and validation MSE as a function of the number of epochs for the gamma ray model.

Before the first assessment of the method, we perform a hyperparameter tuning. This aims to minimize a cost function over a graph-structured configuration space, which involves the identification of optimal network architecture parameters (e.g., the number of convolutional filters/kernels) and algorithm/optimization parameters (e.g., the learning rate) that could be drawn from the space and that can reduce the loss function in further steps (Bergstra and Bengio, 2012). Basically, the main idea is to reduce the MSE, which is evaluated on the validation set by finding the best combination of the model's hyperparameters. This is commonly known as the best trial.

We carry out the tuning process using the Keras tuner library, which offers three different tuning strategies: random search, Hyperband, and Bayesian optimization (O'Malley et al., 2019). Differences between these algorithms are associated with the design of the hyperparameter space and the hyperparameter search strategy, which has an impact on the run time for a given model complexity and data set size. Random search is one class of non-informed exhaustive parameter search. Hyperband is a modification of random search with an adaptive resource allocation process that speeds up the hyperparameter selection. The concept of adaptive resource allocation means that more resources are allocated for the identification and evaluation of hyperparameter configurations that are most likely to be successful while quickly discarding the less successful ones. This allows the exploration of a larger

number of hyperparameter configurations than sampling uniformly distributed hyperparameter spaces trained until completion. The Hyperband strategy relies on an early stopping process to allocate resources (Li et al., 2017). Finally, the Bayesian optimization strategy belongs to the surrogate model category and creates a model of the conditional probability $p(y|\lambda)$ of a configuration's performance on an evaluation metric y , e.g., loss, given a set of hyperparameters λ . Bergstra et al. (2011) and Thornton et al. (2013) showed that this technique outperforms random search, but for high-dimensional problems, its performance and efficiency degrades, and it can then perform similarly to random search (Li et al., 2017). Hyperband can produce good results and has the main advantage of being from 5 to 30 times faster than Bayesian optimization in several deep-learning and kernel-based machine-learning problems (Li et al., 2017).

We define a range of values for each hyperparameter that we want to tune and run the tuning process using the three searching strategies above, selecting the best model based on the final MSE. Each method converges to a different network architecture that is, in most cases, better than the initial model. Table 2 shows the tuning parameters with their corresponding ranges. Note that we keep the number of convolutional layers fixed for all models, as well as their activation functions. For numerical parameters, we show the maximum and minimum values that can be selected, and for no numerical values like the type of activation function, we refer to them as Option 1 and Option 2.

Table 2—Tuning Parameters Selection Range per Layer

Layers	Tuning Parameters	Maximum/ Option 1	Minimum/ Option 2	Default	Step
Convolutional Layer 1	# of kernels	128	8	16	8
	Kernel size	64	8	32	8
	Activation function	NA	NA	ReLU	NA
Max Pooling Layer 1	Pool size	NA	NA	2	NA
	Strides	2	1	1	NA
Convolutional Layer 2	# of kernels	128	8	32	8
	Kernel size	32	8	16	8
	Activation function	NA	NA	ReLU	NA
Max Pooling Layer 2	Pool size	NA	NA	2	NA
	strides	2	1	1	NA
Convolutional Layer 3	# of kernels	128	8	64	8
	Kernel size	16	2	16	4
	Activation function	NA	NA	ReLU	NA
Max Pooling Layer 3	Pool size	NA	NA	2	NA
	Strides	2	1	1	NA
Dense Layer 1	# of units	256	32	128	32
	Activation function	ReLU	Tanh	ReLU	NA
Dropout Layer 1	Dropout rate	0.5	0	0.25	0.05
Dense Layer 2	# of units	256	32	64	32
	Activation function	ReLU	Tanh	ReLU	NA
Dropout Layer 2	Dropout rate	0.5	0	0.25	0.05
Optimizer	Learning rate	1,00E-02	1,00E-04	NA	1,00E-01

Having obtained the improved models after hyperparameter tuning using each of the three methods, we assess each of them by estimating the depth shifts on the test set. At this stage, we are still using the synthetically shifted samples. We compute the MSE for each model, and we choose the one with the lowest MSE. Figure 4 shows an example of the gamma ray models, where the initial model regression line (Fig. 4a) shows good agreement between the actual depth shift and the predicted depth shift, with a maximum discrepancy of around ± 3 samples. Similarly, the random search solution (Fig. 4b) reduces the general variability of the depth shifts and has the same R^2 of 0.996 as the initial model. On the other hand, the Hyperband (Fig. 4c) and Bayesian optimization (Fig. 4d) methods produce models with lower performance. There are three samples with negative depth shifts that seem to be challenging to estimate correctly regardless of the hyperparameter tuning method used. For this example, based on the gamma ray measurements, the best model is found using the random search solution with an MSE = 0.47 on the synthetically shifted test set.

Notice that we do not use the real unseen LWD logs at this stage and use them only when the best model has been selected. Another important aspect is the limited amount of test data we have, which is around 28 and 55 samples, depending on the well and the log type. For example, Well 16/1-9 has the same number of samples for all log

types, whereas Well 16/1-21S has 55 samples for gamma ray, resistivity, and P-wave sonic, but only 32 samples for density, neutron, and PEF logs.

Depth-Shift Inference

After model selection, we take the whole set of synthetically shifted logs and split them again into training and validation sets. The percentage of the validation varies between a range from 12 to 30%; hence, the training also varies between 70 to 88% depending on the log measurement. We proceed to retrain the best model and follow up the behavior of the MSE at each epoch with the validation set to detect any overfitting problem, in addition to the batch normalization and dropout layers. We perform the depth inference testing of our final models using a completely unseen data set from Well 16/1-9 and Well 16/1-21S. These logs are considered raw since they have not been shifted, spliced, or merged. Therefore, the EWL and LWD/MWD logs are separate, and we use them to define our reference and shifted logs, respectively. The test set is preprocessed in the same way as the training set, with the difference that we do not generate overlapping windows. We only extract single windows along the full-depth range. Additionally, we perform a cross correlation between the reference and the shifted log per window to estimate the depth lag, and we save these values in a depth-shift vector for further evaluation and comparisons.

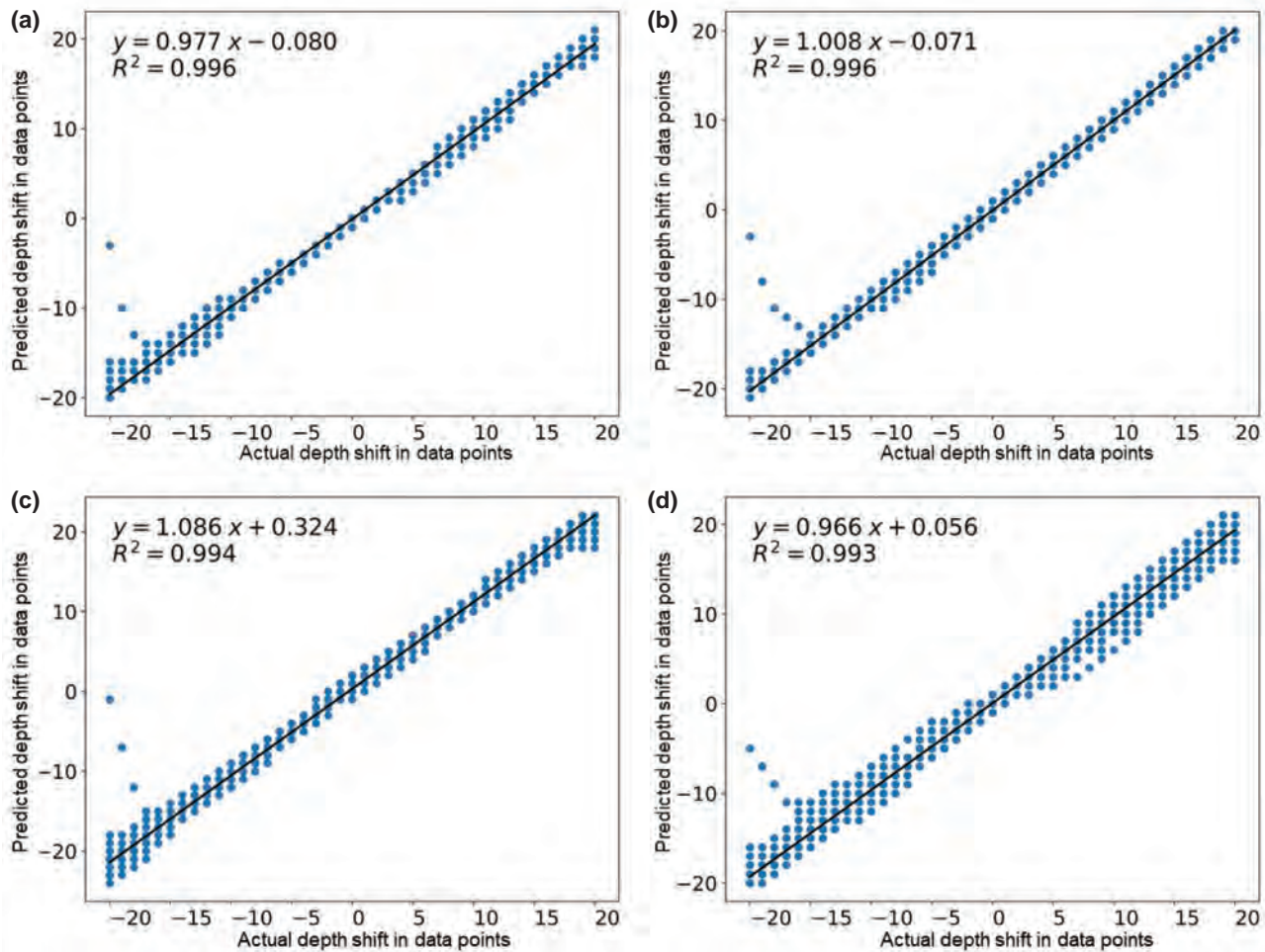


Fig. 4—Regression line on the test set, actual depth shift vs. that predicted with the gamma ray model; (a) Initial model with MSE = 0.52; (b) Random search model with MSE = 0.47; (c) Hyperband model with MSE = 2.02; (d) Bayesian optimization model with MSE = 1.02.

Because of the lack of ground truth labels for the two test wells, we take a different approach to evaluate the results of the depth-shift estimates. We compare some quantitative metrics, such as the Pearson correlation and Euclidean distance, and compute their averages over the total number of samples per log measurement, as well as qualitative visual inspection of log profiles before and after depth matching via CNN and cross correlation. The Pearson correlation coefficient, r , measures how strong the relationship is between two variables or data sets, assuming a linear relation between them. It takes values between -1 and 1 . A Pearson correlation value of -1 indicates a perfect negative correlation, whereas a value of 1 implies a perfect

positive correlation. No linear correlation is indicated when the $r = 0$ or $r \approx 0$ (Bulmer, 1979). The Pearson correlation coefficient is calculated using:

$$r = \frac{\sum_{i=1}^n (x_i - \bar{x})(y_i - \bar{y})}{\sqrt{\sum_{i=1}^n (x_i - \bar{x})^2 \sum_{i=1}^n (y_i - \bar{y})^2}}, \quad (6)$$

where in our case, n is window size (256 data points), x_i and y_i are the individual data points of the depth series within the window, and \bar{x} and \bar{y} are their corresponding mean values.

The Euclidean distance (d) is an alternative metric that measures the similarity between series (time or depth). It is calculated using Eq. 7 (Herrera and van der Baan, 2014):

$$d_{(x,y)} = \sqrt{\sum_{i=1}^n (x_i - y_i)^2}, \quad (7)$$

where in our application $d_{(x,y)}$ is the one-to-one Euclidean distance between the test (LWD/MWD) log x and the reference (EWL) log y , and the index i represents the individual data points in each windowed depth series.

In addition, we use the Pearson correlation coefficient (r) to compute five indicators that help us to judge the quality of the depth matching using the following criteria:

- C1. Number of samples in which the CNN matching improves the depth matching compared with the original log position ($r_{CNN} > r_{orig.}$)
- C2. Number of samples in which the CNN matching worsens the depth matching compared with the original log position ($r_{CNN} < r_{orig.}$)
- C3. Number of samples in which the CNN does not detect any mismatch of the logs ($r_{CNN} = r_{orig.}$)
- C4. Number of samples in which the CNN matching performs better than the cross-correlation matching whenever Criterion 1 is satisfied, i.e., there is a depth alignment improvement ($r_{CNN} > r_{cross-correlation}$)
- C5. Number of samples in which the CNN and the cross correlation perform equally well ($r_{CNN} = r_{cross-correlation}$)

where $r_{orig.}$, r_{CNN} , and $r_{cross-correlation}$ are the Pearson correlation coefficients of the log segments before depth matching, after depth matching with CNN, and after depth matching with cross correlation, respectively. Values of these indicators for Wells 16/1-9 and 16/1-21S are shown in Table 3 and Table 4, respectively. The last two columns of the tables show $Ind_{1\%}$ and $Ind_{4\%}$, respectively. These are indicators C1 and C4 expressed as percentages of the total number of samples for each well. They are defined in Eqs. 8 and 9.

$$Ind_{1\%} = \frac{100}{N} \sum_{i=1}^N I(r_{CNN} > r_{orig.}), \quad (8)$$

$$I = \begin{cases} if(r_{CNN} > r_{orig.}), I = 1 \\ if(r_{CNN} \leq r_{orig.}), I = 0 \end{cases},$$

$$Ind_{4\%} = \frac{100}{N} \sum_{i=1}^N I(r_{CNN} > r_{cross-correlation}), \quad (9)$$

$$I = \begin{cases} if(r_{CNN} > r_{cross-correlation}), I = 1 \\ if(r_{CNN} \leq r_{cross-correlation}), I = 0 \end{cases},$$

where N is the total number of samples of each log measurement for each well.

RESULTS

We obtain seven CNN models corresponding to the seven log types. The architecture of the models and hyperparameters are the same for most of them, except for the gamma ray and S-wave sonic. However, each model has its own final trained weights. We test each of the seven models by predicting depth shifts for their corresponding log types in Wells 16/1-9 and 16/1-21S. Summaries of the results for these wells are shown in Table 3 and Table 4, respectively.

Table 3 shows that there are five log types for which CNN has achieved depth-matching improvements compared to no matching of above 65%, gamma ray, resistivity, P- and S-wave sonic, and neutron. This percentage improvement is computed using Eq. 8. Table 3 also shows that for the gamma ray, resistivity, and the P- and S-wave sonic logs, the CNN correction outperforms the cross correlation in 46.43, 71.43, 57.14, and 46.43% of the total number of samples, respectively. For the density and PEF logs, the CNN percentage of depth-matching improvement over no matching is less than 65%, and for the density and PEF, respectively, the percentages of samples for which CNN depth shifting outperforms the cross correlation are much lower at 17.86, 35.71, and 21.43%.

Results for Well 16/1-21S (Table 4) are quite promising, indicating that CNN can easily recognize the different log type patterns and identify misalignments among them. The CNN percentage of improvement ($Ind_{1\%}$) is above 80% for all the log types in this well and even higher than 90% and equal to 100% for density and resistivity logs, respectively. The 100% improvement of the resistivity implies that all samples after CNN correction have increased their Pearson correlation in comparison with their original values. The PEF log again shows the lowest improvements due to CNN depth matching, as we have seen in the previous well. However, this value is still above 80%, hence more than 20% higher than in Well 16/1-9.

The average percentage of all samples of all log types for which the CNN correction outperforms the cross correlation for Well 16/1-21S is 53.86% but only 39.28% for Well 16/1-9. Although P-wave sonic, neutron, and PEF logs have high percentages of samples that improve their alignment after CNN correction, fewer than half of the samples have higher Pearson correlation values than after cross-correlation depth matching. This indicates that CNN can provide a sensible correction for depth misalignments, but we need to evaluate the overall behavior of other metrics to have a more reliable and conclusive assessment.

For additional assessment of the results, we show example log profiles for some log types. For example, Fig. 5 shows Window No. 17 for gamma ray, density, and neutron porosity logs in Well 16/1-9. We can see that the depth shifts suggested by CNN and cross correlation are quite similar for these example logs and even identical

for the neutron porosity log (Fig. 5c). Similarly, we can see the differences in patterns and values in some specific zones of the logs, as is the case for the density (Fig. 5b) depth samples between 0 and 125. Despite consistent preprocessing of the data, resolution differences are seen between LWD and EWL logs. From the panels, we see that the gamma ray depth shifts using CNN appear visually better than the cross-correlation depth shifts. This is confirmed by the Pearson correlation values equal to 0.94 and 0.93 for CNN and cross correlation, respectively. In contrast, the CNN depth shifts to the density logs for this specific window are not good for this sample, reducing the Pearson correlation from 0.57 down to 0.47 (Fig. 5b). For the neutron porosity, both CNN and cross correlation suggest the same correction of -1 data point; hence, both increase the Pearson correlation to the same value from 0.69 up to 0.71.

Table 3—Summary of Depth-Matching Correction Using CNN for Well 16/1-9*

CNN Model	# Improved Samples CNN (C1)	# Worsened Samples CNN (C2)	# Samples Without Change (C3)	# Samples CNN Better Than Cross Correlation (C4)	# Samples CNN Equal To Cross Correlation (C5)	Matching Improvements CNN Better Than No Shift (%) (Ind ₁ %)	Matching Improvements CNN Better Than Cross Correlation (%) (Ind ₄ %)
GR	23	4	1	13	7	82.14	46.43
Resistivity	21	4	3	20	3	75.00	71.43
P-wave sonic	25	2	1	16	1	89.29	57.14
S-wave sonic	19	9	0	13	3	67.86	46.43
Density	16	10	2	5	6	57.14	17.86
Neutron	19	6	3	10	2	67.86	35.71
PEF	16	10	2	6	3	57.14	21.43

*According to criteria (C1 to C5) based on Pearson correlation coefficients before and after corrections for a total of 28 samples.

Table 4—Summary of Depth-Matching Correction Using CNN for Well 16/1-21S*

CNN Model	# Improved Samples CNN (C1)	# Worsened Samples CNN (C2)	# Samples without change (C3)	# Samples CNN Better Than Cross Correlation (C4)	# Samples CNN Equal to Cross Correlation (C5)	Matching Improvements CNN Better Than No Shift (%) (Ind ₁ %)	Matching Improvements CNN Better Than Cross Correlation (%) (Ind ₄ %)
GR	48	6	1	39	4	87.27	70.91
Resistivity	55	0	0	47	6	100.00	85.45
P-wave sonic	45	9	1	23	7	81.82	41.82
Density	30	1	1	20	5	93.75	62.50
Neutron	27	4	1	12	5	84.38	37.50
PEF	26	6	0	8	2	81.25	25.00

*According to criteria (C1 to C5) based on Pearson correlation coefficients before and after corrections for a total of 55 samples (GR, resistivity and P-wave slowness) and 32 samples (density, neutron, and PEF).

Figure 6 shows the same example log types for Window No. 54 from Well 16/1-21S. Again, the differences between the CNN and the cross-correlation depth shifts are small (here, only differing by one data point); thus, the final corrections are quite similar. However, the CNN is slightly visually and quantitatively better than the cross correlation for gamma ray and density logs (Fig. 6a, and Fig. 6b, respectively). The Pearson correlation is 0.87 and 0.85 for CNN and cross correlation, respectively, for the gamma ray. Their corresponding values for the density log are 0.99 and 0.98, respectively. For the neutron porosity logs, the panels shown in Fig. 6c are more challenging to judge by visual inspection. However, improvement in the depth alignment after depth matching is clear. In this case, the Pearson correlation value is higher for cross correlation than for CNN at 0.82 and 0.78, respectively. Comparing the example logs in Fig. 5 and Fig. 6 from these two wells, the patterns in the LWD and EWL logs look more similar to each other in Well 16/1-21S than in Well 16/1-9.

We want to get a clearer view of how useful the CNN is compared to another common approach to depth matching like the cross correlation, for instance. We, therefore, computed the mean of the Pearson correlation and the Euclidean distance of all the samples in the two test wells before and after depth correction with CNN and cross correlation and compared them. Fig. 5d, Fig. 5e, Fig. 6d, and Fig. 6e show these comparisons for the gamma ray, density, and neutron logs. In Well 16/1 21S, differences between CNN and cross-correlation results are insignificant. For Well 16/1-9, the largest differences in Pearson correlation and Euclidean distance between the two methods are only 0.08 and 1, respectively.

From Fig. 5 and Fig. 6, we see that depth mismatches are successfully reduced by CNN. CNN is performing almost as well as cross correlation in removing mismatches between LWD and EWL logs in real data. Therefore, we can see CNN as a suitable alternative to cross correlation for deploying automatic workflows capable of handling large amounts of data simultaneously. However, we also see that CNN would benefit from improvement for specific log types where the cross correlation shows better results in some individual depth

windows. The average value of the metrics over the whole data set indicates that cross correlation is superior in most of the cases, but CNN still has the potential to be further improved.

For completeness, Fig. 7 shows the mean Pearson correlations and Euclidean distances for all log types in Wells 16/1-9 and Well 16/1-21S. The Pearson correlation increases after CNN depth matching for all log types. Similarly, the Euclidean distance is reduced for both wells. In Well 16/1-9, gamma ray, resistivity, P-wave sonic, and neutron logs show significant improvements with mean Pearson correlation of 0.86, 0.88, 0.57, and 0.71, respectively. However, for Euclidean distance, only gamma ray and resistivity achieved values below 10. For Well 16/1-9, the mean values of the CNN are only superior to the mean values of those for cross correlation for the resistivity logs. The other log types, such as gamma ray and neutron yield metrics that are quite close to those from the cross correlation, but they do not achieve superior values.

For Well 16/1-21S, we see similar trends to Well 16/1-9, where the CNN depth matching improves the alignment significantly, showing values of Pearson correlation across log types above 0.7 for all but one log type. Only the PEF has a low mean Pearson correlation of 0.36. This indicates poor performance. The mean Euclidean distance shows reductions down to half of the original distance, as is the case for the gamma ray, resistivity, and density logs. Notice that for Well 16/1-21S, the CNN depth matching overall performs slightly better than the cross correlation for the resistivity logs and is quite competitive for the gamma ray, P-wave sonic, and neutron logs with differences in Pearson correlation of only 0.01, 0.06, and 0.04, respectively. The density log shows the same mean Pearson correlation of 0.88 after CNN depth matching and cross correlation. The reduction in Euclidean distance in Well 16/1-21S observed after CNN depth matching is larger for three log types, gamma ray, resistivity, and density, than for the others. In general, CNN has a better overall performance in Well 16/1-21S than in Well 16/1-9. We can also distinguish the log types in which CNN performs better, e.g., resistivity, from those for which it gives poorer results, e.g., PEF.

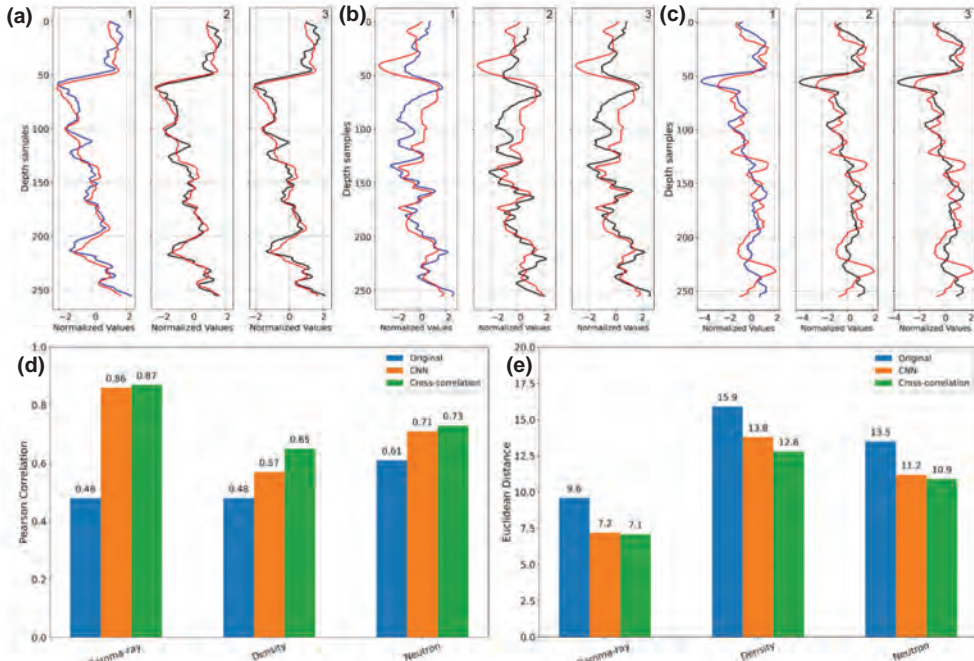


Fig. 5—Log profiles (Window No. 17) for Well 16/1-9 and overall mean Pearson correlation and Euclidean distance metrics for each log type: (a1) gamma ray logs without correction; (a2) gamma ray after CNN correction of -4 data points; (a3) gamma ray after cross-correlation correction of -1 data points; (b1) density logs without correction; (b2) density logs after CNN correction of -6 data points; (b3) density logs after cross-correlation correction of 0 data points; (c1) neutron porosity logs without correction; (c2) neutron porosity logs after CNN correction of -1 data points; (c3) neutron porosity logs after cross-correlation correction of -1 data points; (d) Pearson correlation overall results; (e) Euclidean distance overall results. In (a) to (c), solid blue lines represent the uncorrected LWD curve, red is the reference EWL, and black is the corrected LWD.

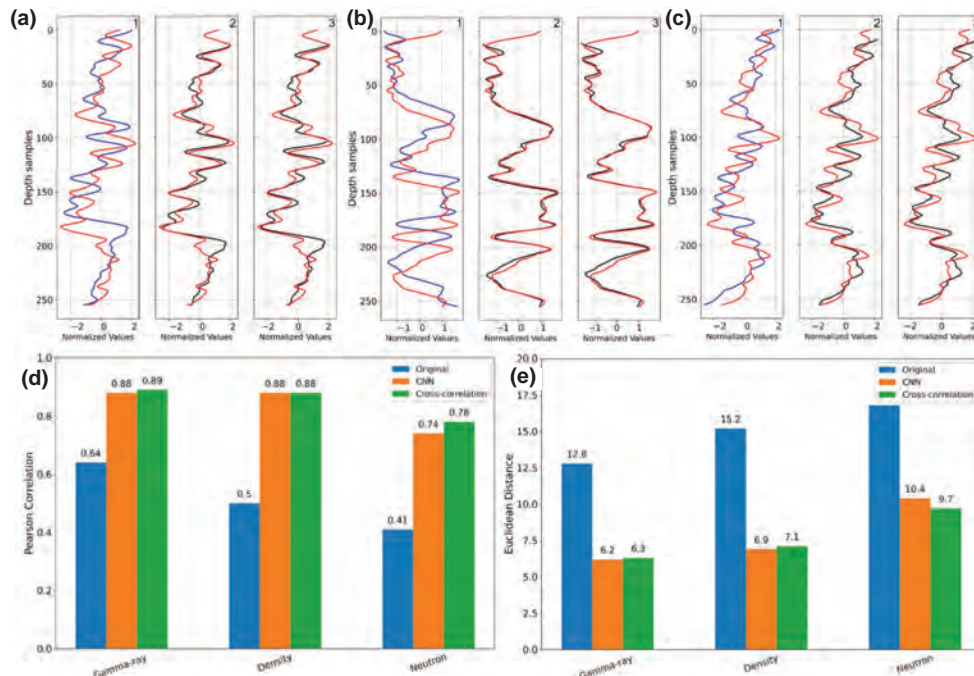


Fig. 6—Log profiles (Window No. 54) for Well 16/1-21S and overall mean Pearson correlation and Euclidean distance metrics for each log type: (a1) gamma ray logs without correction; (a2) gamma ray after CNN correction of -14 data points; (a3) gamma ray after cross-correlation correction of -13 data points; (b1) density logs without correction; (b2) density logs after CNN correction of -12 data points; (c2) neutron porosity logs after CNN correction of -9 data points; (c3) neutron porosity logs after cross-correlation correction of -10 data points; (d) Pearson correlation overall results; (e) Euclidean distance overall results. In (a) to (c), solid blue lines represent the uncorrected LWD curve, red is the reference EWL, and black is the corrected LWD.

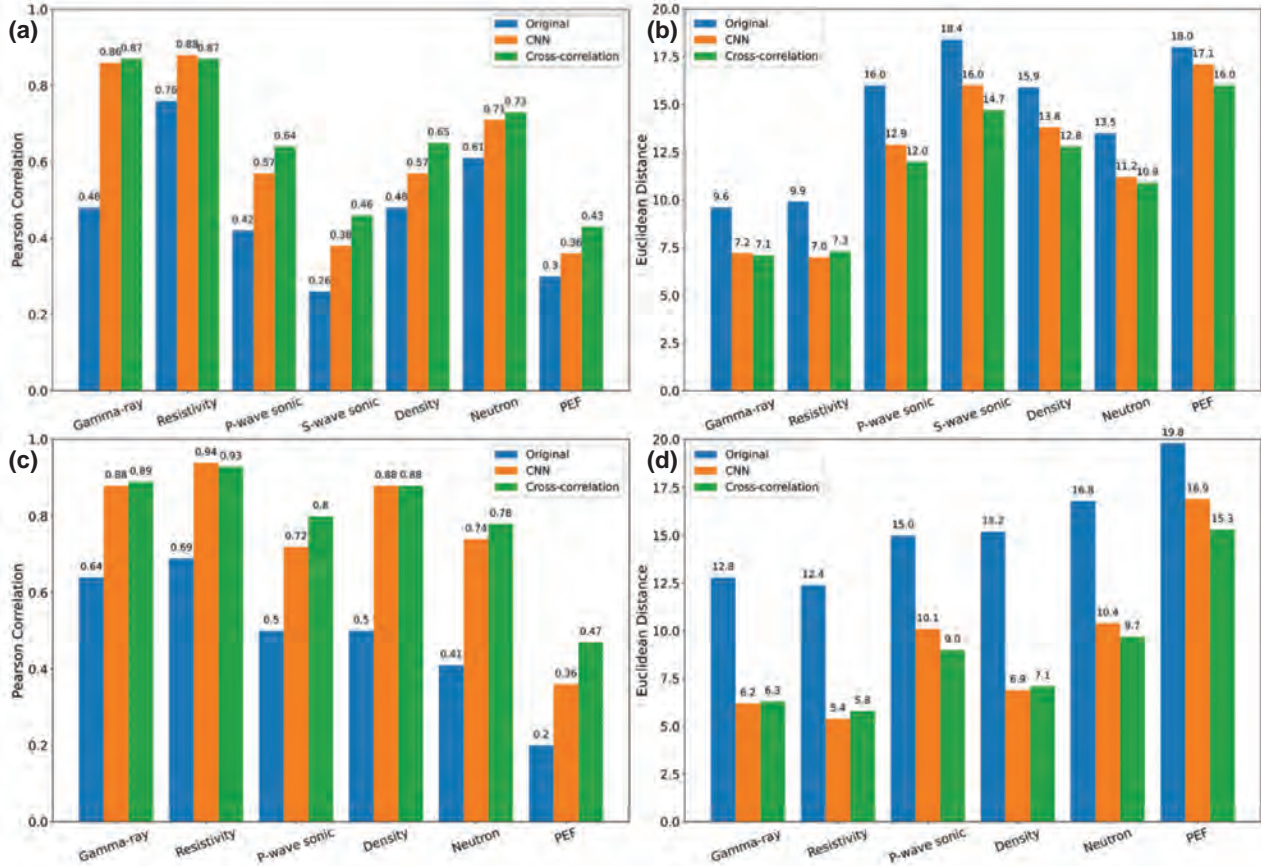


Fig. 7—Comparison of the overall mean Pearson correlation and Euclidean distance metrics before and after depth correction using CNN and cross correlation for each log type in Well 16/1-9 and Well 16/1-21S: (a) Pearson correlation overall results for Well 16/1-9; (b) Euclidean distance overall results for Well 16/1-9; (c) Pearson correlation overall results for Well 16/1-21S; (d) Euclidean distance overall results for Well 16/1-21S.

DISCUSSION

The hyperparameter tuning is the most expensive stage of any deep-learning implementation, and the time needed to perform this is highly dependent on the amount of data, the model complexity, the search strategy, and the available computational resources. The results of testing three different search strategies for the model selection show their relative efficiency in terms of time and performance on a test set. For most of the log types, the best models were found by the Hyperband algorithm. This is also a faster algorithm than random search and Bayesian optimization. Random search is the second-best algorithm for model selection for this specific case. For example, gamma ray, P-wave, and S-wave sonic logs' best models are obtained using random search. In some cases, we see differences of about 20 to 30 minutes in training time between random search and Hyperband. In

general, Bayesian optimization is the costliest process and yields higher MSE errors for all the log type models (see Table 5).

For the depth-shift results, even though we have relatively few test samples (only 28 and 55/32 for Wells 16/1-9 and 16/1-21S, respectively), making the establishment of general trends difficult, these results allow us to make some important observations. We see that the differences between EWL and LWD/MWD logs are a key feature that affects the depth-matching process based on pattern recognition using our implementation. These differences between the reference EWL and the LWD logs are associated with several factors. For example, their vertical resolution differs due to differences in logging speed since LWD is slower than the EWL, and this for a gamma ray log means higher accuracy because there is an increase in the number of samples that are averaged and

assigned to a given depth. Another example is the difference in the tools' characteristics, e.g., dual sensor vs. single sensor, as is the case for Well 16/1-9, where we observe a slightly higher resolution in the LWD compared to the equivalent EWL log. Despite the preprocessing of the logs, which includes filling in of missing data intervals, spike removal, filtering/smoothing, and normalization/standardization to compensate for differences in resolution, missing data, spikes, and value range discrepancies, we can still see pattern differences between the LWD and EWL log responses that affect the CNN performance (See Fig. 5b density panel). In addition, there are environmental factors that change the borehole conditions over time. For this reason, even after standard corrections have been applied to both logs, they might differ due to temporal changes in the borehole conditions between the acquisition of the comparable LWD and EWL logging runs. The impact of this effect depends on how much the relevant borehole conditions have changed during the delay between the comparable LWD and EWL logging runs. This means that depending on the time delay between LWD and EWL logging runs, the logging measurements might be significantly affected despite proper corrections. This can have additional implications for the way contractors implement environmental corrections to log data.

A clear example of this is shown in Fig. 8. This shows quality control log panels for Window No. 17 in Well 16/1-9, which is the same window as shown in Fig. 5. In Fig. 8, the log values are neither normalized nor standardized, so it is easier to see their values and pattern differences. In general, the borehole size in this section is larger than the reference bit size (Fig. 8a). However, a larger diameter was measured during the EWL logging in the shaly zones in the shallower part of the section, approximately the first 50 data points. Then, there is a cleaner section down to about data point 125 where both diameters are similar, and we see overlapping and closer values and similar patterns for density (Fig. 8c) and PEF (Fig. 8e) logs, respectively. Also, we see smaller differences between the neutron logs in areas with similar borehole diameters. On the other hand, no significant pattern differences are seen between the gamma ray logs in the whole window (Fig. 8b). This is as expected since this log type has a higher depth of investigation; therefore, an enlargement of the borehole diameter has a much smaller impact on the gamma ray log. However, we see a constant shift between LWD and EWL logs that might be associated with different constant corrections for mud type, for instance, KCL mud. From a sample around 125, we observe a gradual increase in shale/clay content and a steady enlargement of the borehole for EWL, which reduces the

Table 5—Hyperparameter Tuning Execution Times and MSE Values for Each Log Type and Model Selection Algorithm

CNN Model	Model Selection Strategy	Execution Time (min)	MSE on the Test Set
Gamma ray	Random Search	126.40	0.47
	Hyperband	121.13	2.02
	Bayesian Optimization	237.51	1.01
Resistivity	Random Search	176.29	3.17
	Hyperband	139.74	0.68
	Bayesian Optimization	239.00	4.19
P-wave sonic	Random Search	126.61	0.92
	Hyperband	85.98	0.56
	Bayesian Optimization	157.60	3.89
S-wave sonic	Random Search	184.94	0.73
	Hyperband	49.13	1.00
	Bayesian Optimization	205.29	6.39
Density	Random Search	89.56	1.87
	Hyperband	42.86	1.00
	Bayesian Optimization	101.33	2.38
Neutron	Random Search	69.72	3.75
	Hyperband	44.49	1.13
	Bayesian Optimization	91.26	4.90
PEF	Random Search	90.80	1.24
	Hyperband	45.53	0.57
	Bayesian Optimization	89.29	3.31

density curve and increases the PEF and neutron logs, as well as perhaps causing slight pattern discrepancies. The density correction curve is a good quality control for the density and PEF curves as it is highly sensitive to the borehole diameter and mud type. Here we see that the LWD correction is mostly constant along the section and positive. In contrast, the EWL correction increases and decreases as a function of the EWL borehole diameter changes, e.g., in the zone between 50 and 125 samples' depth, there is almost no correction for the EWL, but there is a positive correction for the LWD. Also, note that, during LWD, tools are run centered; therefore, the standoff of the tools must be accounted for. In contrast, the EWL density-PEF and neutron logs are run eccentric through pads pressed against the borehole wall. Moreover, at this depth, they used water-based mud with 12% barite. Barite is an element with a high-electron density; hence, it has a higher interaction with the gamma rays emitted from the density source, and fewer gamma rays will be detected by the receptors, thus underestimating the density of the formation. The density correction should be positive to compensate for this effect. Similarly, the barite content will have a negative impact on the PEF values since it has such an efficient capacity to absorb gamma rays in lower-energy levels that it is difficult to measure them accurately. Also, the barite has a PEF of 267 barns/electron compared with most of the lithologies that have PEF values of less than 6 barns/

electron. Consequently, the barite content in the mud leads to unreliable PEF values.

Equivalent quality control panels are presented in Fig. 9 for Well 16/1-21S. These show Window/Sample No. 54; hence, they are the same logs as are shown in Fig. 6, except that in Fig. 9, the logs are neither normalized nor standardized. This emphasizes any differences in their values. We see from Fig. 9a that during LWD, the borehole was in gauge along the whole section, and after a couple of hours, a mudcake was built up, which was detected during the EWL acquisition. Small negative corrections are applied to the EWL density log to remove the effects of the mudcake on the density values (Fig. 9d). The opposite applies for the LWD, where slightly larger positive corrections are needed to compensate for the tool standoff, even though the borehole is in good condition. We can see that only pattern differences between LWD and EWL are very small across the log types, even for those with a shallower depth of investigation, such as density and PEF. On the PEF logs (Fig. 9e), we see a mostly constant shift of the LWD toward higher values than its equivalent EWL. This might be related to the cross-section properties of the mudcake and possible corrections applied to the data before we received it. Note that in this section, an oil-based mud was used. It contained some barite traces, which negatively affected the PEF log.

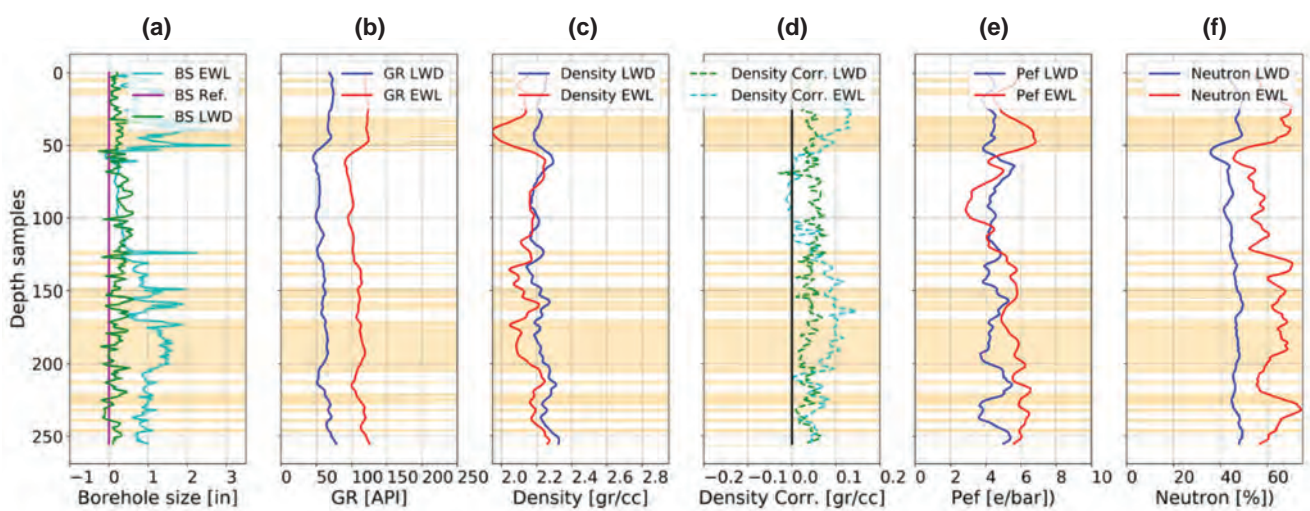


Fig. 8—Quality control panels showing Window No. 17 from Well 16/1-9: (a) borehole size relative to a reference; (b) gamma ray logs; (c) density logs; (d) density correction logs; (e) PEF logs; and (f) neutron porosity logs. Orange indicates the zones where borehole size during EWL logging is larger than the reference bit size (magenta) by more than 1 in.

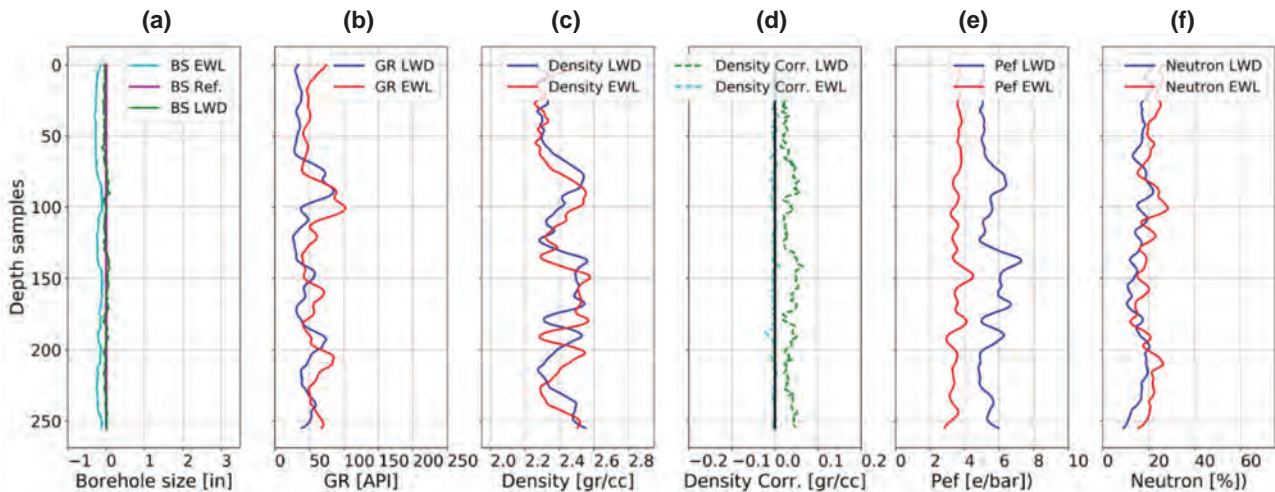


Fig. 9—Quality control panels showing Window No. 54 from Well 16/1-21S: (a) borehole size relative to reference; (b) gamma ray logs; (c) density logs; (d) density correction logs; (e) PEF logs; and (f) neutron porosity logs.

Large gaps of missing data can also create problems for our approach as we use a quick interpolation technique, which might cause pattern differences. Thus, our CNN method can struggle to find a correct depth shift, as we saw for the sonic logs, especially the shear-wave slowness. Another important consideration is the stretch/squeeze effects associated with sticking and slipping of the wireline cable. This effect was not included in the training data but is a common problem during the logging process. Examples of that are seen in Fig. 5b, Fig. 5c, Fig. 6b, and Fig. 6c. The gamma ray log seems not to be significantly affected by this, unlike the density and neutron logs or even other log types like the sonic logs. This might also be related to the depths at which the tool gets stuck and released, and the relative position of the sensors along the tool string.

In general, our CNN has a better performance on logs from Well 16/1-21S than on those from Well 16/1-9. This may be because both log acquisition stages were carried out in the former well by the same logging company. So, even though the tools used are different, due to the nature of the LWD and EWL acquisition processes, the general processing workflows and corrections are likely more similar. Thus, it reduces patterns differences considerably. Well 16/1-21S is also newer, and more sophisticated tools are likely to have been used, as well as there has been little change in the borehole conditions between LWD and EWL acquisitions. When the differences between the reference log and shifted log are smaller, the CNN and cross-correlation solutions differ slightly, and the CNN outperforms the

cross correlation in several individual samples. However, the overall improvement measured with the metrics used (Pearson correlation and Euclidean distance) seems to favor the cross correlation in both wells.

From these insights, it is possible to propose changes to our CNN implementation workflow that could potentially improve the performance of the method beyond that of cross correlation, at the expense of more complex and realistic training models. For instance, we could try to account for dynamic shifts (stretch/squeeze) and introduce more variability between LWD and EWL signals due to borehole condition changes into the training data via more sophisticated data augmentation procedures. This might allow the use of CNN to depth match logs within a fully automated workflow.

CONCLUSIONS

We have demonstrated a simple and practical implementation of 1D CNN as a possible tool to perform well-log depth matching of LWD and EWL measurements for different log type pairs of gamma ray, resistivity, P-wave and S-wave sonic, density, neutron, and PEF logs. It requires little user intervention when the network is trained. Based on pattern similarities, we demonstrated that 1D CNN could detect depth misalignments and suggest sensible depth-shift corrections between raw log curves from different runs through the same wellbore interval. The main advantage of our approach is that it does not require extensive and

complex preprocessing of the data, nor does it require any feature engineering, which is a time-consuming task and requires a high level of expertise and domain knowledge. During the training process, the CNN automatically performs feature extraction from the raw data and identifies relevant patterns in the logs. We also show that the training and hyperparameter tuning process is the most expensive task in terms of computer resources and time. In general, most of the models used in this work were output by Hyperband and random search hyperparameter tuning algorithms, which were much faster training processes than Bayesian optimization. The training and model selection processes for each log type model vary according to the number of samples, model complexity, and search strategy, and it takes between 45 minutes and almost 4 hours. However, once the models are in place, the inference process is performed in less than a minute, which is another advantage of our proposed method, potentially saving hours or days of work for a petrophysicist or rock physics practitioner.

Our results were quality controlled through comparing quantitative metrics, qualitative visual inspection of log profiles comparing the original positions of the logs and their updated versions before and after depth matching using CNN or cross correlation. We demonstrated that most of the windows improved in-depth alignment after CNN corrections; however, the overall improvements using CNN are not better than cross correlation for most of the log pairs. An exception is the resistivity log for both wells. Even though CNN is not superior overall to cross correlation for well depth-shift estimations, several models are quite competitive, which implies that there is room for improvements in the models and the implementation of the algorithm. We also found that CNN struggles to find good solutions when discrepancies between LWD and EWL logs are large, as well as when substantial stretch/squeeze effects exist. This is related to our training data set having been limited to containing only single bulk depth shifts and the use of shifted copies of the logs for training. This limited the capacity of the CNN to deal with stretch/squeeze and to recognize slightly different patterns between logs. Pattern differences are commonly associated with differences in borehole conditions, tool technology, and processing techniques between LWD and EWL log runs.

We implemented our CNN models to estimate the depth shifts between logs from two wells in the Norwegian North Sea as a proof of concept. We plan to investigate further the use of CNN in a more general context by testing whether or not a CNN model can be trained and internally validated on a specific log type and then used to estimate accurately

the depth shifts for other log type pairs. This could save significant amounts of work and time if we can avoid training to build individual models for each log type. We plan a further investigation with improved training sets that include more of the variations and effects present in real data examples.

ACKNOWLEDGMENTS

This research is part of the BRU21 – NTNU Research and Innovation Program on Digital and Automation Solutions for the Oil and Gas Industry (www.ntnu.edu/bru21) and is supported by Aker BP. We also thank NTNU-NPD-Schlumberger Petrel for the ready data set for borehole data and Andrew J. Carter for his suggestions for improving this manuscript. We would like to thank the reviewers and corresponding editor for their valuable feedback, as well as their suggestions for substantially improving the content of this paper.

NOMENCLATURE

Abbreviations

- ANN = artificial neural network
- CNN = convolutional neural network
- EWL = electrical wireline logging
- GR = gamma ray
- KCL = potassium chlorine
- LAS = log ASCII standard
- LWD = logging while drilling
- MSE = mean square error
- MWD = measurements while drilling
- NA = not applicable
- PEF = photoelectric factor
- ReLU = rectified linear unit

REFERENCES

- Abdoli, S., Cardinal, P., and Koerich, A.L., 2019, End-To-End Environmental Sound Classification Using a 1D Convolutional Neural Network, *Expert Systems with Applications*, **136**, 252–263. DOI: [10.1016/j.eswa.2019.06.040](https://doi.org/10.1016/j.eswa.2019.06.040).
- Anderson, K.R., and Gaby, J.E., 1983, Dynamic Waveform Matching, *Information Sciences*, **31**(3), 221–242. DOI: [10.1016/0020-0255\(83\)90054-3](https://doi.org/10.1016/0020-0255(83)90054-3).
- Bergstra, J., Bardenet, R., Bengio, Y., and Kégl, B., 2011, Algorithms for Hyper-Parameter Optimization, *Proceedings, NIPS 25th Annual Conference on Neural Information Processing Systems*, Granada, Spain, 12–17 December. URL: <https://proceedings.neurips.cc/paper/2011/file/86e>

- 8f7ab32cf12577bc2619bc635690-Paper.pdf. Accessed September 27, 2021.
- Bergstra, J., and Bengio, Y., 2012, Random Search for Hyper-Parameter Optimization, *Journal of Machine Learning Research*, **13**(2), 281–305. URL: <https://www.jmlr.org/papers/volume13/bergstra12a/bergstra12a.pdf>. Accessed September 27, 2021.
- Bishop, C. M., 2006, *Pattern Recognition and Machine Learning*, Springer, New York. ISBN: 978-0387-31073-2. URL: <http://users.isr.ist.utl.pt/~wurmd/Livros/school/Bishop%20-%20Pattern%20Recognition%20And%20Machine%20Learning%20-%20Springer%20%202006.pdf>. Accessed September 27, 2021.
- Bolt, H., 2016, Wireline Logging Depth Quality Improvement: Methodology Review and Elastic-Stretch Correction, Paper SPWLA v57n3a5, *Petrophysics*, **57**(3), 294–310.
- Brazell, S., Bayeh, A., Ashby, M., and Burton, D., 2019, A Machine-Learning-Based Approach to Assistive Well-Log Correlation, *Petrophysics*, **60**(4), 469–479. DOI: 10.30632/PJV60N4-2019a1.
- Bulmer, M.G., 1979, *Principles of Statistics*, Courier Corporation. URL: http://www.ru.ac.bd/stat/wp-content/uploads/sites/25/2019/03/102_06_Bulmer_Principles-of-Statistics.pdf. Accessed September 27, 2021.
- Chia, C.R., Laastad, H., Kostin, A.V., Hjortland, F., and Bordakov, G.A., 2006, A New Method for Improving LWD Logging Depth, Paper SPE-102175 presented at the SPE Annual Technical Conference and Exhibition, San Antonio, Texas, USA, 24–27 September. DOI: 10.2118/102175-MS.
- Chollet, F., 2015, Keras, URL: <https://keras.io>. Accessed January 10, 2022.
- Deng, T., Xu, C., Lang, X., and Doveton, J., 2021, Diagenetic Facies Classification in the Arbuckle Formation Using Deep Neural Networks, *Mathematical Geosciences*, 1–22. DOI: 10.1007/s11004-021-09918-0.
- Herrera, R.H., and van der Baan, M., 2014, A Semiautomatic Method to Tie Well Logs to Seismic Data, *Geophysics*, **79**(3), V47–V54. DOI: 10.1190/geo2013-0248.1.
- Hoshen, Y., Weiss, R.J., and Wilson, K.W., 2015, Speech Acoustic Modeling From Raw Multichannel Waveforms, Paper presented at IEEE International Conference on Acoustics, Speech and Signal Processing (ICASSP), South Brisbane, QLD, Australia, 19–24 April. DOI: 10.1109/ICASSP.2015.7178847.
- Imamverdiyev, Y., and Sukhostat, L., 2019, Lithological Facies Classification Using Deep Convolutional Neural Network, *Journal of Petroleum Science and Engineering*, **174**, 216–228. DOI: 10.1016/j.petrol.2018.11.023.
- Ioffe, S., and Szegedy, C., 2015, Batch Normalization: Accelerating Deep Network Training by Reducing Internal Covariate Shift, Paper PMLR 37:448-456, *Proceedings, 32nd Annual International Conference on Machine Learning*, Lille, France, 7–9 July. URL: <http://static.googleusercontent.com/media/research.google.com/en//pubs/archive/43442.pdf>. Accessed September 27, 2021.
- Kerzner, M.G., 1984, A Solution to the Problem of Automatic Depth Matching, Paper VV, *Transactions, SPWLA 25th Annual Logging Symposium*, New Orleans, Louisiana, USA, 10–13 June.
- Kingma, D.P., and Ba, J., 2015, Adam: A Method for Stochastic Optimization, Poster presented at the ICRL 3rd International Conference for Learning Representations, San Diego, California, USA, 7–9 May. URL: <https://arxiv.org/abs/1412.6980>. Accessed September 27, 2021.
- Le, T., Liang, L., Zimmermann, T., Zeroug, S., and Heliot, D., 2019, A Machine-Learning Framework for Automating Well-Log Depth Matching, Paper SPWLA v60n5a3, *Petrophysics*, **60**(5), 585–595. DOI: 10.30632/PJV60N5-2019a3.
- LeCun, Y., Bengio, Y., and Hinton, G., 2015, Deep Learning, *Nature*, **521**(7553), 436–444. DOI: 10.1038/nature14539.
- LeCun, Y., Boser, B., Denker, J.S., Henderson, D., Howard, R.E., Hubbard, W., and Jackel, L.D., 1989, Backpropagation Applied to Handwritten Zip Code Recognition, *Neural Computation*, **1**(4), 541–551. DOI: 10.1162/neco.1989.1.4.541.
- LeCun, Y., Bottou, L., Bengio, Y., and Haffner, P., 1998, Gradient-Based Learning Applied to Document Recognition, *Proceedings of the IEEE*, **86**(11), 2278–2324. DOI: 10.1109/5.726791.
- Li, L., Jamieson, K., DeSalvo, G., Rostamizadeh, A., and Talwalkar, A., 2017, Hyperband: A Novel Bandit Based Approach to Hyperparameter Optimization, *Journal of Machine Learning Research*, **18**(1), 6765–6816. URL: <https://jmlr.org/papers/volume18/16-558/16-558.pdf>. Accessed September 27, 2021.
- Luthi, S.M., and Bryant, I.D., 1997, Well-Log Correlation Using a Backpropagation Neural Network, *Mathematical Geology*, **29**(3), 413–425. URL: <https://link.springer.com/article/10.1007/BF02769643>. Accessed September 27, 2021.
- O’Malley, T., Bursztein, E., Long, J., Chollet, F., Jin, H., and Invernizzi, L., 2019, Keras Tuner, <https://github.com/keras-team/keras-tuner>. Accessed on September 27, 2021.
- Salamon, J., and Bello, J.P., 2017, Deep Convolutional Neural Networks and Data Augmentation for Environmental Sound Classification, *IEEE Signal Processing Letters*, **24**(3), 279–283. DOI: 10.1109/LSP.2017.2657381.
- Sollie, F.O., and Rodgers, S.G., 1994, Towards Better Measurements of Logging Depth, Paper D, *Transactions, SPWLA 35th Annual Logging Symposium*, Tulsa, Oklahoma, USA, 19–22 June.
- Theys, P.P., 1999, *Log Data Acquisition and Quality Control*, Editions Technip. ISBN: 9782710807483.
- Thornton, C., Hutter, F., Hoos, H.H., and Leyton-Brown, K., 2013, Auto-WEKA: Combined Selection and Hyperparameter Optimization of Classification Algorithms, Paper presented at the 19th ACM SIGKDD International Conference on Knowledge Discovery and Data Mining, Chicago, Illinois, USA, 11–14 August. DOI: 10.1145/2487575.2487629.

- Torres, V., Duffaut, K., Stovas, A., Westad, F.O., and Johansen, Y.B., 2020, Automation of Depth Matching Using a Structured Well-Log Database: Prototype Well Example in the North Sea, Paper presented at the SEG 90th Annual Meeting, Houston, Texas, USA, 11–16 October. DOI: 10.1190/segam2020-3424928.1.
- Wang, S., Shen, Q., Wu, X., and Chen, J., 2020, Automated Gamma Ray Log Pattern Alignment and Depth Matching by Machine Learning, *Interpretation*, **8**(3), SL25–SL34. DOI: 10.1190/INT-2019-0193.1.
- Wilson, H., Loftis, J., Page, G., Brooks, A., and Walder, D., 2004, Depth Control: Reconciliation of LWD and Wireline Depths, Standard Practice and an Alternative Simple but Effective Method, Paper SPE-89899 presented at the SPE Annual Technical Conference and Exhibition, Houston, Texas, USA, 26–29 September. DOI: 10.2118/89899-MS.
- Yamashita, R., Nishio, M., Do, R.K.G., and Togashi, K., 2018, Convolutional Neural Networks: An Overview and Application in Radiology, *Insights into Imaging*, **9**(4), 611–629. DOI: 10.1007/s13244-018-0639-9.
- Zangwill, J., 1982, Depth Matching – A Computerized Approach, Paper EE, *Transactions, SPWLA 23rd Annual Logging Symposium*, Corpus Christi, Texas, USA, 6–9 July.
- Zhu, L., Li, H., Yang, Z., Li, C., and Ao, Y., 2018, Intelligent Logging Lithological Interpretation With Convolution Neural Networks, *Petrophysics*, **59**(6), 799–810. DOI: 10.30632/PJV59N6-2018a5.
- Zimmermann, T., Liang, L., and Zeroug, S., 2018, Machine-Learning-Based Automatic Well-Log Depth Matching, Paper SPWLA v59n6a10, *Petrophysics*, **59**(6), 863–872. DOI: 10.30632/PJV59N6-2018a10.

ABOUT THE AUTHORS



Veronica A. Torres Caceres received a BSc degree (2010) in geophysical engineering from the Central University of Venezuela, Caracas, and an MSc degree (2017) in petroleum geophysics from the Norwegian University of Science and Technology (NTNU) in Norway. Veronica is currently

a PhD student at NTNU. Her current research interests include data structuring, petrophysics, rock physics, seismic inversion, machine learning, statistical learning, seismic attenuation, and data integration. From 2011 to 2012, she worked as a geophysicist at IHS Markit as a seismic interpreter and technical support for Kingdom Suite. From

2012 to 2015, Veronica worked as a geophysicist seismic interpreter and velocity model builder for subsalt imaging at PGS, Mexico. From 2017 to 2018, she worked as a research assistant on attenuation estimates and rock physics model simulation. Veronica was the president of the SEG Student Chapter at NTNU from 2019 to 2021, and she is currently a student member of SEG, EAGE, and SPWLA.



Kenneth Duffaut received his MSc degree (1994) in geophysics at the Norwegian University of Science and Technology (NTNU), Norway, and a PhD degree (2011) in geophysics from NTNU. From 1995 to 1997, he worked as a geophysicist in Statoil's petroleum technology department in Norway within field development and geophysical special services. From 1997 to 2015, he worked at the Statoil research centre in Trondheim, Norway, as a research geophysicist in various exploration and production programs. Since 2015, he has worked as an associate professor at the Department of Geoscience and Petroleum at NTNU. Current research interests include landscape dynamics through geological time (tectonic uplift), near-surface geophysics, 4D seismic monitoring, wellbore geophysics, and rock physics analysis combined with machine learning for well and seismic data analysis.



Anis Yazidi received his MSc and PhD degrees from the University of Agder, Grimstad, Norway (2008 and 2012, respectively). He was a senior researcher with NORCE, Norway. From 2014 to 2019, he was an associate professor with the Department of Computer Science, Oslo Metropolitan University, Oslo, Norway, where he is currently a full professor and leading the research group in applied artificial intelligence. He has participated in different EU and RCN projects and leads the AI work package in the EU AI-Mind project. He is also co-coordinating the Excellence Academic Environment NordSTAR at OsloMet. He holds a professor II position with the Norwegian University of Science and Technology (NTNU), Trondheim, Norway, and he is a senior researcher at Oslo University Hospital.



Frank O. Westad received his MSc degree in chemistry and data analysis from the University in Trondheim, Norway (1988) and completed his PhD thesis on “Relevance and Parsimony in Multivariate Modelling” (2000). His work experience includes senior research scientist positions at GE Healthcare and the Norwegian Food Research Institute (Nofima). He has published 50 papers and has also written several chapters in various textbooks on multivariate data analysis. He is now an adjunct professor at the Norwegian University of Science and Technology in the Department of Engineering Cybernetics and holds a position as a chief data analyst at Idletech AS.



Yngve Bolstad Johansen received a Cand.Scient. degree in physics from NTNU, Norway (2000). He joined Schlumberger in 2001 as a field engineer and worked with data acquisition in the Middle East and the North Sea before starting as a logging tool physicist at the Houston Formation Evaluation Center in 2005. In 2009, he began as a principal petrophysicist for Statoil in field development and later R&D. From 2013 to 2020, Yngve was leading petrophysics within Aker BP in the position of chief petrophysicist. Yngve Johansen is currently the principal advisor and coordinates subsurface R&D across all disciplines in Aker BP.

Automated Log Data Analytics Workflow – The Value of Data Access and Management to Reduced Turnaround Time for Log Analysis

Veronica Alejandra Torres Caceres¹, Kenneth Duffaut¹, Frank Ove Westad¹, Alexey Stovas¹, Yngve Bolstad Johansen², and Arne Jenssen³

ABSTRACT

The oil and gas industry of today is undergoing rapid digitalization. This implies a massive effort to transform standard work procedures and workflows into more efficient practices and implementations using machine learning (ML) and automation. This will enable geoscientists to explore and exploit vast amounts of data quickly and efficiently. To address these current industry challenges, we propose a pilot well-log database in HDF5 (Hierarchical Data Format version 5) format that can be continuously extended if new data become available. It also provides versatility for data preparation for further analysis. We show an alternative way to store and use log files in a hierarchical structure that is easy to understand and handle by research institutes, companies, and academia. We also touch upon well-log depth matching, a long-standing industry challenge, to synchronize data from different logging passes to a single depth reference. Having a robust automated solution for depth matching is important to facilitate the use of all available data in a depth interval for analysis by ML. We propose an automatic well-log depth-matching workflow capable

of handling multiple log types simultaneously and its integration with the database. The updated depth-matched logs are added to the database with their corresponding metadata, giving the geoscientist full control. We implemented two algorithms—classical cross correlation combined with a scaling factor to simulate stretch-squeeze effects and a constrained dynamic time warping (DTW). Our results indicate that the classical cross correlation outperforms the warping for both robustness and speed when the DTW is constrained to avoid excessive signal distortion and when the number of processed curves increases, respectively. Some limitations of our approach are related to large changes in the log patterns between the runs, as well as the assumption of negligible depth shift between log types within the same run. The cross correlation also allows a consistent application of depth matching to the metadata. This prototype workflow is tested using two wells from the Norwegian North Sea. We see the potential for extending this automatic database-processing workflow to give geoscientists access to all the data to improve interpretation.

INTRODUCTION

Well-log databases of practical use to geoscientists and petrophysicists are often limited to standardized curves for a specific rock measurement such as those described in the Norwegian Petroleum Directorate (NPD) “Blue Book” (Norwegian Petroleum Directorate, 2021). The “Blue Book” defines which data types are mandatory to report and the formats to use. Even though it establishes some data quality requirements, in some cases, it is not specific enough. This lack of precise specification for data deliverables makes their use difficult. In many cases, addressing the poor data

quality in the original raw data files requires the use of very significant data management resources. This is an example of the negative consequences of a lack of attention to data management for the preservation of legacy data within the industry. This situation is not only associated with old wells but also applies to wells currently being drilled. For instance, it is often common to work with a single spliced final density-log curve instead of having access to all density measurements acquired at different times during the drilling of the wellbore. Looking at a more complete data set can give more insight into changes in formation properties during the drilling of the wellbore (temporal framework). Also, since

Manuscript received by the Editor February 3, 2021; revised manuscript received July 19, 2021; manuscript accepted July 19, 2021.

¹Norwegian University of Science and Technology, veronica.a.t.caceres@ntnu.no; kenneth.duffaut@ntnu.no; alexey.stovas@ntnu.no; frank.westad@ntnu.no

²Aker BP ASA., yngve.b.johansen@akerbp.com

³Excelerity As., arne.jenssen@gmail.com

the final logs have undergone several preprocessing steps, usually carried out by third parties, a lot of information is lost during the process. As a result, the end users will have limited information about the history of these curves, how the borehole conditions evolved before, during, and after logging, and the impact of the log acquisition dates.

It is also quite common for log analysts to face misalignments or desynchronization issues when using multiple logs as input to an equation set. Misalignment or desynchronization is common both in logs acquired during different and the same logging runs. These mismatches could persist all the way to the final processed curves.

Until now, this issue has been addressed by a sophisticated and expert-derived method, with carefully selected depth shifts exactly as needed, but it remains a challenge in the industry and prevents the use of all the available data. Any petrophysical software packages offer approaches for depth matching/synchronization. Several options are available for automating the process. Manual interventions are nevertheless required to reduce residual misalignment among log curves. This is mainly because depth matching/synchronization of well-log data is a crucial step that must be quality controlled as much as possible to keep track of the log curves' misalignment impact for both qualitative and quantitative interpretations. This often becomes a time-consuming and tedious process.

In more specialized petrophysical studies, particularly when training a neural network for ML use, rock physics, and seismic property analysis, depth mismatching can be a main source of error. Moreover, the depth mismatching among logs also has a negative impact on traditional workflows and procedures. It can cause poor log correlations, incoherent interpretation, and analysis. This was explained by Zangwill (1982). He proposed a method that integrates analytical and interactive techniques to achieve accurate depth matching. The optimal solution through his method was to achieve a balance between correlation techniques and the human capabilities of the expert analyst, maximizing the interaction between them. This means that he proposed a curve matching and shifting program based on computerized correlation techniques supervised by an expert operator. He also emphasized the importance of depth matching and possible causes of errors. Depth matching has been researched since the 1960s, when automatic dip computations started. These allow for depth matching using correlation of microresistivity measurements taken at different points along the borehole to correct the dip values.

At the same time, similar work was developed in the pattern recognition field known as the curve matching or

pattern matching problem (Myers, 1980; Müller, 2007). Kerzner (1984) developed software to perform automatic depth matching across wells, considering that different logs in the same well can have the same or different deflection behavior for the same formation. He suggested a cross-correlation coefficient as a measure of similarity between the two log curves. Kerzner's method can be split into two steps. The first involves the computation of the correlation coefficients between two logs, and the second selects optimal displacements with a mathematical optimization model. The optimization model is solved via dynamic programming techniques that find the correct shift considering all possible displacements, choosing the shift which minimizes the curve distortion. Anderson and Gaby (1983) applied dynamic time warping (DTW) as a branch of dynamic waveform matching. DTW is a more general tool to correlate well logs, which is not limited to linear correlations. These techniques are very popular when combined with dynamic programming for solving problems related to speech, voice, and pattern recognition, data mining, information retrieval, and signal processing, among others (Müller, 2007). Even though DTW is designed for time series, it can be used for any type of data arranged as an ordered sequence (time or depth series). For this reason, it has been a very popular technique in a variety of fields, especially for well-log correlation. DTW is gaining popularity in seismic processing and the seismic-well tie process, for example. Hale (2013) modified the DTW algorithm to solve a common problem in seismic image comparison. Munoz and Hale (2014) and Herrera and van der Baan (2014) proposed an automatic seismic-well tie procedure based on DTW that gives superior results to the classical approach of synthetic generation with manual matching.

Recent work concerning the automation of well-log depth matching is presented by Zimmermann et al. (2018), Le et al. (2019), and Liang et al. (2019). They propose a fully automatic workflow that minimizes human intervention by developing a machine-learning pipeline. Their approach was implemented for gamma ray logs from multiple runs in vertical and low-deviation wells. It used a fully connected neural network that self-evolved with cloud-based services and which provides feedback based on manual adjustments from expert petrophysicists. Their neural network algorithm is based on a classification problem type. At the same time, they developed a metric via a k-majority-voting strategy based on different independent metrics to evaluate the performance of the depth-matching process.

We propose as a first stage to build a prototype well-log-structured database format that can store acquired data

in more optimized formats. The purpose is to allow easy access to all available data and get full control of the logs and metadata associated with them. Our database format also has structures for storing preprocessing stages before the data are ready for petrophysical analysis and machine-learning applications. As a second stage, we design a user application to perform depth matching (signal alignment/synchronization) on a chosen log suite in an automatic or semi-automatic way, offering both cross correlation and DTW algorithms. Even though the former is limited to linear correlations, it has the advantage of allowing full user control of the process, and metadata can be depth matched, e.g., temperature, pressure, mud resistivity, etc. Notice that we also consider as metadata some log curves in addition to the traditional metadata as all the parameters and information stated in the file's headers. DTW, in contrast, is an optimization-based approach that computes the optimal warping path to match two signals; therefore, it needs the selection of tuning parameters, and each pair of curves will have a unique warping path that cannot be applied to the metadata (Herrera and van der Baan, 2014). Additionally, we use three different metrics to assess the results of the depth matching quantitatively. They are Pearson correlation, Euclidean distance, and proportion of trace energy predicted. The user has the option to display a log's profile and crossplots as a qualitative assessment throughout the visual inspection. We implement these two stages in two wells from the Ivar Aasen Field in the Norwegian sector of the North Sea. These wells differ considerably in terms of the amount of data, drilling, and logging planning. The processing time to generate a database containing all the data ranges between minutes to a couple of hours depending on the well complexity. These results can be substantially improved by applying parallelization processing on a GPU, as well as some chunking and compression techniques for data storage. Similarly, the depth-matching results show a considerable improvement and reduction in the Pearson correlation, proportional trace energy, and Euclidean distance, respectively, computed by both algorithms. The superiority and versatility of the classical cross correlation over DTW for this application are also emphasized, as well as its lower computational cost.

WELL DATA MANAGEMENT AND FORMATS

The increasing use of automation and machine-learning-based approaches for log quality assessment, analysis, and interpretation requires innovative and modern data structure solutions. A flexible assessment via Python

programming is helpful to ease data assimilation, extraction, and visualization.

The DLIS (Digital Log Interchange Standard) standard from the American Petroleum Institute is a file format designed to solve problems that could not be handled by previously existing formats when more complex logging tools were introduced. Some of these problems that the DLIS format addresses are the variety of data types, e.g., waveforms and arrays, record lengths from a few bits to a thousand bits, and variations in sampling rates recorded during the measuring of a single logging run (Theys, 1999).

Well-log files often have complex binary formats containing a vast amount of information such as log measurements, drilling parameters, tools, description of the mnemonic, acquisition equipment (parts), calibration parameters, and equipment parameters. With DLIS, it is possible to merge, splice, and flip log data, record textual data, include records of indefinite length and encryption data, and avoid limitations related to complex forms of data. However, in some cases, changes in logging parameters (metadata) might be absent from these files because they were not acquired or omission by the operators. Another important piece of information not contained in the DLIS format is the depth cranking/tracking performed to correct depth (Theys, 1999). Besides the lack of depth cranking, there is no quantified depth uncertainty information available after the pertinent corrections have been performed by the logging companies, which adds more challenges to obtain accurate depth measurements and a complete database. The main challenge associated with this data format is that even though it is a followed standard in most cases, vendors and contractors sometimes redefine the standard according to their needs, changing and adding new structures to it, which adds an additional degree of complexity to read the files. Despite their complexity, when it comes to reading and extracting information from the DLIS files, they have the advantage of having been written during acquisition. Therefore, all acquisition parameters are also recorded at the same time (Equinor, 2021).

To address the industry's future data management and big data analytics requirements, we propose a hierarchical restructuration of the data information in DLIS files by converting them into an HDF5 file format. HDF5 is an open-source file format developed for managing, organizing, and storing information with their associated metadata, regardless of size and complexity (The HDF Group, 2016). It is a popular file format in the fields of science and engineering. The flexible nature of HDF5 makes it well suited to research applications. During research, there is

often a need to experiment with different data structures and data processing algorithms. One big advantage of HDF5 is that it is easy to structure the data storage into a format that simplifies subsequent processing steps. A lot of computational and algorithmic complexity can be reduced by storing data in intermediate processing steps. After the research phase is finished, HDF5 is a very high-performing and production file format. HDF5 is widespread, and there exist bindings for most popular programming languages, for example, Java, C++, C#, JavaScript, Python, and MATLAB. HDF5 structures and algorithms developed during research can therefore be easily used in commercial/production settings.

The main structural components of HDF5 files are groups, data set, and attributes. This is also known as part of the building blocks of the HDF5 file data organization and specification. HDF5 is designed to generate a hierarchical organization of heterogeneous data (data sets) into different levels or folders (groups) with their respective metadata (attributes) (The HDF Group, 2016). Figure 1 illustrates the concept of the HDF5 format and shows the interaction of the main structural components.

Data Restructuring From DLIS to HDF5 File Format

We propose a single HDF5 file per well, in other words, an individual HDF5 file containing all data measurements and information from a well. This is simpler than dealing with multiple DLIS files from a well where each file represents a different logging run.

In Fig. 2, we illustrate how a well log, based on multiple DLIS files, can be organized in a hierarchy. We store the raw data in addition to several stages of processed data in the

same HDF5 file. In the illustration, the root group represents the well itself. From that, we create as many groups as DLIS files exist for a given well. In each group, we create subgroups that correspond to the number of depth-sampling frames acquired within a logging run. We assign descriptive data or metadata to each frame, followed by the data sets. The data sets are basically the log curves that were acquired during a specific logging run within a frame. Simultaneously, the metadata associated with each log curve is also assigned during this stage. Note that each group level has its own metadata, which is extracted from the DLIS files and stored in the hierarchical level of the frames, we generate a group called Metadata, which holds several subgroups classifying additional metadata: tools, calibration, coefficients, measurements, equipment, process, and parameters.

We can see the hierarchical buildup of the data as follows. The DLIS files contain a vast amount of data that can be considered as metadata of different data types, and it needs to be sorted under the data it belongs to. For example, the density correction curves should be placed as metadata of the density curve. The monopole acoustic waveforms should be part of the compressional sonic log metadata, and the same occurs for the dipole acoustic waveforms in the case of the shear sonic log, and so on.

As well as the new raw data restructuring, we suggest the inclusion of standardized preprocessing and quality control steps to be followed up. These can be organized in the same manner as subfolders next to the individual runs. They are named Raw Logs, Depth-Shifted Logs, Spliced Logs (optional), and Final Processed Logs.

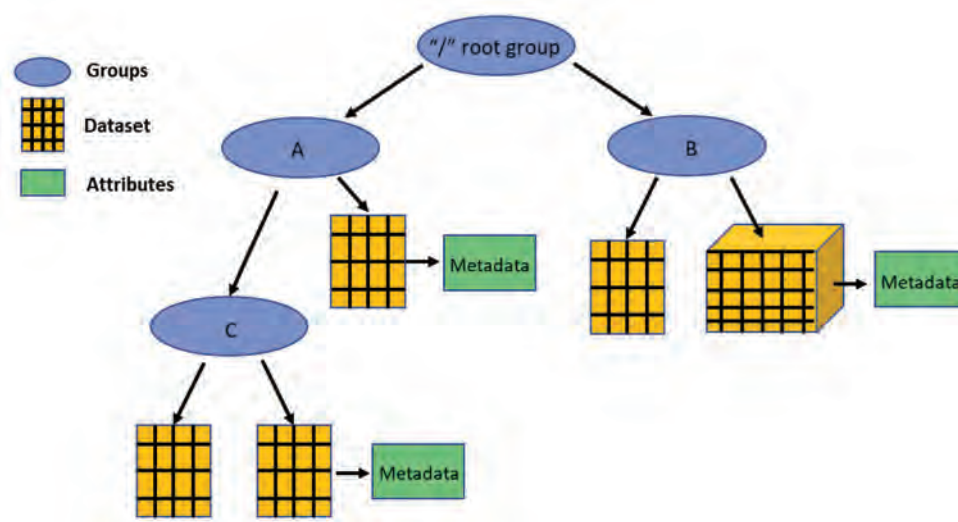


Fig. 1—Example of an HDF5 file structure.

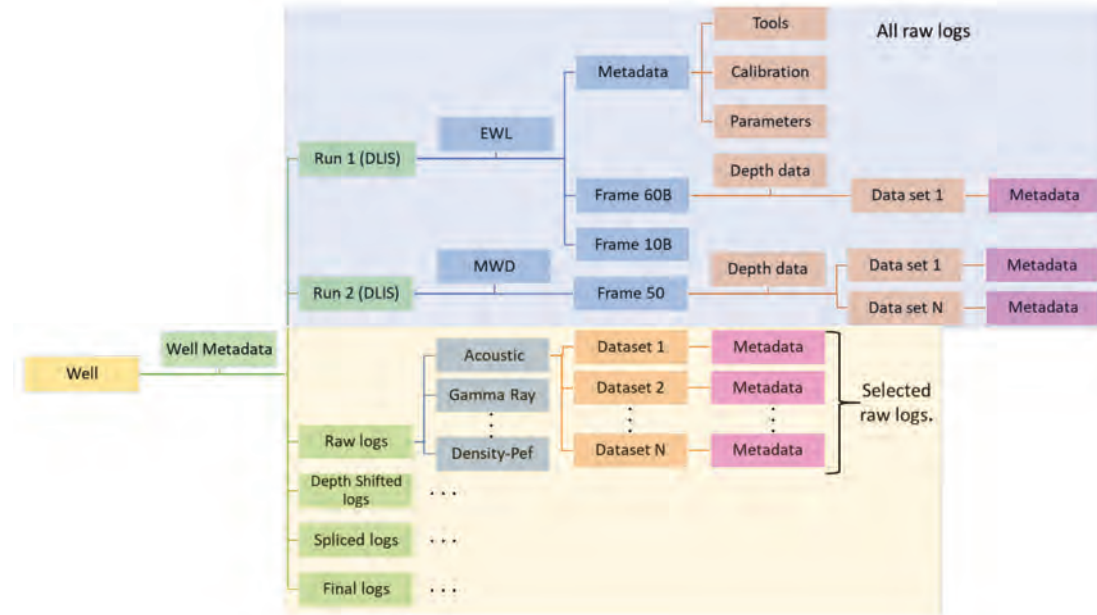


Fig. 2—An example HDF5 file architecture sketch for a single well in which there have been two logging runs. It shows the organization of individual subgroups associated with each logging run, as well as raw, depth-shifted, spliced, and final processed log versions within the file structure. The blue square illustrates the structure for the entire data in the file, while the yellow square emphasizes the organization and structure of the selected logs categorized by petrophysical properties/measurements (acoustics, gamma ray, resistivity, density-PEF, and neutron) as we move further with the process like depth matching and splicing to obtain final logs for petrophysical analysis and interpretation.

The proposed database can be visualized and handled via the HDFView application, which is also an open-source format offered by the HDF5 Group. This is an example of a user interface of our hierarchical log database. Figure 3 depicts several stages during the database building process visualized with HDFView. First, we create the HDF5 file for single-well generating groups per DLIS file. Later, we generate a subgroup for the specific selection of logs considered for petrophysical analysis classified as gamma ray, resistivity, density-PEF, etc. This stage of selection takes all the logs under specific classification guided by mnemonics, for instance, gamma ray logs named as KBGR, BGRC, ECGR, GR, depending on the logging company, which implies that we have a pool of mnemonics per each log measurement. This can be easily expanded by adding new mnemonics to the corresponding list and log category. Afterward, all the gamma ray logs will be placed under the Gamma Ray folder, and they can be identified through their metadata (Fig. 3a). Additionally, the depth measurement corresponding to each run and, therefore, to each suite of logs is also placed under the same folder. In the same way, this information is used to perform further selections such as discriminating repeated sections from main logged sections, for example. The actual database manipulation is done via Python coding; we generate several functions

that take and transform the selected raw log folders into Python DataFrames. Regarding the indexing of the data and to have better control of the depth measurements, two separate DataFrames are created—one for logging-while-drilling (LWD) logs and one for electrical wireline (EWL) logs per log type. We use the first and the last depth value that has a valid measurement. In other words, we identify the first and the last value that is different from -999.25 (no data value) to create a global index vector at the standard depth-sampling rate of 0.5 ft (0.1524 m). This allows us to generate individual DataFrames per log type, allocating the log sections as concatenated small DataFrames in their corresponding depth ranges. One example of this is shown in Fig. 4, where we can see the representation of three sections along the borehole indicated by colors (DataFrames) and concatenated into a single big DataFrame honoring the corresponding depths based on the global index. Once we create the DataFrames, along with keywords, e.g., log type/ log category and mnemonics, those are used as input for a series of sequential functions used to perform the depth-matching workflow that we present in this work. Finally, the results are retrieved from the database and placed under the Depth-Shifted Log folder (see Fig. 3b). The same dynamic could be used for the subsequent steps.

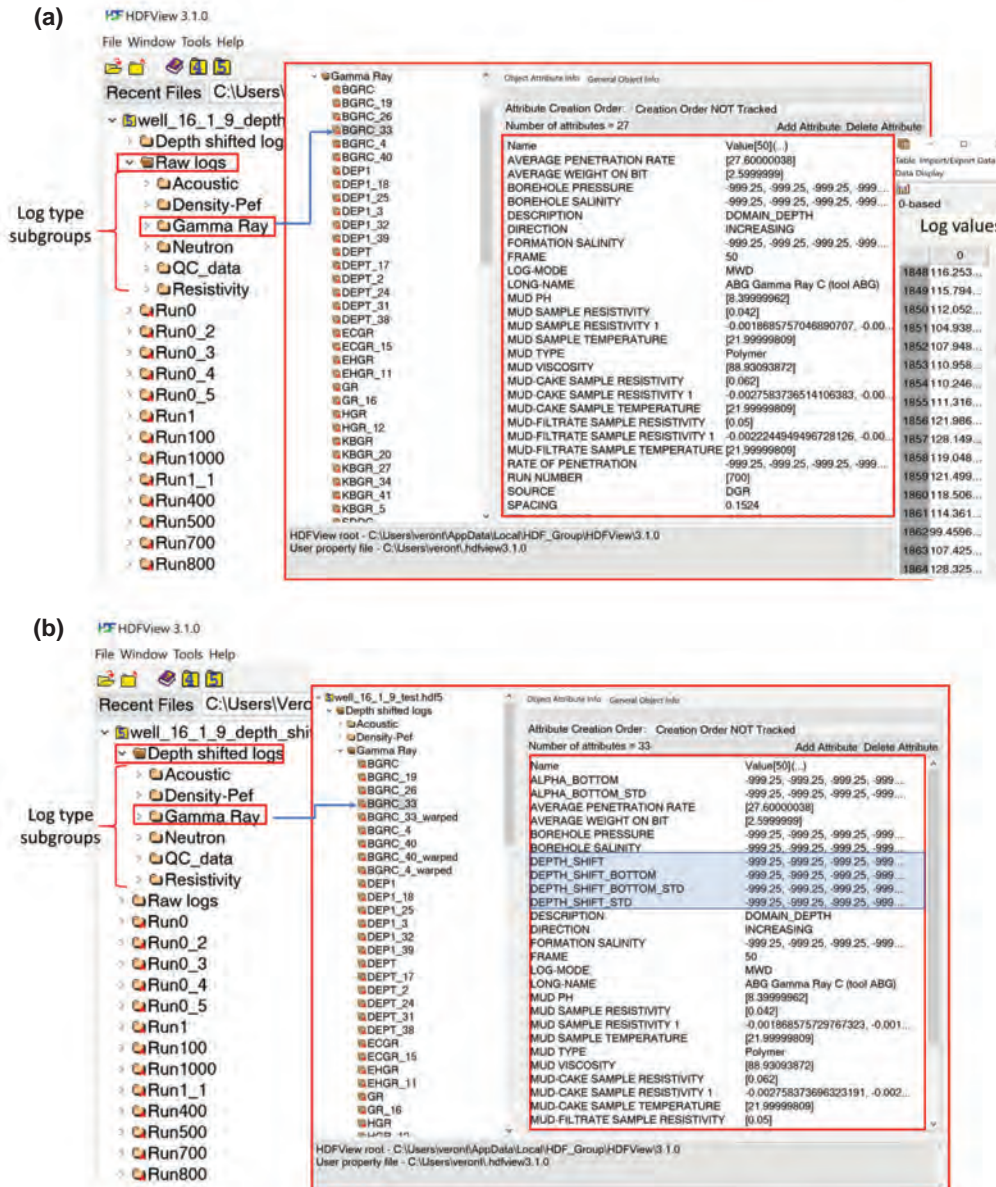


Fig. 3—Database visualization via HDFView for Well 16/1-9: (a) example of the database after raw data selection process, on the left-hand side is the new folder's hierarchy (Raw Logs), and on the right-hand side, all the gamma ray logs and their corresponding depth values from all runs are displayed. The red square indicates the metadata associated with BGRC log and further to the right their values; (b) example of the updated database after the depth-matching process, on the left-hand side is the new folder's hierarchy (Depth-Shifted Logs), and on the right-hand side all the gamma ray logs shifted and warped are displayed. The red square indicates the metadata associated with the BGRC log, and the new metadata values are highlighted in blue.

We implement this idea in Python using h5py and dlsio packages. The former is a pythonic interface to the HDF5 binary data format (Collette et al., 2021). The latter are Python packages written and maintained by Equinor ASA, which allows the reading of DLIS files.

Note that dlsio version 1.14 (used in this implementation) was unable to read files containing tape marks, for example, Halliburton DLIS files*.

*Personal communication with E. Hårstad, 2019, Bergen, Norway: Equinor.

To address this issue, we read the Halliburton DLIS files using a MATLAB application and created an additional function to reformat the data to be placed into an HDF5 format. However, the newer version of dlsio, e.g., version 2.1, has overcome this issue; thus, it can be used for Halliburton DLIS files.

Index	Log 1	Log 2	Log 3	Log 4	Log 5	Log 6	Log 7	Log 8	Log 9	Log N
0				NAN	NAN	NAN	NAN	NAN	NAN	NAN
1			Section 1		NAN	NAN	NAN	NAN	NAN	NAN
2				NAN	NAN	NAN	NAN	NAN	NAN	NAN
3						NAN	NAN	NAN	NAN	NAN
4	NAN	NAN	NAN			NAN	NAN	NAN	NAN	NAN
5	NAN	NAN	NAN			NAN	NAN	NAN	NAN	NAN
6	NAN	NAN	NAN	Section 2		NAN	NAN	NAN	NAN	NAN
7	NAN	NAN	NAN							
8	NAN	NAN	NAN							
9	NAN	NAN	NAN							
.	NAN	NAN	NAN							
.	NAN	NAN	NAN	NAN	NAN	NAN				
.	NAN	NAN	NAN	NAN	NAN	NAN				
M	NAN	NAN	NAN	NAN	NAN	NAN				

Fig. 4—Sketch of a Python DataFrame containing all the existing logs available in a well under a specific category, e.g., Gamma Ray LWD ordered according to their depth position along the borehole via global index. Colors (blue, green, and orange) indicate the depth sections with valid values in the well. The gray color indicates the automatic filling of the not a number (NAN) values, ensuring the correct positioning of the logs guided by the global index vector.

AUTOMATIC DEPTH MATCHING OF WELLBORE-LOG DATA

Depth misalignments between different wellbore measurements, such as LWD/measurement while drilling (MWD) and EWL, are quite common because of ignoring the depth data uncertainty. This uncertainty is the result of several factors such as the depth measurement system itself, calibration accuracy, calculation of environmental factors' corrections during the acquisition, and uncertainty calculations**. In most cases, these depth differences might lead to LWD/MWD logs placed at shallower depths than their EWL equivalent (Chia et al., 2006; Pedersen and Constable, 2007). For example, LWD data are acquired at a variable sampling rate, which is controlled by the drilling rate. In other words, LWD measurements are acquired in a time-driven mode. The depth assignment is based on the driller's depth which is basically the length of the drilling pipe (at surface conditions and under zero tension or compression) projected along the wellbore. The actual length of the pipe (and therefore the depth of the logging sensors) depends on the applied weight on the bit (WOB) and the torque on the pipe as steel is elastic. Also, different rig-states during the drilling process affect the pipe length in different ways adding several levels of complexity for the application of the proper corrections to determine the absolute measured depth, also known as along-hole depth (AHD) (Bolt, 2019). These instantaneous driller's depths are stored with respect to time for later merging with LWD downhole data. On the

other hand, the EWL depth measurements are known as the logger's depth. This is based on the length of cable that has gone into the well. It measures continuous depth as the tool goes up and down, measured either using cable length as defined by calibrated measure wheels or using magnetic marks and measure wheel interpolation (Wilson et al., 2004; Bolt, 2016).

Both driller's and logger's depths are prone to errors that, in most cases, are not accounted for in the correction workflows applied to raw log data directly in the field. For LWD logs, we have the following correction types: pipeline stretch up to a 5- to 10-m increase due to different weights on the bit, thermal expansion (up to 3- to 4-m increase), pressure effects associated with differences between circulation fluid pressure and annular fluid pressure (contributing to an increase of approximately 1 to 2 m), ballooning effects caused by the change in average pressure inside or outside the tubing string (generating errors of about 2 m) causing an extension of the pipe length, as well as an increase in the diameter of the pipe that tends to compensate for the increased length, among others (Theys, 1999; Chia et al., 2006). In addition to this, other factors affect the length of the drillstring depending on a given rig-state, such as changes in fluid composition, flow rate, mud pressure, cuttings volume, helical and spherical buckling, friction, buoyancy, along-hole friction factor, etc. Changes in the penetration rate (ROP) and WOB also affect the length of the drillstring. These two MWD measurements are defined by the movement of the traveling block as well as the bit position. Therefore, there are many corrections associated with the LWD depth measurements. (Bolt, 2019). EWL logs can suffer from tool sticking. This is when the depth recording system keeps measuring the movement of the cable while the tool remains in the same depth recording the log property measurements against that erroneous depth measurement. Cable stretching (elastic and inelastic) is another correction that is already applied at the wellsite before delivering the DLIS file from the first logging pass. The current practice in the industry to correct for this effect is the log-down/log-up correction where the AHD difference between a point near holdup depth (HUD) is seen during run-in-hole (RIH) log-down, and the pull-out-of hole (POOH) log-up is considered to be the stretch correction. A stretch chart is another methodology that is based on a crossplot of the surface tension against depth. The calculated elastic stretch correction considers the thermal expansion of the cable with the elastic stretch. However, sometimes the well path can be complex, and that cable stretching correction is

**Personal communication with H. Bolt, 2021, Crief, Scotland, UK: Depth Solutions.

somewhat simplistic. To mitigate some of the shortcoming and assumptions of the current procedures, Bolt (2016) proposed a waypoint correction for cable stretching that use the cable head tension and the surface tension. He also proposed a correction for the stick-and-pull effects. The application of these methodologies could provide more consistent AHD measurements with reduced differences between LWD and EWL (Bolt, 2016). There are also effects of pressure and thermal expansion of the cable, which often seems to be a negligible correction; therefore, they are not always considered, as well as twisting and rotating effects (Sollie and Rodgers, 1994). Other factors affecting depth accuracy are associated with surface setup stability, tension distribution (friction, tool sticking, cable keyseating), human errors, and measuring wheel accuracy (Theys, 1999).

More detailed explanations of these common issues are presented by Wilson et al. (2004), Brooks et al. (2005), Chia et al. (2006), and Pedersen and Constable (2007). They also showed how it is possible to reduce the initial depth misalignment/desynchronization of logs curves between LWD and EWL if proper correction models are used for each depth measurement system independently (LWD and EWL) to compute the AHD with their corresponding uncertainties having a true-along-hole depth (TAH). In other words, AHD is equivalent to the observed depth with corrections, and the TAH is the AHD with the measured uncertainties. These depth differences can be magnified when data acquisition is carried out by different contractors at the same well since each company uses its own methodology for depth determination, as illustrated by Bolt (2016). As we mentioned earlier, our aim is to generate an automatic workflow to reduce the depth mismatching/desynchronization between well logs from different runs logging the same depth intervals, which are synchronized with respect to a reference depth (EWL suite of logs is considered to be at the correct depth) and incorporated into our database. Therefore, we, unfortunately, do not have a true vertical depth's uncertainty that can be related to the next well. This issue is out of the scope of this work.

We developed a Python-based prototype depth-matching workflow that is founded on an analytical signal processing approach using classical cross correlation and cross correlation with a scaling factor. The latter approach allows the simulation of stretching and squeezing effects. For comparison, we apply depth matching of logs using a DTW algorithm.

Cross Correlation and Cross Correlation With an Additional Scaling Factor

We treat our log curves as a deterministic signal (depth series or depth vector); thus, we use the signal processing cross-correlation method to measure the similarity of two logs as a function of their relative displacement. We define a reference depth series EWL log as $X = (x_1, \dots, x_N)$ and a test depth series LWD log as $Y = (y_p, \dots, y_M)$. Their cross correlation, c , at depth lag $k = 0, 1, \dots, \|X\| + \|Y\| - 2$ is given by Eq. 1:

$$c(k) = (X * Y)(k - N - 1) = \sum_{i=0}^{\|X\|-1} x_i y_{i-k+N-1}^*, \quad (1)$$

where $\|X\|$ is the length of X , $N = \max(\|X\|, \|Y\|)$, and y^* is the complex conjugate of y (Oliphant et al., 2021).

Our implementation is as follows: Firstly, we select a common depth window for each drilled subsection where both LWD and EWL are available across different log measurement types, e.g., gamma ray, resistivity, density, PEF (photoelectric factor), neutron, and acoustics. This is necessary as we aim to obtain a single depth shift for each cross-correlation window for all the log types in a way that their metadata can be shifted accordingly. In other words, all data must be shifted to a common reference depth axis. This common reference depth is defined under certain considerations. For example, we assume that any depth mismatch between logs acquired in the same logging run is negligible. Therefore, we can say, for example, that EWL gamma ray and EWL density logs acquired during the same run are aligned with a tolerance of 2 ft and 4 ft if it is a vertical well or deviated well, respectively (Bateman, 1986). The same assumption is made for LWD logs. The common depth ranges and individual depth intervals for each log type or measurement are determined considering the ranges given by both LWD and EWL. However, the number of logging sections is given by the LWD. In other words, we identify the starting and stopping depth of all valid values (log values different from -999.25) of LWD and EWL log types and runs, which then define each log type depth range. After obtaining these ranges, we identify a common starting and stopping depth across all log types per run. The starting and stopping depths are defined by the log type that starts deepest and the log type that ends shallowest, respectively.

Differences between starting and stopping depths across log types are associated with the sensor positions along the tool string.

Secondly, we select the pairs of logs to be used for the cross correlation, and the reference log is defined as the best EWL (the first up suite of logs to be run in the borehole) environmentally corrected GR for the gamma ray pairs or deep laterolog resistivity for the resistivity pairs, for example.

Thirdly, we preprocess the logs to fill missing data intervals and remove spikes. Missing data are replaced with interpolation or log reconstruction depending on how large the gaps are. The filling of the gaps is constrained to be less than 50 samples that is equivalent to 25 ft (≈ 7.62 m), and it corresponds to less than one-third of the cross-correlation window size. When gaps are larger than this constraint, the log is discarded. However, this is a temporal edition of the data since the cross correlation needs continuous signals and cannot handle not a number (NAN) samples. Thus, after computations, the original data are retrieved. Other examples of preprocessing are filtering/smoothing and normalization standardization to compensate for resolution discrepancies between LWD and EWL. For example, the LWD gamma ray log shows a higher vertical resolution than its equivalent EWL (see Fig. 7). This might be due to differences in logging speed, where the LWD is acquired with lower speed than EWL increasing the statistics and number of samples that are average and assigned to a given depth, as well as differences in sensors, e.g., dual gamma ray sensors vs. single sensor tools. This preprocessing also contributes to alleviate possible noise and range values discrepancies as a result of variation between tools, contractor processing flows and technologies, borehole conditions, and drilling fluids, etc. For example, different parametrization for environmental corrections and changes in the borehole environment can lead to significant variations in the log's patterns and their values. A common example is the GR log that generally shows the same patterns but can present a constant shift in their values (higher or lower) from run to run due to mud type corrections, e.g., KCL mud.

Fourthly, depth matching is performed in a sliding window of length 50 m. This window length was selected based on a sensitivity analysis of variability of the depth shift as a function of window length, which is proportional to the

number of cross-correlation windows, as well as being based on suggestions from expert petrophysicists. We test window lengths of 100, 50, and 25 m, respectively. The larger the window, the more uniform depth shifts are obtained, and global patterns of the logs are used to do the match. On the other hand, smaller windows are more affected by noise in the signals, and the shallow depth of investigation logs tends to show depth shifts highly deviated from the general trend shown by the deep depth of investigation logs. This window length is chosen to satisfy the trade-off between matching both geological low-frequency trends (global and high lithological contrast signatures, e.g., gamma ray deflection between shale and clean limestones) and high-frequency details (local and weak contrast signatures, e.g., gamma ray deflections in a sequence of interbedded shales and sand or shaly sands) for most log types. In addition to the depth-matching computations, some quality control metrics are estimated before and after depth-mismatch corrections for comparison purposes, e.g., Pearson correlation, Euclidean distance, and the proportion of trace energy predicted. For details of these metrics, we refer the reader to Appendix 1. Crossplot and depth section profiles are also output for visual inspection and quality control of the results.

After individual shifts are obtained for each pair of log types (gamma-gamma, density-density, resistivity-resistivity, etc.), they are analyzed in terms of their variability between cross-correlation windows and as a function of their depth of investigation of each sensor, as illustrated in Fig. 5. This shows the general depth dependence of the depth shift (Fig. 5a) and helps to identify outliers. We establish that any depth shift value representing ± 40 samples or more, which is here equivalent to 20 ft (~ 6 m), will be treated as an outlier, and therefore its weight will be set to zero. However, if there are clear limits on the depth data value uncertainty given by operator companies for specific depth sections along the borehole, the user can decide on stricter depth shifts' range to identify outliers. Based on this, the user can also assign weights for each sensor giving higher weights to more reliable tools measurements or the ones less affected by borehole conditions (e.g., gamma ray and resistivity attenuation in this case) and compute a weighted average and standard deviation (uncertainty) in the depth shift, thus obtaining a single common depth shift across log types.

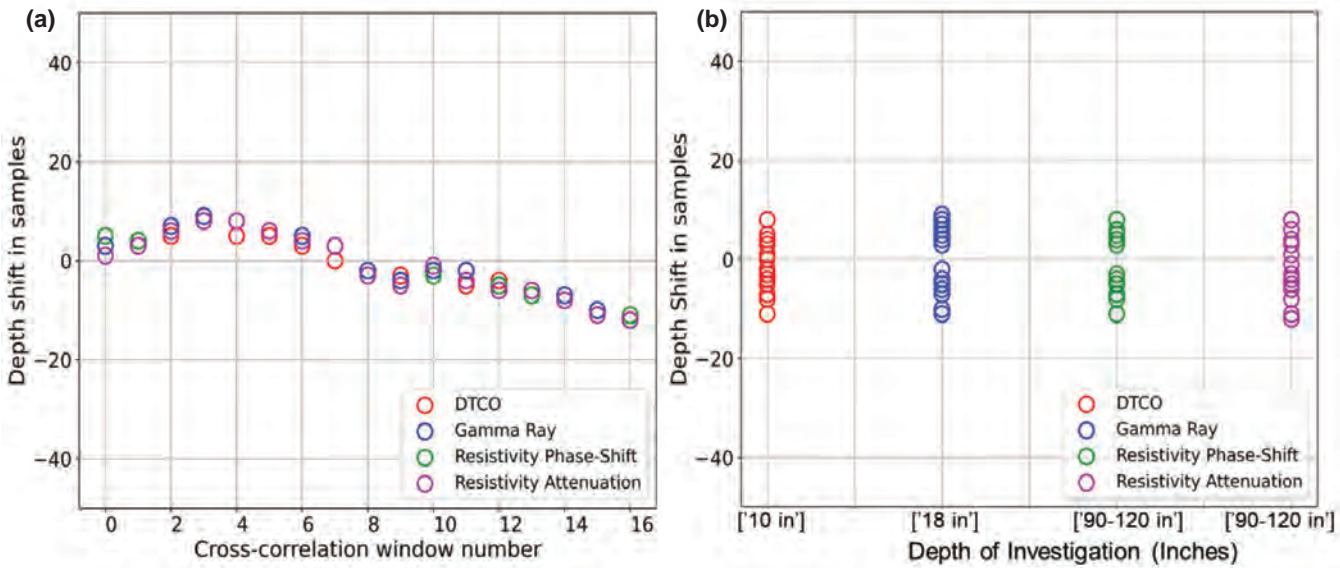


Fig. 5—Example of depth shift variability crossplot for Well 16/1-21S, Drilling Section 1: (a) depth shift variability in samples per cross-correlation window; (b) depth shift variability as a function of sensor depth of investigation. The color code identifies each log type/sensor.

Fifthly, we apply the depth shift to all well-log types together with log reconstruction. The latter approach considers both the top and bottom log sections (tails) that were excluded from the common window selection. These tails are given the shifts applied to the uppermost and lowermost cross-correlation window within a log pass, e.g., the depth shift is held constant within the tails. The bottom of the log might, for this reason, show a strong mismatch and deeper depth position than it should due to accumulated depth shifts applied along the whole wellbore section. To address this problem, we consider a cross-correlation approach that includes stretching and squeezing effects through an additional scaling factor α (that represents a proportionality quantity between the length of the reference log (EWL) and the shifted log (LWD)). For instance, when $\alpha = 1$, a simple bulk shift is carried out, $\alpha < 1$ implies stretching of the shifted log, whereas $\alpha > 1$ implies squeezing.

The scale factor adds an extra degree of complexity to the cross-correlation computation as each cross correlation must be performed as many times as there are α values. This allows the generation of contour maps of cross-correlation coefficients as a function of depth shift (ΔZ) and scaling factor α (Fig. 7). The α range is limited to $0.75 \leq \alpha < 1.25$, which is equivalent to a maximum stretching or squeezing of

about 20 ft (~6 m). The best $\alpha-\Delta Z$ pair is the one that has the highest correlation value closest to 1. This pair is selected for correction of the data. Similarly, as for the common window depth matching, we attempt to find a single $\alpha-\Delta Z$ pair for all log types that have bottom tails such as gamma ray, density, PEF, neutron, and resistivities. The acoustic logs are often positioned at the top of the tool string; hence, they do not have tails at the bottom of the common depth window. The opposite is true for the gamma rays or resistivity logs (as is the case), which are located right after the drilling bit. See a general example of a typical borehole assembly (BHA) in Fig. 6. The common $\alpha-\Delta Z$ pair is computed following the same procedure as before via weighted average constrained by maximum values of ΔZ not larger than ± 10 samples (5 ft ~ 1.52 m) and $\alpha \geq 1$ (only squeezing effect is considered). The final step is the application of the bottom tails' correction and reconstruction of the final log. We assess the quality of the final depth-matched logs by visual inspection and with the previously mentioned metrics. The final corrected log curves are then denormalized and reinserted into the database under a group called "Depth-Shifted Logs." Their corresponding metadata are also shifted when applicable and included in the database. Notice that the depth shift values are also included as metadata.

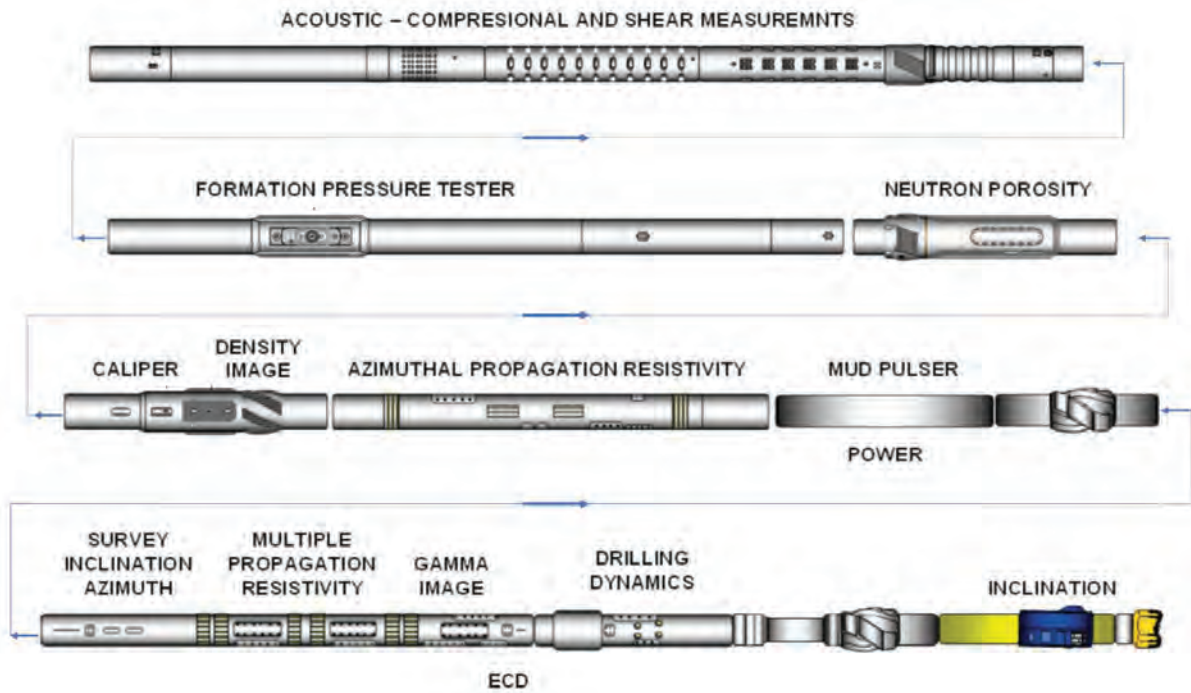


Fig. 6—Schematic diagram of a typical borehole assembly (BHA) with the LWD/MWD sensors. Modified and taken from Klotz et al. (2008).

Dynamic Time Warping (DTW)

DTW is a well-known technique used to find the best alignment between two time series under specific constraints. It provides a distance measure as well as the warping path that optimally deforms the test series to resemble the reference. Therefore, it can be used as a similarity measure between two series. This deformation addresses the possible nonlinear relationship between signals, as well as stretching and squeezing effects. However, it is important to avoid overfitting during the optimization process since this can lead to unrealistic results and excessive distortion of the original signal (Anderson and Gaby, 1983). One potential problem is that DTW may also change the intensity in the signal, not only correcting for shifts in the depth position.

The DTW algorithm can be described by assuming that we have two logs that need to be depth matched. Then, we define the test log as $X = (x_1, \dots, x_N)$ and the reference log as $Y = (y_1, \dots, y_M)$, where the indexing of X is $i = 1, \dots, N$ and Y is $j = 1, \dots, M$. It is also assumed that the dissimilarity distance d is given by a non-negative function f at each pair x_i and y_j as defined in Eq. 2 (Giorgino, 2009).

$$d(i, j) = f(x_i, y_j) \geq 0. \quad (2)$$

The Euclidean distance is commonly used as a dissimilarity measurement along the warping path $\varphi(k)$,

$k = 1, \dots, Z$ that is expressed as $\varphi(k) = (\varphi_x(k), \varphi_y(k))$; the warping functions φ_x and φ_y remap the time/depth indices of X and Y , respectively. With these elements in place, we can compute the average accumulated distance between each pair of points x_i and y_j :

$$d_\varphi(X, Y) = \frac{\sum_{k=1}^Z d(\varphi_x(k), \varphi_y(k)) m_\varphi(k)}{M_\varphi}, \quad (3)$$

where $m_\varphi(k)$ is a per-step weighting coefficient, and M_φ is the normalization constant that ensures that all of the accumulative distances can be compared regardless of the warping path (Giorgino, 2009). Several constraints are imposed within the algorithm to compute a φ that avoids undesirable solutions, for instance, endpoint constraints, local and global path constraints, axis orientation, and local distance measurements, as indicated by Anderson and Gaby (1983). The main idea of DTW is to find the optimal path that gives the minimum global dissimilarity $D(X, Y)$ or DTW distance by minimizing the cost function $d_\varphi(X, Y)$ (Giorgino, 2009):

$$D(X, Y) = \min_\varphi d_\varphi(X, Y). \quad (4)$$

We include DTW as an algorithm option in our prototype depth-matching workflow, as well as cross correlation, since it is relatively fast, even though it has several pitfalls when it comes to generalization in the context of our application. For its implementation, we use the dtaidistance package in Python (Meert, 2018). For example, each type of log will have its unique warping path that cannot be compared with the others; hence, it is not possible to propagate those depth shifts to the sharing metadata (e.g., mud resistivity log)

either to other logs of the same type (e.g., deep and medium resistivity logs). For example, if we depth match bulk density, we need to compute two new warping paths to depth match for long- and short-spacing densities, respectively. Moreover, the application of the warping has fewer steps than those required for the cross-correlation process, as can be seen from Fig. 8.

For depth matching using DTW, first, the data are selected from the “Raw Logs” folder of the database (HDF5

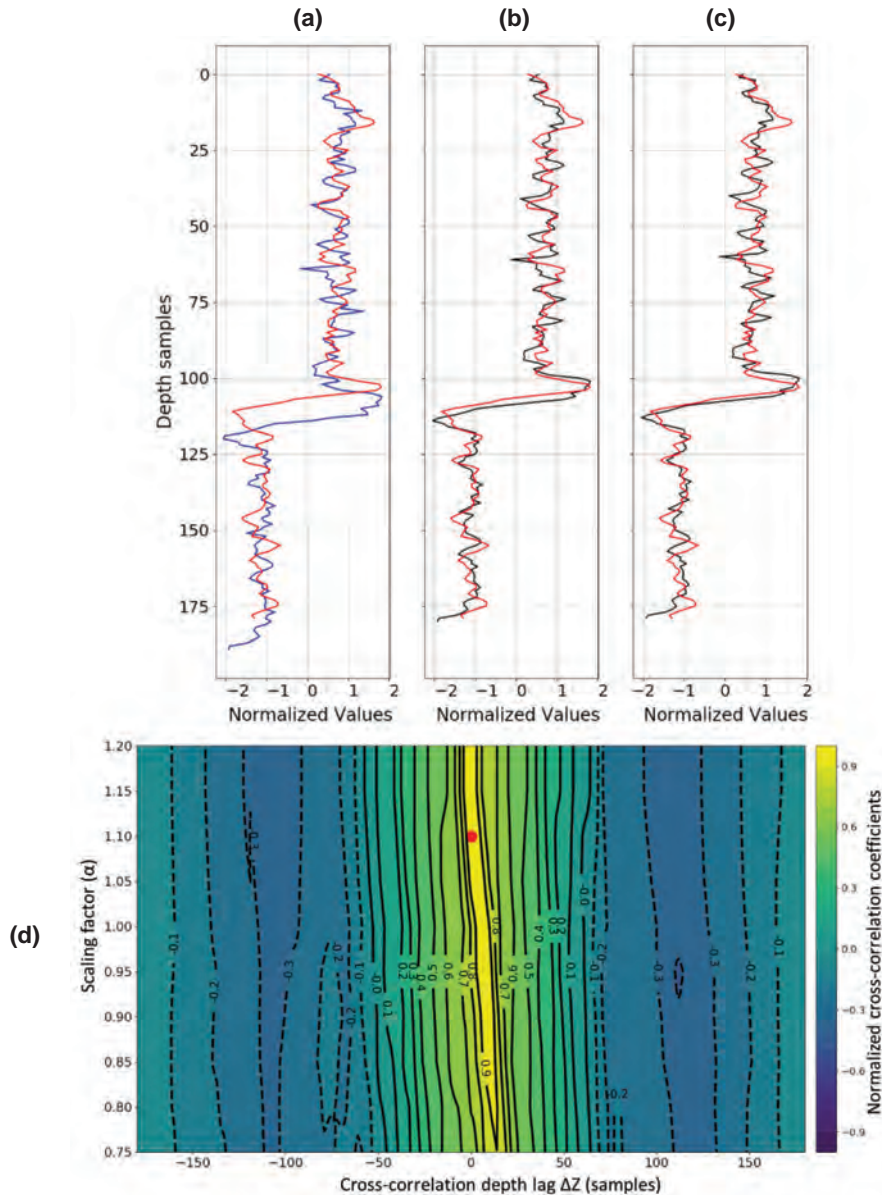


Fig. 7—Depth matching at the bottom tail via cross correlation with scaling factor example for Well 16/1-9 gamma ray logs: (a) gamma ray logs before correction, blue LWD (test) and red EWL (reference); (b) gamma ray logs after squeezing process with $\alpha = 1.1$, black LWD (test) and red EWL (reference); (c) gamma ray logs after squeezing plus shift correction with $\Delta Z = 1$, black LWD (test) and red EWL (reference); (d) contour map of the cross-correlation coefficients as a function of ΔZ and α ; the best $\alpha - \Delta Z$ pair is indicated with a red dot, and ΔZ represents the depth shift in a number of samples.

file). Second, we use the individual depth range for each well-log type, in contrast to when using the cross correlation, where we must constrain our computation to a single common reference window. This is due to the uniqueness of the warping process for each individual log; therefore, we can skip that step. Similarly, we select a reference log (EWL) and a test log (LWD) of the same type, e.g., gamma-gamma, resistivity-resistivity pairs, and so on. Both are preprocessed by filtering/normalization before they are used

in computations. However, filtering is not strictly necessary when we use DTW. We apply the filtering in this work to compare with the cross-correlation results. We predefine the tuning parameters after exhaustive testing for window size, penalty, and the relaxation parameter. From where we observe that the most relevant parameter controlling the quality of the matching is the penalty term by regulating the degree of signal distortion, as shown in Fig. 9, we select a value of 2 for this term that seems to show a good

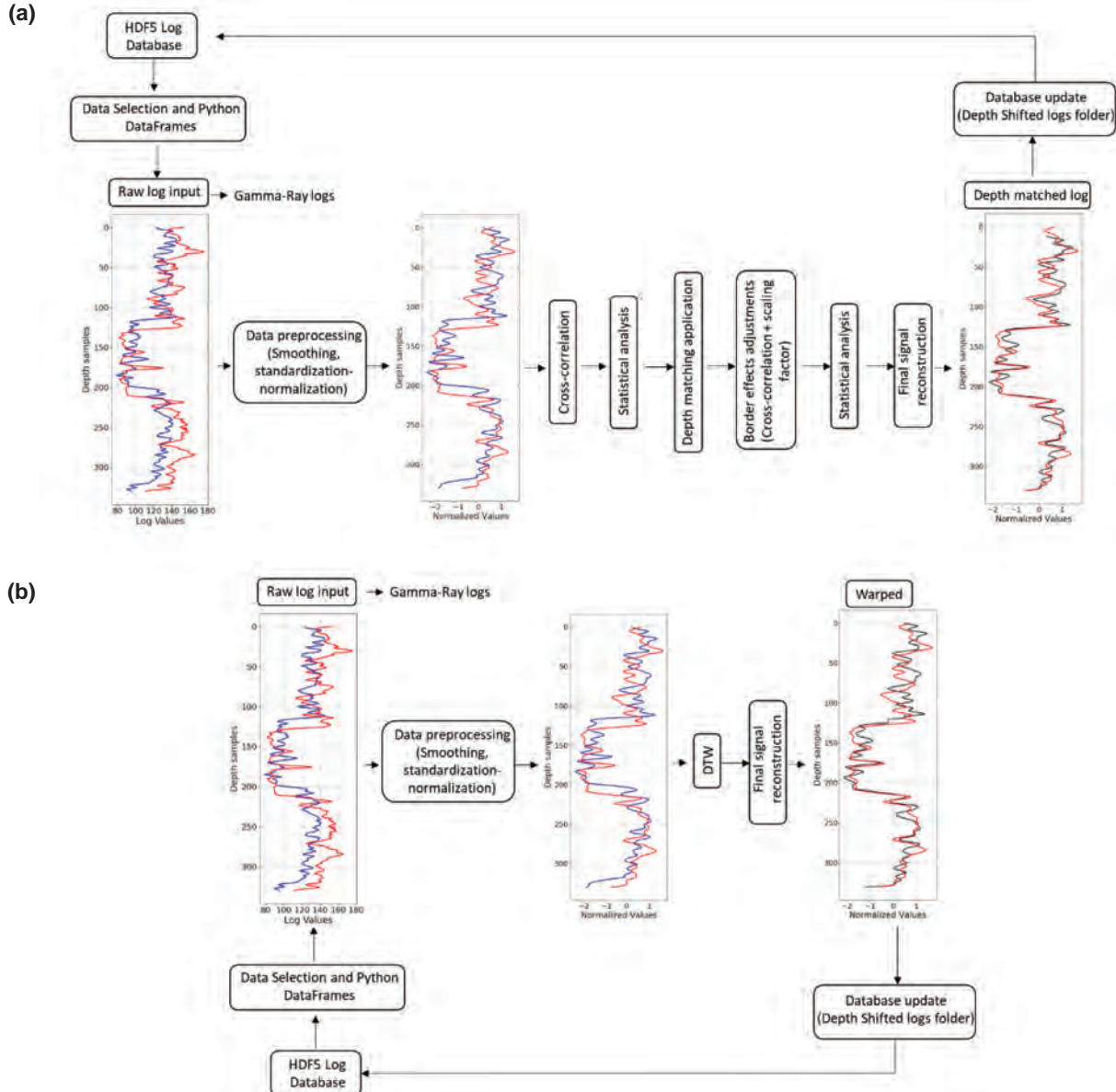


Fig. 8—Schematic diagram of the proposed depth-matching workflow integrated with the log database (HDF5 file) for gamma ray logs. Solid line blue, red, and black represent the LWD log before depth matching, the reference EWL log, and the LWD log after depth matching, respectively: (a) depth-matching process via cross correlation; (b) depth-matching process via DTW.

compromise between the resulting depth matching and the degree of signal distortion. This is important to avoid perfect log alignments at the expense of obtaining an overfitted and highly distorted signal. On the other hand, the window size has a significant impact on the computing time of the distance matrices, therefore the warping process itself, and the maximum shift allowed. We select a window size of 300 and 50, where the only difference in the results is the execution time of the process. The relaxation parameter (PSI) ignores the number of start and endpoints in the signal if this leads to a shorted distance. In our case, this parameter does not substantially affect the depth-matching process; hence, we select to keep the default values $\text{PSI} = 0$. For details of the selected parameters, see Appendix 2.

The results are evaluated via visual inspection and quantitative metrics for the cross correlation. Finally, the warped logs are denormalized and incorporated into the database as a warped version under the “Depth-Shifted Logs” group as an additional available log version. Fig. 8 shows the depth-matching workflow for both options, cross correlation and dynamic time warping, where we can see their interaction with the database. The advantage of the hierarchical structure is that it makes easier the searching and organization of the data. Therefore, via Python coding, we can select the target logs to be input into our proposed workflow. After the logs are depth matched, the updated versions are retrieved into the database under the corresponding group/folder (Depth-Shifted Logs).

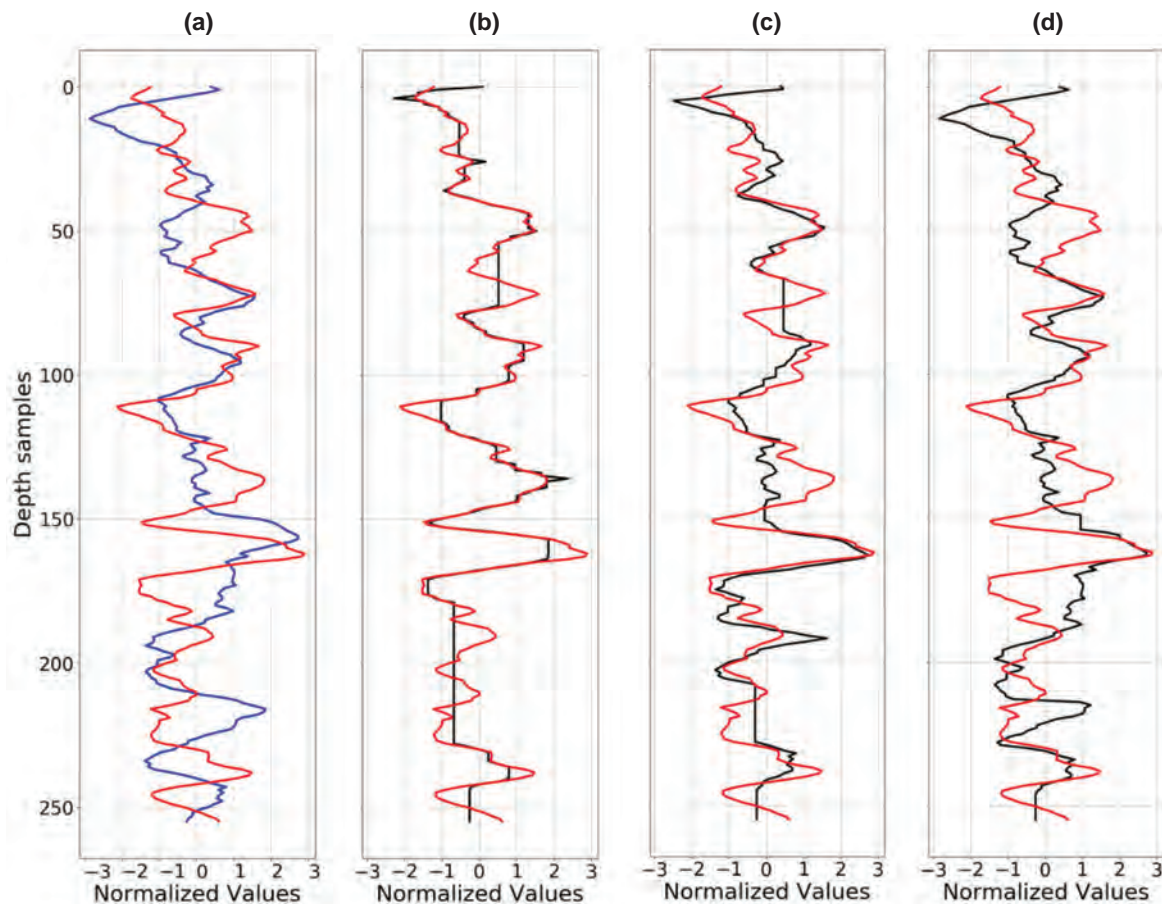


Fig. 9—DTW tuning parameter test for penalty values, example in gamma ray logs for Well 16/1-9. Solid lines (red) indicate the reference log (EWL measurement), and solid lines (blue and black) indicate the test log (LWD measurement) before and after depth matching, respectively where: (a) gamma ray logs before depth matching with a Pearson correlation = 0.198; (b) gamma ray logs after depth matching via DTW, penalty = 0, warping distance = 10.30 and Pearson correlation = 0.929; (c) gamma ray logs after depth matching via DTW penalty = 1, warping distance = 14.49 and Pearson correlation = 0.772; (d) gamma ray logs after depth matching via DTW penalty = 2, warping distance = 18.73, and Pearson correlation = 0.423.

RESULTS

We implemented Python code for generating a structured database as an HDF5 file integrated with the depth-matching workflow in two wells as a prototype test. These wells are key to model the Ivar Aasen Field in the Norwegian North Sea. Example results are shown in Figs. 10 and 11. Note that these two wells have very different drilling planning, process, and amounts of data, and acquisition contractors. Well 16/1-9 was drilled with the drilling services of Halliburton in 2008; therefore, the LWD/MWD data were also acquired by the same company, while the EWL data were acquired by Schlumberger. Well 16/1-21S was drilled with the drilling services of Schlumberger in 2015, and both LWD/MWD and EWL data were acquired by the same company.

From Fig. 10, we can observe the result of using a single cross-correlation window and data from Well 16/1-9 where misalignments exist between gamma ray measurements acquired while drilling and after drilling using wireline tools. After the data are depth matched using both algorithms, there is a substantial improvement in the alignment of the signals, as well as an increase and reduction in their Pearson correlation and Euclidian distance, respectively. Significantly, Fig. 10c shows the cross-correlation results after applying a weighted average bulk shift of -13 depth samples (6.5 ft ~ 2.0 m), which differs slightly from the bulk shift computed only from the gamma ray pair, that is -15 depth samples (7.5 ft ~ 2.3 m) as shown in Fig. 10b. The log shown in Fig. 10c will be the final depth-matched log since we aim to have a common depth reference across all log types so that we can also match the metadata. On the other hand, Fig. 10d shows the results obtained by DTW with an optimal

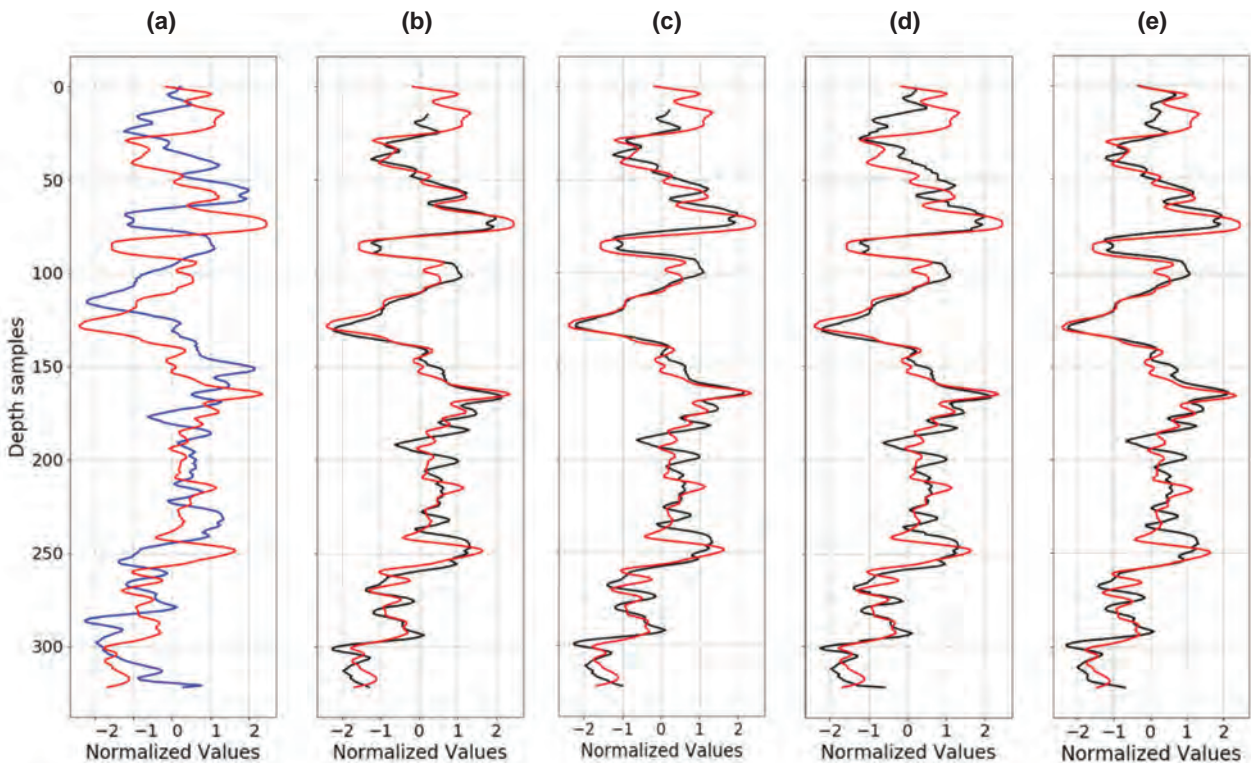


Fig. 10—Depth-matching profile results for gamma ray logs from Well 16/1-9 Section 2 Window 3. Solid lines (red) indicate the reference log (EWL measurement), and solid lines (blue and black) indicate the test log (LWD measurement) before and after depth matching, respectively where: (a) gamma ray logs before depth matching; (b) gamma ray logs after depth matching via cross correlation computed with gamma ray logs only (-15 depth sample shift); (c) gamma ray logs after depth matching via cross correlation computed as a weighted average across all log types, including gamma ray, acoustic, neutron porosity, density, and resistivity (-13 depth sample shift); (d) gamma ray logs after depth matching via DTW with a warping distance = 12.778 ; (e) gamma ray logs after manual depth matching performed by a petrophysicist.

warping distance of 12.8 samples. The first 75 samples show the biggest differences in the depth matching between algorithms. Both cross correlations perform similarly, except for the difference of two samples in the depth shift that is easy to see at the start of the log segment. In contrast, DTW induces a stretching effect trying to compensate for the shifting of the signal downwards, leading to poorer matching in the shallow part. Further down in the section, approximately from depth samples 75 to 324, all three results are quite similar. For the sake of completeness, we present in Fig. 10e the result of a manual depth matching of the LWD log carried out by a petrophysicist (ground truth). We observe that this solution is very similar to the results given by our proposed workflow visually and quantitatively.

Figure 11 shows an example of another way to do quality control of the depth-matching results. This is to compute a least-squares regression line between the signals and estimate the coefficient of determination R^2 . This can be used as an additional metric quality control. In this case, we would expect a 45° regression line if our data are error free, if there are no tool setting parameters and borehole condition differences. Even though this is not the case, we can see that after depth matching, the regression line shows a slope quite close to 45° and that the data align along a straight line. In contrast, the data before depth matching show a random behavior, and the regression line is closer to the horizontal. In addition, we see in dark red and light blue the 95% confident interval of the regression lines (before and after depth matching, respectively), which reflects the uncertainty of the fitted line. Table 1 summarizes the values of the different metrics used to assess and compare the performance of the depth-matching algorithms. This shows quite promising results for both methods compared to the mismatched data and the manual depth-shifted data.

A second example of depth matching is shown in Fig. 12, which depicts a comparison of the depth-matching results obtained by our proposed algorithm via cross correlation (weighted average bulk shift) and the results obtained by manual depth matching done by a petrophysicist. This example shows that our method suggests a similar depth shift improving the correlation and predictability between the logs substantially and reducing the Euclidean distance (see Table 2). Even though the matching is significantly better than the original log position, below 110 depth samples approximately (blue shading zone), our method is unable to produce optimal results. In contrast, we see that the manual depth matching is showing a better solution. This indicates possible stretch/squeeze effects that our cross-

correlation method is unable to deal with, being a limitation of our method. The manual adjustment gives better results since the petrophysicist can manually freely select the number of key data points from the LWD log to be matched with the reference EWL and make the pertinent adjustments stretching and squeezing the signal. In contrast, the cross correlation finds the depth lag at which the correlation between the signals is the highest by displacing one signal with respect to the other one; in this case, the displacement is a constant value applied to all the data points within a window.

The crossplots in Fig. 13 show the clear benefit of applying a robust depth-matching workflow to logs before any petrophysical or rock physics analysis and interpretation, as was pointed out by Zangwill (1982). In Fig. 13a, we see a crossplot of density against neutron porosity before any depth corrections. Only the high gamma ray lithologies (> 100 API) can be discriminated from the rest, and those with medium and lower values ($20 < \text{GR} < 100$, and $\text{GR} < 20$ API) do not follow any distinctive trend. Once the depth correction is applied, we can see a better trend and relocation of the data suggesting clearer lithological zones based on the gamma ray values.

DISCUSSION

Our prototype implementation of the HDF5 format to build structured well databases for Wells 16/1-9 and 16/1-21S allows a wide range of new possibilities since it is open-source software and an open-source format with a high level of versatility allowing easy and quick access to all data acquired in a hierarchical structure. It enables a continuous expansion of the database integrating with a single-well preprocessing workflow, as we show in this work (automatic depth matching). In tests, using a CPU: Intel® Core™ i9-8950 HK @ 2.90 GHz; RAM: 32 GB, we roughly estimated the computational cost of generating the structure database for the two wells. These findings are shown in Table 3. Here we see that it is possible to generate readable and easy-to-use databases in times ranging from minutes to a few hours, depending on the complexity of the drilling plan and the number of logs in a well. However, this effort is worthwhile for access to all the data and to facilitate better analysis and quality assessment, even though these execution times are not optimal now, and one might think that also the storage of these files can be an issue. There is room for improvement using additional features offered by the HDF5 format. For instance, there exist options for chunking and compression

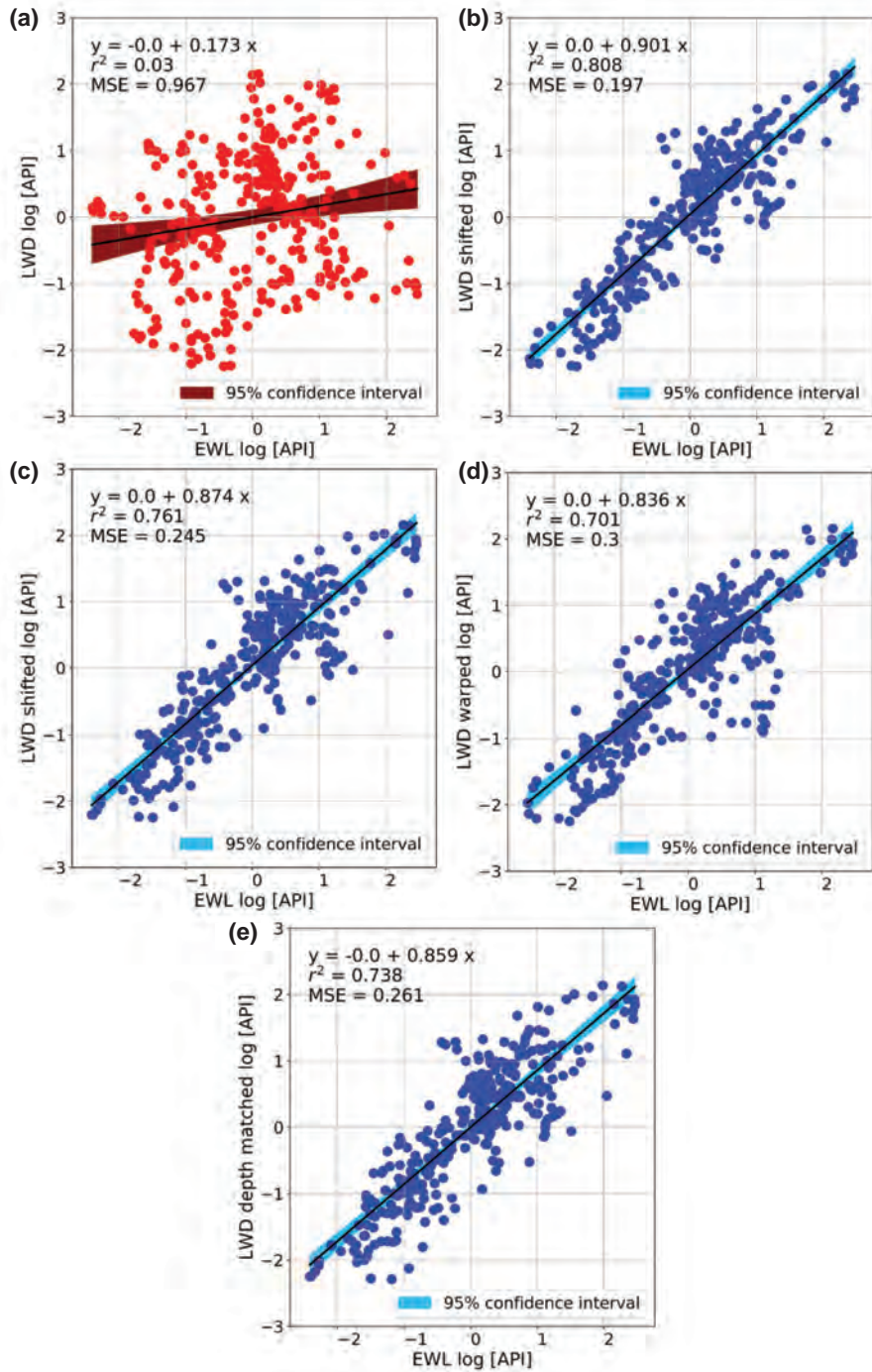


Fig. 11—Gamma ray logs interval normalized values from Well 16/1-9 crossplots before and after depth matching, with least-squares regression lines and their corresponding 95% confidence interval. The solid line (black) is the least-squared regression line best fitting LWD logging plotted against EWL logging. All log values are normalized where: (a) crossplot of gamma ray logs before depth matching; (b) crossplot of gamma ray logs after depth matching via cross correlation computed on gamma ray logs only (-15 depth samples shift); (c) crossplot of gamma ray logs after depth matching via cross correlation computed as a weighted average across all log types, including gamma ray, acoustic, neutron porosity, density, and resistivity (-13 depth samples shift); (d) crossplot of gamma ray logs after depth matching via DTW with a warping distance = 12.8 samples; (e) crossplot of gamma ray logs after manual depth matching performed by a petrophysicist.

for storage purposes. This means that the data set can be created with HDF5's chunked storage layout by dividing the data into regular size blocks, which are stored in a way that there is no specific order and are indexed using a B-tree. In addition, we can apply filter pipelines into the chunked data sets. This will apply transparent compression

and decompression (Collette et al., 2021). In other words, the data are compressed during writing and decompressed during reading. Besides that, parallelization programming by implementing our database workflow in a graphics processing unit (GPU) could be considered to reduce the processing times substantially.

Table 1—Algorithms Performance Based on Different Metrics for Depth-Matching Assessment in Well 16/1-9 Section 2 and Window 1

Metrics	No Correction	Cross Correlation (Bulk Shift)	Cross Correlation (Weighted Bulk Shift)	DTW	Manual Depth Shift (Petrophysicist)
Pearson Correlation	0.17	0.90	0.87	0.84	0.86
Euclidean Distance	23.08	7.81	9.02	10.26	9.53
The Proportion of Trace Energy	-0.65	0.81	0.74	0.67	0.72
R ²	0.03	0.82	0.76	0.70	0.74

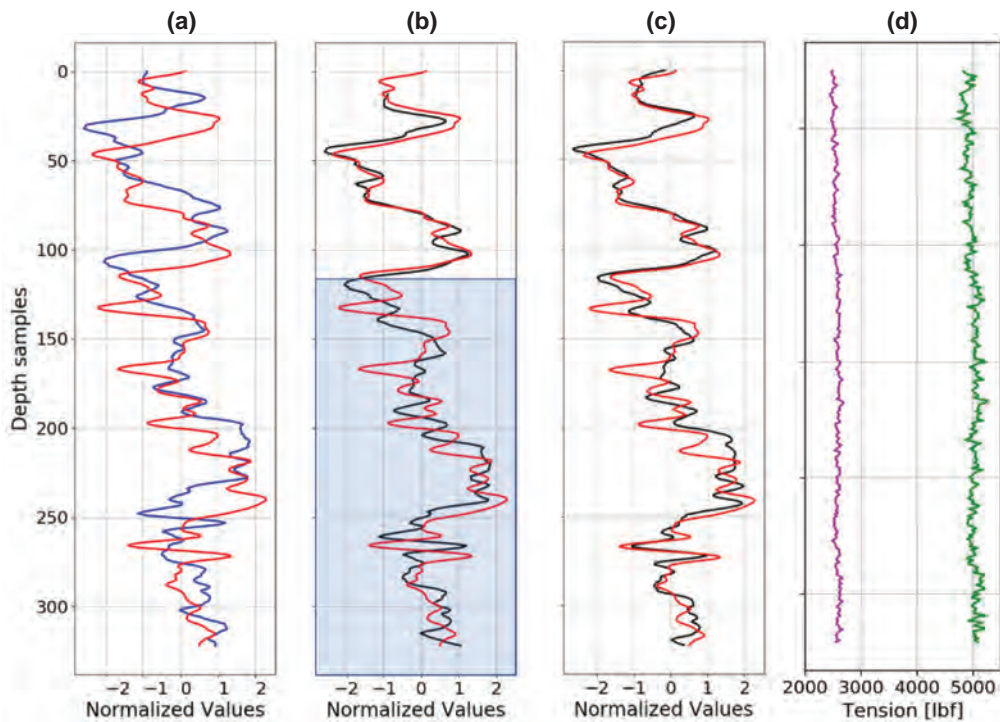
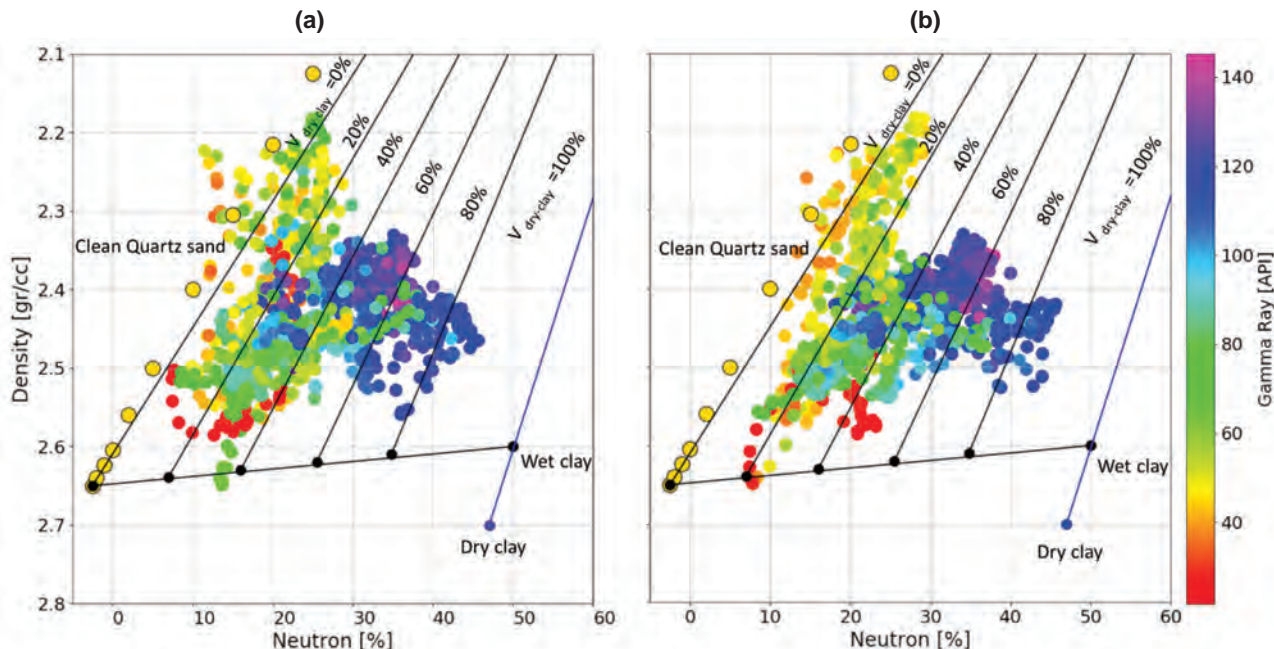


Fig. 12—Depth-matching profile results for gamma ray logs from Well 16/1-9 Section 2 Window 1. Solid lines (red) indicate the reference log (EWL measurement), and solid lines (blue and black) indicate the test log (LWD measurement) before and after depth matching, respectively where: (a) gamma ray logs before depth matching; (b) gamma ray logs after depth matching via cross correlation computed as a weighted average across all log types, including gamma ray, acoustic, neutron porosity, density, and resistivity (-13 depth sample shift); (c) gamma ray logs after manual depth matching performed by a petrophysicist; (d) surface tension (green) and cable head tension (magenta); these two logs are used as a possible indication of stretch/squeeze zones. The blue shading box indicates the zones that required a dynamic depth shift (stretch/squeeze).

Table 2—Algorithms Performance Based on Different Metrics for Depth-Matching Assessment in Well 16/1-9 Section 2 and Window 1

Metrics	No Correction	Cross Correlation (Weighted Bulk Shift)	Manual Depth Shift (Petrophysicist)
Pearson Correlation	0.33	0.76	0.87
Euclidean Distance	20.76	12.32	9.05
The Proportion of Trace Energy	-0.34	0.51	0.75

**Fig. 13**—Density (LWD/MWD) vs. Neutron (EWL) crossplot for Well 16/1-21S at the deepest section, from 7,960 up to 8,551.5 ft (2,426.82- to 2,607.16-m MD): (a) crossplot before depth matching; (b) crossplot after depth matching via cross correlation with a weighted average of all logs. Gamma ray values (API) are shown by color. Yellow dots represent clean quartz sand with variable porosity, black dots represent calculated wet clay points, and blue the dry clay point. All of these are theoretical values.**Table 3**—Execution Times for Well Database Generation

Well	Total # of Logs	Execution Time (min)
16/1-9	1,113	31.52
16/1-21S	6,943	127.00

For the depth-matching process, we observed superior results from cross correlation compared to DTW, even though the difference between these two is not significant, around both visual inspection tools and numerical metrics. In most of the cases, the measured Euclidean distances were reduced substantially by approximately 66% for the best case via cross correlation (gamma ray pairs only) and by 55.58% for DTW. The Pearson correlations were increased by 73%

and 66%, respectively. Similarly, we observed higher values of R^2 after depth-matching corrections for the three cases, where we have increases of about 78% and 67% for cross correlation and DTW, respectively. The proportion of the trace energy or predictability (PEP) also gives consistent results with the other metrics. In this case, we have a negative value of -0.65 before depth matching that becomes a high positive value close to 1 after depth matching. PEP

was introduced by White (1980) as a goodness of fit measure to evaluate the match between synthetic seismograms and seismic traces. It basically measures the proportion of the trace energy predicted by the synthetic seismogram. We adopt this metric to evaluate the proportion of the energy of the reference log that is contained in the test log. Since both logs are measuring the same depth section, when they are aligned, they should be closely equivalent, and the opposite occurs when they are not. The negative value obtained when there is a strong misalignment indicates that the residuals between the reference and the test log are larger than the total reference log energy; therefore, we could expect very low predictability or energy content in the test log.

Comparing our cross-correlation results with a manual depth shift performed by a petrophysicist, we prove that similar results are obtained. The first example, Fig. 12, shows that our proposed cross-correlation workflow produces slightly better metrics than the manual depth matching, for example, a Pearson correlation equal to 0.87 and 0.86, respectively. However, we also show that in zones where strong stretch/squeeze effects are present, our method struggles to find an optimal solution in comparison with the manual work, but it still improves the overall matching visually and quantitatively with respect to the original well position (Fig. 12 and Table 2). This behavior occurs because we are now considering only bulk shift as the first step of an automatic depth-matching workflow.

Even though both approaches are relatively fast and simple to implement, the DTW is a more expensive process than the cross-correlation workflow when the number of processed curves increases. Table 4 shows the comparison in the computational cost of implementing either cross correlation or DTW as a depth-matching algorithm for both wells, using the same CPU characteristics for testing as were used for the speed test of database generation. Execution time for DTW is higher than double the execution time for cross correlation for Well 16/1-9, and the execution time difference between the two wells is quite small when a cross correlation is used. This is because even though Well 16/1-21S has six times as many logs as Well 16/1-9, we only perform depth matching in a small subset of the logs, and from those, only the LWD/MWD logs are processed. In this case, the number of relevant logs for this speed test is 26 in Well 16/1-21S and 21 in Well 16/1-9. However, for DTW, there is a significant increase in execution times

for Well 16/1-21S relative to both cross correlation and DTW execution times in Well 16/1-9, even though the difference in the number of curves processed is only 5. It is known that the DTW has a time and space complexity of $O(N^2)$, which typically limits its use to small series of no more than thousands of samples (Salvador and Chan, 2004). This issue is also mentioned and addressed by Hale (2013) in his implementation of DTW for use on seismic images. The time complexity can be reduced by using constraints on the length of the window, which limits the search for the optimal warping path within the constrained window. However, such window constraints only work if the warping path is close to linear, and it passes through the diagonal of the cost matrix. Otherwise, the performance of the method will not be satisfactory (Salvador and Chan, 2004). In our case, the selection of a penalty = 2 to avoid excessive distortions makes the warping path to be close to the main diagonal of the cost matrix. Hence, we can reduce the window size from 300 to 50 samples. This improves the DTW execution times, as shown in Table 4. From where we can see that DTW is faster than cross correlation in Well 16/1-9, and even though it is still slower than cross correlation in Well 16/1-21S, the original time is reduced by approximately one-third. It might be worth testing the FastDTW Python package that performs DTW with a multilevel approach using recursive projections of the warp path from a coarser to finer resolution and then updates it. This gives an approximation to the DTW solution, and it can also run much faster for larger data sets. However, Salvador and Chan (2004) emphasized that this approach does not guarantee an optimal solution, and additional research is necessary to improve the accuracy of this algorithm. For these reasons, cross correlation yields reliable results in shorter times, thus increasing the efficiency of the workflow without compromising accuracy.

Table 4—Depth-Matching Algorithm Execution Times per Well

Well	Depth-Matching Method	Execution Time (min)
16/1-9	Cross correlation	10.56
16/1-9	DTW	28.38
16/1-9	DTW window size = 50	8.98
16/1-21S	Cross correlation	10.99
16/1-21S	DTW	64.20
16/1-21S	DTW window size = 50	20.37

Cross correlation also has several advantages that better fulfill our requirements based on the concept we want to develop and implement. To be more specific, cross correlation is a simple analytical process that allows full control of what the algorithm is doing. We also easily establish a weighted average to be applied to all the log types. This allows the metadata to be synchronized correspondingly. This is a feature that has not been considered in well-log storage formats before, as far as we are aware. In contrast, the DTW, even though it produces good results, acts as a shaping filter that is prone to overfitting the data if the regularization parameters used during the optimization process are not tuned properly. This was demonstrated by Herrera and van der Baan (2014), who implemented DTW for tying well logs and seismic data. They emphasized that unconstrained DTW can achieve an optimal signal match; however, this may also lead to non-physical velocities and time-depth functions. The same applies to our case, as was shown in Fig. 9. Therefore, the parameter tuning stage is important. It also adds another level of complexity, user intervention, and additional time to the process. We have constrained DTW to avoid perfect matching between the reference (EWL) and test (LWD/MWD) logs, resulting in a slightly lower performance than cross correlation and speeding up the process. After all, we are not aiming to transform the test log (LWD) into the reference log (EWL); we also want to preserve as much as possible of the original log retaining the inherent difference and just perform the log alignment as accurately as possible. Similarly, each pair of curves will have its own unique warping solution that cannot be standardized and applied to the metadata.

Anderson and Gaby (1983) and Hale (2013) showed that simple cross correlation could yield good results providing that the reference and the test signal have similar patterns, and the time difference between them is neither too large nor too rapidly varying. We also saw a few cross-correlation windows in which erroneous lags were determined due to the lack of distinctive patterns within the window, for example, zones containing only a single lithology type (shaly interval). In addition, we found poor matching performance in zones with large differences between LWD and EWL patterns; these were most present in shallow depth of investigation sensors. Those might be associated with areas where the borehole conditions have changed significantly between runs, for example, borehole enlargement and barite content in the mud, which deteriorates the PEF signal, making it unreliable. In the same way, these conditions affect the density even though the corrections have been made. Another

case could be shallow or medium resistivity measurements in high-porosity formations, where the drilling fluids can invade the formation quickly, and patterns differences might be easily detected between LWD and EWL if a considerable difference in resistivity exists between drilling fluids and formation fluids. Therefore, in these cases, we should not expect sensible results. However, we alleviated this problem by imposing maximum and minimum acceptable depth shift values (± 30 depth samples that are equivalent to ± 15 ft) to detect outliers or unreasonable results and by introducing a weighted average into the final depth shift estimation. The need to set these limits could be interpreted as a disadvantage of the cross correlation, as it needs more user intervention than DTW.

The results obtained from the density vs. neutron crossplots shown in Fig. 13 are a good example of the importance of depth synchronization or alignment when it comes to petrophysical analysis and interpretation, which combines LWD/MWD and EWL data. These results come from the deepest section of Well 16/1-21S, which is about 591.5 ft (180.34 m) thick. This section includes two geological groups such as the Viking and Hegre Groups of the Norwegian North Sea. The Viking Group consists of the Draupne (identified as source rocks) and Heather Formations. The former is characterized by carbonaceous claystones with very high radioactivity and low velocities and densities, and the latter is rich in silty claystones with some limestone stringers. On the other hand, the Hegre Group in this well consists of the Skagerrak Formation, which has interbedded conglomerates, sandstones, siltstones, and shales. In addition, this formation includes anhydrite, dolomites, and limestones (Norwegian Petroleum Directorate, 2020). These distinctive lithologies can be easily identified on the depth-corrected crossplot where the shales and claystones after correction move toward high neutron porosity and low to moderate densities, falling in the range from 40 to 100% volume of dry clay, whereas the cleaner sandstones with porosities about 20% and 25% are well separated moving toward lower density values about 2.2 to 2.4 gr/cc, suggesting possible hydrocarbon-bearing sands that were proved in this formation at this depth interval via core analysis and fluid sampling tests. We also see that these reservoir sands have a lower percentage of clay, less than 20%. Similarly, very low gamma ray values < 20 API, low neutron porosity $< 10\%$, and high density above 2.7 gr/cc can be associated with the dolomite, marls, and limestone stringers. In contrast, the same crossplot before depth synchronization leads to misinterpretation and poor lithological discrimination.

CONCLUSION

We presented a novel database structure format optimized toward automation and machine-learning-based approaches applied to well-log data analysis. We suggested a hierarchical restructuration of the complex DLIS files to a more comprehensive and versatile HDF5 formatted file, as well as the estimated execution times for two wells from the Norwegian North Sea with different drilling planning strategies, acquisition contractors, and numbers of logs. This fully automated database generation is done in either minutes or a few hours, depending on the amount of data in a well. The shortening of workflow execution times is important for the oil industry to improve efficiency. Similarly, there is room for improvement in the research Python code for code generalization and to speed up the execution times through parallel processing of the data by using GPU and reductions of files size without compromising the data itself via chunking and compression filters as HDF5 features, for instance. In addition, our database prototype proposal seems to fit with the Open-Source Data Universe (OSDU) vision, sharing the aim to organize and manage data in an innovative way that suits the current digital transformation across different industries. Our hierarchical structure can be a starting point to explore new possibilities of data management.

We also compared two different algorithms for automated well-log depth matching. We demonstrated the use of a few of these methods integrated into a single workflow. Considering that our main aim is to get better control of the data and simultaneously depth match the metadata, the traditional cross-correlation algorithm plus scaling factor (α) for the log tails is the best method applied here. This also provides the best results qualitatively (via crossplots) and quantitatively (QC metrics) with good agreement among all metrics. DTW shows good alignments but, at the same time, introduces some artifacts in zones with high stretching effects. Additionally, the non-uniqueness of the warping logs to each log type makes it unstable when estimating a single depth shift that can be applied across all logs along with their metadata, which is one of the innovative features of our workflow. In addition, the cross-correlation approach outperforms with execution times around one-third when compared to those for the DTW, providing that no window length constrains are applied, although it required more user intervention and a more complex workflow than the warping. On the other hand, DTW can be sped up when the warping path's searching grid is constrained; however, we showed that it would be more costly than cross correlation whenever

the number of log curves increases. We emphasized the importance of depth matching and the necessity of providing a quick and robust solution to this long-standing problem via automation by demonstrating the benefit of depth matching exemplified as classical log analysis and lithological interpretation.

Our new framework has been prototype tested in two Norwegian North Sea wells. However, the implementation of this automated database and workflow for more wells would allow us to improve the generality of the research Python code, as well as the robustness of the depth-matching estimates and possible implementation of new metrics. Toward automation and reduction of user intervention, we envisage several possibilities to improve our current proposal, for example, a hybrid solution in which the cross-correlation workflow is run first, and a second run is performed via DTW. This will alleviate the issues of stretch/squeeze that the former cannot handle. It will potentially simplify the proposed cross-correlation workflow by suppressing the need to apply a cross correlation with a scaling factor to adjust the tails of the log section. Similarly, the usage of ML to replace the statistical analysis step from the cross-correlation workflow and to automatically select and adjust a window size for depth synchronization analysis will bring benefits in terms of automation. We will further evaluate the feasibility of applying this approach to a massive number of wells, potentially significantly contributing to reducing well-log processing times and introducing a hierarchical organization of the data. We believe that better data management enables new possibilities for exploring, assimilating, and using all the data acquired more wisely to enable a faster and better understanding of data quality, data measurement sensitivity, and data mining. Additionally, it would be valuable to give as an input suite of logs already referenced to an AHD and TAH that honor the operator requirements of quality. Therefore, the initial misalignment between LWD and EWL logs will be less, and at the same time, this will output depth-matched logs aligned and referred to a more accurate absolute depth.

ACKNOWLEDGMENTS

This research is part of the BRU21 – NTNU Research and Innovation Program on Digital and Automation Solutions for the Oil and Gas Industry (www.ntnu.edu/bru21) and is supported by Aker BP. We also thank NTNU-NPD-Schlumberger Petrel ready data set for borehole data and Andrew J. Carter for his suggestions for improving this

manuscript. Additionally, we thank the reviewers and the editor for all their constructive comments and suggestions that have helped to improve this manuscript substantially.

NOMENCLATURE

Abbreviations

AHD =	along-hole depth
BHA =	borehole assembly
DLIS =	digital log interchange standard
DTW =	dynamic time warping
EWL =	electrical wireline logging
GPU =	graphics processing unit
GR =	gamma ray
HDF5 =	Hierarchical Data Format version 5
HUD =	holdup depth
LWD =	logging while drilling
MWD =	measure while drilling
PEF =	photoelectric factor
PEP =	proportion of the trace energy or predictability
POOH =	pull out of hole
RIH =	run in hole
ROP =	rate of penetration
TAH =	true along-hole depth
WOB =	weight on the bit

REFERENCES

- Anderson, K.R., and Gaby, J.E., 1983, Dynamic Waveform Matching, *Information Sciences*, **31**(3), 221–242. DOI:10.1016/0020-0255(83)90054-3.
- Bateman, R.M., 1986, *Openhole Log Analysis and Formation Evaluation*, Springer. ISBN: 978-9027721327.
- Bolt, H., 2016, Wireline Logging Depth Quality Improvement: Methodology Review and Elastic-Stretch Correction, Paper SPWLA v57n3a5, *Petrophysics*, **57**(3), 294–310.
- Bolt, H., 2019, Correction of Driller's Depth: Field Example Using Driller's Way-Point Depth Correction Methodology, Paper SPWLA v60n1a7, *Petrophysics*, **60**(1), 76–91. DOI: 10.30632/PJV60N1-2019a7.
- Brooks, A.G., Wilson, H., Jamieson, A.L., McRobbie, D.P., and Holehouse, S.G., 2005, Quantification of Depth Accuracy, Paper SPE-95611 presented at the SPE Annual Technical Conference and Exhibition, Dallas, Texas, USA, 9–12 October. DOI: 10.2118/95611-MS.
- Bulmer, M.G., 1979, *Principles of Statistics*, Courier Corporation. URL: http://www.ru.ac.bd/stat/wp-content/uploads/sites/25/2019/03/102_06_Bulmer_Principles-of-Statistics.pdf. Accessed September 23, 2021.
- Chia, C.R., Laastad, H., Kostin, A.V., Hjortland, F., and Bordakov, G.A., 2006, A New Method for Improving LWD Logging Depth, Paper SPE-102175 presented at the SPE Annual Technical Conference and Exhibition, San Antonio, Texas, USA, 24–27 September. DOI: 10.2118/102175-MS.
- Collette, A., and contributors, 2021, H5py: Documentation Release 3.4.0, URL: <https://buildmedia.readthedocs.org/media/pdf/h5py/stable/h5py.pdf>. Accessed September 23, 2021.
- Equinor, 2021, dlisio: Documentation Release 0.3.5, URL: https://dlisio.readthedocs.io/_downloads/en/latest/pdf/. Accessed September 23, 2021.
- Giorgino, T., 2009, Computing and Visualizing Dynamic Time Warping Alignments in R: The dtw Package, *Journal of Statistical Software*, **31**(7), 1–24. DOI:10.18637/JSS.V031.I07. URL: <https://cran.r-project.org/web/packages/dtw/vignettes/dtw.pdf>. Accessed September 24, 2021.
- Hale, D., 2013, Dynamic Warping of Seismic Images, *Geophysics*, **78**(2), S105–S115. DOI: 10.1190/geo2012-0327.1.
- Herrera, R.H., and van der Baan, M., 2014, A Semiautomatic Method to Tie Well Logs to Seismic Data, *Geophysics*, **79**(3), V47–V54. DOI:10.1190/geo2013-0248.1.
- Kerzner, M.G., 1984, A Solution to the Problem of Automatic Depth Matching, Paper VV, *Transactions, SPWLA 25th Annual Logging Symposium*, New Orleans, Louisiana, USA, 10–13 June.
- Klotz, C., Kaniappan, A., Thorsen, A.K., Nathan, E., Jahangir, M., and Lie, L., 2008, A New Mud Pulse Telemetry System Reduces Risks When Drilling Complex Extended Reach Wells, Paper SPE-115203 presented at the IADC/SPE Asia Pacific Drilling Technology Conference and Exhibition, Jakarta, Indonesia, 25–27 August. DOI: 10.2118/115203-MS.
- Le, T., Liang, L., Zimmermann, T., Zeroug, S., and Heliot, D., 2019, A Machine-Learning Framework for Automating Well-Log Depth Matching, Paper SPWLA v60n5a3, *Petrophysics*, **60**(5), 585–595. DOI:10.30632/PJV60N5-2019a3.
- Liang, L., Le, T., Zimmermann, T., Zeroug, S., and Heliot, D., 2019, A Machine Learning Framework for Automating Well Log Depth Matching, Paper S, *Transactions, SPWLA 60th Annual Logging Symposium*, The Woodlands, Texas, USA, 15–19 June. DOI: 10.30632/T60ALS-2019_S.
- Meert, W., 2018, Dynamic Time Warping (DTW), URL: <https://dtaidistance.readthedocs.io/en/latest/usage/dtw.html#dtw-distance-measure-between-two-series>. Accessed September 24, 2021.
- Müller, M., 2007, Dynamic Time Warping, Chapter 4, in *Information Retrieval for Music and Motion*, 69–84, Springer, Berlin, Heidelberg. DOI: 10.1007/978-3-540-74048-3_4.
- Munoz, A., and Hale, D., 2014, *Automatic Simultaneous Multiple-Well Ties*, Center for Wave Phenomena, Report CWP-788, 41. URL: <https://cwp.mines.edu/wp-content/uploads/sites/112/2018/08/cwp788.pdf>. Accessed September 24, 2021.
- Myers, C.S., 1980, *A Comparative Study of Several Dynamic Time Warping Algorithms for Speech Recognition*, Doctoral dissertation, Massachusetts Institute of Technology, Cambridge, Massachusetts. URL: <https://dspace.mit.edu/handle/1721.1/27909>. Accessed September 24, 2021.
- Norwegian Petroleum Directorate (NPD), 2020, Fact Pages, URL: <https://factpages.npd.no/en/wellbore/pageview/exploration/all/7529>. Accessed September 24, 2021.

- Norwegian Petroleum Directorate (NPD), 2021, Guidelines for Reporting Well Data to Authorities After Completion “Blue Book,” Version 13.0, URL: https://www.npd.no/globalassets/1-npd/regelverk/forskrifter/en/b_og_b_digital_rapportering_e.pdf. Accessed September 24, 2021.
- Oliphant, T., and contributors, 2021, `scipy.signal.correlate`, URL: <https://docs.scipy.org/doc/scipy/reference/generated/scipy.signal.correlate.html>. Accessed September 24, 2021.
- Pedersen, B.K., and Constable, M.V., 2007, Operational Procedures and Methodology for Improving LWD and Wireline Depth Control, Kristin Field, Norwegian Sea, Paper SPWLA v48n2a3, *Petrophysics*, **48**(2).
- Salvador, S., and Chan, P., 2004, FastDTW: Toward Accurate Dynamic Time Warping in Linear Time and Space, *Intelligent Data Analysis*, **11**(5), 70–80. URL: <https://cs.fit.edu/~pkc/papers/tdm04.pdf>. Accessed September 24, 2021.
- Sollie, F.O., and Rodgers, S.G., 1994, Towards Better Measurements of Logging Depth, Paper D, *Transactions, SPWLA 35th Annual Logging Symposium*, Tulsa, Oklahoma, USA, 19–22 June.
- The HDF Group, 2016, High Level Introduction to HDF5, URL: <https://support.hdfgroup.org/HDF5/Tutor/HDF5Intro.pdf>. Accessed September 24, 2021.
- Theye, P.P., 1999, *Log Data Acquisition and Quality Control*, Editions Technip. ISBN: 9782710807483.
- White, R.E., 1980, Partial Coherence Matching of Synthetic Seismograms With Seismic Traces, *Geophysical Prospecting*, **28**(3), 333–358. DOI: 10.1111/j.1365-2478.1980.tb01230.x.
- White, R.E., and Simm, R., 2003, Tutorial: Good Practice in Well Ties, *First Break*, **21**(10), 75–83. DOI: 10.3997/1365-2397.21.10.25640.
- Wilson, H., Loftis, J., Page, G., Brooks, A., and Walder, D., 2004, Depth Control: Reconciliation of LWD and Wireline Depths, Standard Practice and an Alternative Simple but Effective Method, Paper SPE-89899 presented at the SPE Annual Technical Conference and Exhibition, Houston, Texas, USA, 26–29 September. DOI: 10.2118/89899-MS.
- Zangwill, J., 1982, Depth Matching – A Computerized Approach, Paper EE, *Transactions, SPWLA 23rd Annual Logging Symposium*, Corpus Christi, Texas, USA, 6–9 July.
- Zimmermann, T., Liang, L., and Zeroug, S., 2018, Machine-Learning-Based Automatic Well-Log Depth Matching, Paper SPWLA v59n6a10, *Petrophysics*, **59**(6), 863–872. DOI: 10.30632/PJV59N6-2018a10.

APPENDIX 1: SUMMARY OF METRICS USED FOR DEPTH-MATCHING ASSESSMENT

Pearson Correlation Coefficient

The Pearson correlation coefficient, r , is often used to measure the degree of relationship between two variables assuming that there is a linear relation between them. Its values lie between -1 and 1 , where a value of -1 implies perfect negative correlation and a value of 1 implies perfect positive

correlation. Values equal to zero or close to zero indicate that there is no linear correlation (Bulmer, 1979). The correlation coefficient is defined by the following equation:

$$r = \frac{\sum_{i=1}^n (x_i - \bar{x})(y_i - \bar{y})}{\sqrt{\sum_{i=1}^n (x_i - \bar{x})^2 \sum_{i=1}^n (y_i - \bar{y})^2}}, \quad (\text{A1.1})$$

where n is the sample size, x_i and y_i are the individual sample points of the depth series, and \bar{x} and \bar{y} are the corresponding mean values for x and y .

The Proportion of Trace Energy Predicted

The proportion of trace energy predicted by synthetic seismograms, also called predictability (P), was introduced by White (1980) as an additional output from wavelet estimation through matching. This concept is used as a goodness of fit measure to assess the reliability of a well-seismic tie. There are two terms that need to be defined—trace energy and residual energy. The energy of a trace, TE , which in our case is the reference log, is the sum of the squares of the amplitude of a segment of the time/depth series. See Eq. A1.2. The residuals energy is the square of amplitude difference between the samples of a seismic trace (reference log) and its matched synthetic seismogram (test log) after depth shifting. See Eq. A1.3 (White and Simm, 2003).

$$TE = \sum_{i=1}^n x_i^2, \quad (\text{A1.2})$$

$$RE = \sum_{i=1}^n (x_i - y_i)^2, \quad (\text{A1.3})$$

where n is the sample size, x_i and y_i are the individual sample points of the reference and test logs, respectively.

The predictability (P) is given by:

$$P = 1 - \frac{RE}{TE}. \quad (\text{A1.4})$$

Euclidean Distance

Euclidean distance, also known as the L_2 -norm, is an alternative metric to measure the degree of similarity between time and depth series as given by Eq. A1.5 (Herrera and van der Baan, 2014):

$$D_{euclid(x,y)} = \sqrt{\sum_{i=1}^n (x_i - y_i)^2}, \quad (\text{A1.5})$$

where $D_{eucli(x,y)}$ is the one-to-one Euclidean distance between the test (LWD/MWD) $\log x$ and the reference (EWL) $\log y$, the index i representing the individual sample points in each depth series.

APPENDIX 2: DTW PARAMETRIZATION

The dtw.distance.dtw function provides several options for addressing the complexity of DTW. For instance, even though the distance function has a linear complexity in space, the complexity is still quadratic in the time domain. The most common approach to overcome this is using a window that constrains the maximum shift allowed. Any shift larger than the window length will be rejected. This is a direct implementation of the global constraints widely used to speed up DTW, e.g., the Sakoe-Chiba Band (Herrera and van der Baan, 2014). As well as the window length, we have three more parameters that trigger early rejection of some or all paths the dynamic programming explores (Meert, 2018):

- max_dist: stop the computation if the distance is larger than this value.
- max_step: path searching steps cannot be larger than this value.
- max_length_diff: return infinity if the difference in length of the two series is larger than the given value.

There are two additional options that are considered as tuning parameters for the optimization process; in other words, they tune how the cost is computed (Meert, 2018):

- penalty: penalty added to the distance if compression or expansion is applied (distortion).
- psi: relaxation to ignore the beginning and/or end of sequences.

We have used the following values for these parameters: window = 50, max_dist = 100, max_step = 50, penalty = 2, psi = 2, where the three first parameters are represented as the number of samples.

ABOUT THE AUTHORS



Veronica A. Torres Caceres received a BSc degree (2010) in geophysical engineering from the Central University of Venezuela, Caracas, and an MSc degree (2017) in petroleum geophysics from the Norwegian University of Science and Technology (NTNU) in Norway. Veronica is currently

a PhD student at NTNU. Her current research interests include data structuring, petrophysics, rock physics, seismic inversion, machine learning, statistical learning, seismic attenuation, and data integration. From 2011 to 2012, she worked as a geophysicist at IHS Markit as a seismic interpreter and technical support for Kingdom Suite. From 2012 to 2015, Veronica worked as a geophysicist seismic interpreter and velocity model builder for subsalt imaging at PGS, Mexico. From 2017 to 2018, she worked as a research assistant on attenuation estimates and rock physics model simulation. Veronica was the president of the SEG Student Chapter at NTNU from 2019 to 2021, and she is currently a student member of SEG, EAGE, and SPWLA.



Kenneth Duffaut received his MSc degree (1994) in geophysics at the Norwegian University of Science & Technology (NTNU), Norway, and a PhD degree (2011) in geophysics, at NTNU. From 1995 to 1997, he worked as a geophysicist in Statoil's petroleum technology department in Norway within field development and geophysical special services. From 1997 to 2015, he worked at the Statoil research centre in Trondheim, Norway, as a research geophysicist in various exploration and production programs. Since 2015, he has worked as an associate professor at the Department of Geoscience and Petroleum at NTNU. Current research interests include landscape dynamics through geological time (tectonic uplift), near-surface geophysics, 4D seismic monitoring, wellbore geophysics, and rock physics analysis combined with machine learning for well and seismic data analysis.



Frank Westad received his MSc degree in chemistry and data analysis from the University in Trondheim, Norway (1988) and completed his PhD thesis on “Relevance and Parsimony in Multivariate Modelling” (2000). His work experience includes senior research scientist positions at GE Healthcare and the Norwegian Food Research Institute (Nofima). He has published 50 papers and has also written several chapters in various textbooks on multivariate data analysis. He is now an adjunct professor at the Norwegian University of Science and Technology in the Department of Engineering Cybernetics and holds a position as a chief data analyst at Idletechs AS.

Alexey Stovas received his MSc degree from the Mining Institute (Dnepropetrovsk) and PhD degree from the Institute of Geophysics (Kiev). Currently, he is working as a professor at the Norwegian University of Science and Technology (Trondheim). His areas of interest are anisotropy, seismic wave propagation, and modeling.



Yngve Bolstad Johansen received a Cand.Scient. degree in physics from NTNU, Norway (2000). He joined Schlumberger in 2001 as a field engineer and worked with data acquisition in the Middle East and the North Sea before starting as a logging tool physicist at the Houston Formation Evaluation Center in 2005. In 2009, he began as a principal petrophysicist for Statoil in field development and later R&D. From 2013 to 2020, Yngve was leading petrophysics within Aker BP in the position of chief petrophysicist. Yngve Johansen is currently the principal advisor and coordinates subsurface R&D across all disciplines in Aker BP.



Arne Jenssen has a PhD degree in acoustics from NTNU, Norway. He currently works as an independent consultant in full-stack software development.

Ultrasonic Logging of Creeping Shale

Anja Diez¹, Tonni F. Johansen¹, and Idar Larsen²

ABSTRACT

With the end of oil production, the need for safe and economically efficient plug and abandonment (P&A) operations increases. Due to the high costs related to traditional P&A processes, the possibility of shale bonding to the well casing, forming a natural barrier, is explored. Here, we present a unique laboratory experiment of creeping shale in a pressure cell, which is monitored during the creep and bonding processes using the ultrasound pulse-echo (PE) and pitch-catch (PC) measurement techniques. The combination of continuous PE and PC measurements in one direction, with discrete measurements in 5° intervals, and the logging of confining pressure, temperature, and permeability allows an improved understanding of the bonding processes and the interpretation of parameters derived from PE and PC

measurements. We find that the initial creep of the shale occurs when the confining pressure is increased from 5 to 9 MPa, resulting in significant changes observed in the acoustic impedances derived from PE and PC measurements. However, as permeability is still high, we assume that channels are still open. With the increase in confining pressure to 13 and 14 MPa, respectively, we observe a decrease in permeability corresponding to an overall decrease in signal strength for the PC data of up to 25 dB and a decrease in the PE group delay parameter of up to 0.6 µs corresponding to a change in acoustic impedance from about 1 MRayl to about 3 to 3.5 MRayl. Large variations with direction can be observed. Combining the information of PE and PC gives a good impression of the bonding processes.

INTRODUCTION

Oil and gas wells that reach the end of their production cycle need to be plugged to prevent unwanted leakage of fluids before abandonment. In the next decade, a large number of oil-production fields will be abandoned on the Norwegian Shelf, where costs of the plug and abandonment (P&A) operations can be as large as 25% of the drilling exploration (Khalifeh and Saasen, 2020). Hence, efforts are made to develop safe and more efficient methods for the P&A process (Vrålstad et al., 2019).

One possibility to create a more cost-efficient plug-in well abandonment is to use shale formations that can build a natural barrier around the casing. Shale creeps, often posing a problem during drilling processes. This means, at the same time, that creeping shale can build a barrier with the casing, preventing oil from escaping through the annulus to the surface (Williams et al., 2009).

To be able to use shale as a barrier, the quality of the bonding needs to be quantified through pressure tests (Raaen

and Fjær, 2020) and measurements within the casing. Sonic and ultrasonic methods are usually used. For the ultrasound methods, an acoustic pulse is emitted from a tool within the casing (Thierry et al., 2017; Lavery et al., 2019). The acoustic wave travels through and/or along the casing, losing energy due to reflections and signal emission along the travel path. The amount of lost energy depends on the properties of the material surrounding the casing. Hence, the energy level of the recorded signal can be analyzed to derive information on the conditions outside the casing and can, therefore, be used to evaluate the state of bonding of the surrounding formation (Froelich, 2008).

Two different ultrasound techniques—the pulse-echo (PE) and the pitch-catch (PC) technique—are commonly used to investigate the surrounding formation. In the PE measurement, a beam is transmitted and reflected from the casing wall under normal incidence. The transmitted signal is reflected back and forth within the casing wall, where the reflection strength at the outer wall depends on the impedance of the material behind the casing. Hence,

Manuscript received by the Editor December 16, 2020; revised manuscript received May 20, 2021; manuscript accepted June 16, 2021.

¹SINTEF Digital, anja.diez@sintef.no; Tonni.F.Johansen@sintef.no

²SINTEF Industry, Idar.Larsen@sintef.no

analyzing the reverberation signal can give information on the local conditions behind the casing (Hayman et al., 1991; Viggen et al., 2016a; Sirevaag, 2020). In the PC measurement, a beam is transmitted under an angle, exciting a wave that travels along the casing wall. The amount of energy transmitted to the outside of the casing depends on the acoustic impedance of the material outside the casing. The energy of the measured signal from a PC measurement can, therefore, give information about the conditions behind the casing averaged along the travel path of the wave within the casing wall (Viggen et al., 2016b, 2017; Wang et al., 2016; Klieber et al., 2017; Sirevaag et al., 2020).

PE and PC measurements are standard measurement techniques in the oil and gas industry to evaluate the bonding of cement behind the casing (Khalifeh and Saasen, 2020; NORSO standard D-010, Rev 4 2013). However, they come with challenges due to the high acoustical contrast between the low acoustical impedance of the fluid inside the pipe and the formation surrounding the casing, in contrast to the high acoustical impedance of the steel casing.

Here, we exploit the possibility of shale as a barrier for P&A operations and the reliability of PE and PC measurements to measure the state of the bonding between the shale formation and the casing wall using laboratory measurements. The laboratory measurements give a unique possibility to study the creeping shale and the corresponding results of the ultrasound measurements in a controlled environment that additionally allows the observation of permeability to be able to clearly judge the success of the bonding process.

MATERIALS AND METHODS

In this section, we first describe the setup of the experiment in the pressure cell, followed by the setup of our ultrasound measurements. Afterward, the basic theory of the PE and PC techniques is described. To be able to derive the acoustic impedance from the parameters measured with PE and PC, an empirical relationship is needed. We use bench measurements to establish this connection, described in the last section.

The Pressure Cell

We present the results of experiments carried out in a hydrostatic pressure cell (Fig. 1), using a jacketed hollow cylinder sample with a nominal size of 100-mm diameter,

100-mm height, and 20.5-mm center hole diameter. The center hole of the sample is accessible from outside the cell through a hole in the top of the cell and the top piston (Fig. 1d). The hole is sealed to confine the pressure. A stainless-steel pipe is used, similar to a casing, between the top and bottom pistons. The pipe is machined out of a rod to ensure the accuracy of the dimensions required for the ultrasound measurements. Through the pipe, an annulus is closed off from the hole in the cell between the top and bottom piston such that it is possible to maintain pressure in the annulus and prevent fluid loss. Ultrasonic tools designed to measure through the casing are inserted into the steel pipe through this hole during the test (Sirevaag, 2020). Due to the setup of the experiment, we refer to the materials outside the steel pipe and the processes happening there as the annulus.

The pore pressure of the sample is not controlled directly but indirectly by controlling the screen pressure, attached to a metal screen on the outer side surface of the sample, and the annulus pressure (Fig. 1d). The top and bottom pistons have fluid ports for fluid pressure control of the annulus. The fluid ports in the pistons allow to set up a small pressure difference between the pistons, and this is used to estimate the annulus permeability from the measured pressure equalization (transient pulse-decay method based on the principles of Brace et al. (1968)). This method is normally used for low permeability ($\leq 100 \mu\text{D}$). At the beginning of the experiment, when the annulus is open, measured values of permeability are significantly larger than $100 \mu\text{D}$. Those measurements have a large uncertainty and are, therefore, only used to identify an open annulus with fluid flow (Fjær et al., 2018). Two linear variable differential transformers (LVDT) are used to measure deformation between the top and bottom pistons. No radial deformation is measured in this cell.

The shale used in this project is an outcrop, Pierre II, with porosity, mineralogy, and rock mechanical properties, as given in Table 1. The shale was cored perpendicular to the bedding. This means that the shale layering in our experiment is horizontal. To prevent dehydration, the shale was stored in oil, and cored plugs were drilled using oil. During testing, the shale was exposed to kerosene on screen and in the annulus, and we expect that full saturation of the sample is obtained during initial hydrostatic loading and consolidation. The Pierre II shale has a characteristic acoustic impedance of $Z_s = 4.2 \text{ MRayl}$ at consolidation stress.

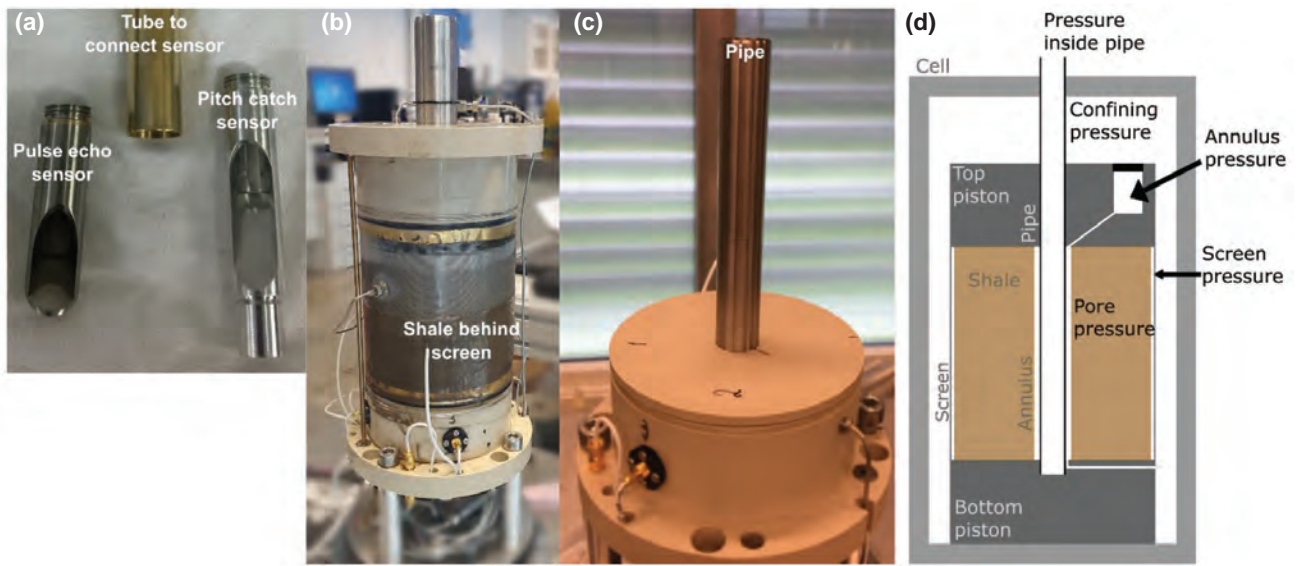


Fig. 1—Experiment setup as used in the laboratory. (a) PE and PC sensor with acoustic mirror and tube they get attached to, (b) the setup after mounting the sample, and (c) the cell with pipe. (d) A sketch of the pressure cell indicating where the different pressures are measured.

Table 1—Properties of Shale Pierre II Used in the Experiments

Porosity	40.3%
Bulk Density	2.06 g/cm ³
TOC	1.2%
BET	27 m ² /g
Permeability (0°)	147 nD
Friction Angle (0°)	13.3°
Uniaxial Strength	6.35 M
Hollow Cylinder Strength	6.0 MPa
P-wave Velocity	2,100 m/s

Experimental Setup

PE and PC measurements are used in the industry for logging well integrity. The used frequency is in the range of 200 to 700 kHz, chosen so that half the wavelength ($\lambda/2$) of the compressional wave corresponds to the casing thickness. The ultrasound transducer is placed about 25 to 40 mm away from the casing wall, and the transducer aperture is about 25 mm. Both PE and PC can be located in the same tool, and measurements are done with up to 5° resolution while pulling the tool up (e.g., Govil et al., 2020).

Our experiment is scaled down 10 times in relation to the casing diameter and 20 times in relation to the casing thickness compared to the industry scales. We use a stainless-

steel pipe with an inner diameter of 16.1 mm, a thickness of 0.55 mm, and a characteristic acoustic impedance of $Z_p = 43.5$ MRayl as casing. The used ultrasonic pulse frequency was chosen to be about 5 MHz so that the half-wavelength corresponds to the pipe thickness.

Adjustments in comparison to the industry tool design were necessary to be able to fit from-the-shelf transducers to our experiment setup. Due to the size of the transducer (36.8-mm length) and the pipe diameter (16.1 mm), it was not possible to place the transducers inside the pipe such that the incident angle of the ultrasound beam on the inner pipe wall is normal incidence for the PE measurement and 29° for the PC measurement. Therefore, the transducer is placed parallel to the long axis of the pipe, and an acoustic mirror is used so that the correct incident angle on the pipe wall is ensured. This results in a significantly longer distance between transducer and pipe wall in comparison to the industry setup taking the scaling factor for pipe radius, thickness, and pulse frequency between laboratory and industry setup into account. The transducer has a focal length of about 18 mm and an aperture of 6.4 mm. The ultrasound transducer was chosen so that the size of the footprint of the ultrasonic pulse between the scaled-down laboratory and industry setups is comparable.

The PE and the PC tool are two different tools in our experiment (Fig. 1a). It is neither possible to measure at the same time nor the same location, and one tool needs to be removed to carry out the complementing measurement. However, it is possible to measure during the same stress conditions due to the time scale of our experiment with constant pressure for hours to days.

We present results from two experiments. For both experiments, Experiment 1 (E1) and Experiment 2 (E2), the setup was the same at the start of the experiment. At the beginning of the test, a gap of 2 mm exists between the pipe and the shale (Fig. 2a). The pipe and the gap are filled with kerosene ($Z_s = 1.1 \text{ MRayl}$). The experiments were carried out over 42 days for E1 and 28 days for E2, respectively. Computer tomography images taken of the shale after the experiment show that cracks develop during the pressurization (Fig. 2b). These cracks indicate where strain is highest during the experiment. While the cracks are open after the experiment, we assume that they are closed during the experiment with increasing pressure and, therefore, do not influence the ultrasound measurements.

An initial loading to 5-MPa confining pressure and 3-MPa pore pressure was done for both experiments. The stress level was chosen to be below a stress level where deformation of the hole wall (based on hollow cylinder strength) could be expected. After consolidation, the screen pressure and annulus pressure were kept constant, meaning that the pore pressure is constant, while the confining pressure was increased stepwise with periods of constant

confining pressure (Fig. 3 and Fig. 1d). During E1, the confining pressure was increased from the consolidation pressure at 5 MPa in four steps to 14 MPa over 10 days at a rate of 2 MPa/day. After keeping the confining pressure at 14 MPa for 5 days, it was decreased in steps again over the next 7 days. During E2, the confining pressure was increased in five steps from 5 MPa to 13 MPa at a rate of 4.8 MPa/day. After increasing the pressure to the next level, it was held constant. After 27 days, the confining pressure was decreased. The choice of steps for the pressure increase for both experiments was arbitrary besides the hold periods that were used so that the pore pressure could equilibrate.

The annulus pressure was monitored and is equal to the screening pressure throughout the test (Fig. 3 and Fig. 1d), except for two short periods where the pressure was reduced at the end of test E2. The pressure inside the pipe was equal to atmospheric pressure. Further, we monitored the room temperature (purple line) and the temperature within the cell (gray line). The cell temperature was raised in comparison to the room temperature to avoid temperature fluctuations. This is important as, among others, changes in temperature influence the elastic properties of the materials and thus influence the ultrasonic measurements. Hence, keeping the temperature constant increases the comparability and eliminates possible errors analyzing the ultrasound data. Axial deformation (Fig. 3, black line) was measured every 50 seconds during the test using the LVDTs. Permeability in the annulus was measured seven times during E1 and five times during E2 (Fig. 3, red dots).

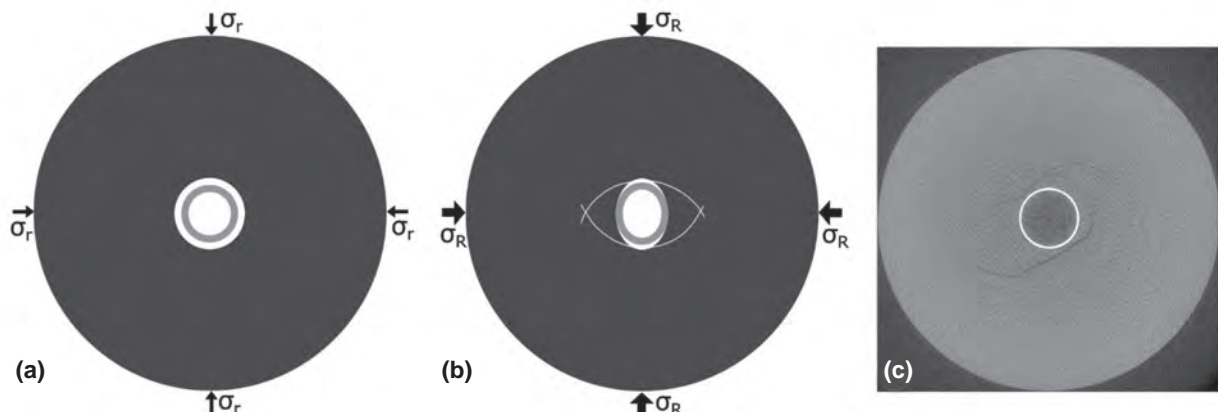


Fig. 2—Sketch of the cell tests. (a) At the beginning of the test, a 2-mm-wide gap (white) exists between the pipe (gray) and the surrounding shale (black). The shale is uniformly put under pressure σ_r (small black arrows). **(b)** During the experiment, the pressure σ_R is increased (big black arrows), and the shale bonds to the pipe while cracks around the pipe develop. An anisotropic stress field develops with the main direction of stress, leading to the varying quality of bonding and an ovalization of the pipe. **(c)** A computer tomography image was taken after the experiment with pipe (white) still in place, showing locations of cracks.

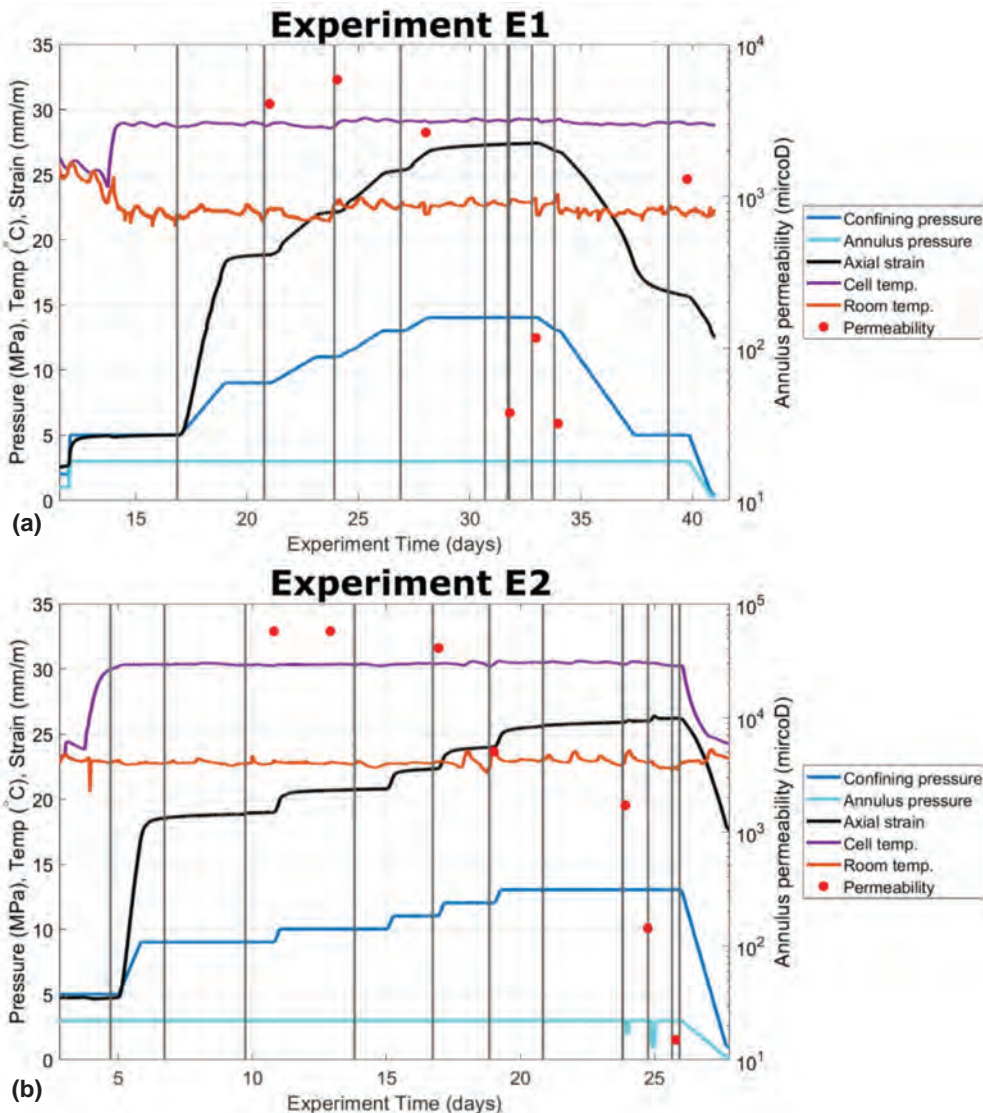


Fig. 3—Continuous logging measurements of (a) E1 and (b) E2. The vertical gray lines indicate the locations where the tool was removed and inserted again. (a and b) The confining pressure (blue) was stepwise increased, while the annulus pressure (cyan) is kept constant. The axial strain (black) follows the variation of the confining pressure. The cell temperature (purple) is stable over most of the period, while the room temperature (brown) shows larger variations. The red dots show the decrease in permeability with increasing confining pressure.

Pulse-Echo Technique

In the case of the PE measurements, a beam is emitted and reflected from the inner casing wall with normal incidence (Fig. 4a). Part of the energy is transmitted into the casing wall and reflected from the outer casing wall. The reflection strength of this signal depends on the properties of the material outside the casing. The signal is then reflected back and forth within the casing wall, transmitting energy to the transducer at every reflection from the inner casing

wall. In a plate, this wave corresponds to an S1 mode of a Lamb wave. The decay of this reverberation signal (Fig. 4b) is depending on the characteristic impedance of the casing and the material outside of the casing. As the casing impedance is known, it can be used to derive information on the material outside of the casing. The PE measurement is a point measurement, and, thus, localized information is gained.

To derive information on the material behind the casing from the PE measurement, different analysis techniques exist. The ringdown can be analyzed by calculating the envelope of the signal and estimating the energy decay of the reverberation signal from the slope of the envelope. A similar approach is the calculation of the cumulative sum and the estimation of the energy decay of the reverberation signal from the slope of the cumulative sum (Schroeder, 1965). Another possibility is the analysis of the group delay, a technique called T³ (Hayman et al., 1991), which in our case yielded more reliable results and was, therefore, chosen as the preferred method.

From our data, we calculate the spectrum of a normalization window (S_N) that mainly contains the first reflection from the inner casing wall and the spectrum of a processing window (S_p) with the same start time as the normalization window, but which additionally contains a significant portion of the reverberation signal. For our data, we chose a normalization window of $\pm 0.6 \mu\text{s}$ (about ± 2 periods) and a processing window of -0.6 to $3 \mu\text{s}$ from the peak energy. We then calculate the phase of the difference of these two spectra ($\varphi = \arg(S_p / S_N)$) to derive the group delay as

$$\tau \approx \frac{\Delta\varphi}{\Delta\omega}, \quad (1)$$

with the circular frequency $\omega = 2\pi f$ using the frequency f . A clear minimum can be observed in this group delay function (Fig. 4c). The frequency of this group delay minimum f_{\min} is determined by the thickness d of the casing and the compressional-wave velocity v_p with

$$f_{\min} = \frac{v_p}{2d} 0.95. \quad (2)$$

Due to the propagation behavior of the S1 mode in a pipe and a resulting negative group velocity, this correction factor of 0.95 needs to be included (Sirevaag, 2020). The size of this group delay minimum is determined by the material properties behind the casing. In the following, we will use the absolute of the group delay minimum ($|\tau_{\min}|$) and refer to it as the group delay parameter.

The smaller the difference between the characteristic impedance of the casing and the characteristic impedance of the material behind the casing, the smaller is the reflection from the outer casing wall. We, therefore, observe a decrease in the the group delay parameter with an increase in the characteristic impedance of the material

behind the casing. Figures 4b and 4c show an example of a measurement at the beginning of the experiment (black) and maximum confining pressure (red). At the beginning of the experiment, the gap filled with kerosene exists, i.e., the reflection coefficient at the outer pipe wall is about -0.95 , and a long ringdown can be observed. Toward the end of the experiment, when the confining pressure is at its maximum, and we assume the gap is closed, we can estimate a reflection coefficient of -0.82 , and the reverberation signal is damped more quickly. The change in the conditions outside the pipe is well visible in the decrease of the minimum of the group delay.

In the case of a gap behind the casing, a reverberation from within the gap can be observed, interfering constructively and destructively with the reverberation from within the casing depending on the gap size in relation to the wavelength (Jutten and Hayman, 1993). A gap will, therefore, influence the analyses of the group delay parameter, and the result does not only reflect the characteristic impedance of the material behind the casing but is a combination of the characteristic impedance of the material behind the casing and the gap size.

One of the main challenges in the analysis of the PE measurement is that values of the group delay parameter strongly depend on the choice of window length and tapering. Hence, for a comparison of different measurements, the data need to be calibrated or normalized, and the same window length and tapering methods need to be chosen for all analyses.

Pitch-Catch Technique

In case of the PC measurements, the transducer is tilted so that the focused pulse reaches the casing wall under an angle of 29° . In a plate, this excites the A0 mode of a leaky-Lamb wave (Fig. 4d). The pipe is regarded as a finite, localized plate in which the Lamb waves follow the curvature of the pipe (Gazis, 1959; Li and Rose, 2001). Hence, Lamb-like guided waves can be observed traveling along the casing wall, continuously transmitting energy to the inside as well as to the outside of the casing. The amount of energy transmitted to the outside depends on the impedance of the material outside the casing. Hence, the decay of the mode amplitude can be used to derive material properties outside the casing, averaged along the travel path.

An example of this difference in energy of the Lamb-like guided wave is shown in Fig. 4e with a signal from

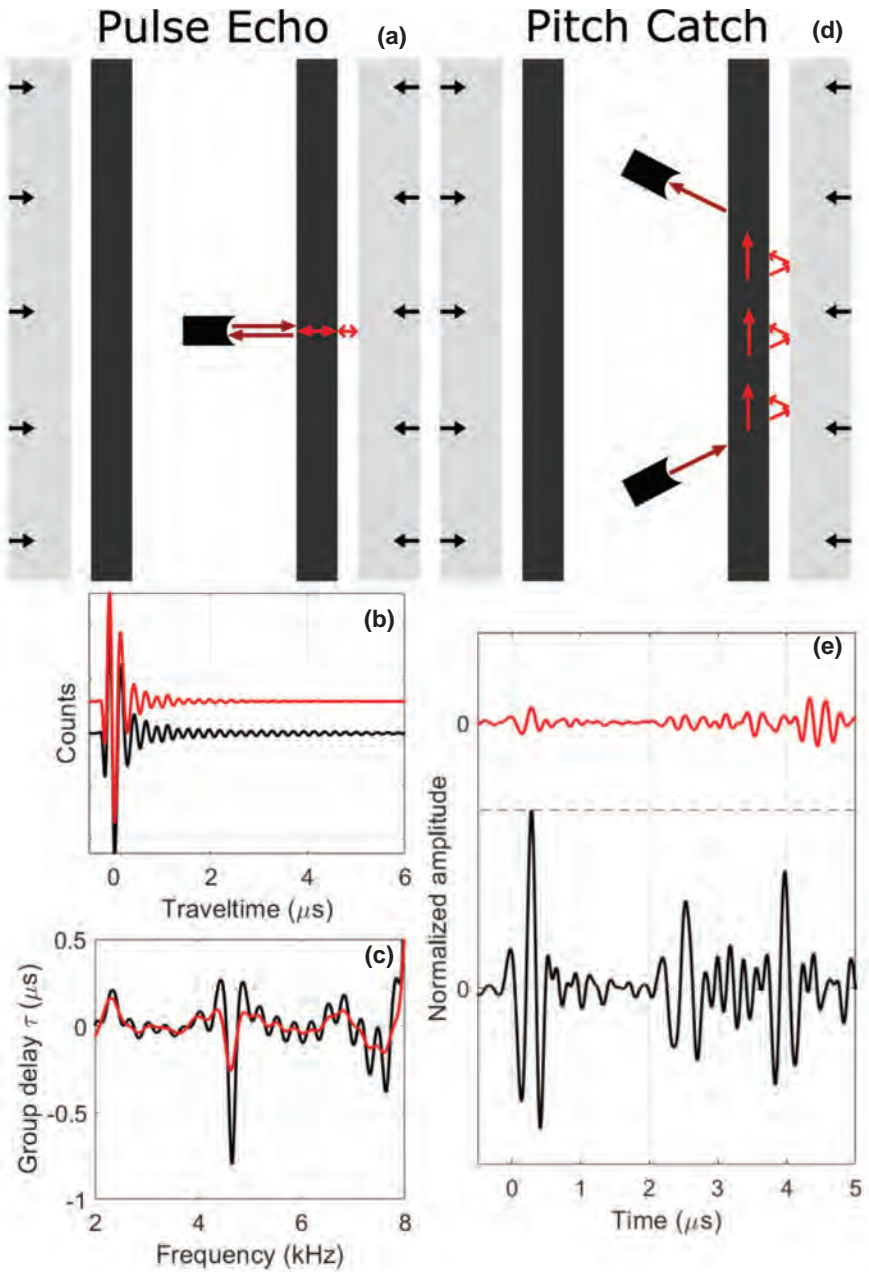


Fig. 4—Sketch of (a) PE and (d) PC measurements with the surrounding formation (gray), the casing (black), and the gap between (white). The black arrows indicate the applied pressure. (b) PE signal as recorded and (c) group delay calculated from measurements at low-confining pressure (black) and high-confining pressure (red). (e) Pitch-catch signal normalized to the same maximum from measurement at the low-confining pressure (black) and the high-confining pressure (red).

the beginning of the experiment (black) and at maximum confining pressure (red) normalized to the same maximum. The energy of the first arrival is significantly larger in the case of a measurement at the beginning of the experiment when the 2-mm gap still exists (black), i.e., when the impedance behind the casing is small compared to the measurement at the end of the experiment (red) when the shale is bonded to the casing.

Additionally, a third interface echo (TIE) can be observed (Fig. 4e, black) between 2 and 3 μ s. This echo is caused by the wave emitted from the Lamb-like guided wave traveling along the casing and reflected on the shale in case of a gap between casing and shale. The time difference between the first arrival and the TIE gives information about the thickness of the gap (Sirevaag, 2020).

The PC measurement is normally carried out at multiple distances to the transducer so that the attenuation rate can be calculated and compared. However, for the continuous PC measurement in E2, only one distance was measured. Therefore, we directly compare the signal strength of the first arrivals here. To set this value of signal strength (E) into perspective, we estimated the attenuation rate α . Therefore, we use the known travel path length in the casing of $L = 31$ mm and estimate the signal strength of the transmitted pulse (E_T) to be $E_{T1} = 14$ dB and $E_{T2} = 9$ dB for E1 and E2, respectively, using measurements at multiple distances from circumferential measurements. The attenuation rate is then calculated using $\alpha = (E_T - E)/L$. These attenuation rates are rough estimates to be able to derive impedance values. As this is an estimate, we will discuss the change in signal strength in the following section.

Correlation to Impedance

We carried out a number of measurements on a bench setup in preparation of the discussed cell measurements. The basic setup of the experiments for the PE and PC was the same as for the pressure cell setup. However, we did not apply pressure but fill the annulus with a variety of fluids and solids. The measurements and results are discussed in detail in Sirevaag et al. (2018). The advantage of these measurements is that the impedance of the material behind the pipe is known. We can use them to link the group delay parameter and the attenuation rate to the impedance.

For the linear trend between impedance and group delay parameter (PE) as well as attenuation rate (PC), we use measurements carried out on different fluids, mud, and epoxy materials (Fig. 5). From the PE bench measurements,

we find the relationship for group delay parameter $|\tau_{\min}|$ and impedance Z ($[Z] = \text{MRayl}$) of

$$Z = -5.18 \log_{10} |\tau_{\min}| + 0.48, \quad (3)$$

and from the PC bench measurement, the relationship for attenuation-rate α and impedance Z ($[Z] = \text{MRayl}$) of

$$\alpha = 3.07\alpha - 1.25. \quad (4)$$

Important here is to differentiate between the impedance derived from the PE and PC measurements using the above relationship and the characteristic impedance of a material. The characteristic impedance is a material property, while the impedance derived from the PE and PC measurement is information of the material properties and potential gap sizes as well as the material properties of the material filling the gap. Using the above-described empirical relationship, we can calculate the impedance from the group delay parameter and signal-strength measurements. We include these derived impedance values in the figures for comparison but concentrate on the discussion of group delay parameters and signal strength as these are the parameters derived from the experiment.

ULTRASOUND DATA

Differences in the results from PC and PE can be expected as PE and PC measurements cannot be carried out at the same depth location along the pipe. Further differences need to be expected as the PE measurement is a point measurement, while the PC measurements give

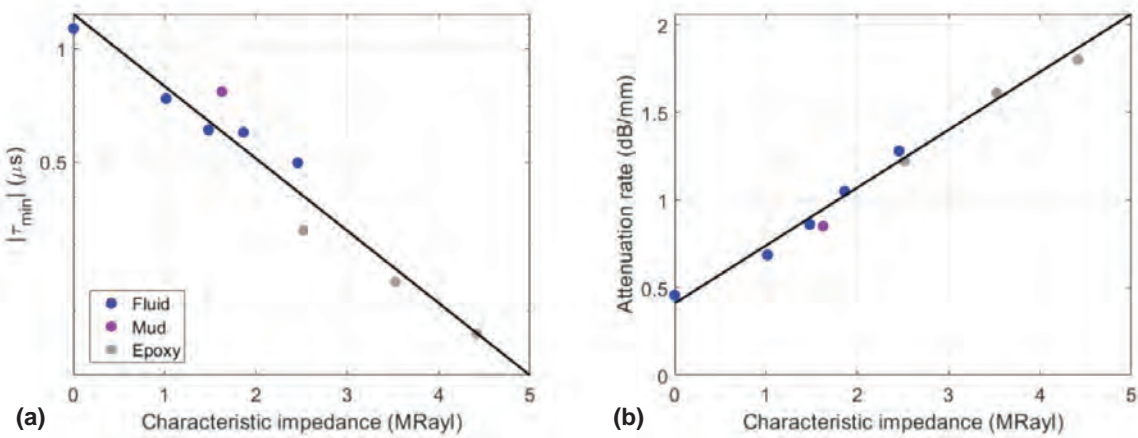


Fig. 5—Connection of impedance with (a) group delay parameter derived from PE measurements and (b) attenuation rate derived from PC measurements for a variety of fluids and solids.

average information of the conditions along the travel path between transmitter and receiver.

In E1, the 0° direction was continuously monitored with the PE tool (Fig. 6). One measurement was done every 10 minutes. In regular intervals of a few days (vertical black lines, Fig. 3a and Fig. 6), the PE tool was rotated, and a measurement was taken every 5° . Additionally, the PE tool was removed so that it was possible to carry out PC measurements in 5° intervals, too. For PE and PC measurements, 128 measurements were carried out each time and averaged to improve the signal-to-noise ratio of the data.

In E2, the 0° direction was continuously monitored with the PC tool (Fig. 7). Again, one measurement was carried out every 10 minutes and in regular intervals of a few days (vertical black lines, Fig. 3b and Fig. 7). The PC tool was rotated to carry out measurement in 20° steps and for four distances. Additionally, the PC tool was removed so that it was possible to carry out PE measurements for multiple directions in steps of 5° and 20° , respectively. This was the first experiment we carried out using the pressure cell. After analysis of the data, we realized that logging with a 5° resolution greatly improved the interpretability of the results. Again, 128 measurements were averaged at each location to improve signal-to-noise ratio.

In the following, we first present the PE measurements of the continuous measurement (E1), then the PC measurements of the continuous measurement (E2), followed by a comparison of PE and PC measurements for the different axial directions (E1).

Continuous Pulse-Echo Measurement

Data from the continuous PE measurement are shown in Fig. 6a. The data were normalized, and the first trace was subtracted from the following ones within the block in which the tool was not removed. This was done to visualize better the changes occurring over time. We explain the fact that the first amplitudes do not vanish, subtracting a trace with the increased ovalization of the pipe during the experiment and a change in reflection angle associated with that. The group delay parameter calculated from this data set is shown in Fig. 6b, together with confining pressure and permeability for comparison. Abrupt changes in the group delay parameter can be observed where the tool was removed on Days 17, 21, 27, and 34 (vertical black lines). Even though we have a scale at the top of the cell where we insert the tool to adjust the azimuth orientation,

small variations are possible. These can have a notable influence on the measurements as the PE measurement is a point measurement. These abrupt changes when the tool has been removed should, therefore, not be mistaken as signals.

The abrupt change in the data and the group delay parameter at Day 14 is caused by the increase in cell temperature (Fig. 3a). Most variability occurs between Day 16 and 24, i.e., with an increase of confining pressure from 5 to 11 MPa, where we observe repetitive patterns of signals appearing at shorter traveltimes (Fig. 6a). At the same time, this is an area where we observe variations in the group delay parameter between 0.85 and 0.58 μs (Fig. 6b).

After Day 24, significantly less variability is visible in the data, corresponding to a slow decrease of the group delay parameter. The group delay parameter keeps decreasing while the confining pressure is kept constant at 14 MPa, reducing to a minimum of 0.66 μs (1.36 MRayl; Fig. 6b). With the decrease in confining pressure towards the end of the experiment, we can observe an increase in the group delay parameter, with large variations at Day 37.

Between Day 16 and 24, we observe a variability in the measured values between 0.8 to 1.7 MRayl and at Day 37, between 0.55 to 1.32 MRayl. This variability is small compared to the change in impedance we expect from kerosene with 1.1 MRayl to shale with 4.2 MRayl. However, for the measured direction, we only observe a change in impedance from 0.8 MRayl at the beginning of the experiment to 1.36 MRayl at maximum confining pressure. The observed variability between Day 16 and 24 and at Day 37 is, therefore, significant.

Continuous Pitch-Catch Measurement

The data of the continuous PC experiment are shown in Fig. 7a. The data were aligned to the maximum of the first arrival visible at 0- μs reduced traveltime. The signal strength of this first arrival is also given in Fig. 7b for better comparison with the confining pressure and permeability. No abrupt changes can be observed when the tool is removed and reinserted as visible in the PE measurements. There is one exception where the signal strength drops for the interval at Days 17 and 18. As the signals of the intervals before and after are in line, we assume an error in the measurement here, most likely due to the presence of an air bubble in front of the transducer. The shift in signal strength for the interval at Day 17 and 18 is, therefore, not taken into account in the discussion.

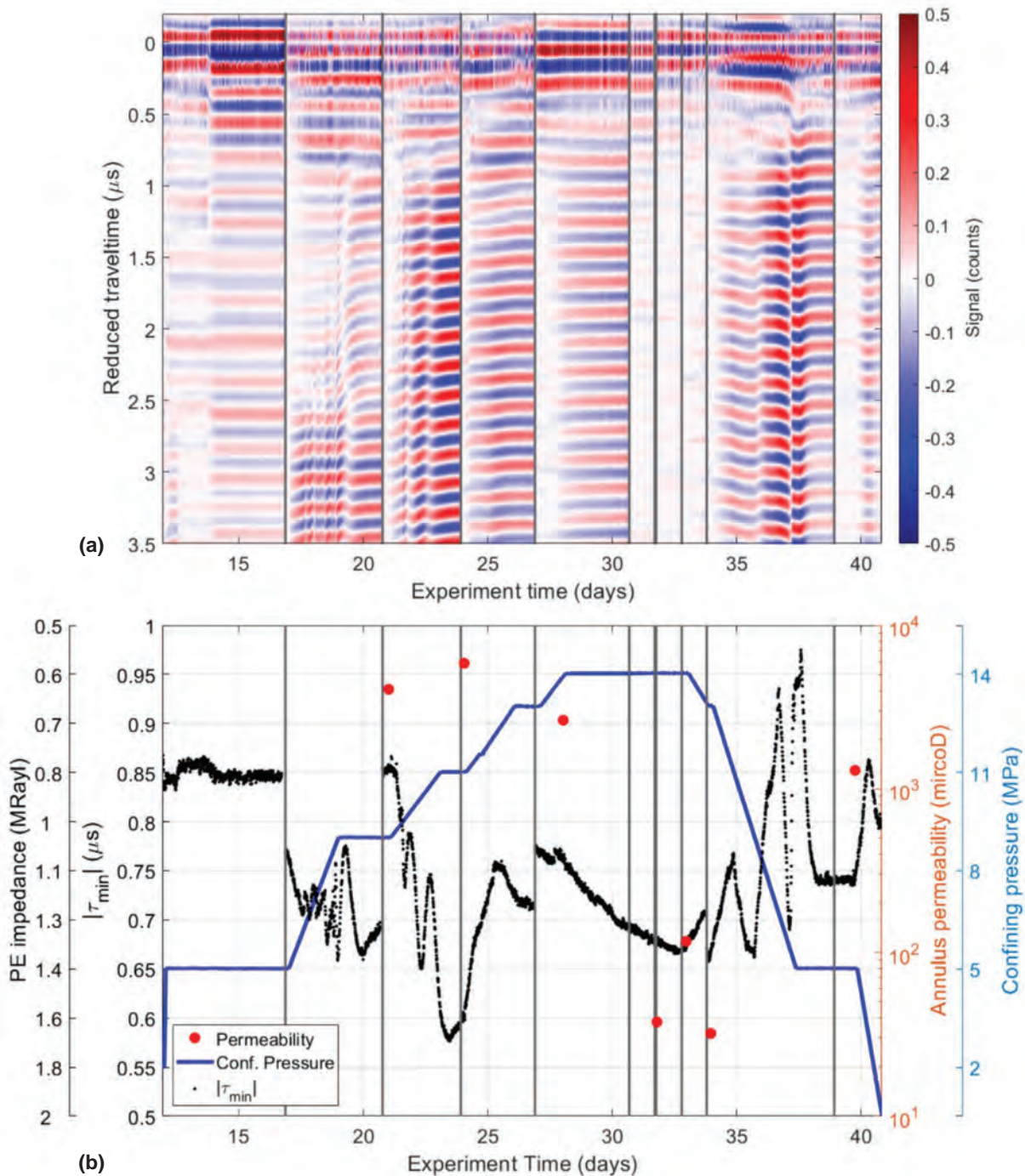


Fig. 6—Ultrasonic data from continuous PE logging of E1. The black vertical lines indicate the locations where the tool was removed. (a) For each of these blocks of measurements where the tool was not removed, the first measurement was subtracted from the following measurements after aligning and normalizing the first arrival. (b) Variation of group delay parameter $|\tau_{\min}|$ derived from continuous PE logging. Confining pressure and permeability are plotted for comparison.

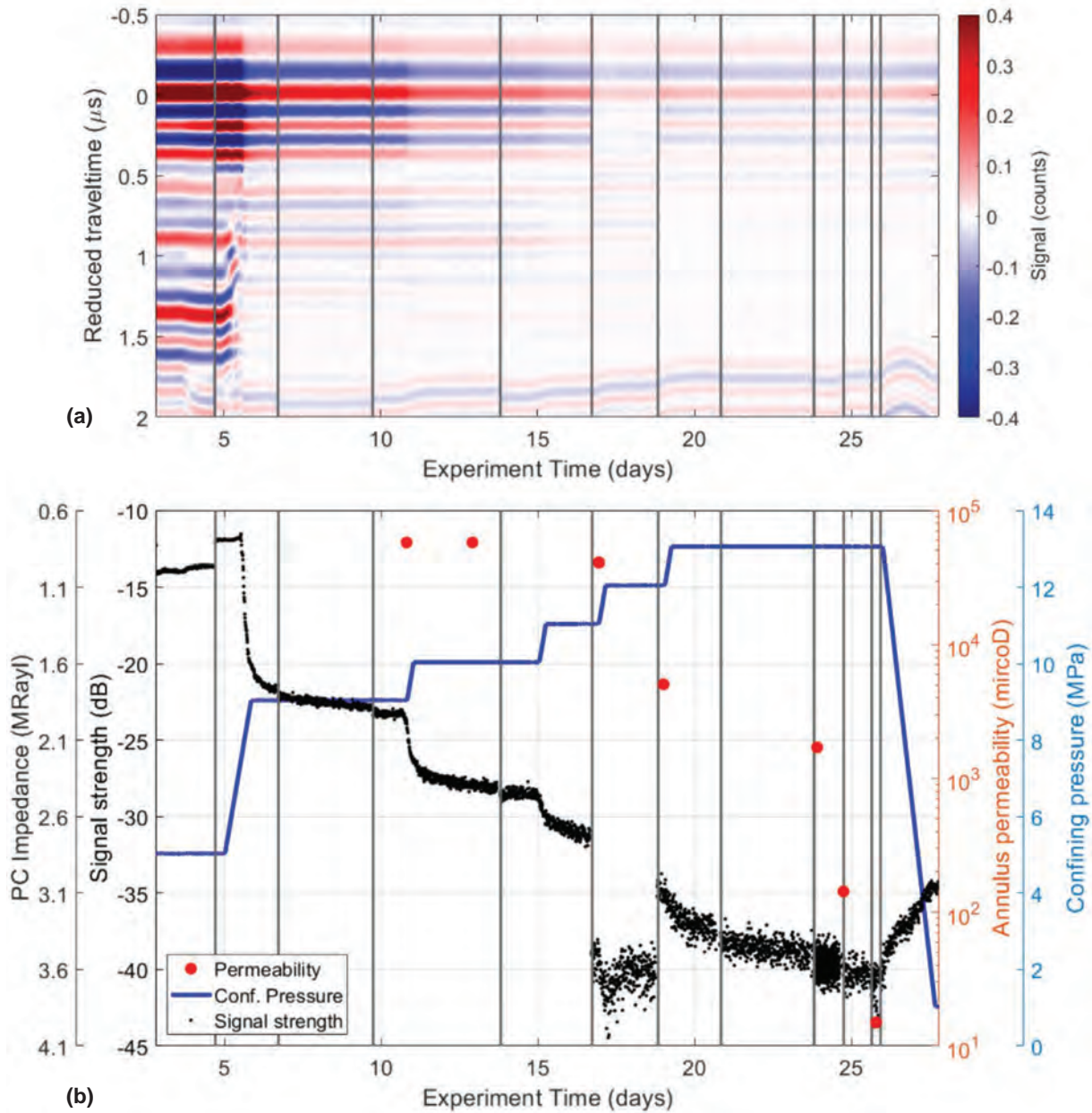


Fig. 7—Ultrasonic data from continuous PC measurement of E2. The black vertical lines indicate the locations where the tool was removed. (a) The transducer-receiver distance is constant, and the maximum of the enveloped was aligned at 0 μ s. Visible is the decrease in signal strength of the Lamb wave (first arrival) over the experiment time and the disappearance of the TIE at 1.4 μ s on Day 5. (b) Variation of signal strength of the first arriving Lamb-like guided wave. Confining pressure and permeability are plotted for comparison.

At the beginning of the experiment, the TIE is visible in the data at about 1.4 μ s (Fig. 7a), in agreement with the 2-mm large gap. The signal strength for these first 5 to 6 days is around –12 to –14 dB. Once the pressure increases from 5 to 9 MPa, the TIE appears gradually earlier and disappears after 5.5 days. With the disappearance of the TIE, we observe a significant drop in signal strength of the first

arrival of 10 dB (Fig. 7b). The signal strength shows only little change while the confining pressure is kept constant and drops rapidly with every increase in confining pressure. Thus, over the entire experiment time, we observe a decrease in signal strength of 25 dB. With the rapid decrease in confining pressure towards the end of the experiment, the signal strength increases again by 5 dB.

Circumferential PE and PC Measurements

For both experiments (E1 and E2), measurements were carried out with PE and PC around the circumference in steps of 5° and 20°, respectively. Here, we concentrate on discussing the measurements from E1 as these measurements were done with a 5° resolution and, therefore, show variations and trends more clearly; however, the changes in derived parameters due to the increasing pressure we discussed were observed in both experiments. Traveltime information is shown for both PE and PC data (Figs. 8a and 8c). The group delay parameters of the PE measurement are given in Fig. 8b, and signal strengths of the PC measurement are shown in Fig. 8d. Figure 8 shows the measurement during the increase in confining pressure, while Fig. 9 shows the same results for measurements during the decrease in confining pressure.

During the experiment, PE and PC measurements are not aligned at 0°. To ensure comparability of the different measurements, we used the traveltimes and estimation of pipe thickness to align PE and PC measurement directions. The continuous PE measurement (Fig. 6) was carried out in the 0° direction.

The trends observed in the traveltimes from PE and PC measurement with increasing confining pressure are the same (Figs. 8a and 8c). Traveltimes increase in the directions 0°/360° and 190° and decrease in the directions of 90° and 270°. The traveltimes of the PE measurements are a direct measurement of the distance between the transducer and inner pipe wall. The PC measurements are traveltimes of the distance to and from the pipe plus the traveltimes of the Lamb-like guided wave in the pipe wall. Therefore, more variations are visible in those measurements. From the traveltimes of the point measurement of the PE measurement, we can derive the change in the pipe radius, showing the increase in ovalization with increasing confining pressure.

In the PC measurements, we observe very weak signals for the direction from 220° to 240°. Therefore, some of these directions do not have results (Figs. 8c, 8d) as it was not possible to identify the first arrival here. For these directions, we also observe the lowest values in the group delay parameter (Fig. 8b), as low as 0.5 μs already at 5 MPa confining pressure and very little change with increasing pressure. However, this effect is not visible in the traveltimes derived from the first reflection of the PE measurement (Fig. 8a). In all laboratory measurements we carried out with pipes manufactured the same way, we observe a range of directions with very weak signals. We carried out a number of tests with the bench setup, using different materials behind the pipe, rotating the pipe,

removing and reinserting the tool to identify the cause of this discontinuity that is visible in all these measurements independent of the material behind the pipe. We concluded that this is most likely an effect of a discontinuity within the pipe from pipe manufacturing. This discontinuity is not visible on the inner pipe wall as it is not detectable in the signal of the first arrival of the PE. Hence, it is most likely a discontinuity within the pipe or on the outer pipe wall as it is visible in the analyses of the group delay parameter of the PE measurement and in the PC measurement, i.e., waves that propagate within the pipe.

For the results from the PC measurement, we observe a drop in signal strength when the confining pressure is increased from 5 to 9 MPa (Fig. 8d). In the directions of 25° to 130° and 245° to 300°, a significant drop in amplitude of around 10 dB can be observed with this pressure increase. In the perpendicular directions around 180° and around 0°/360°, this change in amplitude strength is not visible. Afterward, with increasing confining pressure, the signal strength for all directions decreases by an additional 10 to 15 dB.

For the group delay parameter (Fig. 8b), we observed a similar variation with direction as the variation we observe for the signal strength from the PC measurement. However, the variability of neighboring estimates of the group delay parameter is high, especially for the measurement at 9 and 11 MPa compared to the variations we observe in the PC measurements. We observe a drop of the group delay parameter when the pressure is increased from 5 to 9 MPa in the direction between 30° to 140° and 245° to 300° of around 0.2 μs, similar to the observations made for the PC measurement. Increasing the pressure further to 14 MPa results in a further decrease of the group delay parameter of around 0.1 to 0.2 μs for all directions.

Toward the end of the experiment, the confining pressure is decreased in three steps. With the decrease in pressure, the PC signal strength increases between 5 and 15 dB, depending on the direction (Fig. 9d). The increase is only 5 dB in directions where we previously observed the abrupt drop in signal strength with the increase in pressure from 5 to 9 MPa (30° to 140° and 245° to 300°). For the other directions (around 0°/360° and 180°), the signal strength increases by 10 to 15 dB. Thus, the signal strength is at the same level as it was at the beginning of the experiment for those directions.

Similar to the PC measurement, we observe an increase of the group delay parameter with decreasing pressure in the directions around 0°/360° and 180° to the initial values at the beginning of the experiment (Fig. 9b), while the increase in the other directions is small (< 0.1 μs) in comparison.

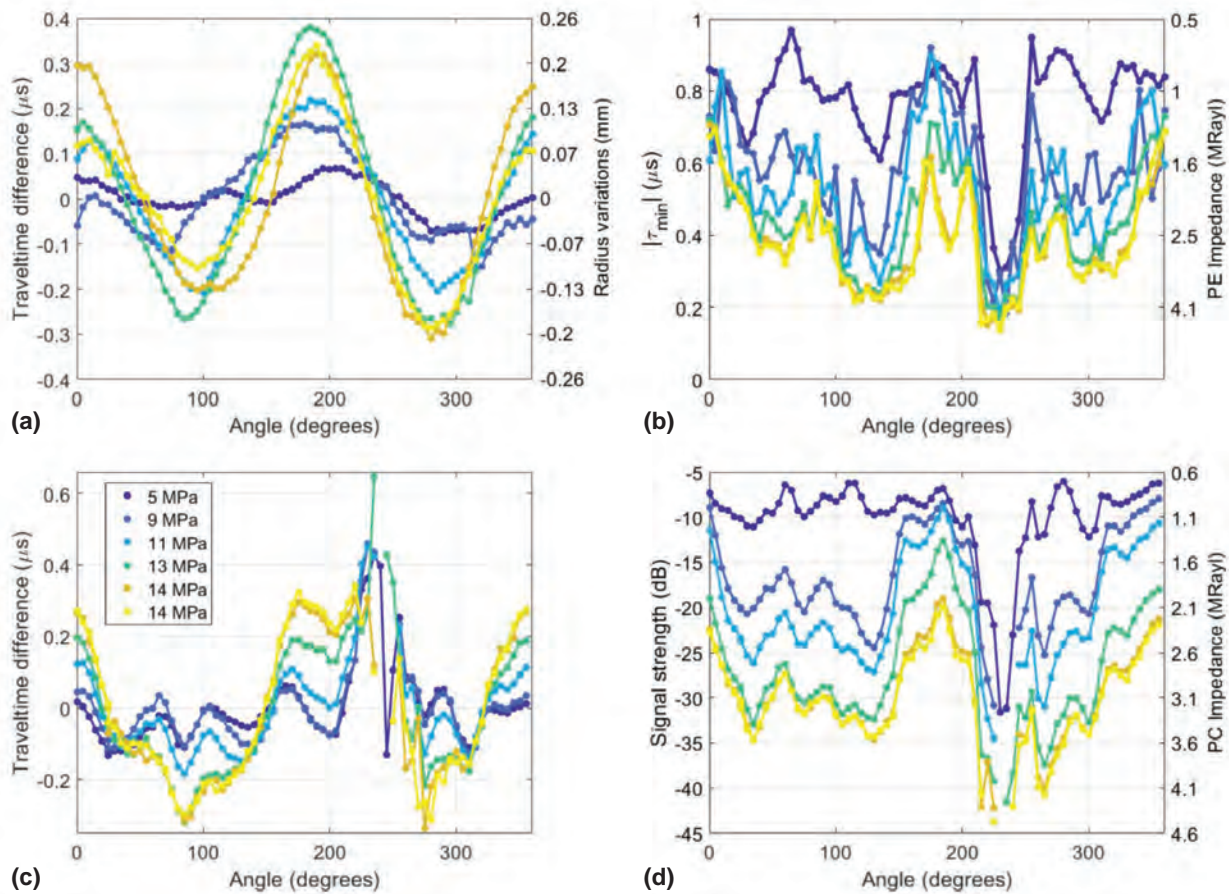


Fig. 8—(a) Traveltime and (b) group delay parameter derived from PE measurement and (c) traveltimes and (d) signal strength from PC measurements for different angle directions from E1 during a stepwise increase in confining pressure. These measurements correspond to the location of the black vertical lines in Fig. 6.

Results

The shale is consolidated at constant confining and pore pressure for 5 days at the beginning of both experiments. The stress-strain curves for the two experiments show a good match, although loading rate and stress hold periods are not the same (Fig. 10). Therefore, we expect that the state of the annulus in both experiments is similar at the same axial strain levels. Note that it is not possible to identify any borehole failure or changes in borehole radius from the axial strain measurements.

In both experiments, we can observe that the permeability only decreases once a confining pressure of 13 MPa is reached (Fig. 3). For lower-confining pressure, the permeability values are larger than 1,000 μD . Results for these measurements with high permeability have large uncertainties but show that the annulus or parts of the annulus are still open such that fluids can still circulate. Reaching 13 MPa confining pressure, the permeability drops down to values below 100 μD , corresponding to a permeability as can be expected for cement under field conditions (Khalifeh and Saasen, 2020).

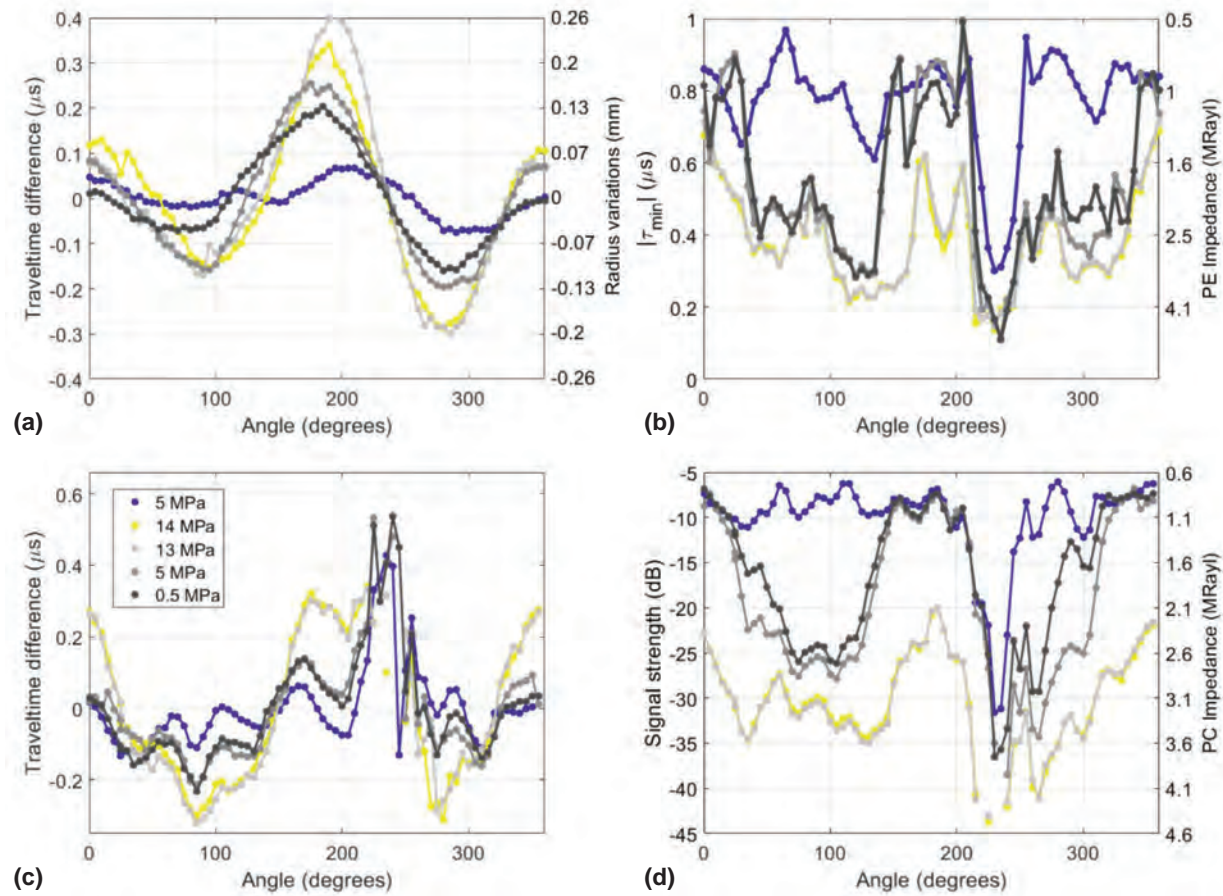


Fig. 9—(a) Traveltimes and (b) group delay parameter derived from PE measurement and (c) traveltimes and (d) signal strength from PC measurements for different angle directions from E1 during a stepwise decrease in confining pressure. These measurements correspond to the location of the black vertical lines in Fig. 6. The data for 5 and 14 MPa have been shown in Fig. 8 and are plotted here for comparison.

The ultrasonic-logging equipment of the experiment was designed to reflect the industry setup in a scaled-down version as exact as possible. The most significant difference is the increased distance between the transducer and the pipe in the laboratory measurement that had to be introduced to be able to fit the off-the-shelf transducers into the pipe using an acoustic mirror. This allowed us to analyze more wave cycles in the analysis of the PE data than is done in the industry, where a second reflection from tool and pipe can be observed after about seven wave cycles. This means that the connection we derive between the characteristic impedance and the group delay parameter (PE), and attenuation rate (PC), respectively (Fig. 5), cannot be applied to industry data

directly. Important here is, however, that our different laboratory measurements and analyses are consistent with each other and that the trends and changes we observe are comparable to those observed in industry setups and can, therefore, be used to understand results from industry measurements better.

Trends in Continuous PE and PC Results

We explain the largest variations in the group delay parameter observed in the continuous PE measurement (E1) between Day 16 and 24 with the moving in of the shale and the closing of the gap (Fig. 6a). Jutten and Hayman (1993) analyzed the effect of micro-annuli on PE measurements and showed that large variations

in the derived parameters could be expected. The observed variations in the group delay parameter and the interpretation that this indicates a closing of the gap agrees with the observed patterns in the data (Fig. 6a). These observed repeating patterns of shifts to earlier traveltimes can be expected when a gap, larger than half the wavelength (0.13 mm), is closed. They are caused by repetitive patterns of constructive and destructive interference of the reverberation within the pipe and the gap.

The gap seems to close with the increase in confining pressure to 9 MPa; nevertheless, we observe a further decrease in the group delay parameter over the next days with increasing pressure (Fig. 6b). The decrease in permeability corresponds to a decrease of the group delay parameter to values below 0.7 μ s. Hence, with increasing pressure, flow channels that still exist after the initial closing of the gap likely close so that permeability decreases, corresponding to a reduction in group delay parameter. It should be noted that a single measurement during gap closure can also lead to a low group delay parameter. This does not reflect a well-bonded, nonpermeable material but is then an effect of interference patterns and can make interpreting the PE results difficult. The impedance values derived from the group delay parameter using Eq. 3 show that the impedance values change only from 0.8 MRayl at the beginning of the experiment to 1.35 MRayl at maximum confining pressure. The comparison of these results to the circumferential measurements (Fig. 8b) shows that the continuous measurement was carried out in the direction

(0°) with the smallest variation in impedance. Hence, even though the variation in derived impedance for the continuous measurement is very small, the overall observed change in impedance within the experiment is about six times larger. The impedance of 0.8 MRayl is also lower than the impedance we expect from kerosene (1.1 MRayl). However, for the circumferential measurements (Fig. 8b) at 5 MPa confining pressure, we can observe variations between 0.6 to 1.6 MRayl, so that the low-impedance value for the direction of the continuous measurement (Fig. 6b) can be explained with the variability likely due to variations in thickness, roughness, and curvatures of the pipe.

In the continuous PC measurement (E2), a similar trend can be observed with large changes in the data at the beginning of the experiment that does not correspond to a decrease in permeability (Fig. 7). Here, we observe the disappearance of the TIE at Day 5 with the increase in confining pressure from 5 to 9 MPa, indicating the moving in of the shale and the closing of the gap. Measurements of permeability are, however, still above 1,000 μ D after Day 10, indicating that flow channels still exist. We explain the disappearance of the TIE with the fact that the shale will most likely not move evenly towards the pipe. Hence, an even reflection interface for the TIE along the travel path of the Lamb-like guided wave does not exist any longer. Even though waves are still reflected from this interface, they no longer interfere constructively such that a distinct TIE cannot be observed anymore. Hence, the disappearance of the TIE is not a good indication for well-bonded shale with low permeability. However, an ongoing decrease in signal

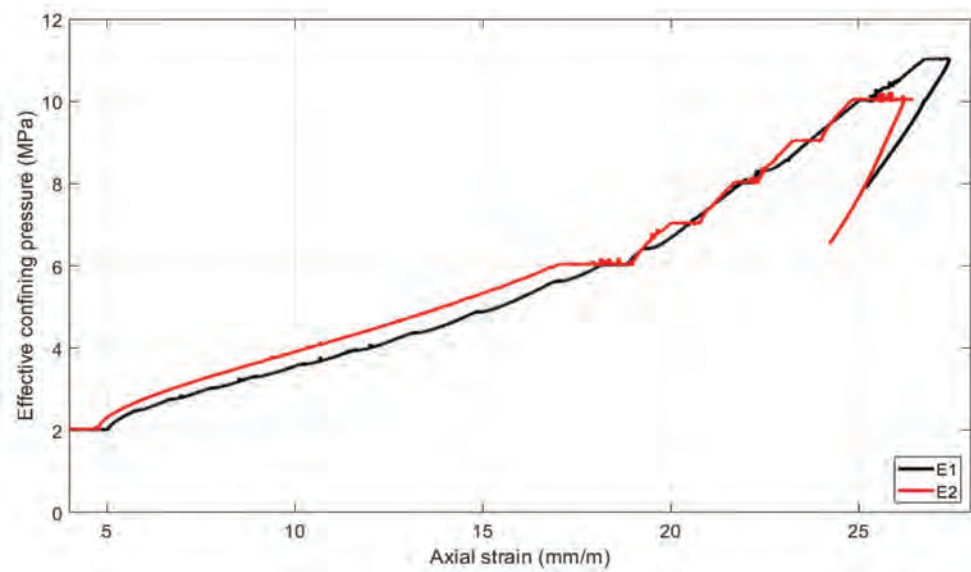


Fig. 10—Net confining pressure vs. axial strain for the two experiments. The loading rate and stress hold periods are different for the two experiments.

strength of 20 dB can be observed. This ongoing decrease in signal strength correlates with the decrease in permeability and can, therefore, be a good indicator for the bonding and impermeability of the shale behind the pipe.

The change in impedance we derived from the change in signal strength using Eq. 4 shows a decay from 1 MRayl to 3.6 MRayl at maximum confining pressure. This is in good agreement with the characteristic impedance of kerosene and is slightly lower than the impedance of intact shale.

Even though the continuous measurements were done during two separate experiments with differences in confining-pressure load rate, the stress-strain curves show that they are well comparable (Fig. 10). For both experiments, we observe the same trends in the PE and PC results. First, the shale moves in and closes the gap when the confining pressure increases from 5 to 9 MPa and 11 MPa, respectively. This is visible in the data by the disappearance of the TIE in the PC measurement and large variations of the group delay parameter in combination with characteristic interference patterns for the PE measurement. In both experiments, no significant decrease in permeability can be observed for this initial closing of the gap. Hence, we conclude that the shale moves in closing the gap; however, channels through which liquids can flow are still open.

Above 11 MPa confining pressure, we observe a decrease in permeability with the further increase in confining pressure. This corresponds to a significant decrease in signal strength (20 dB) for the PC measurement and a decrease in the group delay parameter of up to 0.2 μ s for the PE measurement compared to the beginning of the experiment. An explanation for this decrease in signal strength and group delay minimum could be the closure of flow channels around the pipe, which would correspond to the significant reduction in permeability. However, while we derive an increase in impedance to 3.6 MRayl for the PC measurement, we only derive an increase in impedance to 1.35 MRayl in the case of the PE measurement. The difference can, of course, be expected between these two measurements, as they are from two different experiments, and large angular variations exist as observed in the circumferential measurements (Figs. 8 and 9).

Comparison of Circumferential PE and PC Results

While it is easy to observe changes in the derived PE and PC parameters in the continuous measurements, it can be more challenging to interpret discrete measurements, as the measurements are done around the circumference (Figs. 8 and 9). Due to the combination of continuous and discrete measurements, we can, however, link them to improve our understanding.

The clear directionality of the change in PE group delay parameter, PC signal strength, and the traveltimes is visible both during the increase and decrease in pressure. Here, the directions of the ovalization of the pipe align with the PE and PC results. Along the long axis of the ovalized pipe ($0^\circ/180^\circ$), we observe that PE group delay parameter and PC signal strength do not drop at the beginning of the experiment with the increase in confining pressure from 5 to 9 MPa. At the same time, values go back to those at the beginning of the experiment when the confining pressure is reduced again. Along the short axis of the ovalized pipe ($90^\circ/270^\circ$), the significant drop in PE group delay parameter and PC signal strength can be observed with the initial increase in confining pressure from 5 to 9 MPa. PE group delay parameter and PC signal strength increase again with decreasing confining pressure from 14 to 0.5 MPa but stay clearly below the values at the beginning of the experiment (5 MPa). Even though the confining pressure on the sample outer surface is isotropic, an anisotropic stress field develops within the sample, reflected in the ovalization of the pipe and the corresponding variation in PE group delay parameter and PC signal strength. The location of cracks, shown in Fig. 2b, observed in computer tomography images of the shale after the experiment (Fig. 2c), indicates the location of maximum strain and supports the observation of an anisotropic stress field within the shale. The shale is relatively homogeneous with isotropic elastic properties in the transverse plane. From experiments and theory, it is known that when an isotropic hydrostatic loading is applied, an isotropic strain around the borehole can only be expected up to the failure point (Vardoulakis and Sulem, 1995; Fjær et al., 2008). Once the shale fails and creeps, failure planes develop that redistribute the stresses around the borehole, explaining the toroidal-shaped fractures seen in the computer tomography images taken of the samples after testing (Fig. 2c).

Hence, the shale creeps in towards the pipe, coming in contact with the pipe in the $90^\circ/270^\circ$ direction, leading to the ovalization of the pipe already at the beginning of the experiment with the increase in pressure to 9 MPa. Some flow channels likely still exist in the direction of the short axis. Along the long axis, the pipe is pushed outwards from its original position towards the shale, while the shale is also pushed towards the pipe. However, with the lower pressure in this direction of the short axis, the shale probably also moves in less. At the same time, more closely located flow channels can develop in this direction (Fig. 2b). With increasing pressure, all these flow channels are slowly closed, decreasing permeability, which is reflected in the PE group delay parameter and PC signal strength.

With the decrease in pressure at the end of the experiment, flow channels likely open up again, leading to a small decrease in PE group delay parameter and PC signal strength in all directions. At the same time, the pipe deforms partly back towards the round pipe (Figs. 9a and 9c), likely decoupling from the shale in the directions of the long axis while still being in contact in the directions of the short axis, which moves outwards during pressure decrease. Therefore, we observe a significant increase in PE group delay parameter and PC signal strength in the direction of the long axis, where values go back to those observed at the beginning of the experiment while the increase in these values is small in the directions of the short axis where shale and pipe are likely still in contact.

The interangular variability of the PE measurement is larger than those of the PC measurement, especially for the measurements at 9 and 11 MPa, and decreases for the measurements at 14 MPa. Two effects play a role here. Firstly, when the shale moves in, it strongly influences the estimate of the group delay parameter, leading to a large variability as visible in the continuous PE measurement for the increase from 5 to 11 MPa (Fig. 6b). Secondly, large variations can be expected during close locations as the PE measurement is a point measurement while the PC measurement is an average over a distance. Especially when the shale moves towards the pipe and a lot of open channels and gaps exist, large differences can be expected between neighboring locations. With increasing confining pressure and closure of these channels, conditions behind the pipe become more uniform, resulting in less variability.

For a combined analyses of PE and PC measurement, the PE group delay parameter can be plotted over the PC signal strength as presented in Fig. 11. The second axes show the values for the derived PE and PC impedance. At consolidation pressure of 5 MPa, high values for the group delay parameter and signal strength can be observed, but values are concentrated with a small spread. With the increase in pressure to 9 MPa, which we link to the closing of the initial 2-mm gap and the appearance of flow channels, the area of group delay parameter/signal strength is shifted to lower values with a large spread. With increasing pressure (14 MPa), we observe a further shift to smaller values in combination with a decrease in the spread, leading to the conclusion that conditions on the outside of the pipe are more uniform again, resulting in better bonding, which is supported by the decrease in permeability.

With the decrease in pressure, we can observe the spread of group delay parameter vs. signal strength increases again, shifting to higher values. At the same time, values seem to separate into two groups. One group exists with a group delay parameter around 0.8 μ s and -10 dB signal strength, corresponding to the direction of the long axis that likely decouples from the shale with decreasing pressure. The other group with group delays between 0.3 to 0.6 μ s and signal strength between -30 to -5 dB corresponds to the direction of the short axis, where flow channels probably open but connections between shale and pipe still exist. Hence, the difference between the change in these parameters between increase and decrease in pressure reflects the irreversible part of the deformation.

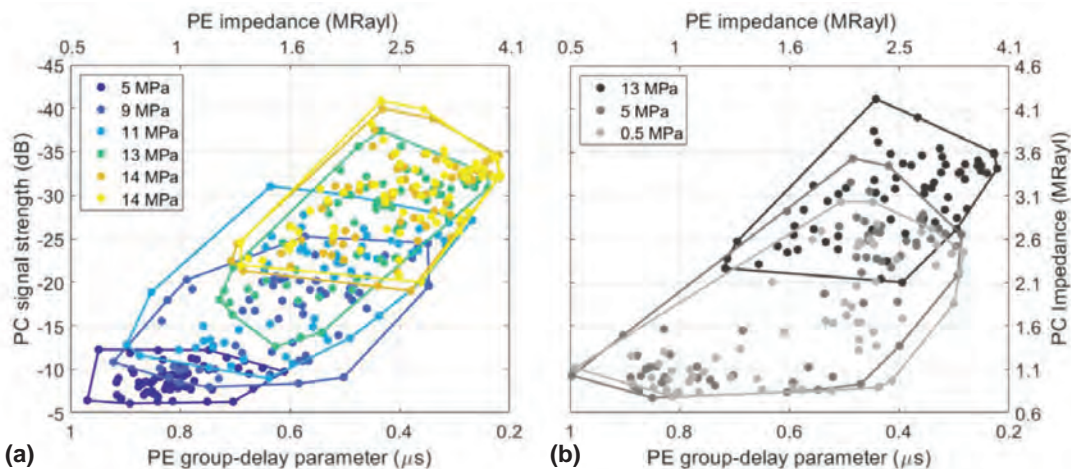


Fig. 11—PE and PC results from E1 show the decrease in signal strength (increase in attenuation rate) in correspondence with the decrease in PE group delay parameter for increasing pressure. Not taken into account here are the directions between 210° to 255° with strongly disturbed signals. (a) shows results during pressure increase and (b) during pressure decrease. Contours for visualization of the data spread.

Fig. 12 shows the mean PE and PC impedance of the results shown in Fig. 11 and the same results from E2. Both PE- and PC-derived impedance show good agreement with an increase in impedance with increasing pressure. In comparison with the same values derived from the bench measurements (Fig. 5), we can observe how the derived impedances shift from low values in the beginning (kerosene, 1.1 MRayl) to fluids with higher impedance and on to solid materials in agreement with the closing of the initial 2-mm gap and following the closure of flow channels.

CONCLUSIONS

The unique combination of high-resolution PE and PC measurements through a pipe in time and space during pressure increase under controlled conditions allows us to improve our understanding of the processes, leading to the bonding of shale with the casing. From the combination of all these experiments, we conclude that the Pierre II shale creeps towards the pipe with the increase in pressure from 5 to 9 MPa. This leads to the disappearance of the TIE observed in the PC measurement. In the PE measurement, we observe a large variability in the group delay parameter and characteristic interference patterns in the data. This initial moving in of the shale does not lead to a significant reduction in permeability, as channels are likely still open, allowing fluids to flow.

With a further increase in confining pressure, these channels are, over time, likely closed off, leading to the observed drop in permeability and the bonding of the shale with the pipe. This corresponds to a further significant decrease in signal strength for the PC measurement and a decrease in the PE group delay parameter with a reduction in interangular variability, reflected in the derived increase in the impedance values. With the decrease in pressure at the end of the experiment, flow channels likely open again, and debonding leads to reduced signal strength and group delay parameter.

While a general reduction in signal strength and group delay parameter can be observed for all directions, a clear variation with 90° is observable, which agrees with the directions of ovalization of the pipe. Even though the applied pressure on the cell is isotropic, we observe that an anisotropic stress field develops within the sample around the hole with an axis with the largest pressure and a second axis perpendicular to that where the pressure is smaller. The axis with the largest pressure corresponds to the short axis of the ovalized pipe and the directions where we observe an immediate and significant drop in signal strength and group

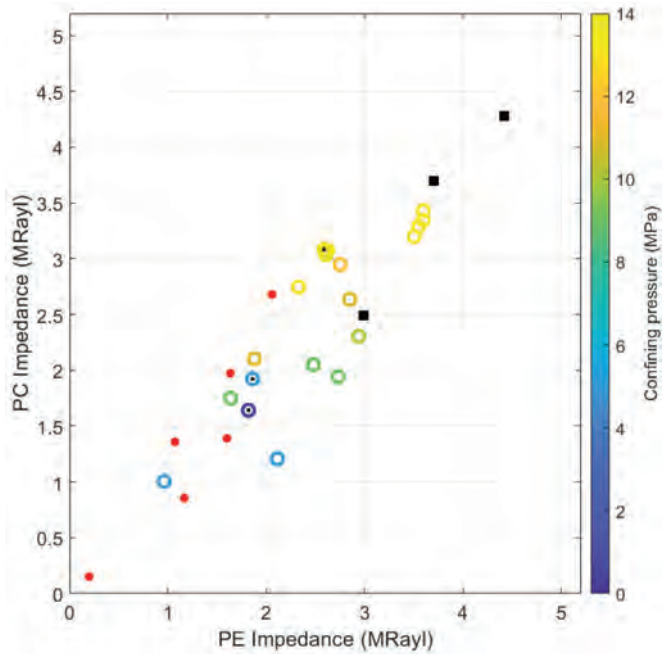


Fig. 12—Shown is the change in mean impedance derived from PE and PC measurement with a change in confining pressure in relation to the mean PE and PC impedance derived from the bench measurements. Red dots are impedances for fluids, and black squares are impedances for solids from the bench measurements (Fig. 5). Plotted are results from E1 and E2. The three rings with a black dot in the middle are the measurements where the pressure was decreased during E1.

delay parameter. Hence, we assume that in the direction of the short axis, the shale creeps towards the pipe with the pressure increase to 9 MPa, coming into contact with the pipe and leading to the pipe ovalization. This significant drop of the group delay parameter cannot be observed for the other directions which correspond to the long axis of the ovalized pipe, i.e., an area where the pipe is elongated towards the shale, and even though the shale probably moves towards the pipe, it is not in contact with the pipe early on as pressure in this direction is likely smaller. Similarly, we observe a variation with 90° when the pressure is decreased, leading to a debonding of the shale in the direction of the long axis of the ovalized pipe.

The variation in group delay parameter and signal strength for different directions and the difference in the process of the shale bonding with the pipe means that there is not a simple threshold value we can define for those two parameters that indicate bonding with the pipe. However, in combining both parameters and taking their spread into account, conditions can be judged more reliable. In both experiments, good bonding between pipe and shale was achieved with confining pressures above 12 to 13 MPa.

Combining PE and PC measurements, it was possible to detect this bonding.

Even though some differences exist between the laboratory and industry setup, and derived values for group delay parameter and attenuation rate in connection to impedance cannot be applied directly to industry measurements, trends and changes observed in the results from the laboratory experiments are comparable. These results can, therefore, be used to understand observations from industry measurements better. Understanding shale creep with the complexity of the orientation of the layering is an open research field. In the presented laboratory experiment, we simplified this problem somewhat by using shale that was cored perpendicular to the bedding, such that the layers within the shale were horizontal and isotropic in the radial direction in our experiment. We, nevertheless, observe an anisotropic stress field as the shale did not creep uniformly. Still, when the pressure was high enough, the shale bonded with the pipe, and a good seal between pipe and shale was achieved. This was confirmed by the drop in permeability and observed in the drop of group delay parameter and signal strength with the PE and PC measurements, respectively. Those results show the importance of PE and PC measurements with a high-azimuth resolution to be able to identify possible weaknesses in the seal quality of the shale and identify a good seal due to well-bonded shale.

ACKNOWLEDGMENTS

The authors acknowledge the technical and financial support of the Research Council of Norway, Aker BP ASA, BP Exploration Operating Company Ltd, ConocoPhillips Skandinavia AS, Equinor Energy AS, Lundin Norway AS, Petrobras, Shell Exploration & Production Company, and Total E&P Norge AS through the KPN projects “Logging Shale Barrier Before Well Abandonment” (Grant no. 255365/E30) and “Shale Barrier Toolbox: Designing Future Wells for Efficient Completion and Simpler P&A” (Grant no. 280650/E30) at SINTEF Industry. The authors further thank Serhii Lozovyti and Sigurd Bakheim for their support in carrying out the experiments.

NOMENCLATURE

Abbreviations

- BET = Brunauer–Emmett–Teller
- E1 = Experiment 1
- E2 = Experiment 2

- LVDT = linear variable differential transformer
- P&A = plug and abandonment
- PC = pitch catch
- PE = pulse echo
- TIE = third interface echo
- TOC = total organic carbon

Symbols

- d = casing thickness, m
- E = signal strength, dB
- E_T = signal strength transmitted signal, dB
- f = frequency, Hz
- f_{\min} = frequency of group delay minimum, Hz
- L = travel length of Lamb wave in casing, m
- S_N = spectrum of normalization window
- S_P = spectrum of processing window
- Z = Impedance, MRayl
- α = attenuation rate, dB/m
- σ = circular frequency, rad/s
- τ = group delay, s
- τ_{\min} = group delay minimum, s
- $|\tau_{\min}|$ = group delay parameter, s
- v_p = compressional wave velocity, m/s
- φ = phase, rad

REFERENCES

- Brace, W., Walsh, J.B., and Frangos, W.T., 1968, Permeability of Granite Under High Pressure, *Journal of Geophysical Research*, **73**(6), 2225–2236. DOI: 10.1029/JB073i006p02225.
- Fjær, E., Holt, R.M., Raaen, A.M., and Horsrud, P., 2008, *Petroleum Related Rock Mechanics*, Developments in Petroleum Science, Volume 53, 2nd Edition, Elsevier, Amsterdam. ISBN: 9780444502605.
- Fjær, E., Stenebråten, J.F., and Bakheim, S., 2018, Laboratory Test for Studies on Shale Barrier Formation, Paper ARMA-2018-1146 presented at the 52nd US Rock Mechanics/Geomechanics Symposium, Seattle, Washington, USA, 17–20 June.
- Froelich, B., 2008, Multimode Evaluation of Cement Behind Steel Pipe, *The Journal of the Acoustical Society of America*, **123**(5), 3648. DOI: 10.1121/1.2934929.
- Gazis, D.C., 1959, Three-Dimensional Investigation of the Propagation of Waves in Hollow Circular Cylinders, I. Analytical Foundation, *The Journal of the Acoustical Society of America*, **31**(5), 568–573. DOI: 10.1121/1.1907753.
- Govil, A., Gardner, D., Obando, G., Beltran-Jimenez, K., and Skadsem, H., 2020, Validating Ultrasonic Log Response Against Reference Barrier Cells Simulating Downhole Well Conditions Encountered During Well Construction and

- Abandonment Operations, Paper SPE-199578 presented at the IADC/SPE International Drilling Conference and Exhibition, Galveston, Texas, USA, 3–5 March. DOI: 10.2118/199578-MS.
- Hayman, A., Hutin, R., and Wright, P., 1991, High-Resolution Cementation and Corrosion Imaging by Ultrasound, Paper KK, *Transactions, SPWLA 32nd Annual Logging Symposium*, Midland, Texas, USA, 16–19 June.
- Jutten, J., and Hayman, A., 1993, Microannulus Effect on Cementation Logs: Experiments and Case Histories, Paper SPE-25377 presented at the SPE Asia Pacific Oil and Gas Conference, Singapore, 8–10 February. DOI: 10.2118/25377-MS.
- Khalifeh, M., and Saasen, A., 2020, *Introduction to Permanent Plug and Abandonment of Wells*, Springer Nature.
- Klieber, C., Lemarenko, M., and Catheline, S., 2017, Effect of Microannuli on Ultrasonic Pulse-Echo Resonance and Flexural Lamb-Wave Cement-Evaluation Measurements, *Proceedings, Mtgs. Acoust.*, Acoustical Society of America.
- Lavery, D., Jambunathan, V., and Shafikova, G.M., 2019, Turning a Negative Into a Positive: Shale Annular Barrier Identification for Plug and Abandonment, Paper LL, *Transactions, SPWLA 60th Annual Logging Symposium*, The Woodlands, Texas, USA, 15–19 June. DOI: 10.30632/T60ALS-2019_LL.
- Li, J., and Rose, J.L., 2001, Excitation and Propagation of Non-Axisymmetric Guided Waves in a Hollow Cylinder, *The Journal of the Acoustical Society of America*, **109**(2), 457–464. DOI: 10.1121/1.1315290.
- Raaen, A.M., and Fjær, E., 2020, Pressure Testing of Barrier Integrity, Paper OMAE2020-18713 presented at the ASME 2020 39th International Conference on Ocean, Offshore and Arctic Engineering, virtually/online, 3–7 August. DOI: 10.1115/OMAE2020-18713.
- Schroeder, M.R., 1965, New Method of Measuring Reverberation Time, *The Journal of the Acoustical Society of America*, **37**(3), 409–412. DOI: 10.1121/1.1909343.
- Sirevaag, T., Johansen, T., Larsen, I., and Holt, R., 2018, Laboratory Setup for Improved Behind Casing, Paper I, *Transactions, SPWLA 59th Annual Logging Symposium*, London, UK, 2–6 June.
- Sirevaag, T., 2020, *A Study of the Ultrasonic Measurements for Logging Behind a Steel Pipe: Expanding the Processing to Improve the Differentiation Between Heavy Fluids and Light Solids*, PhD thesis, Norwegian University of Science and Technology (NTNU). URL: <https://ntnuopen.ntnu.no/ntnu-xmlui/handle/11250/2643395>. Accessed July 6, 2021.
- Sirevaag, T., Johansen, T.F., Larsen, I., and Holt, R.M., 2020, A Study of the Flexural Attenuation Technique Through Laboratory Measurements and Numerical Simulations, *Petrophysics*, **61**(4), 334–351. DOI: 10.30632/PJV61N4-2020a1.
- Thierry, S., Klieber, C., Lemarenko, M., Brill, T., Le Calvez, J.-L., Mege, F., Barrou, T., Lavrentiev, M., and Constable, K., 2017, Ultrasonic Cement Logging: Expanding the Operating Envelope and Efficiency, Paper WWW, *Transactions, SPWLA 58th Annual Logging Symposium*, Oklahoma City, Oklahoma, USA, 17–21 June.
- Vardoulakis, I., and Sulem, J., 1995, *Bifurcation Analysis in Geomechanics*, 1st Edition, CRC Press, London. DOI: 10.1201/9781482269383.
- Viggen, E.M., Johansen, T.F., and Merciu, I.-A., 2016a, Analysis of Outer-Casing Echoes in Simulations of Ultrasonic Pulse-Echo Through-Tubing Logging, *Geophysics*, **81**(6), D679–D685. DOI: 10.1190/geo2015-0376.1.
- Viggen, E.M., Johansen, T.F., and Merciu, I.-A., 2016b, Simulation and Modeling of Ultrasonic Pitch-Catch Through-Tubing Logging, *Geophysics*, **81**(4), D383–D393. DOI: 10.1190/geo2015-0251.1.
- Viggen, E.M., Johansen, T.F., and Merciu, I.-A., 2017, Simulation and Inversion of Ultrasonic Pitch-Catch Through-Tubing Well Logging With an Array of Receivers, *NDT & E International*, **85**, 72–75. DOI: 10.1016/j.ndteint.2016.10.008.
- Vrålstad, T., Saasen, A., Fjær, E., Øia, T., Ytrehus, J.D., and Khalifeh, M., 2019, Plug & Abandonment of Offshore Wells: Ensuring Long-Term Well Integrity and Cost-Efficiency, *Journal of Petroleum Science and Engineering*, **173**, 478–491. DOI: 10.1016/j.petrol.2018.10.049.
- Wang, H., Tao, G., and Shang, X., 2016, Understanding Acoustic Methods for Cement Bond Logging, *The Journal of the Acoustical Society of America*, **139**(5), 2407–2416. DOI: 10.1121/1.4947511.
- Williams, S., Carlsen, T., Constable, K., and Guldahl, A., 2009, Identification and Qualification of Shale Annular Barriers Using Wireline Logs During Plug and Abandonment Operations, Paper SPE-119321 presented at the SPE/IADC Drilling Conference and Exhibition, Amsterdam, The Netherlands, 17–19 March. DOI: 10.2118/119321-MS.

ABOUT THE AUTHORS

Anja Diez is a research scientist at SINTEF Digital Acoustics. She joined SINTEF in 2019, and her work focuses on ultrasonics, seismics, signal processing, and numerical simulations. Anja received a diploma in geophysics from the Karlsruhe Institute of Technology (KIT) in 2010 and a PhD (Dr. rer. nat.) from the KIT in 2013.

Tonni F. Johansen is a research scientist with SINTEF Digital Acoustics, which he joined in 2011. He was with the Ultrasound group at the Faculty of Medicine, NTNU, from 1998, where he holds a researcher position. His research interests include acoustics, ultrasonics, numerical simulation, signal processing, transducer design, and laboratory development. Tonni received his Siv.Ing. degree from the Department of Telecommunications at the

Norwegian University of Science and Technology (NTNU) in 1984, and a PhD degree from the same department in 1991.

Idar Larsen is a senior project manager at SINTEF Industry, Petroleum Department. He joined SINTEF in 1995 and has since worked on research projects in the Formation Physics group with a focus on rock physics and rock mechanics. Idar received a Cand.Scient degree in applied mathematics from the University of Tromsø in 1995.

Evaluating Petrophysical Properties and Volumetrics Uncertainties of Sand Injectite Reservoirs – Norwegian North Sea

Artur Kotwicki¹, Mirza Hassan Baig², Yngve Bolstad Johansen¹, Guro Leirdal¹, Brage Vikaune Aftret¹, Odd Arne Sandstad¹, Anne Mette Anthonsen¹, Bruis Gianotten², Tor Arne Hansen², and Mauro Firinu²

ABSTRACT

Sand injectites on the Norwegian Continental Shelf have proven their commercial significance. Some are already producing, e.g., Volund, Viper, Balder, Ringhorne, and Kobra Fields, while others such as in production licenses (PL) 340 and 869 have recently been discovered and appraised. Extensive literature on the geology of sand injectites has been published (e.g., Jenssen et al., 1993; Jolly and Lonergan, 2002; Huuse et al., 2003; Hurst et al., 2005). However, few references are available on the petrophysical and geophysical aspects of sand injectite reservoirs. This paper discusses the petrophysical properties of sand injectite facies, dykes, sills, and brecciated sands, along with their identification from seismic data. A perception that volumetrics of sand injectite reservoirs cannot be reliably evaluated is assessed.

Sand injectites in PL 340 and 869 were interpreted as remobilized sands from the Hermod and Heimdal Formations of Paleocene age injected into the overlying Balder Formation and Hordaland Group mudstones of Eocene age. The mudstones acted as a seal, forming an intrusive stratigraphic trap. The trap geometry varied locally depending upon the dyke and sill geometries of the sandstone. Dykes had large vertical reach with the corresponding high-hydrocarbon column, while sills had low-vertical relief with large lateral extent. Intervals of brecciated sands were also observed within the injectite complex, especially where sands were thin. These brecciated sands contained large amounts of angular mudstone clasts of different dimensions suspended in an overall sandy matrix. Close examination of cored dykes made it possible to observe this, while it might not be as obvious when looking at bulk well logs.

Petrophysical-log responses for clean sills and dykes behaved the same way as they would in a clean sandstone reservoir. If sills and dykes were very thin, they would also risk not being counted as net or pay (Suau et al., 1984;

Dromgoole et al., 2000; Flølo et al., 2000;). Such errors can impact in-place volumes in a significant way. Sills appeared as blocky clean sand on logs, but it was difficult to differentiate a dyke from a sill or thin sands using logs. Dykes are high-angle features and are identified either by core studies or borehole images when intersected by a well or, if large enough, observable on seismic. Brecciated sand intervals appeared with cm-to-dm-scale mudstone clasts suspended in sand with approximately 40 to 60% net to gross. Log responses over these intervals indicated shaly sand or thin sands. Resistivity and thermal neutron porosity logs were highly affected by the shale clasts. For this reason, a fractional net/gross interpretation technique was used to evaluate the sand content and hydrocarbon pore volume. To further verify these results, they were compared to observations directly on the core.

To qualify to what extent petrophysical logs and interpreted products thereof can be relied on to evaluate hydrocarbon volumes of sand injectite reservoirs, a high-resolution petrophysical interpretation was generated using a computerized tomography (CT) scanned core image. Core image sand counting and image-derived high-resolution bulk density logs with shale-corrected resistivity were used. Results of this high-resolution interpretation featured an excellent match with routine core analysis data and manual core observations in the core laboratory. The fractional net/gross method used is the modified Thomas-Stieber method (Johansen et al., 2018). Its results compared well to the high-resolution CT-scan image results and better evaluated the hydrocarbon pore volume of sand facie compared to the conventional bulk formation evaluation approach. This result confirms that the Thomas-Stieber method can be used for brecciated rocks, which leads to some useful recommendations on how to best log and perform a petrophysical evaluation in such reservoirs.

Manuscript received by the Editor February 9, 2021; manuscript accepted May 29, 2021.

¹Aker BP ASA, artur.kotwicki@akerbp.com; yngve.b.johansen@akerbp.com; guro.leirdal@akerbp.com; brage.vikaune.aftret@akerbp.com; odd.arne.sandstad@akerbp.com; anne.mettedanthonsen@akerbp.com

²Vår Energi AS, mirza.hassan@varenergi.no; bruks.gianotten@varenergi.no; tor.arne.hansen@varenergi.no; mauro.firinu@varenergi.no

INTRODUCTION

The Froskelår Main discovery is one of the three successes within the regionally large Frosk area injectite complex (Frosk, Froskelår Main, and Froskelår North-East). Injectites are created through post-depositional remobilization of fluidized sands injected into the surrounding stratigraphy (Huuse et al., 2003). The controlling mechanisms of clastic intrusions are further described by Jolly and Lonergan (2002) and are related to the buildup of overpressure in a sand, which exceeds the seal capacity of the host rock, generating fractures. This results in a large pressure differential in the sand body, which enables fluidization, allowing sand to flow with the overpressured fluid into the open fractures. The resulting injected sands in the forms of dykes, sills, or injection breccias can form excellent pay zones and typically improve reservoir connectivity. The separation between dykes and sills is done according to the injectites' cross-cutting relationships with bedding (Hurst and Cartwright, 2007), where dykes cut across stratigraphy at a high angle, whereas sills are parallel to subparallel to stratigraphy. In PL 340 and 869, the sand injection process typically enhanced reservoir properties, with average porosity of approximately 32% and permeabilities up to 10 Darcy.

In this paper, data from the Froskelår Main discovery are discussed. Three wells were drilled to test the Froskelår Main part of the injectite complex. The main bore aimed at a dyke that could be mapped directly on seismic. A technical sidetrack was drilled for coring the main reservoir interval at a distance less than 15 m from the main bore. This approach gave valuable information on reservoir variations within the scale of a typical geomodel grid cell. The log responses were different in the technical sidetrack than in the LWD-logged main bore over the reservoir section. The large-scale pattern was the same; rapid changes in injectite presence are not unexpected when comparing with observations from outcrops (Hurst et al., 2016). A geologic sidetrack was drilled to further improve the understanding of net reservoir presence in between the large seismically visible dykes and to test the possibility for a deeper oil-water contact in the north. This well provided useful insights into the ability to detect dykes on seismic.

GEOLOGICAL ASPECTS OF SAND INJECTITES

Sandstone intrusions, often termed sand injectites, show a wide range of orientations relative to the host rock

(Huuse et al., 2003), which are typically finely laminated mudstones. Sand injectites are of erosive nature, forming discordant contacts with surrounding strata. They display marked erosional characteristics along their boundaries and clear cross-cutting relationships. While many intrusions are structureless, some intrusions exhibit internal structures consistent with their emplacement processes, such as flow banding, alignment of clasts, and dewatering structures. Grain sizes within injectites are typically uniform; however, variation across individual intrusions and along the direction of fluidized sand flow has been observed.

The Froskelår Main technical sidetrack was drilled through a suite of different types of sand injectites: dykes, injection breccia, a few thin sills, and an extrudite. The thickest dykes are easy to detect from seismic data (Fig. 1), core, and outcrop, but thinner dykes are more difficult to find and predict. Injection breccia is easily detectable in core and outcrops but challenging to identify on seismic and sometimes even on logs. The most demanding to identify in seismic, core, and outcrop are extrudites. In addition, few outcrop analogs exist in literature. The upper part of the Froskelår Main core shows similar characteristics to extrudites seen in the Panoche Giant Injection Complex (PGIC) in California. The interpreted extrudite is a well-laminated and slightly bioturbated sandy to clay-rich deposit occurring above an injection breccia. This deposit may represent an extrusion of sand as the fluidized sands reaching the paleo seafloor (Hurst et al., 2006). A top injectite complex horizon has been interpreted in the Froskelår area (Fig. 1). This marks the interpreted upper boundary of the injectite complex. No sand injectites have been observed in wells above this event. One possible explanation is that this surface is close to the paleo seafloor, further supported by the interpreted extrudite in core at a similar depth.

The typical sandstone facies observed in the Froskelår Main well are as described below.

1. Structureless sandstone, mainly interpreted as dykes in core – These facies consist of fine-grained structureless sandstone lacking recognizable depositional sedimentary structures. Deformational structures are absent. Structureless sandstone frequently occurs throughout the core (Fig. 2).
2. Injection breccia – These facies consist of fine-grained structureless sandstone with angular mudstone clasts. The mudstone clasts are scattered within the sandstone matrix. Injection breccia is widely observed in the core (illustrated with two examples in Fig. 2).

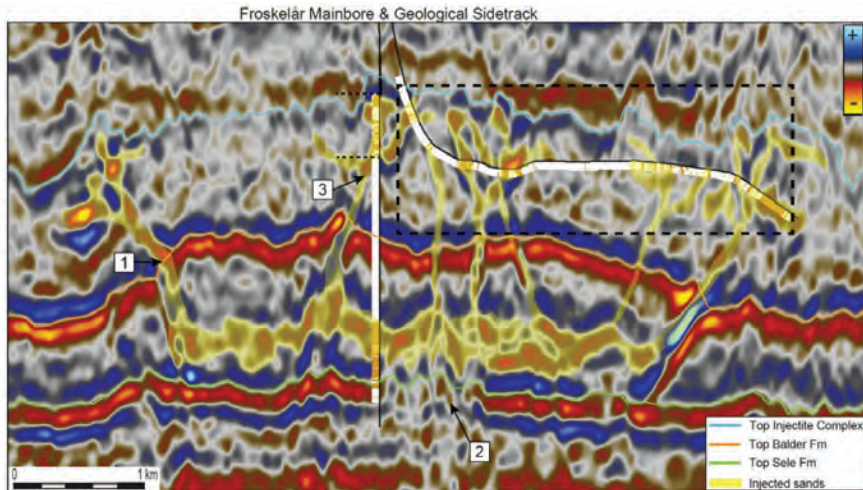


Fig. 1—Seismic section along Froskelår Main wells with interpretation. All wells are shown with reservoir flag logs from CPI (white is non-net; brown color is net). Some key features of the injectite complex: (1) Balder Formation jackup with wing-like dyke, (2) subtle dykes from depositional sands below, and (3) dyke intersected by main bore and technical sidetrack.

3. Laminated sandstone – These facies consist of fine-grained sandstone with subparallel laminae. Similar parallel structures are ascribed to large-scale consolidation laminae and dish structures (Plint, 1983). Such structures can be formed by the subhorizontal movement of high-viscosity fluidized sand. Two examples are illustrated in Fig. 2c1 and 2c2—the former showing an interpreted sill, and the latter displaying a sandstone with laminae interpreted as differential slip surfaces.

Bringing outcrop knowledge into the interpretation of core facies helps to understand the external geometry of the subsurface reservoir sandstone. A comparison of the Froskelår Main core with sandstone intrusion exposures from the PGIC in California has been carried out. One of the benefits of these outcrops is that geometric relationships between parent units and sand injections are well exposed. The study profited from independent work conducted by the Sand Injection Research Group (SIRG, based at the University of Aberdeen with collaborative partners at the University of Manchester and Wales). In Fig. 3, photos from three different outcrops in the PGIC show examples of a dyke with structureless sandstone, injection breccia, and laminated sandstone facies (sill), similar to the facies found in the Froskelår Main core.

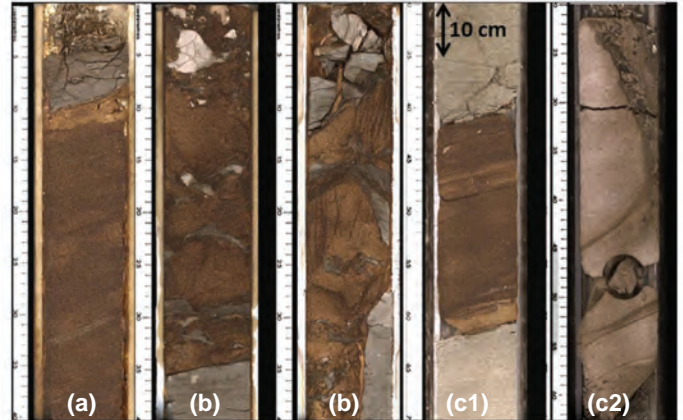


Fig. 2—Core photos with examples from different facies found in the Froskelår Main core: (a) structureless sandstone interpreted as dyke, (b) injection breccia, (c1) weakly laminated sandstone interpreted as sill, and (c2) laminated sandstone.

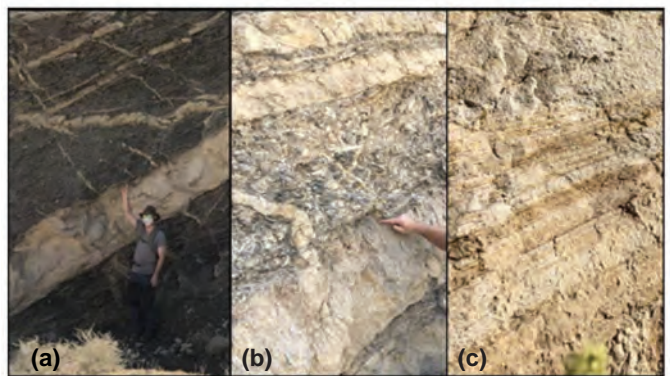


Fig. 3—Outcrops analog from the PGIC showing different facies found in the Froskelår Main core: (a) dyke with structureless sandstone, (b) injection breccia: the zone above the pointing finger, and (c) laminated sandstone, internal banding in a sandstone sill.

SAND INJECTITES PETROPHYSICS

In this section, petrophysical data from the technical sidetrack are discussed. Comprehensive and advanced formation evaluation logs (GR, neutron, density, triaxial resistivity, NMR, formation tester pressure, and sampling data) together with core data for comparison were available for this well. Petrophysical properties of sand injectite reservoirs are assessed with three different methods:

1. Conventional formation evaluation approach using the commonly used bulk deterministic method.
2. A high-resolution petrophysics using core CT-scan images and considered as a reference. Manual sand counting on physical cores was also performed to quality check software-processed results.
3. A modified Thomas-Stieber (Johansen et al., 2018) approach

Bulk Conventional Analysis

For bulk conventional analysis (BCA), gamma ray, resistivity, and neutron-density logs were used. Formation evaluation was performed using a deterministic approach where sand and wet-shale endpoints were picked on gamma ray and neutron-density logs. Total porosity ($PHIT$) was solved using neutron-density logs, and a shaly-sand saturation equation was used for total water saturation (S_{wt}). This interpretation approach determines the bulk rock properties. Effective porosity ($PHIE$) of the sand fraction was calculated as a supplement and described by Eq. 1.

$$PHIE = PHIT - V_{sh} * PHIT_{sh} \quad (1)$$

where V_{sh} is wet shale fraction, and $PHIT_{sh}$ is the shale total porosity whose endpoint was picked from the NMR porosity in the neighboring shale. V_{sh} was estimated from the density-neutron method in the oil zone and the average of density-neutron and gamma ray in the gas zone.

The permeability log was estimated using Herron's (1987) intrinsic permeability correlation (Eq. 2).

$$K = \left(A_f \frac{PHIT^3}{(1-PHIT)^2} \right)^{\sum B_i M_i} \quad (2)$$

where K is permeability, B_i and M_i are constants and weight fractions of each mineral, respectively, and A_f is the function of maximum feldspar content (which was not present or solved for in this formation).

Results of the conventional approach are shown in Fig. 4 and compared with routine core analysis data. To keep the discussion focused on characteristics of sand injectites, the interval is divided into brecciated gas sand, brecciated

oil sand, and clean dyke, though hydrocarbon saturation was also observed in some other intervals within thin sills/sand laminations. Sills are not specifically mentioned as they appeared as thin sands in this well and can be within the brecciated interval or between dykes, hence difficult to identify or differentiate from logs. Sills, if encountered, are expected to have excellent petrophysical properties as observed in dykes.

The following observations can be made from BCA results:

- Clean dykes presented excellent petrophysical properties. Shale content is very low; total and effective porosity are about the same, reaching 36 to 38%; total water saturation is less than 10%; permeability is greater than 1 Darcy, and grain density is 2.65 g/cc of clean quartz sand. Log-derived answers have a good match with core data.
- In the brecciated oil interval, log-derived $PHIT$ has a good match with core porosity (core plugs with slight bias to sand phase). Microporosity in shale/mudstone clasts is in the range of 26 to 28%. Porosity from the bulk density measurement (sensor size ~40 cm), when investigating both the sand phase and small-scale/large-scale shale/mudstone clasts, has produced a $PHIT$ curve showing a good comparison to the core. The match would not have been good if shale porosity was contrasting (e.g., 15 to 20%) from the sand. There is a poor match between log-derived permeability and grain density with core data. The reason for such disparities is mainly the low resolution of logs. Core plugs were regularly sampled and had little bias towards the sand phase. Only four core saturation plugs were available in this interval. Though the match looked acceptable, the mismatch of permeability and core grain density points towards the underestimation of sand content and $PHIE$ in this interval.
- The petrophysical findings for the brecciated gas interval are similar to the brecciated oil intervals. The porosity match is good because the shale clasts suspended in the sands have similar porosity. As mentioned for the brecciated oil section, this mitigates much of the porosity error one would have seen if the shale phase had, e.g., much lower porosity. But looking at the saturation, permeability, and grain density, one can see that the log-derived results are significantly off the core results.
- Looking at core petrophysical properties in brecciated intervals to those in dykes indicates that the sand properties in brecciated intervals, for the most part, have as good porosity, saturation, and permeability as the sands in the clean dykes/sills.

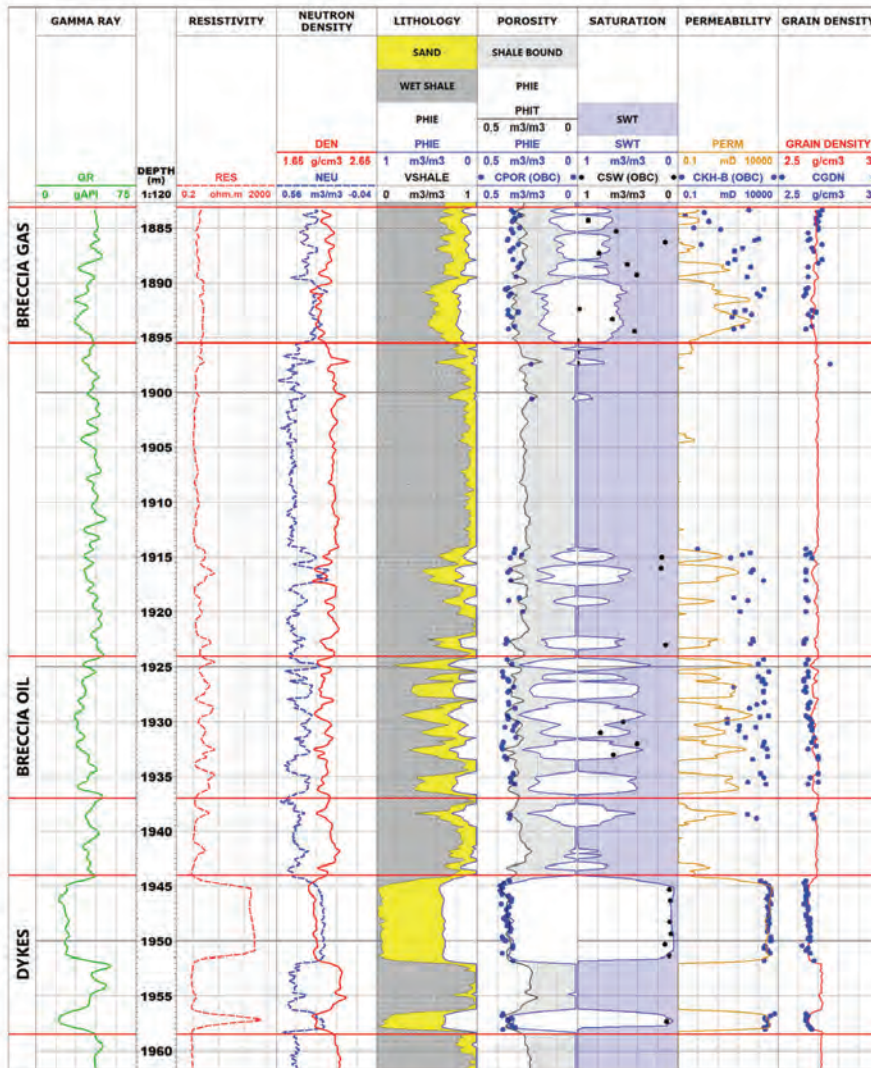


Fig. 4—Basic wireline logs and comparison of conventional formation-evaluation-derived porosity, saturation, permeability, and grain density with routine core analysis. Core data displayed are overburden corrected.

The core CT scan and ultraviolet (UV) fluorescence were examined to understand the disparity between logs and core in brecciated intervals. In Figs. 5 and 6, a significant presence of shale clast (light gray color on the CT scan) can be observed in the sands (dark gray color). Brecciated sand is the result of a network of small-scale injectites, which surrounds pieces of host rock and leaves them as floating disconnected clasts. The clasts are not expected to move

significantly from their origin. The porosity of the sand facies in brecciated intervals is very good. The presence of clasts originating from the non-net host rock has no adverse effect on sand properties. GR, neutron, and density logs will respond similarly to shaly sand, and formation resistivity will be suppressed by the conductive shales. An additional note to make is that it can be harder to spot good sands in the geometry of breccia than when distributed in the lamina.

In the brecciated gas interval, neutron-density logs are not only affected by high-shale content but also by the presence of gas. Resistivity is low and generally less than $5 \Omega\cdot m$. No fluorescence was observed on UV photos as gas vaporized when the core was pulled out to ambient atmospheric conditions. For the brecciated oil interval, shale clasts can be observed on both the CT scan and UV photos. CT-scan images shown are from whole unslabbed core, while

the UV photo is from the slabbed core. Hence, the presence of shale clast on the two images can have a slightly different appearance but corresponds to the same feature at the same depth. Heterogeneity of the brecciated interval, the presence of shale clast, and sand changes within a few inches. This sometimes has the potential to have different results between logged and cored formation.

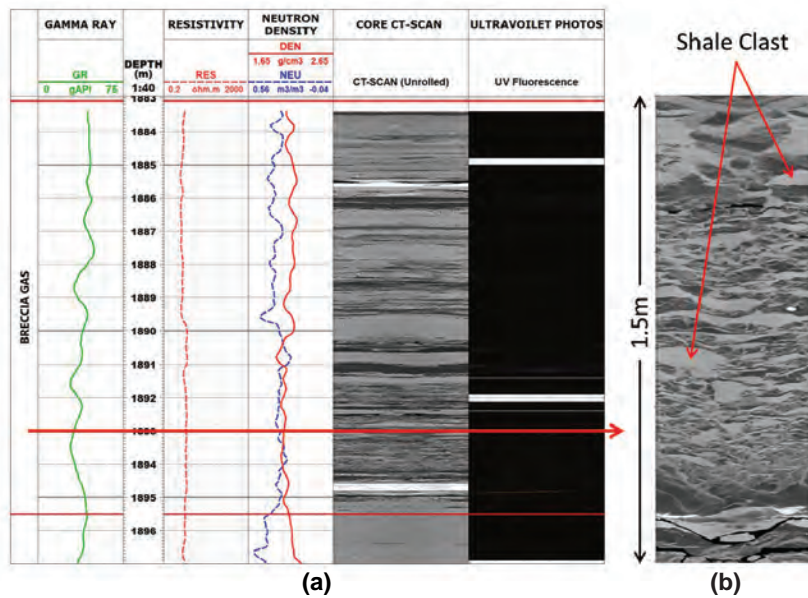


Fig. 5—Petrophysical log responses, core CT scan, and ultraviolet fluorescence photos in a brecciated gas interval. (b) The 1.5-m section magnifies CT image details from depth 1,893-m MD to 1,894.5-m MD.

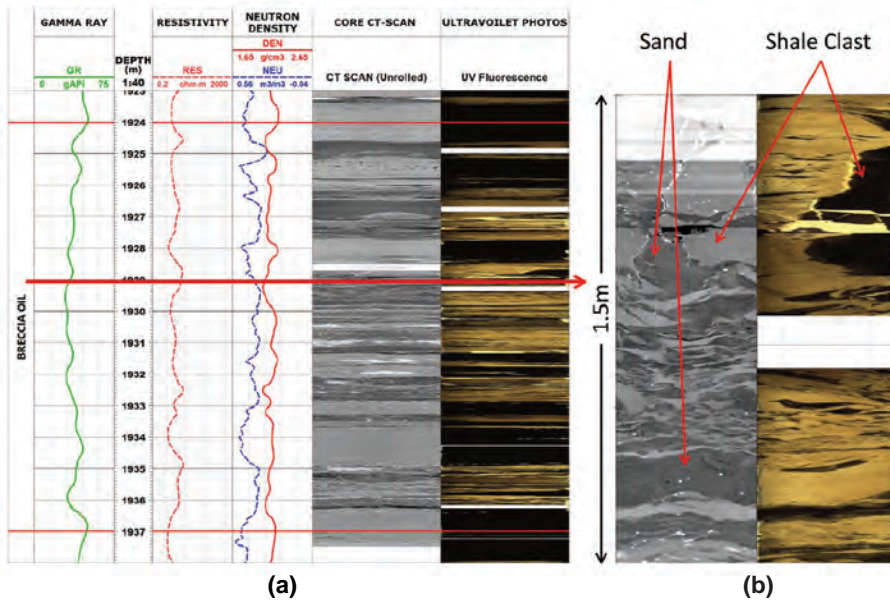


Fig. 6—Petrophysical log responses, core CT scan, and ultraviolet fluorescence photos in a brecciated oil interval. (b) The 1.5-m section magnifies CT and UV image details from depth 1929-m MD to 1930.5-m MD.

Dykes, as shown in Fig. 7, are clean sands. No shale clasts were observed on core images. It is interpreted as a low-angle dyke because of cross-cutting relation to the host rock bedding. Sills are expected to extend laterally with a low dip. Log responses in large clean dykes are like any other clean sand with bed boundary effects above and below.

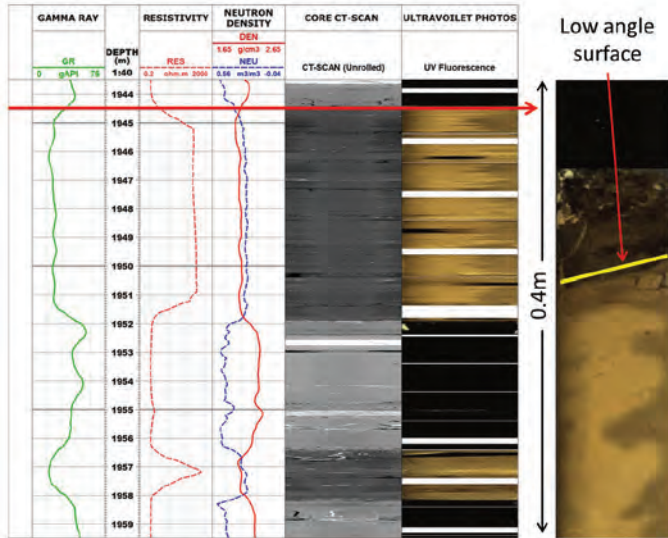


Fig. 7—Petrophysical logs, core CT scan, and ultraviolet fluorescence photos in dykes. Because of the low-angle surface and seismic indication, it is interpreted as a low-angle dyke. Support for this is found in triaxial resistivity dips data. Sills are expected to have a much lower dip.

High-Resolution Petrophysical Answers From Core CT-Scan Images

Sand Counting on Core CT Scan: To determine the correct (and high-resolution) sand content of the formation, sand counting was performed on core CT-scan images by using image analysis techniques on grayscale color intensity. Four bins were chosen to differentiate shale, sand, bright features, and bad data on the image, as shown in Fig. 8. The quality control of this technique is the comparison of the actual CT-scan image with the binned image, as shown in Fig. 9. The two images look identical by visual inspection. A similar quality control was applied on all CT scans in 1-m sections throughout the cored interval. CT-scan images were not corrected for dip effect because, unlike normal sedimentary deposition, injectite systems are remobilized sands through fractures and comprised of a mix of high-angle dykes, sills, and complex breccia where their presence and dips vary rapidly along the well. Dip correction can distort these features. At depths where the CT-scan image was bad, sand counting was determined from the UV image.

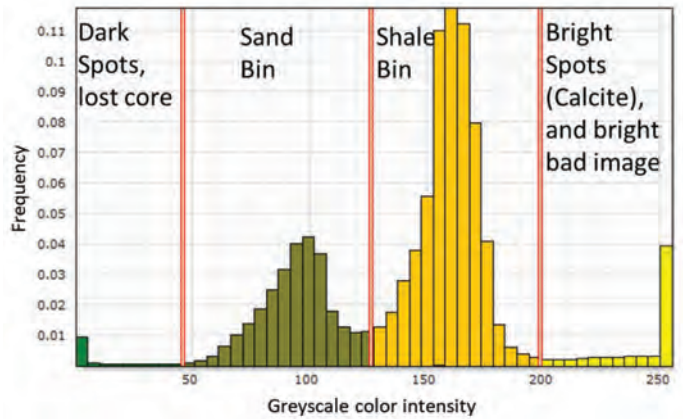


Fig. 8—Bin cutoffs on CT-scan grayscale color intensity to quantify formation contents as sand, shale, and special mineral (mainly calcite).

A manual sand count exercise was also conducted on physical cores to validate software-derived sand counting/identification. Details of this manual sand count exercise and its comparison with software-derived analysis are discussed in Appendix 2.

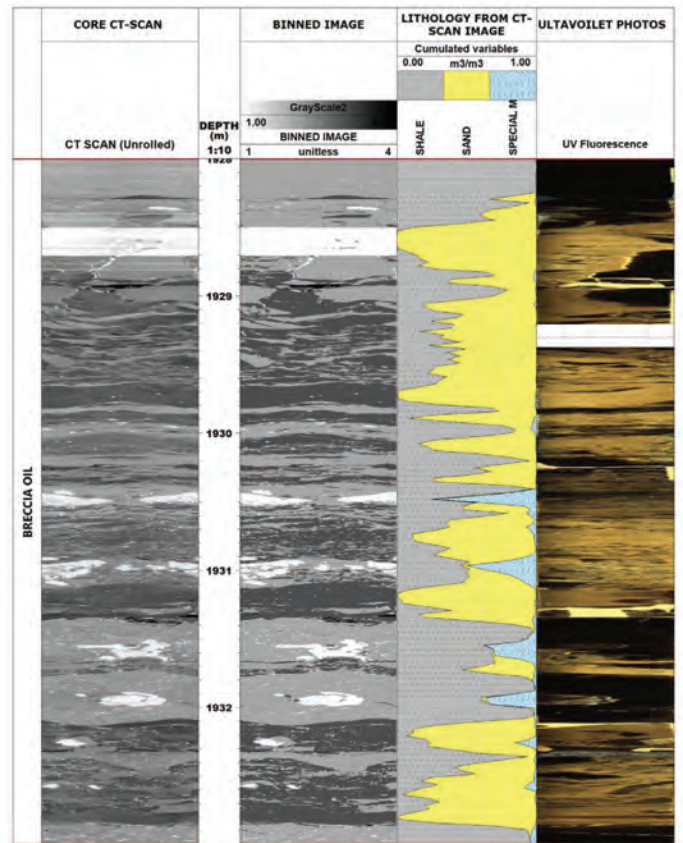


Fig. 9—Comparison of the binned image with the actual CT-scan image and the resulting lithology fractions as sand, shale, and special mineral (mainly calcite) side by side with core UV fluorescence image.

High-Resolution Logs: One of the objectives of this paper is to quantify/understand to what extent logs can underestimate volumetrics in a brecciated interval or in general in sand injectite reservoirs. To get a reference volumetrics assessment, a CT-scan image was calibrated to wireline logs to generate high-resolution density, neutron, and resistivity logs. An example of image calibration to logs is shown in Fig. 10. The density log to be calibrated is on the y-axis and calibrated against the core image's grayscale color intensity. These high-resolution logs were then used quantitatively in a CT-scan-based log analysis similar to bulk conventional analysis.

To validate the results of high-resolution logs, they were upscaled using a Gaussian filter of 0.5 m. These upscaled logs showed a good match to wireline logs, as shown in Fig. 11. For example, high-resolution density log comparison to wireline (WL) resolution on an x-y crossplot showed an R^2 value of 0.80. Resolution difference, lateral heterogeneity, and minor depth mismatch contribute to the delta between the two methods. Density-log calibration showed the best result. The resistivity calibration plot was of the poorest quality and implies that the CT-scan image is not that useful when trying to describe large-scale resistivity in a brecciated interval.

High-Resolution Petrophysics: The main objective of creating high-resolution (HR) logs from the CT-scan image was to derive a quantitative high-resolution petrophysical analysis that can determine the full hydrocarbon potential of sand injectite reservoirs, including the more complex parts not standing out easily at WL logs' resolution. There was

not a need to take into account the invasion and geometrical factor of the logs because wireline logs themselves with these inherent properties were used in the logs-to-image calibration step. This HR interpretation will serve as a reference while evaluating how much hydrocarbon volume (HVOL) has been underestimated with the BCA approach and if advanced laminated sand analysis (LSA) techniques like Thomas-Stieber are suitable to best evaluate the hydrocarbon potential of sand injectite reservoirs.

At this point, there are two ways to achieve high-resolution $PHIT$ and S_{wt} answers to use in a high-resolution HVOL computation. One way is to use HR logs as an input to a formation evaluation program; however, this approach was not implemented because the HR-calibrated resistivity log was not reliable for S_{wt} . In the alternate approach, one can apply F_{sd} (sand fraction), F_{sh} (shale fraction) from the CT-scan image directly to Eqs. 3 and 4 to get $PHIT$ and S_{wt} . Since sand and shale in the discussed injectite system are remarkably uniform in properties throughout the analyzed interval, the latter approach was used. Other than sand and shale, a third rock fraction (special mineral, $F_{sp,min}$, mainly calcite nodules) was also quantified from the CT-scan image. Its fraction was observed negligible in the reservoir intervals.

$$PHIT = PHIT_{Sand} * F_{sd} + PHIT_{Shale} * F_{sh} \quad (3)$$

$$S_{wt} = \frac{BVW_{Sand} * F_{sd} + BVW_{Shale} * F_{sh}}{PHIT} \quad (4)$$

$$CGDN = F_{sd} * RHOMA_{Sand} + F_{sh} * RHOMA_{Shale} \quad (5)$$

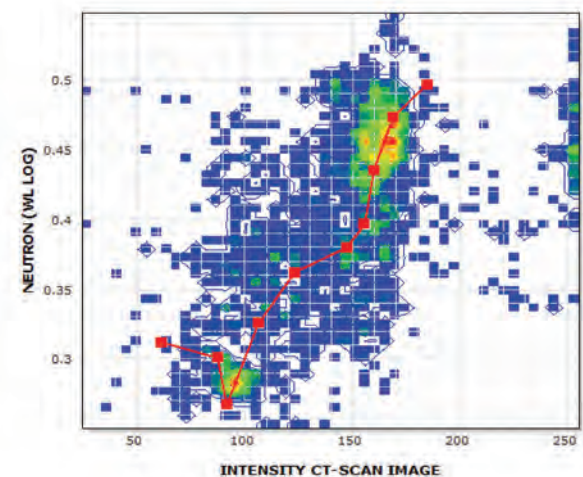
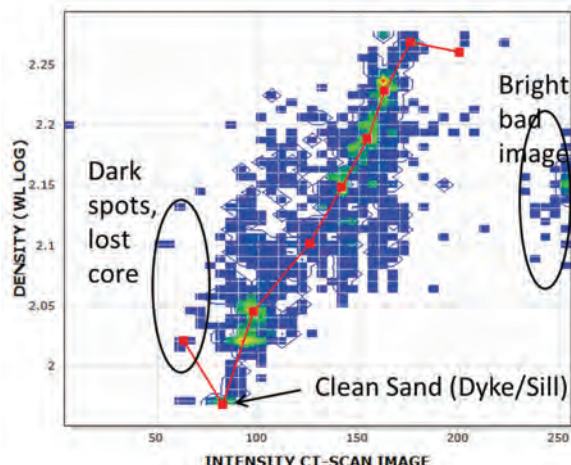


Fig. 10—(a) CT-scan image calibration to wireline density log for the whole injectite sand interval (from top of gas breccia to bottom of oil dyke). Data points' color based on data density. (b) CT-scan image calibration to wireline neutron log. Due to the nature of the CT-scan image being the color intensity, it can be used best to calibrate density log and does not remarkably correlate to other logs like neutron, gamma ray, and resistivity.

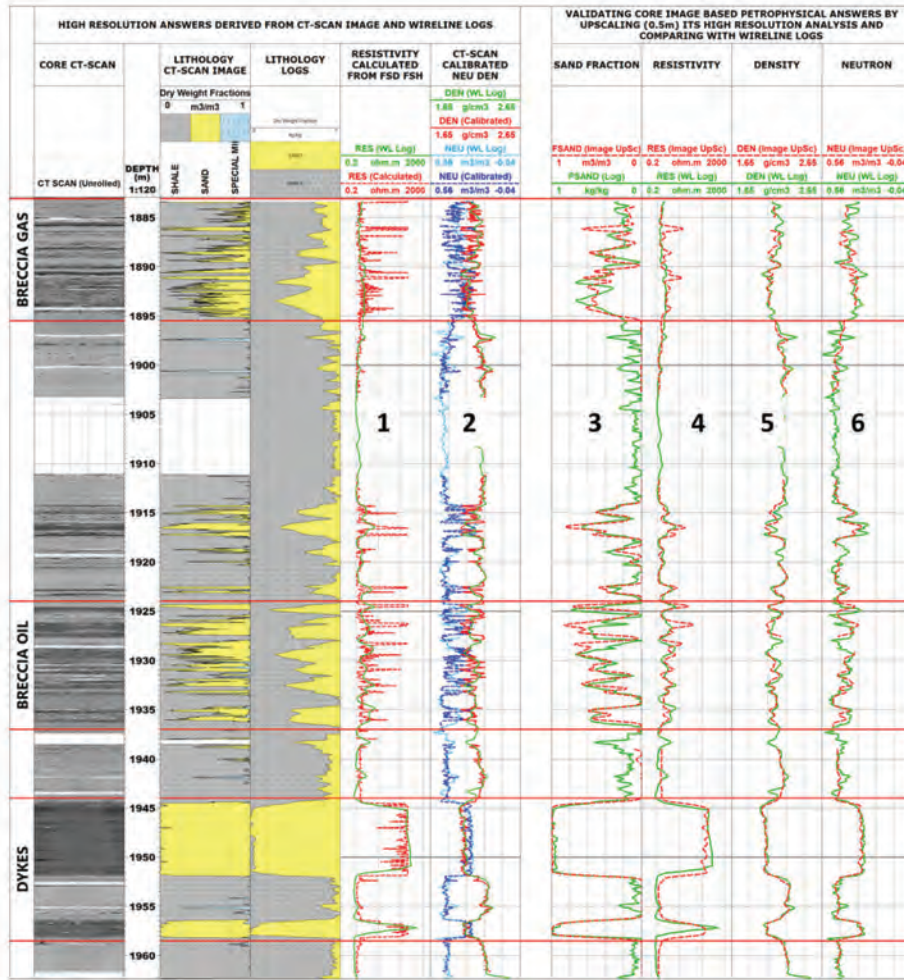


Fig. 11—CT-scan-image-calibrated, high-resolution, and upscaled logs compared to wireline (WL) logs. In Tracks 1 and 2, high-resolution logs are shown together with WL logs. Tracks 3 through 6 are upscaled logs in comparison to WL logs.

Sand properties were picked from clean dykes and set to the same value as used later in the Thomas-Stieber method. The sand phase present in the brecciated interval is the same as in the clean dykes/sills, and the input $PHIT_{Sand}$ (36 to 38%) is therefore representative for the entire interval. Shale properties were picked from the neighboring shales. Eq. 4 was used for the final saturation calculation. We picked the BVW_{Sand} value from the clean sand and used this value as a constant for the entire interval. These sands are at a significant height above the free-water level, and in multi-Darcy sand, the BVW has reached an asymptote value. Hence, we assumed to use a constant BVW value for the entire interval. The approach of using a constant value of BVW will not be appropriate if the sands are too close to the free-water level. The results of this approach were compared with petrophysical analysis if using HR logs of Fig. 11, which showed similar results.

Figure 12 shows the results from the CT-scan-image-based sand count and HR logs compared to routine core analysis. Petrophysical properties of porosity, water saturation, permeability, and grain density (Eq. 5) have a good match with routine core analysis data. Effective porosity ($PHIE$) using Eq. 1 in brecciated intervals is similar to $PHIT$ at many depths indicating that sand content is very high and of good quality. This is something that is not obvious when looking at BCA results derived directly from wireline logs (Fig. 4). The grain density match also indicates that the correct sand content of the formation in brecciated intervals is determined by using CT-scan images. As an additional quality control measure, the F_{sd} and F_{sh} were verified by manual sand count on the core (see Appendix 2). The high-resolution answers can be relied upon as a reference and close to the ground truth.

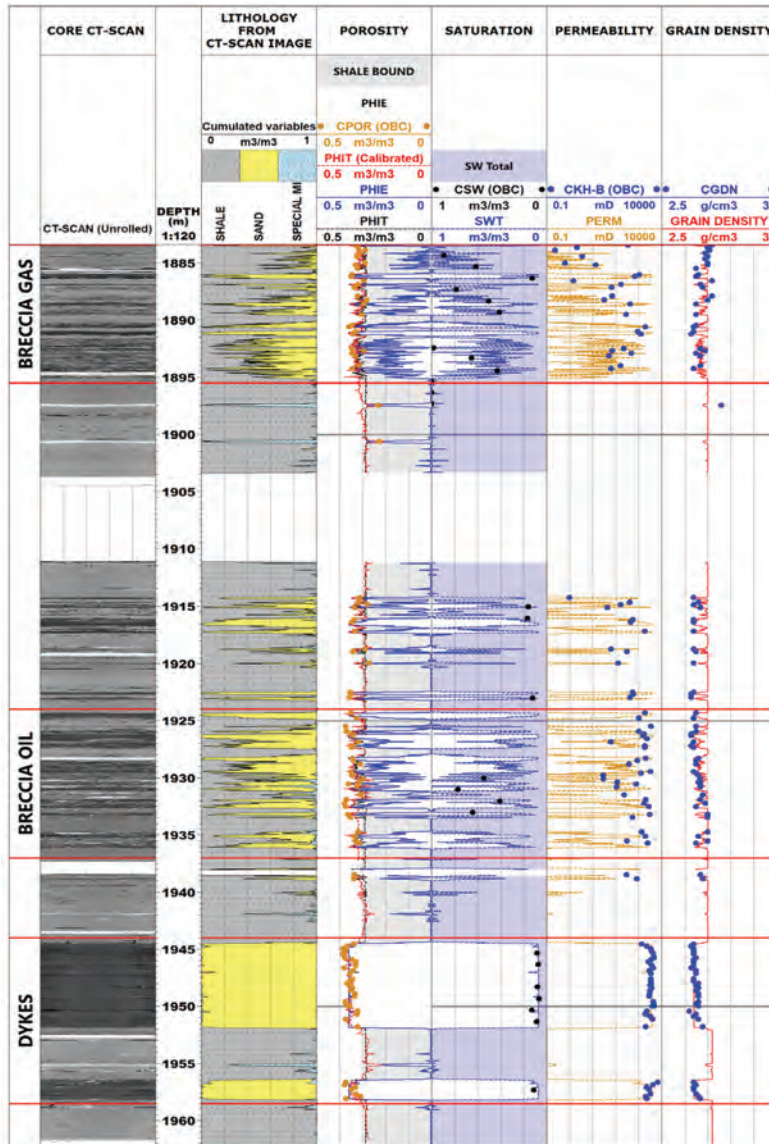


Fig. 12—High-resolution petrophysical answers from Eqs. 3 and 4 and CT-scan-derived F_{sh} and F_{sd} PHIT derived from the high-resolution logs of Fig. 12 is also displayed in the porosity track (red curve). It can be observed that it matches PHIT from Eq. 3. It also matches routine core analysis.

Modified Thomas-Stieber Analysis (Johansen et al., 2018)

Methodology. The workflow is a modified Thomas-Stieber (TS) used in Aker BP as described in Johansen et al. (2018). Input to this method is total porosity and V_{sh} . The outputs are sand fraction, sand porosity, and degree of dispersed shale in the sand. From these results, one can also derive net fraction, sand resistivity, and sand saturation. The original method was published in 1975 by E.C. Thomas and S.J. Stieber on how to estimate sand fraction and sand

porosity in a thinly bedded reservoir by use of laminous and porosity lines. In this case, the method was tested for sand injectite reservoirs. This is because the shale clasts and sand phase in brecciated intervals have their porosity preserved in much the same way as in a thin-bedded reservoir. The only difference being that sand laminas can have any orientation within the injectite brecciated interval, not necessarily being distributed in horizontal parallel laminas. In many of these injectites, the rock is so intensely laminated with sands in all directions that the rock looks like a sand suspension with

large shale clasts floating within. These clasts should still be considered as lamina by the TS protocol since these clasts replaced matrix and pore volume simultaneously, as would be the case for laminated shale. Shale clasts should, e.g., not be considered as structural shale as that is a distribution type that replaces matrix volume alone. Shale or clay replacement load-bearing matrix alone is rare to see in rocks on the Norwegian continental shelf. Dykes and sills can be thin beyond the log's resolution, where laminated sand analysis approaches like Thomas-Stieber become applicable. The method will work regardless of the direction of the sand laminae, and an assumption was made that shale clasts are not structural. Results from the analysis performed in great detail on core images and manual sand count performed on the core, as described in Appendix 2, were used as a reference and to validate the TS approach in the injectite sand shale systems (Fig. 13).

The method produces outputs such as the fraction of sand laminations that can be considered as net within the bulk volume measured (FNTG, fractional net to gross), total porosity within the sand ($\text{PHIT}_{\text{Sand}}$), dispersed shale volume in the sand (DISPERSIVENESS), and structural shale volume (STRUCTURALNESS). These are the outputs that follow as a consequence of this method by use of the inputs: porosity (PHIT) and shale volume (V_{sh}). $\text{PHIT}_{\text{Model}}$ is also produced, and that's $\text{PHIT}_{\text{Sand}}$ multiplied by FNTG. $\text{PHIT}_{\text{Model}}$ is typically produced in this workflow to be able to import a net-weighted pore volume into the geomodel for the use of geomodelers. In total porosity (PHIT), we calculate benefits from the TS method because sand total

water saturation ($S_{wt\text{Sand}}$) is upscaled to total water saturation (S_{wt}) and therefore gets improved fluid density. The same is also done for matrix density ($RHOMA$) as we upscale sand and shale matrix density ($RHOMA_{\text{Sand}}$ and $RHOMA_{\text{Shale}}$, respectively).

Interpretation. For water saturation in the sand ($S_{wt\text{Sand}}$), an inverted Poupon model was used to find $R_{ts\text{Sand}}$ (sand phase true resistivity) before calculating $S_{wt\text{Sand}}$ by using Archie saturation equation.

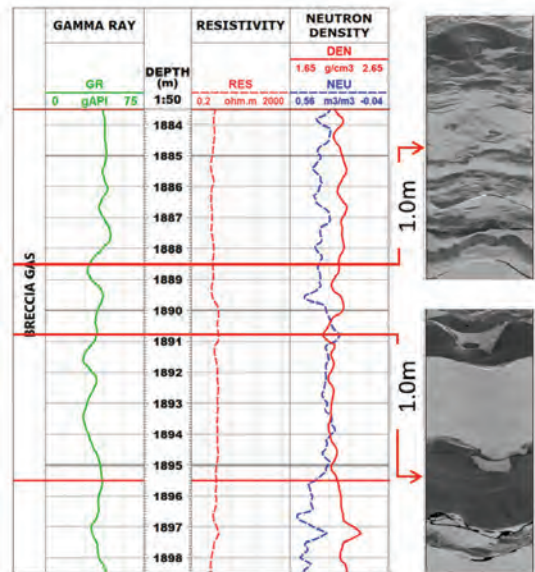


Fig.13—Comparison of WL density-neutron response vs. brecciated and clean injectite from core 3D CT scan (UNR), showing the inability of WL logs to reflect all injectite features due to resolution.

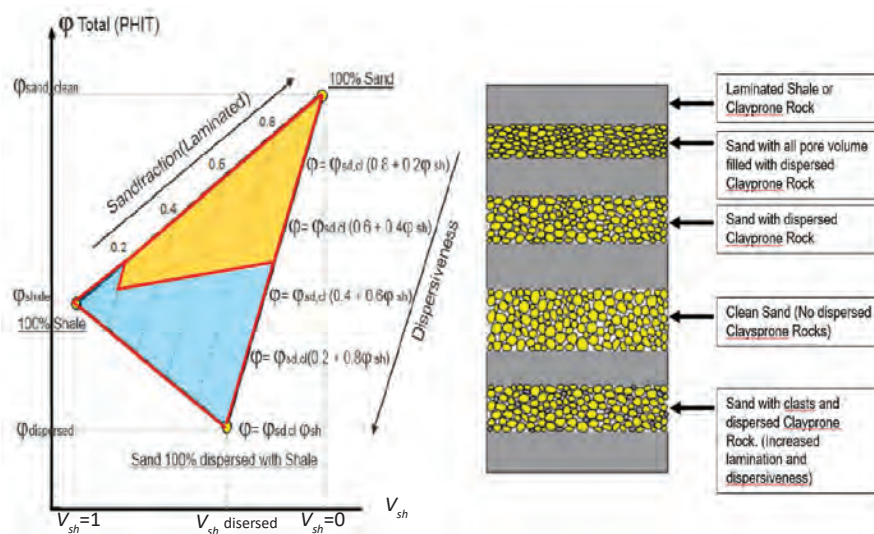


Fig. 14—Thomas-Stieber (TS) diagram for dispersed and laminated shale. The light gray lines springing out of the shale point in a fanlike shape are porosity lines. The light gray dashed lines parallel to the dispersion line are laminous lines. $\Phi_{\text{sand},\text{cl}}$ is the porosity of the cleanest possible sand ($V_{sh} = 0$). Φ_{shale} is porosity of 100% shale. $\Phi_{\text{dispersed}}$ is the total porosity of the sand with pores entirely filled with shale. The part of the TS diagram shaded in blue is considered as non-net (FNTG = 0). The part of the TS diagram colored orange is considered as net (FNTG = SANDFRAC).

On the TS crossplot (Fig. 15), the cleanest sand and shale points need to be established. The porosity of the cleanest sand is 36 to 38%. Unfortunately, no shale porosity was measured on the core as all shale plugs (collected offshore from the center of each core and preserved in mineral oil) got broken. However, regional shale porosity data points to a shale porosity ~27%. NMR data indicated the same shale porosity, and it was set to 27%. $PHIT_{Sand}$ was then calculated using Eq. 3.

Results of the TS model together with core data are shown in Fig. 16. A V_{sh} estimate from NMR is displayed in the lithology track (determined from Cao Minh and Sudararaman, 2006; Appendix 1). Improvement in hydrocarbon saturation was observed because, in the TS type laminated sand analysis approach, we are solving for petrophysical properties of the sand phase instead of the bulk rock. This is particularly applicable for sand injectites and breccias of PL 340 and 869, where porosity, saturation, and permeability within the sand phase (also around breccia) were observed as good as the intervals with 100% clean sand with no shale.

FNTG and V_{sh} curves, shown in the lithology track of Fig. 16, are about the same. This is due to sands (even in breccia intervals) being very clean with negligible dispersed shale fraction. In the interval 1,930- to 1,935-m MD, Dean-Stark plugs do not match S_{wtSand} from the TS method. These plugs have some of the shale breccia within the plug; hence, DS saturation is representative of S_{wt} rather than sand phase saturation S_{wtSand} .

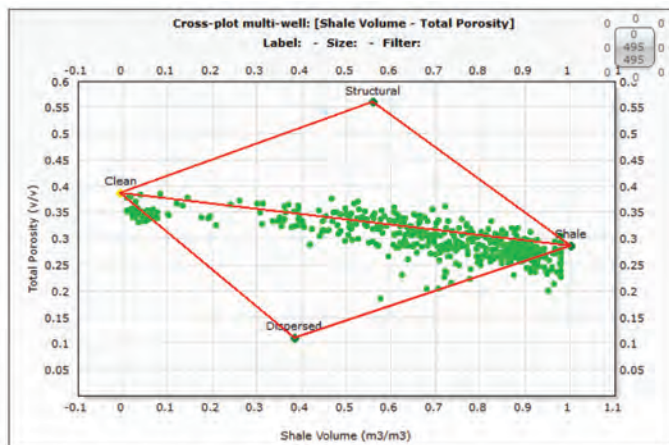


Fig. 15—Thomas-Stieber plot for the three intervals, brecciated and clean injectites. Clean sand and shale points are displayed.

VOLUMETRICS

Sand Counting

Sand counting can be a net-to-gross (NTG) indicator of the formation. We first looked at the optimum value of the F_{sd} cutoff (or V_{sh}), which gives the least percentage difference in net sand fraction between BCA and CT scan. As discussed in previous sections, CT scan, due to its high resolution, is used as a reference and is believed to provide sand estimates as close to reality as possible. Eq. 6 was used for sand counting. Figure 17 showed that the least percentage difference for brecciated intervals occurs in the F_{sd} range of 0.28 to 0.33. Thick dykes (also applicable to sills) being clean sands were observed insensitive to F_{sd} cutoffs. It implies $F_{sd} > 0.30$ (or $V_{sh} < 0.70$) is the best cutoff value that can be further used for sand count analysis from other available measurements. The same cutoff value will be used in the next section for net thickness and hydrocarbon volume height (HVOLH).

$$\text{Sand Count} = \sum F_{sd} * \Delta \text{Depth} \quad (6)$$

Other than conventional logs and CT-scan images, triaxial resistivity (R_h and R_v) and nuclear magnetic resonance (NMR) data were analyzed for sand counting. A sand fraction from NMR was determined from Cao Minh and Sudararaman (2006) and is discussed in Appendix 1. The Klein crossplot graphical technique (Cao Minh et al., 2008) was used to determine laminated sand-shale fraction from R_h and R_v resistivities. Wireline borehole image data were not logged. In Fig. 18, sand counting results from these methodologies (BCA, CT scan, NMR, and Klein plot) at $F_{sd} \geq 0.30$ cutoff are compared.

Sand counting between BCA and CT scan is comparable due to the reason explained in Fig. 17, where $F_{sd} > 0.30$ gave the least percentage difference between the two interpretations. A net fraction from NMR tends to bias towards a low-net fraction, especially in the brecciated gas interval. This is due to the lower-resolution bulk response of the NMR measurement and some uncertainty on its gas-corrected porosity. Modified Klein crossplot tends to bias towards high-net fraction and does not seem to resolve correct sand fraction in brecciated intervals. The result is presented, as this overestimation of sand from the Klein crossplot may be useful to identify brecciated intervals in sand injectite reservoirs when compared with other methods.

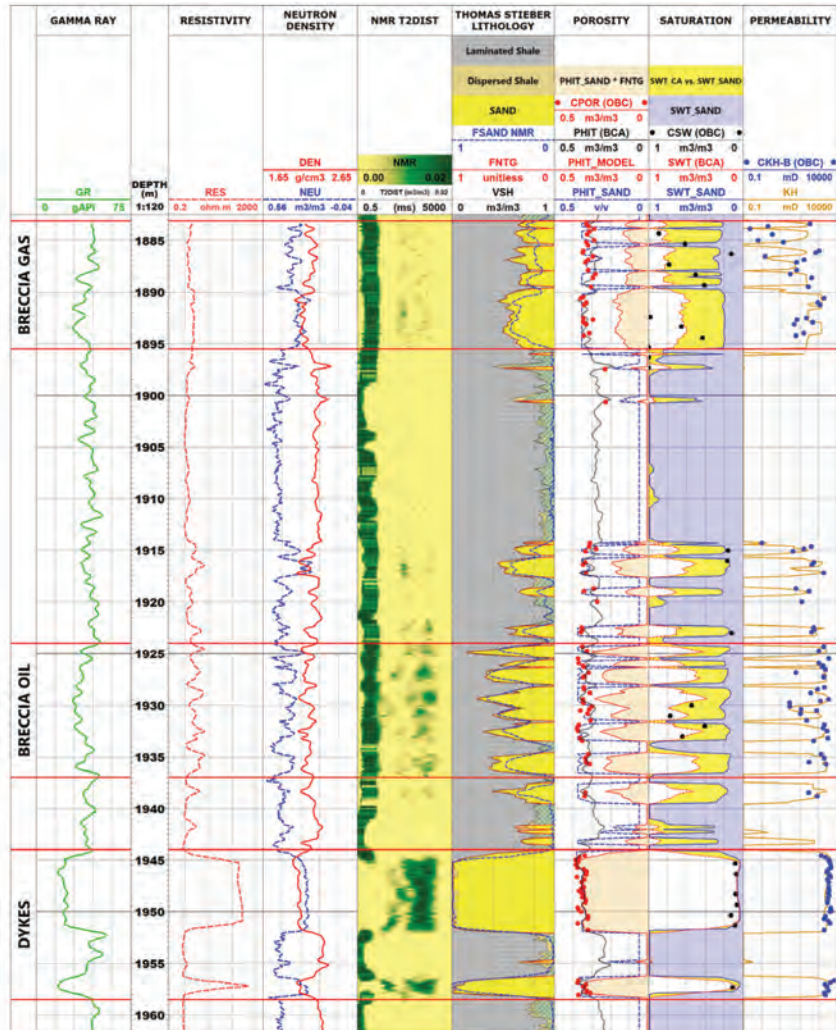


Fig. 16—Modified Thomas-Stieber (Johansen et al., 2018) derived formation evaluation results. Yellow shading in the saturation track showing the difference in water saturation of the bulk rock vs. saturation within the sand phase.

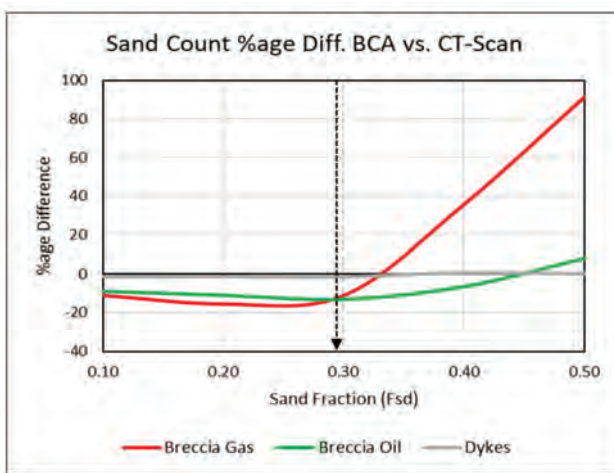


Fig. 17—The sand count percentage difference between BCA and CT scan. For sand count from BCA, $(1-V_{sh})$ curve was used, and for the CT scan, it was F_{sd} curve from the core CT-scan image.

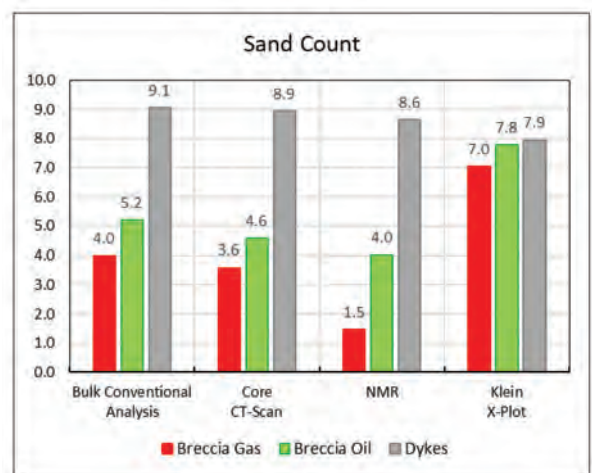


Fig. 18—Sand counting comparison from different logging and interpretation techniques at $F_{sd} \geq 0.30$ cutoff.

Petrophysical Summaries

To establish averaged petrophysical properties, net thickness, and hydrocarbon-volume-height (HVOLH), F_{sd} and S_{wt} cutoffs of 0.30 and 0.65, respectively, are used. Porosity in sand and shale is high; hence, $PHIT$ cutoff makes no difference unless in rare cemented clasts or stringers. The porosity cutoff was set at 0.15.

The BCA and CT-scan analysis discussed in this paper are both bulk methods. Their net thickness and HVOLH are calculated by using Eqs. 7 and 9. However, for the Thomas-Stieber (TS) type approach, which evaluates petrophysical properties of sand phase only, its net and HVOLH shall be calculated differently and as per Eqs. 8 and 10. Since the net is a fractional number at every depth for the TS method, the net thickness is the summation of the term FNTG (explained in Fig. 14). Reported petrophysical properties in Table 2 are arithmetic averages. Note that while averaged $PHIT$ and S_{wt} are reported for BCA and CT-scan analysis, $PHIT_{Sand}$ and S_{wtSand} properties in the sand phase are reported for the Thomas-Stieber method.

$$\text{Net (BCA \& CTScan)} = \sum \Delta \text{Depth} \quad (7)$$

$$\text{Net}_{TS} = \sum FNTG * \Delta \text{Depth} \quad (8)$$

$$\text{HVOLH (BCA \& CTScan)} = \sum (\text{Net} * PHIT * (1 - S_{wt})) \quad (9)$$

$$\text{HVOLH}_{TS} = \sum (\text{Net}_{TS} * PHIT_{Sand} * (1 - S_{wtSand})) \quad (10)$$

HVOLH for brecciated gas, brecciated oil, and dykes is shown in Fig. 19. The difference in HVOLH between the

three interpretation approaches is mainly due to S_{wt} (Table 2). Porosity would have contributed more to this difference if shale and sand porosity were at a higher contrast than in this case study.

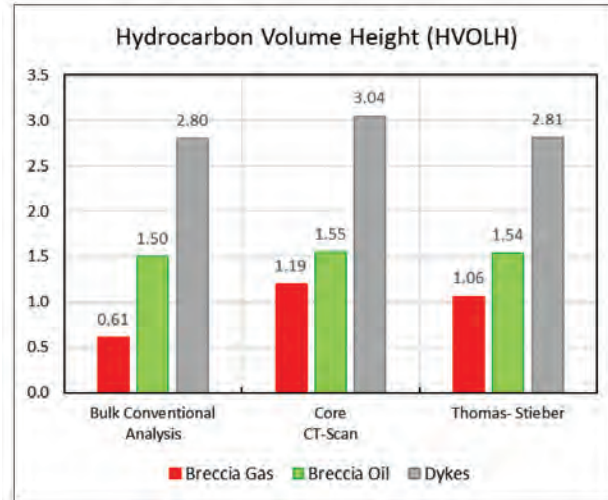


Fig. 19—Hydrocarbon pore volume thickness (HVOLH) comparison from different interpretation techniques ($F_{sd} \geq 0.30$, $S_{wt} \leq 0.65$, and $PHIT \geq 0.15$).

Table 1—Gross Thicknesses of the Intervals of Interest

Zones	Gross	
	m	frac
Breccia Gas	12.4	
Breccia Oil	13.0	
Dykes	14.5	

Table 2—Petrophysical Summaries From Conventional, CT-Scan Images, and Thomas-Stieber Analysis*

Conventional Analysis (BCA)					
Zones	Net Pay	HVOLH	PHIT	S_{wt}	F_{sd}^*
	m	m	frac	frac	frac
B. Gas	4.6	0.61	0.32	0.58	0.45
B. Oil	9.0	1.50	0.32	0.48	0.54
Dykes	8.8	2.80	0.35	0.10	0.93
Core CT-Scan-Derived Analysis					
Zones	Net Pay	HVOLH	PHIT	S_{wt}	F_{sd}
	m	m	frac	frac	frac
B. Gas	5.6	1.19	0.33	0.36	0.60
B. Oil	6.4	1.55	0.34	0.29	0.68
Dykes	9.3	3.04	0.36	0.08	0.97
Modified Thomas-Stieber Approach (Johansen et al., 2018)					
Zones	Net Pay*	HVOLH	$PHIT_{Sand}$	S_{wtSand}	F_{sd}
	m	m	frac	frac	frac
B. Gas	4.0	1.06	0.34	0.23	0.40
B. Oil	5.2	1.54	0.36	0.18	0.54
Dykes	8.5	2.81	0.35	0.07	0.93

*Uses cutoffs $F_{sd} \geq 0.30$, $S_{wt} \leq 0.65$ and $PHIT \geq 0.15$. F_{sd} for BCA is derived from $(1 - V_{sh})$. Net for TS is reported as per Eq. 8 accounting for sand content.

HVOLH from the TS method is very similar to the results from the CT scan. Looking at the net pay, it seems to be slightly pessimistic for brecciated intervals when compared to the CT-scan method. It is because, for bulk methods like BCA and CT scan, net thickness is the summation of depth intervals passing the cutoff (Eq. 7), but for TS, an additional term FNTG is multiplied, which in brecciated intervals is less than 1. Another thing to keep in mind is that the volume analyzed with BCA and TS methods is from the investigated volume in front of the logging tools' sensor. CT scan is based on the core; small differences due to lateral heterogeneity are expected, as explained in the geology section. This could also be a contributing factor.

In Table 3, the percentage difference in HVOLH from BCA and modified TS methods with reference to CT-scan-derived analysis is shown. V_{sh} cutoff of 0.50 is the rule of thumb cutoff for net reservoir properties when using a BCA method. For the sake of interest, Table 3 also demonstrates how this cutoff can underestimate HVOLH by up to 2 to 92% in brecciated intervals. The current case study demonstrated how more advanced data and more work put into setting of the V_{sh} cutoff, e.g., 0.70 for breccia ($F_{sd} \geq 0.30$), can reduce this error. The HVOLH difference from BCA reduced to 3 to 49% with improved cutoffs. With the modified Thomas-Stieber type of approach, the error is less than -11% regardless of the type of formation evaluated. Looking at the applicability of TS type approaches in such an environment, porosity and saturation of sand phase are comparable to CT-scan results, and it has shown better HVOLH over BCA.

RECOMMENDATIONS

This section discusses how to best reduce uncertainties in volumetrics and recommend logging technologies that can help with better petrophysical characterization of sand injectite reservoirs.

Recommendations on Net Thickness

Typically, in clastic reservoirs, shale cutoff values of 0.50 and less are used, but in sand injectites of PL 340 and 869, it was observed that V_{sh} values as high

as ~0.70 ($\sim F_{sd} \geq 0.30$) could be considered as an interval that can contribute to net. However, using V_{sh} cutoff 0.7 straightforward without any fractional consideration would get some false positive net and pay flagging.

Due to the nature of sand injectites encased in a shale, net to gross from well to well varies significantly. Demonstrated with a "generic sketch" in Fig. 20, Well 1 encountered breccia, sill and drilled along a dyke, with a different NTG than Well 2, which penetrated one single sill only. Well 3 was drilled as a horizontal well targeting a wider reservoir section as compared to vertical Wells 1 and 2, which is seen as important to understand reservoir NTG. It is suggested to use measured depths of gross and net thickness for NTG parameters instead of converting them to vertical depths and using a weighted average for mean NTG from drilled wells. The minimum and maximum range of NTG can be determined based on the results of the wells.

To determine true or understand better the NTG of sand injectites, it is advisable to drill several wells and to continually update NTG as weighted averages as data from new wells becomes available.

Recommendations on HVOLH

As observed in Table 3, HVOLH in brecciated intervals will be underestimated with BCA and its traditional cutoffs because porosity and saturation in the net are typically towards pessimistic values. CT-scan image, literature, and working experience suggest that it is a reasonable assumption to use the same values of porosity and saturation in brecciated intervals as of clean dykes/sills, or alternatively use advanced petrophysical interpretation techniques like modified Thomas-Stieber to determine petrophysical properties specific to sand phase.

The interpretation discussed in this paper has shown that conventionally determined averaged values can be taken as a minimum range of PHIT and $(1 - S_{wt})$. Petrophysical properties observed from clean sills/dykes define the maximum range of porosity and hydrocarbon saturation. It has been shown that advanced shaly-sand interpretation techniques like the modified Thomas-Stieber method are more fit to evaluate these complex nets.

Table 3—HVOLH Percentage Difference of Conventional and Thomas-Stieber Analysis as Compared to CT-Scan Image-Derived Analysis*

Zones	BCA @ $F_{sd} \geq 0.50$	BCA @ $F_{sd} \geq 0.30$	Thomas-Stieber @ $F_{sd} \geq 0.30$
Breccia Gas	-92	-49	-11
Breccia Oil	-22	-3	0
Dykes	-7	-8	-8

*For $F_{sd} \geq 0.30$ (and ≥ 0.50), $S_{wt} \leq 0.65$ and $PHIT \geq 0.15$. Negative numbers mean BCA and TS have underestimated HVOLH as compared to reference CT-scan analysis and vice versa.

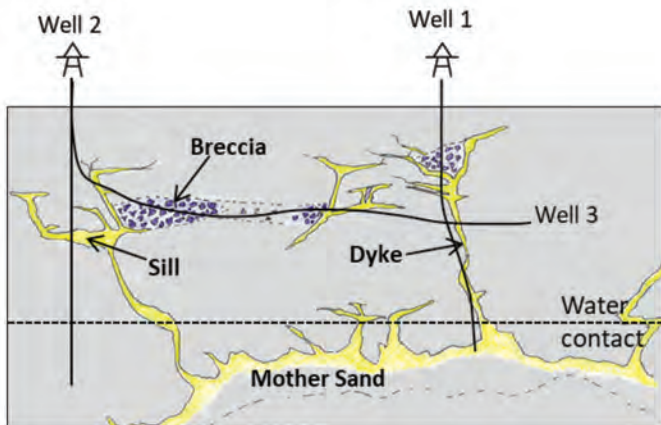


Fig. 20—A generic sketch showing the sand injectite system and NTG encountered by wells.

Recommendations on Logging

As shown in the current case study, basic petrophysical logs like gamma, resistivity, neutron, and density do respond to sand fractions within brecciated sands and in thin dykes and sills but within the limitation of their vertical resolution and sensitivity. When planning for the formation evaluation of injectites, it is recommended that high-resolution and high-accuracy logging equipment is used. For this reason, there can be extra value in logging wireline equipment. Also, we see great value in more advanced logging suites such as NMR; it identifies the presence of free fluids in apparently shaly brecciated sands and in thin dykes and sills. It is a bulk response and confirms the presence of producible fluids. It is also an independent source of sand counting and can provide useful insights into resistivity-independent saturation. Triaxial resistivity also seems to add value as the measurement enables us to assess R_v and R_h , which has the potential to increase the knowledge about actual resistivity in the sand phase (R_{Sand}). As briefly mentioned further up in the text, it also seems like the delta between the Klein plot predicted net and other logging technologies' predicted net can be a good indicator of the shale being distributed in brecciated clasts instead of thin-bed laminations. Core data and CT scans of core data also proved to be very useful for verifying and increasing log-based formation evaluation confidence. It is recommended that operators evaluating injectites and brecciated injectites acquire high-quality, dual-energy CT scans to be able to verify and increase confidence in the data set by the sand count procedures described in this paper.

SHORT NOTE ON GEOPHYSICAL CHARACTER OF SAND INJECTITES

The seismic expression of injectites is dependent on numerous factors (e.g., acquisition direction, dip, porosity, thickness) and requires careful interpretation to avoid pitfalls in the delineation of the trap geometry. In addition, focusing on improved seismic imaging of injectites in processing can significantly impact the ability to map injectite complexes with confidence. The first step in detecting injectites on seismic is recognizing the geometric relationship with the surrounding host strata. Huuse et al. (2003) describe two major classes of such geometries: cross-cutting, wing-like reflections and conical discordant amplitude anomalies. The former of these classes is typically associated with the edges of steep-sided mounds (Jenssen et al., 1993; Huuse et al., 2004; Wild and Briedis, 2010). Another important characteristic of sand injection is the presence of a jackup structure, as described by Hurst et al. (2016), readily observable in the Frosk area injectite complex.

The injectites, which are resolvable on seismic, are important as well targets in exploration and production. However, the nonresolvable injectites can constitute a substantial part of the volume of an injectite complex (Huuse et al., 2004; Grippa et al., 2019) and improve reservoir connectivity (Hurst and Cartwright, 2007; Grippa et al., 2019). Having a good understanding of the geological concept and understanding the limits of seismic data are crucial for a robust interpretation. In this context, relevant outcrop analogs can be of great importance to get an optimal subsurface definition (Hurst et al., 2016).

The PL 340 and 869 injectite complex is recognized by a significant jackup of the top Balder Formation marker horizon on seismic (Fig. 21). This feature is caused by a lower sill, which is injected into the lower part of the Balder Formation with a thickness up to 90 m observed in wells. Below this level, subtle breaks are observed on seismic interpreted as high-angle dykes linking the depositional sands to the injectite complex above.

All around the edge of the Balder jackup, large-scale dykes set up wing-like reflections that can be tracked from the lower sill up into the Hordaland Group shales (Fig. 21). In addition, numerous dykes are observed within the Balder jackup area, like the ones intersected by the Froskelår wells. The roots of these dykes, linking them to the lower sill, can, in cases, be inconspicuous, likely a result of a high dip. Subtle breaks are visible on seismic, indicating the presence

of a discordant feature. Following the trends of these features and coupling them with amplitudes observed above, dykes can be interpreted with confidence. In places, the top part of the interpreted dykes displays decreasing dip on seismic, partly explaining the improved detectability.

The interval of interest described in the petrophysical evaluation discussed in previous sections and shown in Fig. 21 is the reservoir section of the coring sidetrack. The well targeted the same interpreted dyke as was drilled in the main bore. This dyke can be interpreted down into the intra Balder sill below and up to the interpreted top of the injectite complex, where these discordant features terminate. Slightly below where the well intersects the dyke, it appears to bifurcate on seismic, splitting into two separate, high-dip angle, low-impedance bodies. Without considering possible well mispositioning, most of the reservoir section drilled through the interpreted westernmost branch of the bifurcated dyke and close to the bifurcation point towards the bottom of the reservoir section. The complexity observed at the log scale is not well reflected in the seismic response. Within a seismic amplitude of similar character, great formation variability was observed, ranging from massive clean sands in the lower part (oil leg) to brecciated sands in the upper part (gas cap). This suggests that it is difficult to separate clean dykes and sills from injection breccia on seismic alone.

Even with the high-quality seismic data available for mapping the PL 340 and 869 injectite complex, there are

sands that fall below seismic detectability. This is evident when comparing the reservoir flag logs in the Froskelår wells with the seismic responses in Fig. 21. The amplitude-based interpretation would greatly underestimate the net sand fraction within the injectite complex. One data set which is available to try to bridge the gap between log and seismic-based interpretation is ultradeep resistivity data, shown in Fig. 21. This data can, in parts, be tied directly to the amplitude-based seismic interpretation. Other parts provide some significance to the subseismic sands indicated by the reservoir flag logs, attempting to resolve sand geometries some distance away from the wellbore.

CONCLUSIONS

- HVOLH in brecciated intervals and in thin dykes and sills was underestimated using traditional V_{sh} cutoff in an approach based on bulk conventional analysis. This is primarily due to the low resolution of the logs and resistivity data getting suppressed by conductive shales and shale clast, hence overestimating water saturation. The current case study showed that an F_{sd} cutoff of 0.50 and S_{wt} cutoff of 0.65 could return an HVOLH 90% too low for the most complex interval. This number was improved to ~50% with improved cutoffs.
- Advanced interpretation techniques like Thomas-Stieber and laminated sand analysis determine petrophysical properties of the sand phase only. It improved HVOLH and matched better the HVOLH result derived directly from the core. The similarity in estimated petrophysical properties and HVOLH supports that the modified Thomas-Stieber method is also suitable for use on brecciated sand shale systems.
- Petrophysical properties in brecciated intervals and in thin dykes and sills were observed of as good quality as in thick sills/dykes with total porosity of 36 to 38%, water saturation less than 10%, and permeability in the Darcy range. This observation makes laminated sand analysis techniques like Thomas-Stieber applicable in sand injectite reservoirs, as such techniques focus on properties of sand facie only within a bulk rock.
- Based on volumes (HVOLH) shown in this paper, brecciated intervals and thin dykes/sills can be significant contributors to volumetrics. Unfortunately, it is not always observable on seismic.
- Integration of all logging technologies is key to defining sand content and hydrocarbon potential. They should complement each other within their limitations of vertical resolution, physics, and

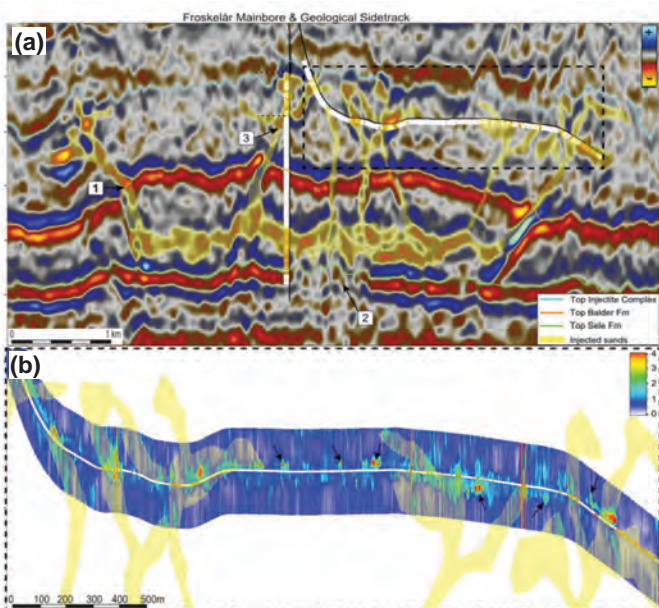


Fig. 21—Ultradeep resistivity inversion along Froskelår geological sidetrack with seismic interpretation. The section outline is shown as a stippled black box in (a). Black arrows indicate near-wellbore sands not captured in seismic interpretation.

interpretation techniques. It is important that all techniques show some indication of sand or hydrocarbon potential at a given depth. Over or underestimation from the various techniques should be understood and adequately dealt with in the final interpretation.

ACKNOWLEDGMENTS

The authors wish to thank Aker BP ASA and their partners (Vår Energi AS and Lundin Energy Norway) for the permission to publish this work. We would also like to acknowledge the contribution of Federica Colombo (senior petrophysicist, ENI/Vår Energi) for her technical help in the manual sand count exercise on physical cores and to the anonymous reviewers and their feedback.

NOMENCLATURE

Abbreviations

BCA	= bulk conventional analysis
CA	= conventional analysis
CGDN	= core grain density
CPI	= computer-processed interpretation
CPOR	= core porosity
CSW	= core Dean-Stark saturation
CT	= computerized tomography
DISPERSIVENESS	= dispersed shale volume in the sand
DMRP	= density magnetic resonance porosity
FNTG	= fractional net to gross
GDN	= grain density
GR	= gamma ray
HCPVT	= hydrocarbon pore volume thickness
HI	= hydrogen index
HR	= high resolution
HVOLH	= hydrocarbon volume height
NCP	= net confining stress or pressure
NMR	= nuclear magnetic resonance
NTG	= net to gross
OBC	= overburden corrected
PGIC	= Panoche Giant Injection Complex
PL	= production license
RCA	= routine core analysis
SCAL	= special core analysis
STRUCTURALNESS	= structural shale volume
TS	= modified Thomas-Stieber analysis
UNR	= unrolled CT scan
WL	= wireline

Symbols

A_f	= function of maximum feldspar content
B_i	= constant for each mineral
BVW_{Sand}	= bulk volume water in sand
BVW_{Shale}	= bulk volume water in shale
F_{sd}/F_{Sand}	= sand fraction
F_{sd-NMR}	= sand fraction from NMR
F_{sh}	= shale fraction
$F_{sp,min}$	= fraction of special mineral
K	= permeability
M_i	= weight fraction for each mineral
$PHIE$	= effective porosity
$PHIT$	= total porosity
$PHIT_{Sand}$	= total porosity of sand facie
$PHIT_{Shale}$	= shale total porosity
$PHIT_{Model}$	= PHIT_Sand multiplied by FNTG
R_h	= horizontal resistivity, parallel to bedding
$RHOMA_{Sand}$	= sand matrix density
$RHOMA_{Shale}$	= shale matrix density
R_{iSand}	= resistivity of sand facie
R_v	= vertical resistivity, perpendicular to bedding
S_{wt}	= total water saturation
S_{wtSand}	= total water saturation of sand facie
V_{sh}	= wet shale volume
$\phi_{dispersed}$	= total porosity of the sand with pores entirely filled with shale
ϕ_{sand_cl}	= porosity of the cleanest sand
ϕ_{shale}	= porosity of 100% shale
$\phi_{sp,min}$	= porosity of special mineral
ϕ_{Total}	= total porosity

REFERENCES

- Cao Minh, C., and Sudararaman, P., 2006, NMR Petrophysics in Thin Sand/Shale Laminations, Paper SPE-102435 presented at the SPE Annual Technical Conference and Exhibition, San Antonio, Texas, USA, 24–27 September. DOI: 10.2118/102435-MS.
- Cao Minh, C., Clavaud, J.P., Sundararaman, P., Froment, S., Caroli, E., Billon, O., Davis, G., and Fairbairn, R., 2008, Graphical Analysis of Laminated Sand-Shale Formations in the Presence of Anisotropic Shale, Paper SPWLA v49n5a1, *Petrophysics*, **49**(5), 395–405.
- Dromgoole, P., Bowman M., Leonard, A., Weimer, P., and Slatt, R.M., 2000, Developing and Managing Turbidite Reservoirs – Case Histories and Experiences, Results of the 1998 EAGE/AAPG Research Conference, *Petroleum Geosciences*, **6**(2), 97–105. DOI: 10.1144/petgeo.6.2.97.

- Flølo, L.H., Kjærefjord, J.M., Arnesen, D.M., Menard, W.P., and Weissenburger, K.W., 2000, Revealing the Petrophysical Properties of a Thin Bedded Rock in a Norwegian Sea Reservoir With Logs, Core, and Miniperm Data, Paper SPE-64273, *SPE Reservoir Evaluation & Engineering*, **3**(3), 249–255. DOI: 10.2118/64273-PA.
- Grippa, A., Hurst, A., Palladino, G., Iacopini, D., Lecomte, I., and Huuse, M., 2019, Seismic Imaging of Complex Geometry: Forward Modeling of Sandstone Intrusions, *Earth and Planetary Science Letters*, **513**, 51–63. DOI: 10.1016/j.epsl.2019.02.011.
- Herron, M., 1987, Estimating the Intrinsic Permeability of Clastic Sediments From Geochemical Data, Paper HH, *Transactions, SPWLA 28th Annual Logging Symposium*, London, England, 29 June–2 July.
- Hurst, A., Cartwright, J.A., Duranti, D., Huuse M., and Nelson M., 2005, Sand Injectites: An Emerging Global Play in Deep-Water Clastic Environments, *Petroleum Geology*, **6**, 133–144. DOI: 10.1144/0060133.
- Hurst, A., Cartwright, J.A., Huuse, M., and Duranti, D., 2006, Extrusive Sandstones (Extrudites): A New Class of Stratigraphic Trap?, in Allen, M.R., Goffrey, G.P., Morgan, R.K., and Walker, I.M., editors, *The Deliberate Search for the Stratigraphic Trap*, Geological Society, London, Special Publications, **254**, 289–300. DOI: 10.1144/GSL.SP.2006.254.01.15.
- Hurst, A., and Cartwright, J., 2007, Sand Injectites: Implications for Hydrocarbon Exploration and Production, *AAPG Memoir* **87**, 1–19. DOI: 10.1306/M871209.
- Hurst, A., Huuse, M., Duranti, D., Vigorito, M., Jameson, E., and Schwab, A., 2016, Application of Outcrop Analogues in Successful Exploration of a Sand Injection Complex, Volund Field, Norwegian North Sea, in Bowman, M., Smyth, H.R., Good, T.R., Passey, S.R., Hirst, J.P.P., and Jordan, C.J., editors, *The Value of Outcrop Studies in Reducing Subsurface Uncertainty and Risk in Hydrocarbon Exploration and Production*, Geological Society, London, Special Publications, **436**, 75–92. DOI: 10.1144/SP436.3.
- Huuse, M., Duranti, D., Groves, S., Guargena, C., Prat, P., Holm, K., Steinsland, N., Cronin, B.T., Hurst, A., and Cartwright, J.A., 2003, Sandstone Intrusions: Detection and Significance for Exploration and Production, *First Break*, **21**(9), 15–24. DOI: 10.3997/1365-2397.2003014.
- Huuse, M., Duranti, D., Steinsland, N., Guargena, C.G., Prat, P., Holm, K., Cartwright, J.A., and Hurst, A., 2004, Seismic Characteristics of Large-Scale Sandstone Intrusions in the Paleogene of the South Viking Graben, UK and Norwegian North Sea, in Davies, R.J., Cartwright, J.A., Stewart, S.A., Lappin, M., and Underhill, J.R., editors, *3D Seismic Technology: Application to the Exploration of Sedimentary Basins*, Geological Society, London, Memoirs, **29**, 263–277. DOI: 10.1144/GSL.MEM.2004.029.01.25.
- Jenssen, A.I., Bergslien, D., Rye-Larsen, M., and Lindholm R.M., 1993, Origin of Complex Mound Geometry of Paleocene Submarine-Fan Sandstone Reservoirs, Balder Field, Norway, in Parker, J.R., editor, *Petroleum Geology of Northwest Europe: Proceedings of the 4th Conference*, Petroleum Geology Conference Series, **4**, 135–143. DOI: 10.1144/0040135.
- Johansen, Y., Christoffersen, K., Chatterjee, A., Elfenbein, C., Olsborg, L., Kvilaas, G., Baig, M.H., Datir, H., Bachman, N., Kausik, R., and Hurlmann, M., 2018, Use of Advanced Wireline Logs to Reduce Uncertainties in a Complex Reservoir: A Case Study From the Ivar Aasen Oilfield in the Norwegian Central North Sea, Paper N, *Transactions, SPWLA 59th Annual Logging Symposium*, London, United Kingdom, 2–6 June.
- Jolly, R.H., and Lonergan, I., 2002, Mechanisms and Controls on the Formation of Sand Intrusions, *Journal of the Geological Society*, **159**(5), 605–617. DOI: 10.1144/0016-764902-025.
- Plint, A.G., 1983, Liquefaction, Fluidization and Erosional Structures Associated With Bituminous Sands of the Bracklesham Formation (Middle Eocene) of Dorset, England, *Sedimentology*, **30**(4), 525–535. DOI: 10.1111/j.1365-3091.1983.tb00690.x.
- Saua, J., Albertelli, L., Cigni, M., and Gragnani, U., 1984, Interpretation of Very Thin Gas Sands in Italy, Paper A, *Transactions, SPWLA 25th Annual Logging Symposium*, New Orleans, Louisiana, USA, 10–13 June.

APPENDIX 1: SAND FRACTION FROM NMR

A sand fraction from NMR was determined using the methodology explained in Cao Minh and Sudararaman (2006). It states, in the presence of sand/shale laminae as shown in the middle (Fig. A1.1), the tool will measure “linearly” and cumulatively all signals. Since shales generally have shorter T_2 than sands, the T_2 distribution will exhibit the characteristic bimodal distribution as seen in the leftmost picture. The important point is that the NMR response is independent of the lamination distribution and geometry, i.e., two or three shale layers joined together will give the same bimodal T_2 distribution as long as their total volumetric fraction does not change.

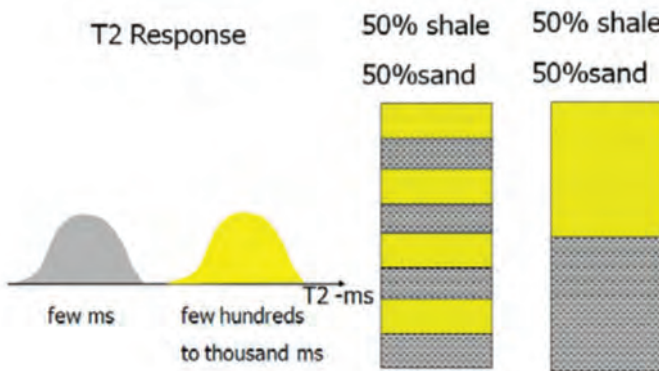


Fig. A1.1—NMR bimodal T_2 distribution in a laminated shale-sand sequence.

Such bimodal T_2 distribution response was clearly observed in brecciated intervals of the well presented in this paper. Knowing the sand porosity from the clean sill or dyke (i.e., 0.38 p.u.), F_{sd} was determined using the equation below. A shale bin porosity cutoff of 5 ms was picked at the rightmost edge of early T_2 , as shown in Fig. A1.2. NMR porosity was corrected for gas effect (DMRP). For comparison, V_{sh} from conventional analysis (CA) is also displayed.

$$F_{sd_NMR} = \frac{(DMRP - Shale_Bin_Porosity)}{Porosity_Clean_Sand}$$

Significant NMR porosity under call in shale intervals above and below the main injectite sands was observed, creating challenges in interpreting NMR porosity and F_{Sand} . Highlighted with blue arrows, it was found that these intervals show anomalous magnetometer response indicating possible ferromagnetic elements (pyrite) according to mudlog. However, x-ray diffraction (XRD) done on SCAL plugs show only traces of this element in sands. NMR measurement from another vendor in the neighboring field had also shown the same anomalous behavior in shales.

APPENDIX 2: MANUAL SAND COUNTING ON PHYSICAL CORES

To confirm the volume of sand delivered from 3D CT scans, it was decided to do manual sand counting on the core (B slab). Two teams were involved and performed visual sand counting with slightly different approaches. One team focused on rock fabric/grain size, while the other did

sand counting based on color, rock texture, grain size, and looking at the areal distribution of sand levels and/or shale clasts per 10 cm of core length. Due to time constraints, it was not possible to examine all cores, but the most critical gas-bearing interval was examined by both groups. Results are displayed in Figs. A2.1 to A2.3. At the end, the average manual sand counting log was estimated for the parts where results from both groups overlapped. Where the overlap was missing, the final curve was filled with data directly from the group that examined the given interval.

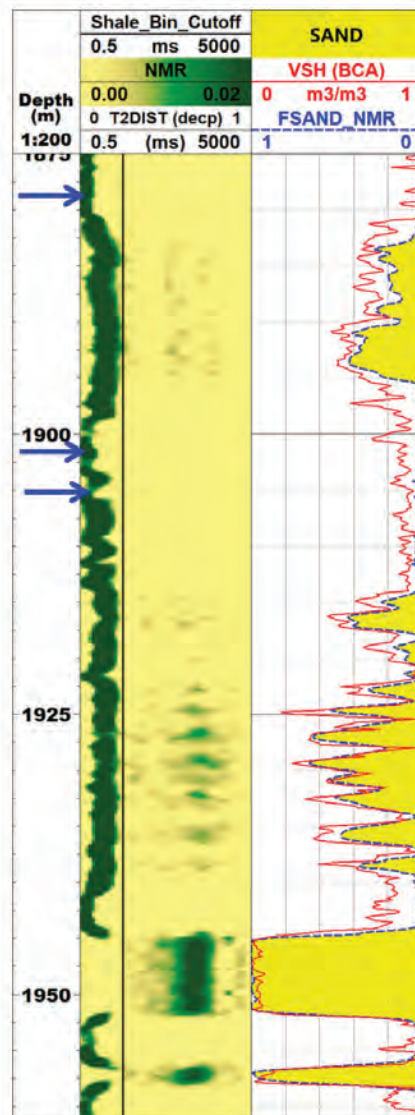


Fig. A1.2—Sand fraction from NMR and its comparison with bulk conventional analysis V_{sh} .

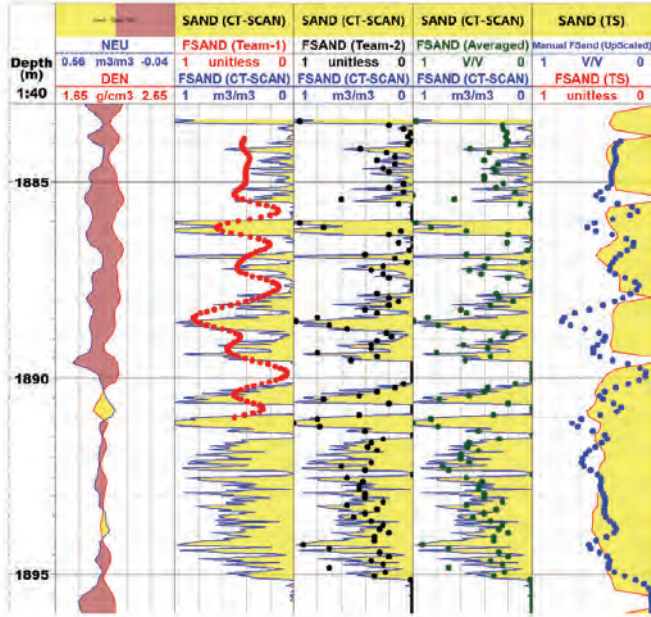


Fig. A2.1—Manual sand counting in the brecciated gas interval. Track 3: Team-1 manual sand counting, red dotted curve. Track 4: Team-2 black dotted curve. Track 5: averaged results (where both teams overlap). Track 6: (blue dotted curve), spliced and upscaled manual sand counting of two teams and its comparison with fractional net to gross (FNTG) from modified Thomas-Stieber analysis.

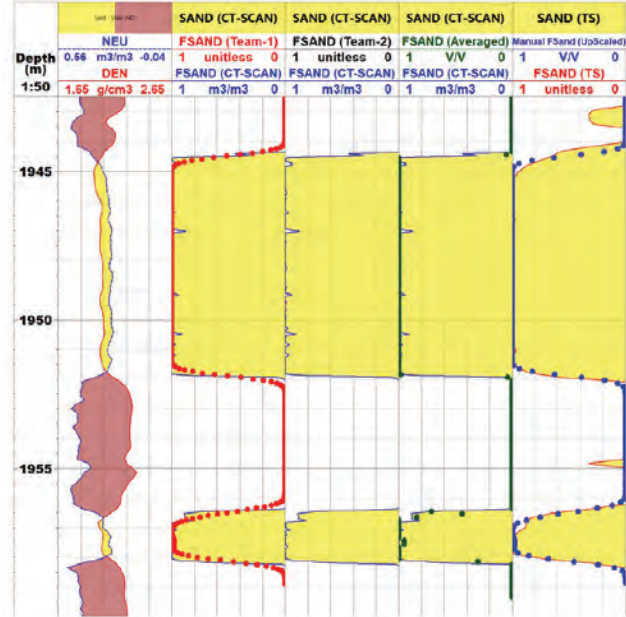


Fig. A2.3—Manual sand counting in clean oil intervals (dykes). Track 3: Team-1 manual sand counting, red dotted curve. Track 4: Team-2 black dotted curve. Track 5: averaged results (where both teams overlap). Track 6: (blue dotted curve), spliced and upscaled manual sand counting of two teams and its comparison with fractional net to gross (FNTG) from modified Thomas-Stieber analysis.

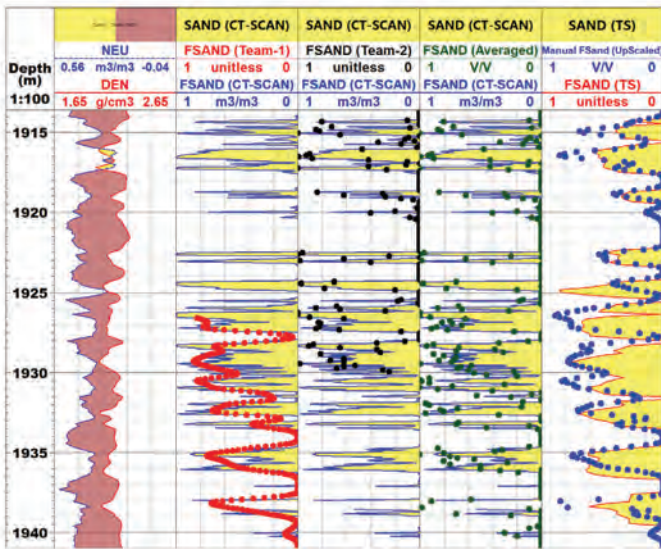


Fig. A2.2—Manual sand counting in brecciated oil interval. Track 3: Team-1 manual sand counting, red dotted curve. Track 4: Team-2 black dotted curve. Track 5: averaged results (where both teams overlap). Track 6: (blue dotted curve), spliced and upscaled manual sand counting of two teams and its comparison with fractional net to gross (FNTG) from modified Thomas-Stieber analysis.

Figure A2.4 shows an example of intervals where the biggest disparities occurred between the team's interpretation.

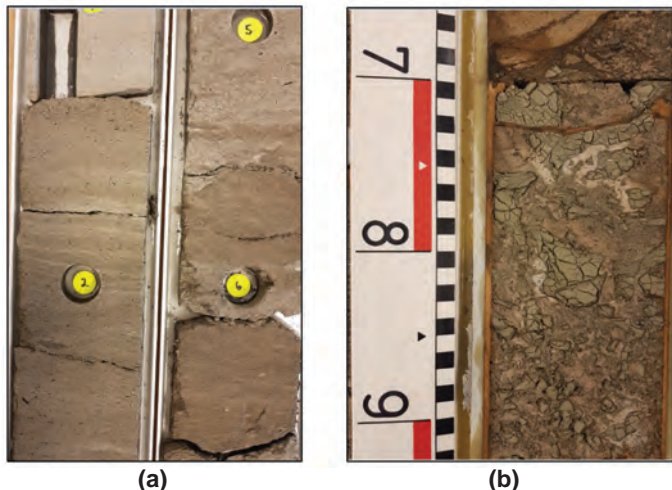


Fig. A2.4—Example of core from the (a) shallow gas zone and (b) brecciated oil; both made the manual sand counting difficult due to the (a) texture of the rock or (b) level of breccia present.

ABOUT THE AUTHORS

Artur Kotwicki is a senior petrophysicist at Aker BP. He started at the Oil and Gas Institute in Poland as a petrophysicist and later worked as a seismologist in the Institute of Geophysics Polish Academy of Sciences. From 2008, Kotwicki continued working as a petrophysicist in Norway with different assets in North Energy ASA, then Marathon Oil, Det Norske Oilselskap, and finally Aker BP.

Mirza Hassan Baig is a senior petrophysics advisor at Vår Energi AS. He started his professional career in 2005 at Pakistan Oilfields Limited as a reservoir engineer. In 2008, Baig joined Schlumberger as a petrophysicist, and in 2021, he moved to work for Vår Energi. Baig has a master's degree in petroleum engineering and has experience working in Asia, Africa, and Europe. His areas of interest are formation evaluation of clastic reservoirs and multidomain data integration.

Yngve Bolstad Johansen is the chief petrophysicist for Aker BP. He received a Cand.Scient. degree in physics from NTNU, Norway (2000). He joined Schlumberger in 2001 as a field engineer and worked with data acquisition in the Middle East and the North Sea before starting as a logging tool physicist at the Houston Formation Evaluation Center in 2005. In 2009, he began as principal petrophysicist for Statoil in field development and later R&D. From 2013, Johansen has been leading petrophysics within Aker BP.

Guro Leirdal is a senior geologist who has been working for Aker BP/Det Norske Oljeselskap/Pertra since 2007. From 1997 to 2007, she worked for Norsk Hydro ASA. Leirdal has experience from both the North Sea and the Norwegian Sea, and with both license and regional work. She holds a Cand.Scient degree in sedimentology from the University of Oslo.

Brage Vikaune Aftret is a senior geologist at Aker BP. Aftret holds a master's degree in petroleum geophysics from the Norwegian University of Science and Technology. Aftret began his career in 2013 as a geoscientist in the production department of ExxonMobil, working a suite of both operated and non-operated licenses, mainly in the North Sea. In 2019, Aftret started in Aker BP as part of the greater Alvheim area exploration team.

Odd Arne Sandstad is a lead geophysicist at Aker BP. Sandstad holds a master's degree in petroleum geophysics from the Norwegian University of Science and Technology. Sandstad began his career in 2007 as a geophysicist in Pertra, which transferred into Det Norske and then Aker BP.

Anne Mette Anthonsen is a senior exploration geophysicist at Aker BP. Anthonsen holds a master's degree in petroleum geophysics from the Norwegian University of Science and Technology. Anthonsen began her career in Det Norske Oljeselskap ASA in 2009 as a geophysicist in the exploration department. Her focus is to identify, evaluate, and mature prospects through license and regional work. Anthonsen joined the greater Alvheim area exploration team in 2015.

Bruis Gianotten is a senior geologist who has been working for Vår Energi/Point Resources/Core Energy since 2013. He started his working career in 2001 at Norsk Hydro. Gianotten has experience from the Norwegian Continental Shelf, the Middle East, and the Americas. He holds an MSc degree in structural geology from the Amsterdam Free University.

Tor Arne Hansen is a geoscientist for Vår Energi, which he joined via Point Resources and Spike Exploration in 2012. He started working the NCS for Esso Norge as a seismic interpreter in 1993 and holds a Cand.Scient degree in sedimentology from the University of Tromsø. He has spent 10 years exploring in Libya, Angola, and Brazil for Statoil. His area of interest is prospect evaluation and integration of geology and geophysics.

Mauro Firinu graduated in geology and mining engineering from Royal School G. Aspronri (Italy) and has 30+ years of experience in the oil and gas industry. He served operational geology and petrophysical activities for ENI in several countries (Europe, North and West Africa, Asia, the US, Australia). Firinu is an author of several technical papers and was recognized for a Distinguished Contribution to Petroleum Engineering Formation Evaluation by SPE (June 2013). He is currently coordinating the operations geology and petrophysical activities for Vår Energi in Stavanger (Norway).

Investigating Delaware Basin Bone Spring and Wolfcamp Observations Through Core-Based Quantification: Case Study in the Integrated Workflow, Including Closed Retort Comparisons

Stephanie E. Perry¹, J. Alex Zumberge¹, and Kai Cheng¹

ABSTRACT

The Delaware Basin of the greater Permian Basin system has been the focus of continually increased attention in the exploration, appraisal, and development phases of unconventional oil and gas potential over the past decade. While the industry continues to drill horizontal wells for the exploitation of producible hydrocarbon, subsurface disciplines continue to investigate the rock and fluid properties of the stratigraphy through the application of various technological tools. In this study, we focus on five wells spatially covering Loving, Ward, and Reeves Counties in West Texas, where whole core samples were acquired and investigated to compare variations in the Bone Spring and Wolfcamp Formations across varying geological contexts. Samples taken from

the whole conventional core were investigated in the laboratory setting, and a series of measurements were acquired on each sample. The laboratory measurements distinguished trends and changes in the rock property volumes (i.e., porosity, saturation, total organic carbon) over stratigraphic intervals. The utilization of nuclear magnetic resonance, as well as acquired geochemical data, allows an innovative approach and application of a correction factor to be applied to the saturation quantification. Integration of geological context with measured laboratory data constraints and petrophysical wireline-log-based interpretation links predictive trends from the defined rock and fluid property distributions and may aid in predicting hydrocarbon vs. water production.

INTRODUCTION

The Delaware Basin, a sub-basin component of the Permian Superbasin, continues to experience unconventionally driven oil and gas exploration and development into the new decade (Fig. 1). The advancements of horizontal stimulated fracturing technology, downhole real-time monitoring technology, and continued subsurface characterization and investigation lead to continued growth and opportunities. The overall basin history and evolution is complex, with multiple episodes of uplift and burial as well as asymmetric tilting post-Permian deposition. The Permian-aged stratigraphic column, consisting of various rock types, including source, reservoir, and interbedded formation units, continues to be the main liquid-prone exploited column (Silver and Todd, 1969). Specific interest and study are focused on the Wolfcampian-aged Wolfcamp A-B-C and D benches as well as the Leonardian Bone

Spring sand and lime units. In this study, we focus on the Wolfcamp A and B benches as well as Bone Spring 2 stratigraphic intervals (Fig. 2). We use five key well locations in the Texas extent of the Delaware Basin with spatial locations including three wells in Loving County across a west to east expanse, one well in central Reeves County, and one well in southern Reeves County (Fig. 1). Each well has various stratigraphic sample coverage; however, collectively, they offer a critical opportunity to integrate geology, geochemical and petrophysical observations (Figs. 3 and 4). The spatial expanse of the well locations is important to note as there are significant variations in the properties of the Wolfcamp and Bone Spring Formations depending on whether a well is west or east of the current-day Pecos River. In addition, the overall depositional patterns, as well as hydrocarbon system elements, do vary across these spatial locations. In this study, we compare the wireline-log signatures, measured rock and fluid properties via an innovative laboratory

Manuscript received by Editor March 18, 2021; revised manuscript received August 10, 2021; manuscript accepted August 12, 2021.

¹GeoMark Research Ltd., sperry@geomarkresearch.com; azumberge@geomarkresearch.com; kcheng@geomarkresearch.com

workflow (modified from Luffel et al., 1993; Luffel et al., 1996; Durand et al., 2019), integrate the measured rock properties to petrophysical context and evaluation, and provide insight into an innovative laboratory retort methodology that increases the accuracy of measured fluid-filled storage volume (Fig. 5). The applied technique and results build on legacy approaches to accurately quantify unconventional rock properties based on crushing a sample and performing laboratory measurements (Spears et al., 1992; Handwerger et al., 2011; Blount et al., 2017). This study provides insight and justification into the value

of information of subsurface characterization and how the value of measured subsurface properties, integrated into a regional and local context, can impact exploration to development decision making. An additional focus and value of this study come from our ability to teach and share how to put data in context. We all strive to improve our quantification of properties and understanding in our noted subdisciplines. This study bridges the focus on improved quantification to how to then use the generated data to impact understanding, context, and decisions.

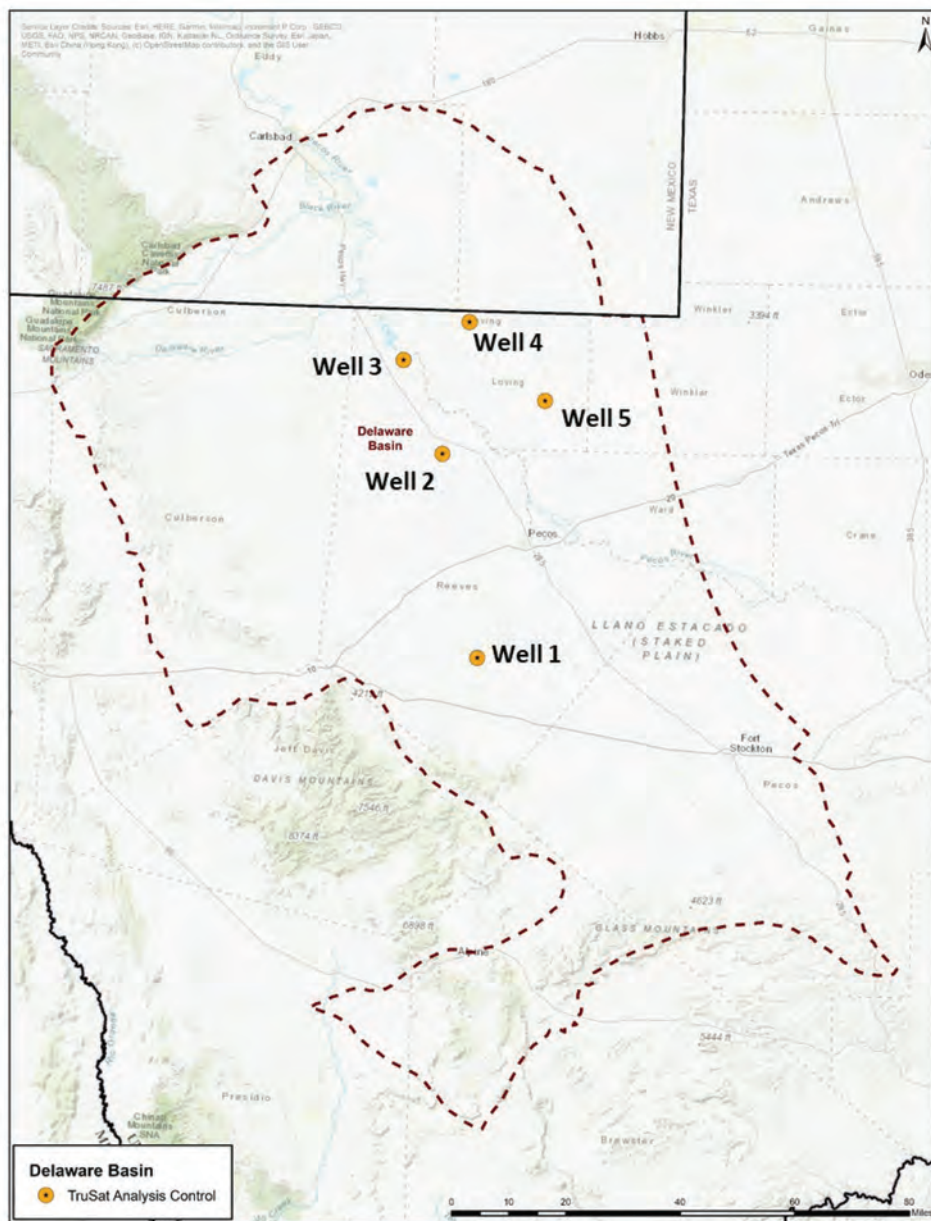


Fig. 1—Well locations of whole core samples and data measured and compared in this study.

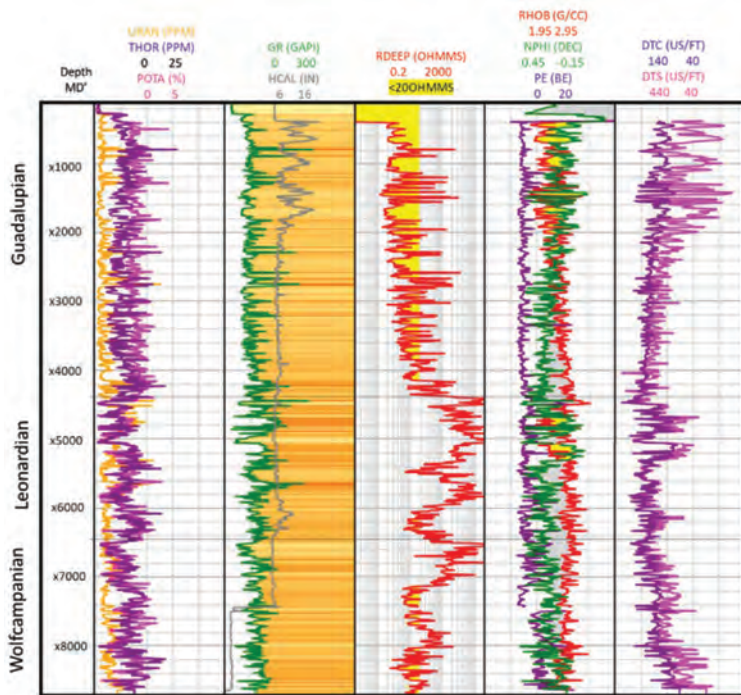


Fig. 2—Based on the openhole wireline characteristics in geological and petrophysical contexts, a scientist can then unlock the unconventional potential and represent quick-look mapping attributes that highlight variation in each stratigraphic interval.

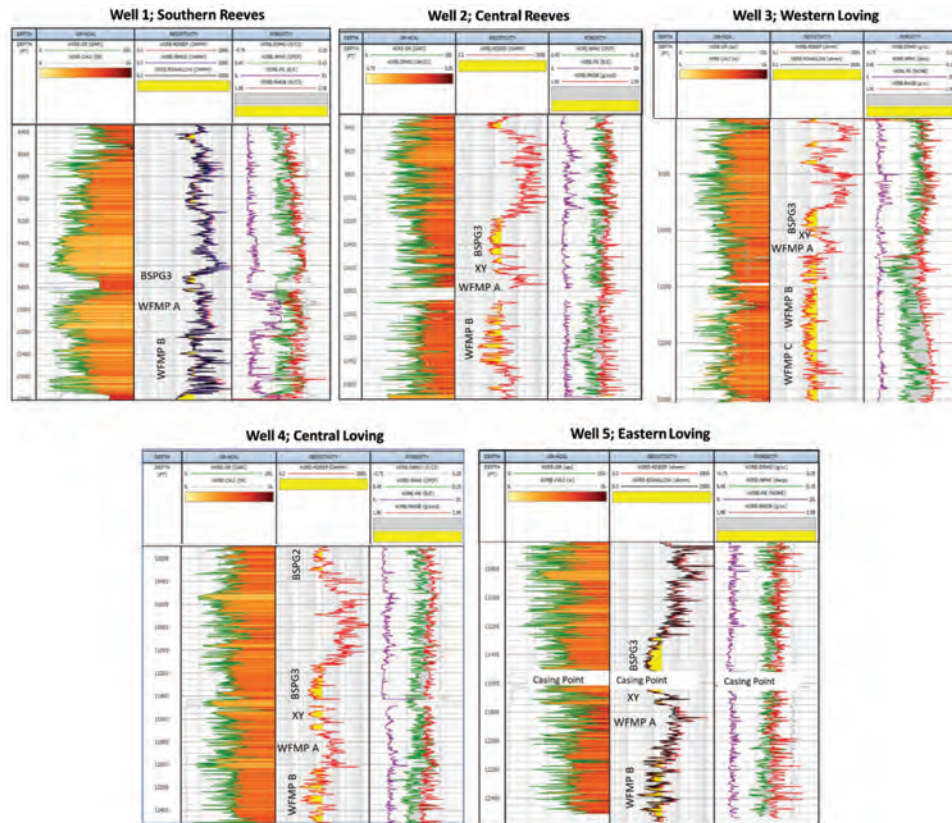


Fig. 3a—Openhole wireline gamma ray (GR-GAPI), resistivity (RDEEP-ohm), and neutron porosity (NPHI-v/v), and bulk density (RHOB-g/cc) logs. Caliper is shown in the GR track (CALL-in.) and photoelectric factor (PE-b/e), and density correction (DRHO-g/cc) is also shown. RDEEP is color filled less than 20 Ω as yellow to highlight the low-resistivity, low-contrast pay of the Bone Spring and Wolfcamp XY stratigraphy. Variability in the Wolfcamp B (WFMP B) regarding the amount of NPHI-RHOB separation does exist and can therefore be related to overall changes in clay content between the well locations. The thickness of the Bone Spring and Wolfcamp XY low-resistivity sands also varies and is important to note.

**Investigating Delaware Basin Bone Spring and Wolfcamp Observations Through Core-Based Quantification:
Case Study in the Integrated Workflow, Including Closed Retort Comparisons**

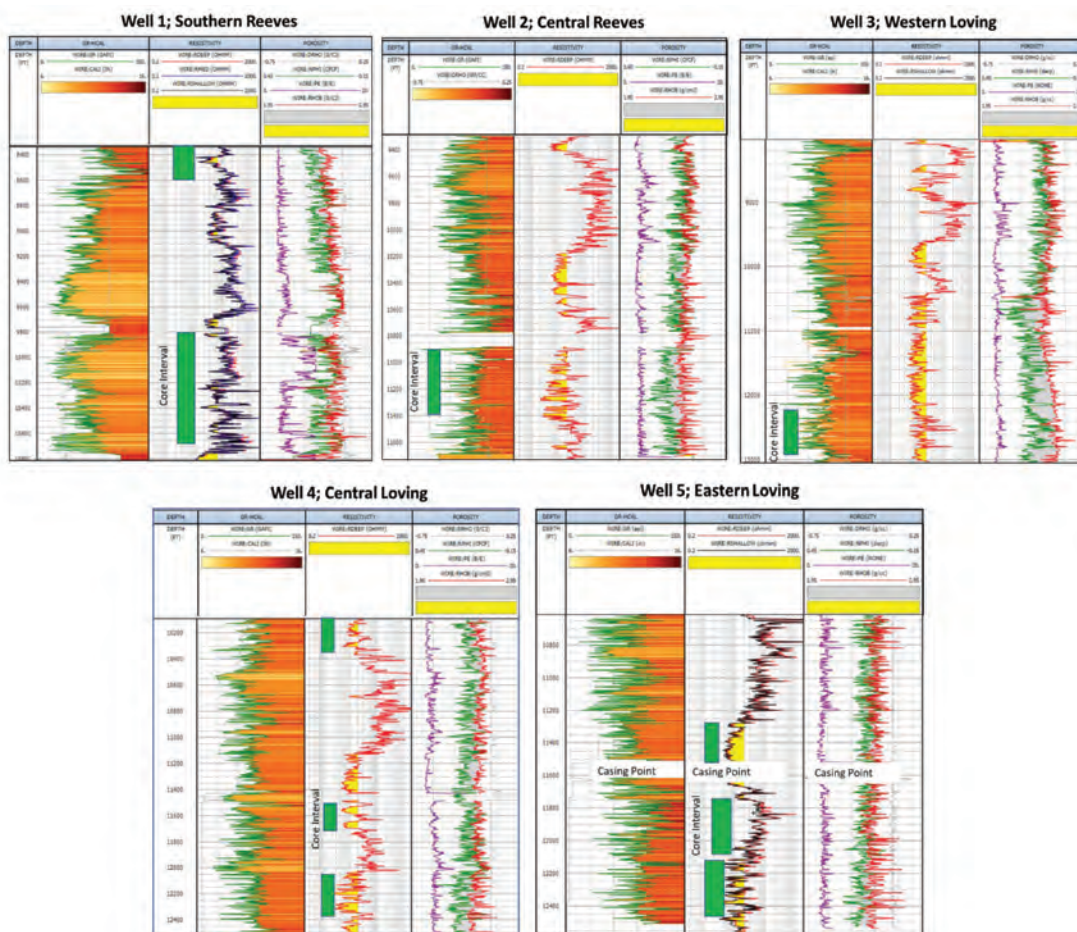


Fig. 3b—Whole core intervals in each well location noted. Coverage varies between the Bone Spring and Wolfcamp stratigraphy.

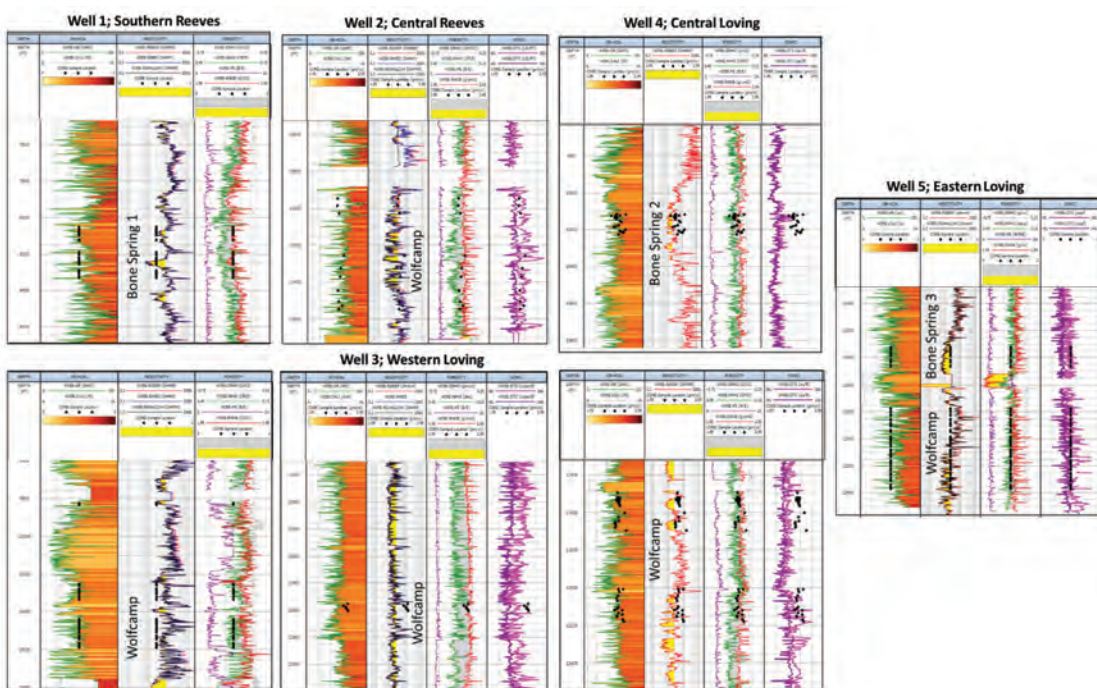


Fig. 4—Single-depth core plug sample locations plotted on the openhole wireline signature for each well in this study.

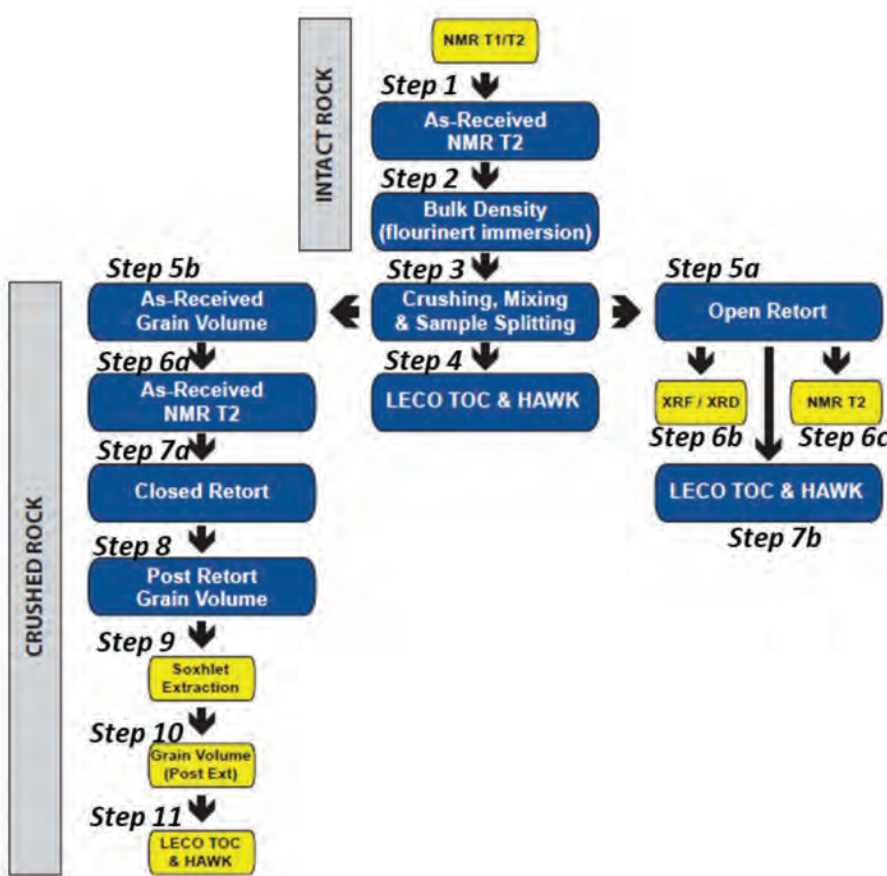


Fig. 5—Single core plug laboratory measurement workflow depicting each overall step and resulting measurement data generated for use in evaluation and comparison (modified from Durand et al., 2019).

METHODS

The study consists of five separate well locations, all of which are sites where the subsurface conventional whole core was acquired in the Delaware Basin. Each acquired conventional whole core is ~4 in. in diameter. The coring condition for each acquisition was an oil-based-mud system. Each core acquired greater than 120 ft per stratigraphic section investigated, and each well has ~40 or more single depths where 1.5- by 3-in. plugged sections were taken and removed to have rock properties measured on the samples (Fig. 4). Each conventional core investigated was preserved by either a wax preservation method or a double barrier preparation and kept in chilled storage for the lifetime of the core until we were able to acquire the needed stratigraphic core plug samples. Core plugs were taken under chilled conditions with a nitrogen fluid as coolant with the drill press. The core plugs had no exposure to any water during the core removal, slabbing, or plugging processes. Once plugged, samples were wrapped in foil, then plastic wrap

and kept under refrigerated conditions at ~45°F. Samples were kept chilled but never frozen. Plug locations were determined by physical investigation of the whole core with varying color and bed boundaries identified as well as integration with acquired wireline logs. Samples selected spanned the variation in gamma ray (GR-GAPI), resistivity (RDEEP-ohm), bulk density (RHOB-g/cc), neutron porosity (NPHI-v/v), photoelectric factor (PE-b/e), and where present, compressional sonic (DT/DTC-us/ft).

For each sample, the following laboratory measurement workflow was applied (Fig. 5). At each step in the following process, a sample weight is measured and recorded in cc per gram (weight by mass).

Step 1. With core plugs in an intact state and with greater than 100 g of total mass, a nuclear magnetic resonance (NMR) acquisition with a 2-MHz frequency, 0.1-ms inter-echo (TE), and signal-to-noise ratio (SNR) of ~60 is acquired.

Step 2. Immerse the sample in a fluorinert bath and, via bulk fluid displacement, measure the sample's intact bulk density in g/cc.

Step 3. Intact sample mass is then crushed to a specified particle-size fraction with the removal of fines via an applied sieving process. Approximately 5 to 7 g of as-received crushed mass is then removed from the sample and used to execute LECO® total organic carbon (TOC-wt%), and HAWK® programmed pyrolysis. The sample mass is then divided into two fractions where Sample Mass A (typically ~50 g) is executed through a standard workflow on an open retort laboratory design. For the purposes of this study, we will not investigate the quantified bound vs. free water volumes measured from the open retort design and instead focus on the application, results, and learnings from the closed retort design. We will touch briefly on the open retort learnings; however, the results and interpretation will be brief. After the open retort thermally based extraction, a post-retort NMR acquisition is performed at 2 MHz, TE of 0.1 ms, SNR as high as achievable, and Alpha of 3.

Step 4. In addition, an as-received grain volume measurement is acquired via helium porosimeter technique in vacuum mode.

Step 5. Each sample is then placed and sealed into a closed retort chamber and, therefore, not open to the atmosphere. The objective is to mitigate continued fluid loss from the rock mass post-crushing of the material mass and while executing a thermally based retort extraction. Fluids can only come out of the chamber through a gravity-driven condensation into a precision glassware tube. The methodology is innovative and optimized to address the challenges with open retort extraction designs where a sample is being exposed to the atmosphere as well as a needed nitrogen purge and cooling unit process to condense any thermally extracted fluids. With the open retort design, it is likely that continued volatile fluid loss (water + light end hydrocarbon) will continue throughout the laboratory measurement process, calling into question the accuracy of the open retort saturation quantification.

Step 6. The closed retort thermal extraction is executed, and bulk oil and water are extracted from the sample. All extracted fluids are saved for any further investigation of fluid properties (for example, saturate and aromatic fractions).

Step 7. A post-thermally based extraction grain density via helium porosimeter is acquired.

Step 8. A post-thermally extracted sample mass of ~5 to 7 g is removed.

Post-measured data acquisition, results are processed for quality control assessment and validation. The resulting data can then be integrated with acquired wireline-log data. Primarily the bulk density, total porosity, and bulk volume oil and water saturations will be used to construct and/or validate a petrophysical model and the parameters

used to justify the wireline-log-based quantification. For petrophysical evaluation, a multimineral inversion model approach was employed. A resulting best-fit interpreted lithology, total porosity, and saturation were derived.

RESULTS AND INTERPRETATION

Comparing the nuclear magnetic results from both intact fluid-filled quantification to post-laboratory crushing fluid-filled quantification allows us to observe differences in the lost fluid resulting from the laboratory methodology. By crossplotting the NMR signal of intact vs. crushed from as-received state analysis, we can observe variability in the total lost fluid per stratigraphic zone and per well (spatially) in the Delaware Basin. In general, as total porosity increases, the fluid loss from laboratory crushing increases (Fig. 6a). Laboratory crushing is executed manually to a predefined particle size with the sample sieved to remove fines within ~5 minutes time. Time is not a variable when looking at quantified fluid loss results, as the samples are all prepared with the exact same steps in the exact same amount of time. Fluid loss involves the loss of both volatile hydrocarbon and water in the preparation process. For all five wells in this study, the variance off the 1:1 NMR cc line (pink) is interpreted as the fluid loss associated with the crushing of material in the laboratory environment. Samples with increased total porosity also have increased fluid loss associated with the volatile fluid being able to liberate the pore volume (water and/or hydrocarbon). Bone Spring and Wolfcamp XY have similar fluid loss profiles dominated by light hydrocarbon and water loss. Wolfcamp A stands out and is similar across the five well locations, with primarily hydrocarbon and water lost from the pore system. Wolfcamp B and C are dominated by water loss from the pore volume and a significant volume of it, on the order of 10 to 20% of total water-saturated volume. In addition, crossplotting total porosity calculated by Boyle's law vs. that of fluid summation highlights any underestimation with deviation from a 1:1 line due to the loss of evacuated fluid-filled pore volume because of laboratory preparation. The Boyle's law approach is important as the post-closed retort grain densities prove the efficiency of the evacuation and quantification of mobile fluid volumes with no residual matrix-associated grain density left over impacting results.

Based on NMR $T_1 T_2$ acquisition and resulting 2D maps where fluid-filled pore volume can be compared before and after the crushing process (Fig. 6b), the main fluid that dominates the loss fraction is water in the Delaware Basin Wolfcamp C and B benches as well as the Bone Spring and Wolfcamp XY sands. The Wolfcamp A stratigraphy experiences both hydrocarbon and water loss.

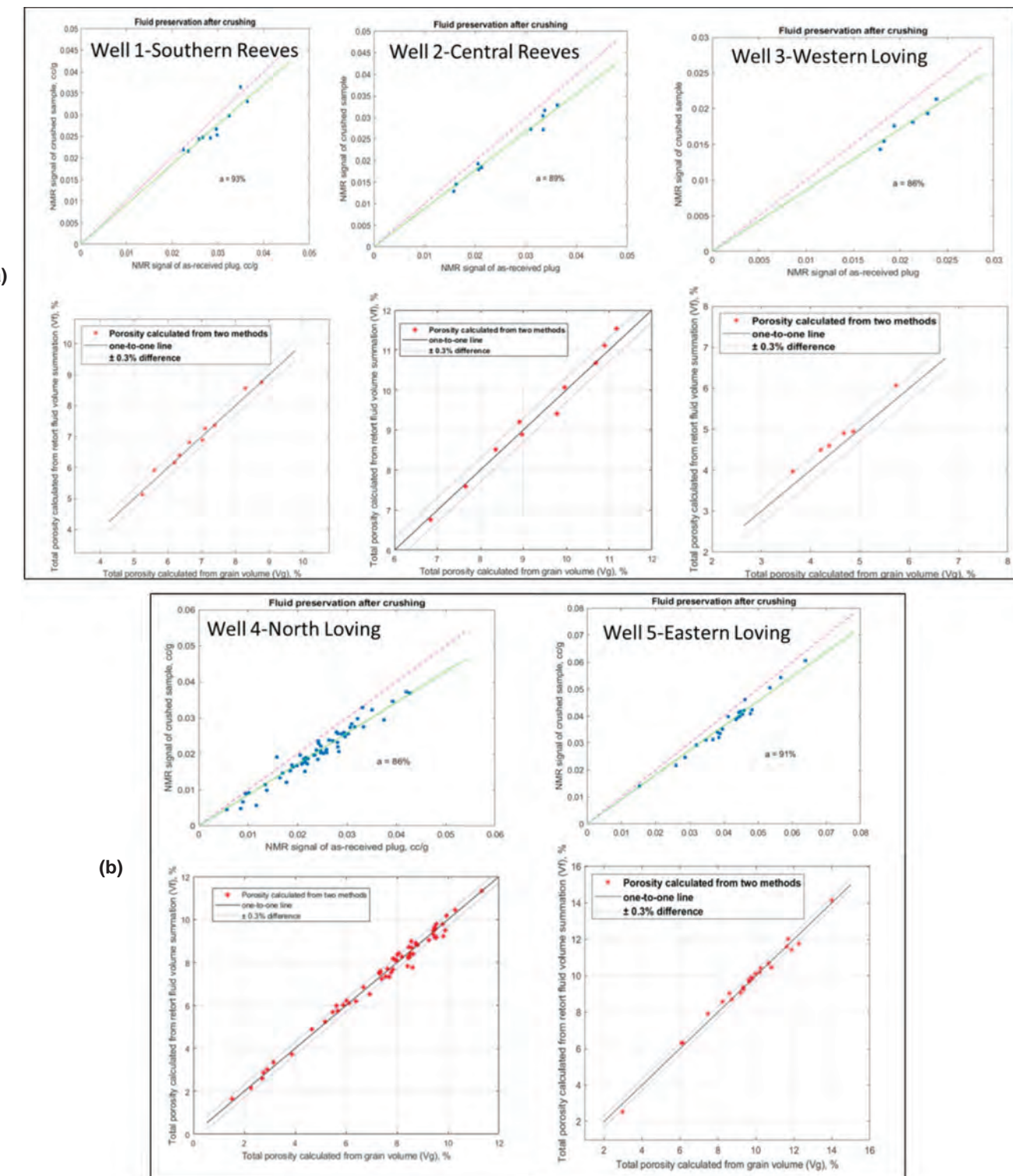


Fig. 6a—For all five wells in this study, plot (a) represents the single core plug results for the nuclear magnetic resonance signal (NMR-cc) from an intact state on the x-axis and then the NMR signal measured on the same sample's crushed rock aliquot on the y-axis. Plot (b) demonstrates the two methods for total porosity are calculated from the acquired bulk density, grain density, and then fluid summation methodology for each sample.

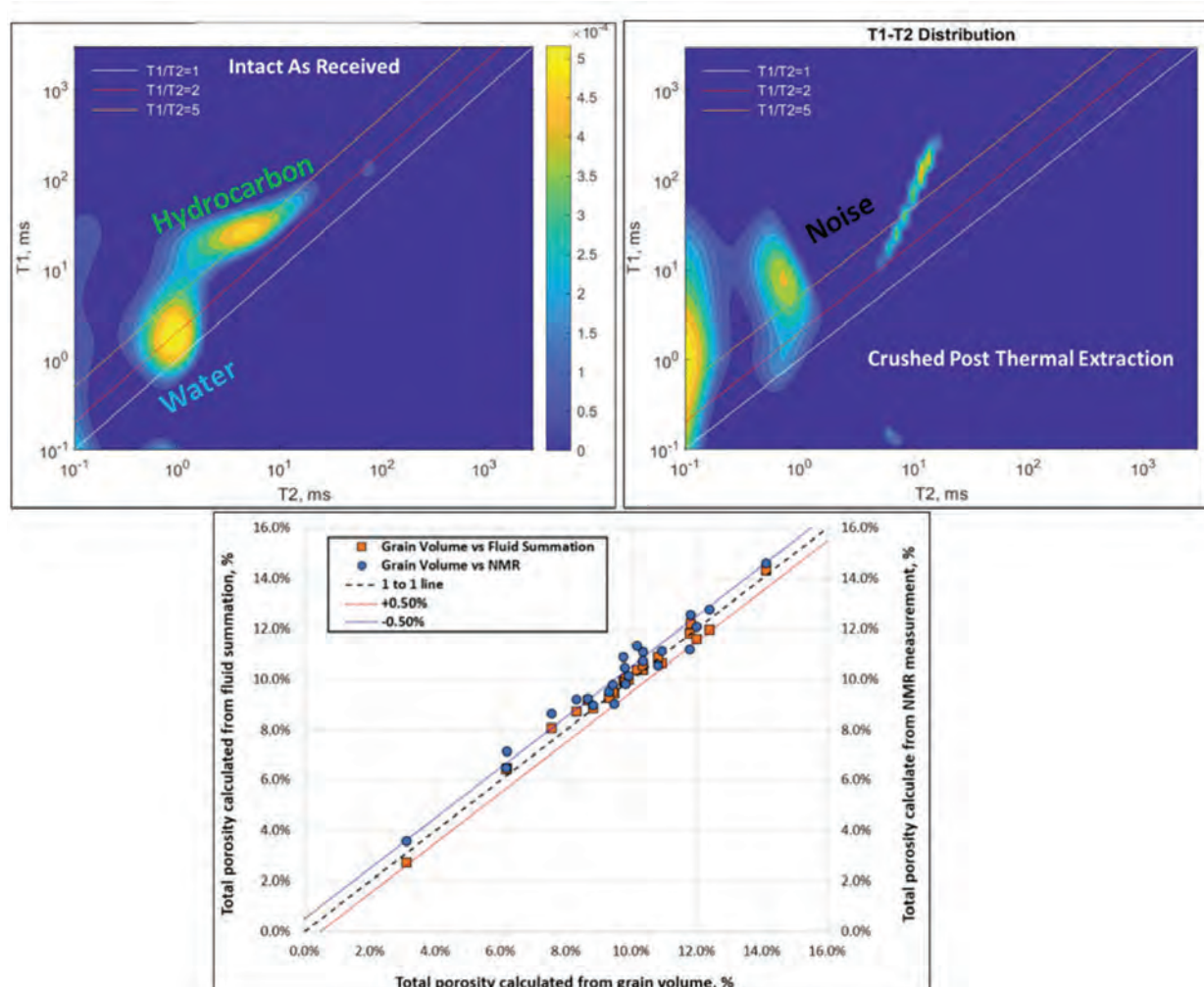


Fig. 6b—Comparison of as-received NMR $T_1 T_2$ results vs. post-thermally extracted $T_1 T_2$ results. Visual as well as direct quantification of the removed water and hydrocarbon-prone volume can be made, thus gaining an understanding of the pores that under thermal conditions liberate fluid and do not require the presence of a chemically based solvent to be removed or extracted.

The well located in western Loving has greater than ~15 to 20% of the fluid-filled pore volume that must be accounted for when considering the total water or oil saturation of given samples in the Wolfcamp B Formation. The north Loving location also demonstrates significant fluid loss with increasing total porosity ranging from 10 to 15% in the Bone Spring, Wolfcamp XY, and Wolfcamp B stratigraphy. As an interpreter uses the hydrocarbon-in-place quantification from core to wireline-log-based interpretation, a correction to that estimate must be applied. The southern Reeves and eastern Loving locations experienced the least significant loss representing correction factors for the Bone Spring, Wolfcamp A, and Wolfcamp B.

We also use two independent calculations from acquired laboratory data to compare total porosity. A crossplot of the two methods' comparisons shows the Boyle's law-based results using grain and bulk densities on the x-axis and fluid-summation-based total porosity on the y-axis (Fig. 6a). If two independent ways to compare the storage quantification is not enough, we then use the nuclear magnetic resonance as a third independent metric for total porosity comparison (Fig. 6b). Approaching the storage quantification from this multitool approach results in rigorous cross checks on quantification, highly constrained error for a log analyst to consider, and a validation of the efficiency of the laboratory closed retort process and results. Comparing these total porosities

ensures that the post-thermally extracted closed retort grain density is accurate and precise.

An important aspect of our results is to share the impact of open vs. closed retort quantification. In Fig. 7, we show the fluid collection efficiency of the open vs. closed retort thermally extracted results from the five wells. On average, the open retort fluid collection efficiency is ~80%, which is an improvement from the early open retort methodology and designs. However, that also indicates that 20% of the investigated fluid-filled pore volume was lost with the open retort design application. That fluid loss could have occurred from either exposure to the atmosphere or related to the methodology design. An open retort system uses a nitrogen purge to a condensing line process to facilitate liquid phase accumulation into the glassware where extracted fluids are recovered. Alternatively, the closed retort technique mitigates the above design and uses natural gravitational and adiabatic forces to accumulate the thermally extracted fluids into glassware for quantification.

By utilizing the thermally extracted, open retort collected water volumes, a comparison between free vs. bound water volume can be made across the data set (Fig. 8). For the

purposes of this study, free water is defined as the accumulated water volume when exposed to temperature $\geq 105^{\circ}\text{C}$ and can be compared to NMR T_2 distributions with a defined cutoff of ~10 ms. Bound water is defined as the thermally liberated water volume for a given sample when exposed to a temperature of 105°C to 300°C for a defined time duration. For the open retort time duration, a minimum of ~4 hours at both the 105°C and the 300°C steps is executed. As such, we observe that Wolfcamp C and B have the highest bound water volume (typically correlated with clay volume) in all locations and relatively high free water behavior. Variability in the results per sample can be explained by a variation in facies sampled and measured with the organically lean lithofacies having the highest relative bound water and the organically enriched lithofacies having the lowest (Figs. 9 and 10). The Bone Spring and Wolfcamp XY have the highest free water volume with very little bound water presence, and Wolfcamp A has the lowest free and bound water component. That said, the Wolfcamp A is not void of free water content and can help justify known produced water-oil ratios for horizontally drilled and stimulated wells of 2:1, 3:1, and, in some cases, 4:1.

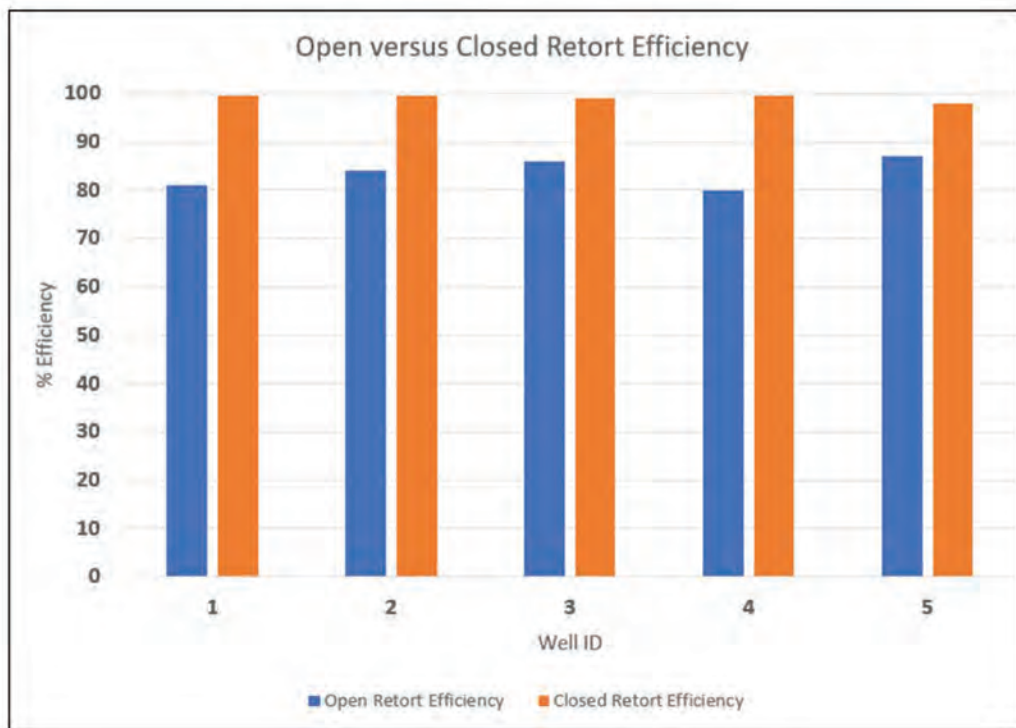


Fig. 7—Five well comparison of open retort fluid collection efficiency vs. closed retort fluid collection efficiency. The closed retort approach increases fluid collection efficiency by a significance of greater than an additional 10 to 15% improvement. The efficiency then translates into increased accuracy in measured fluid saturation results.

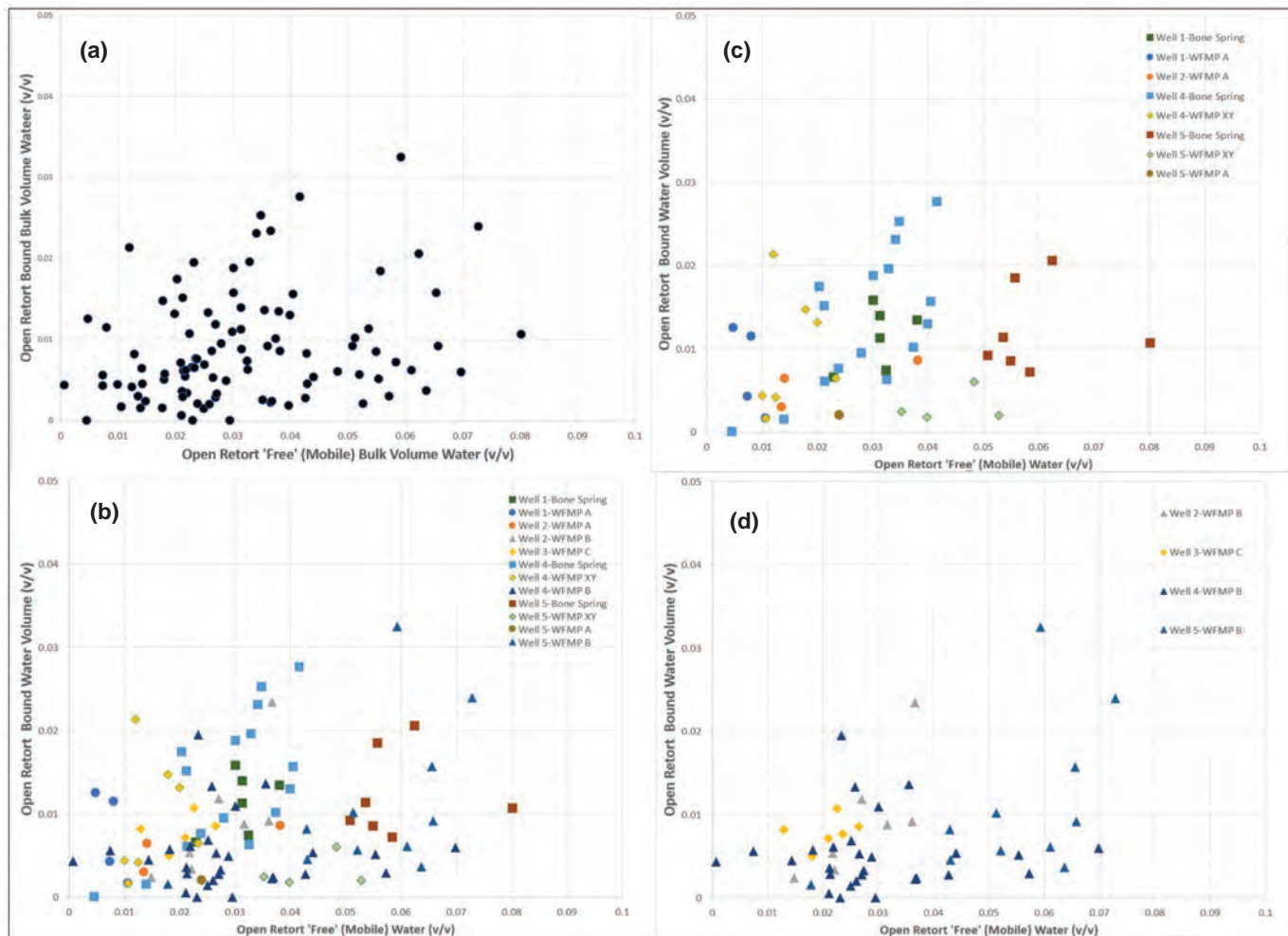


Fig. 8—Crossplots per stratigraphic formation by well of measured open retort free water volume defined as water released and quantified from 105°C to 300°C vs. bound water volume quantification defined as water released at 300°C for a time of ~8 hours. In general, the Bone Spring and Wolfcamp XY have increased free water volume compared to bound water volume. Wolfcamp A has the least quantified bulk volume water total, and Wolfcamp B-C has the highest bulk volume water total. The Wolfcamp B-C has the highest bound water volume vs. free water volume content as well and can be correlated to increased volume of clay content in the stratigraphic section.

Correlations between measured as-received total organic carbon (wt%) and programmed pyrolysis S1 fraction (mg/g) can be observed (Fig. 9). In the as-received state, the S1 fraction (mg/g) that results from programmed pyrolysis can be used as a qualitative proxy for the presence of volatile hydrocarbon in the investigated rock volume (Jarvie, 2017). The measurement is made by taking a small amount of rock mass, crushing to a homogenized particle size, placing it into a ceramic crucible inside the instrumentation, and then heating the rock mass to ~300°C. The sample, regardless of lithology, is typically held for ~8 hours at the 300°C

hold. In this study, all samples were executed consistently. However, for future applications, we note that the time and temperature ramp settings and execution can be adjusted. The released or volatized hydrocarbon fraction is then measured by a detector in the instrument, and a resulting mg/g equivalent result is provided. In the extracted state, the S2 fraction (mg/g) represents the remaining hydrocarbon generative potential and can be used to assess the source rock quality present for a given sample (Dembicki, 2009). In addition, correlations between programmed pyrolysis as received and extracted S2 fractions (mg/g) to total organic

carbon and measured S1 (mg/g) can also be made. These correlations from measured point data sets can then allow a subsurface expert to derive a continuous wireline-log-based interpretation of the geochemical proxies for volatile hydrocarbon presence and kerogen quality indices. An important observation is the correlation of closed retort bulk volume oil vs. programmed pyrolysis S1 and S2 fractions (mg/g) (Figs. 10 and 11). Generally, comparing measured total porosity vs. total water saturation (modified Buckle's plot), one can observe that the Wolfcamp C and B have total porosities that range from ~2 to 14%, with the porosity system being dominated by micropores (defined as clay-size to fine siltstone with a fracture width of < 5 μ) related to clay

presence and a range of total water saturation from 20 to 90% (Fig. 12). Observe the higher overall total water saturation (> 40%) in the Bone Spring and Wolfcamp XY stratigraphy than the Wolfcamp A. Figure 8b: Here we highlight the Wolfcamp B-D stratigraphy. Variability is invoked because of the zones encompassing multiple types of lithofacies, such as carbonates, silty shales, and mudstones. The trend of samples with < 40% total water saturation highlights the organically enriched shale facies in these zones. The samples with total water saturation > 40% and a range in porosity constitute carbonates and highly clay-prone, organically lean silty shales and shales. Clay content increases > 20% in those samples.

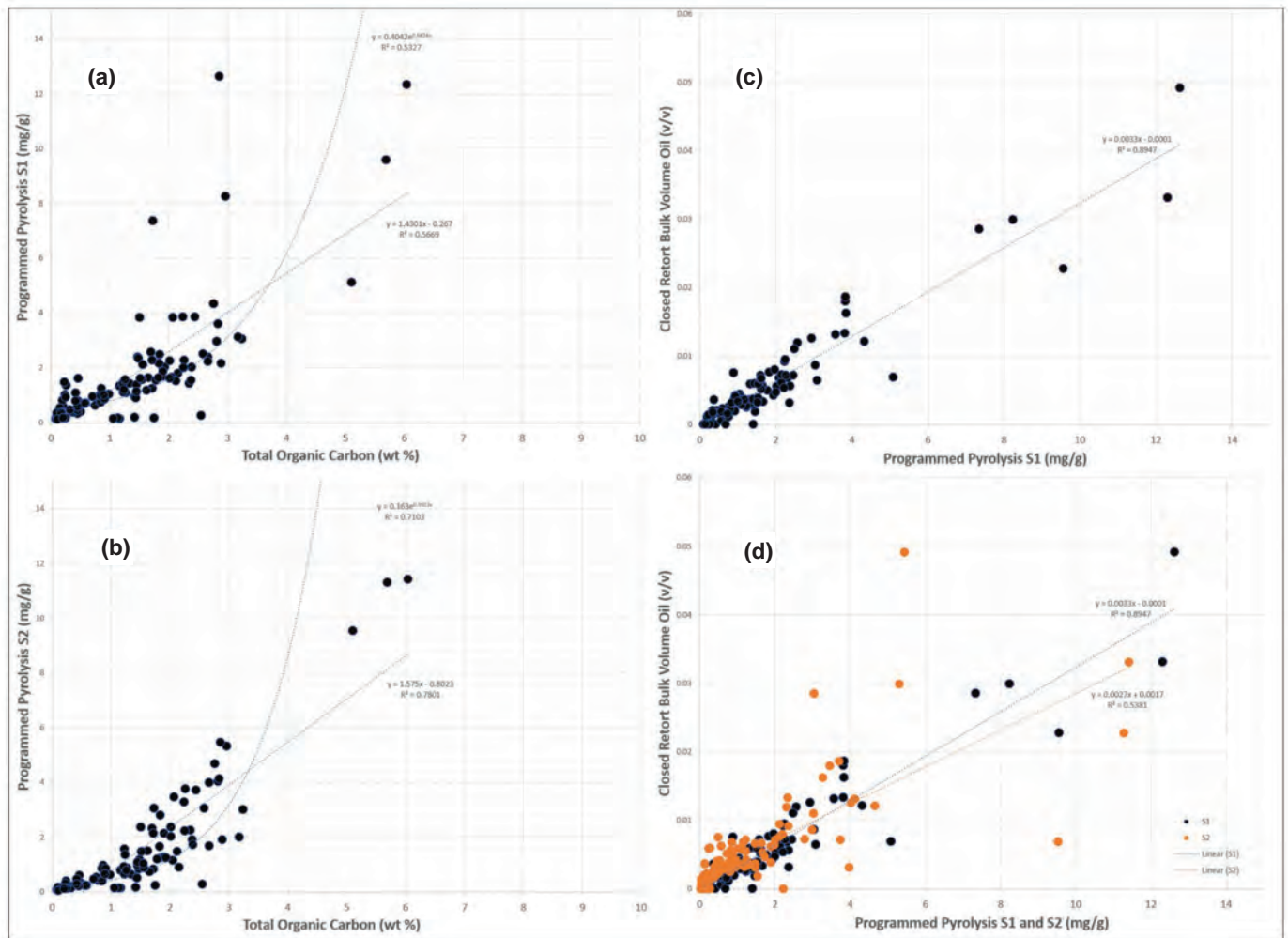


Fig. 9—(a) Crossplot of measured LECO total organic carbon (wt%) vs. HAWK programmed pyrolysis S1 (mg/g) volatile fraction. Correlations provided. (b) Crossplot of HAWK programmed pyrolysis S1 (mg/g) volatile fraction vs. closed retort bulk volume oil. Correlations provided. (c) Crossplot of measured LECO total organic carbon (wt%) vs. HAWK programmed pyrolysis S2 (mg/g) kerogen potential fraction. (d) Crossplot of HAWK programmed pyrolysis S1 (mg/g) and S2 (mg/g) fractions vs. closed retort bulk volume oil. Correlations provided.

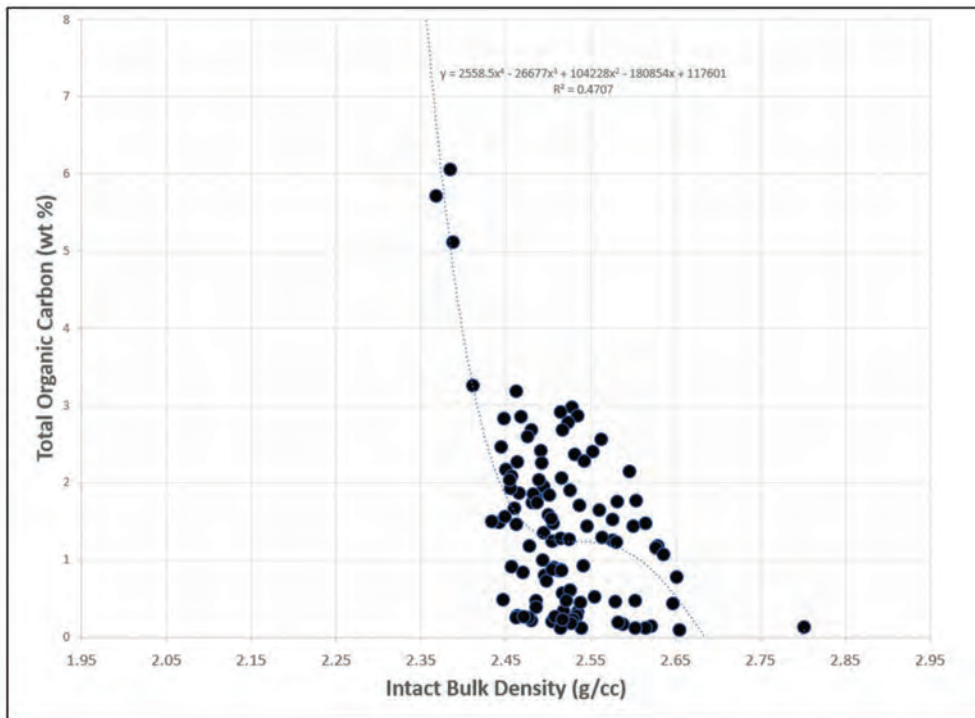


Fig. 10—Crossplot of measured bulk density (g/cc) vs. total organic carbon (wt%). Here a polynomial fit, rather than the more fundamental exponential fit, was used to honor the high side curvature and the decrease in organic content with an increase in bulk density relationship. The correlation and principle follow Schmoker's law (Schmoker, 1979) and can allow a subsurface expert to derive continuous TOC from wireline logs in the basin across the stratigraphic stack.

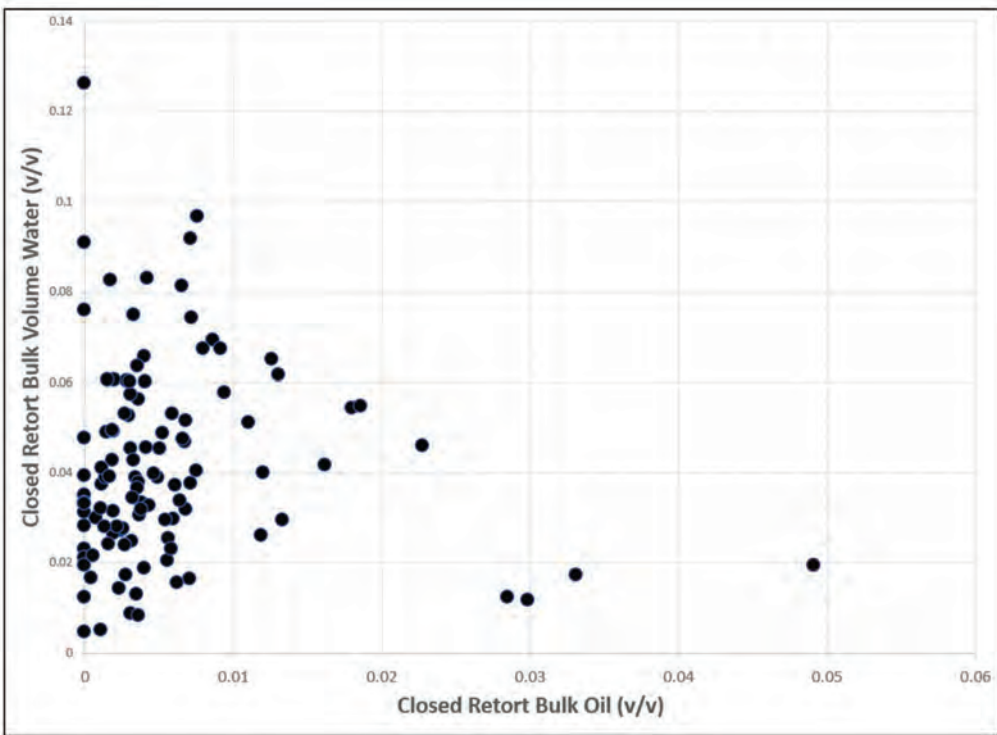


Fig. 11—Crossplot of closed retort bulk volume oil vs. closed retort bulk volume water for all samples in this study. Note the threshold of ~0.01 v/v for facies in the stratigraphy with increased free/mobile oil potential vs. mobile water potential. Below 0.01 closed retort bulk volume oil, a facies or sample has an equal thermally released volume of water-oil ratio, not taking into consideration pressure or wettability impacts.

Alternatively, the Wolfcamp A total water saturation does not exceed ~60% total water saturation. The Bone Spring and Wolfcamp XY are mesopore (defined as fine siltstone to coarse silt and a fracture width of ~5 to 50 μ) dominated related to silty-sand lithofacies and range in total porosity from 2 to 12% and total water saturation typically greater than 50% (Fig. 12).

Closed retort bulk volume oil is quantified by the measurement of oil liberated from a sample exposed thermally to a temperature of 300°C for a set duration (Fig. 13). Equivalent and comparable is the programmed pyrolysis S1 fraction, which is time-temperature-based volatilization at 300°C, whose results then serve as a proxy for volatile hydrocarbon presence.

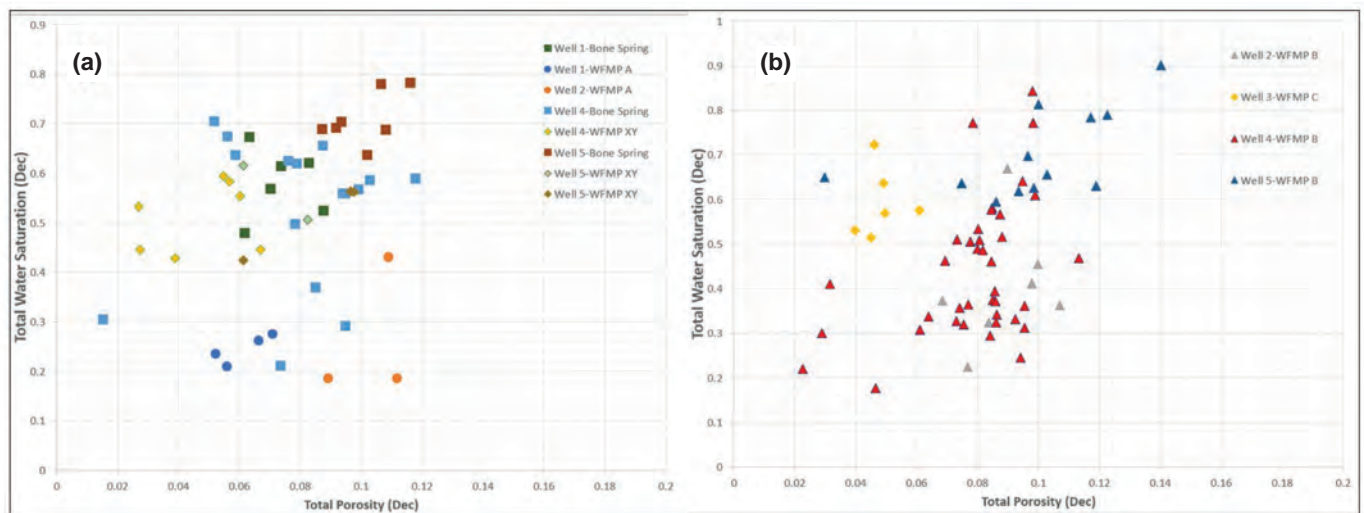


Fig. 12—(a) Crossplot of total porosity (dec) on the x-axis vs. total water saturation (dec) (modified Buckle's plot) on a per stratigraphic zone, per well basis. In this plot, we highlight the Bone Spring, Wolfcamp XY, and then Wolfcamp A ranges and trends.

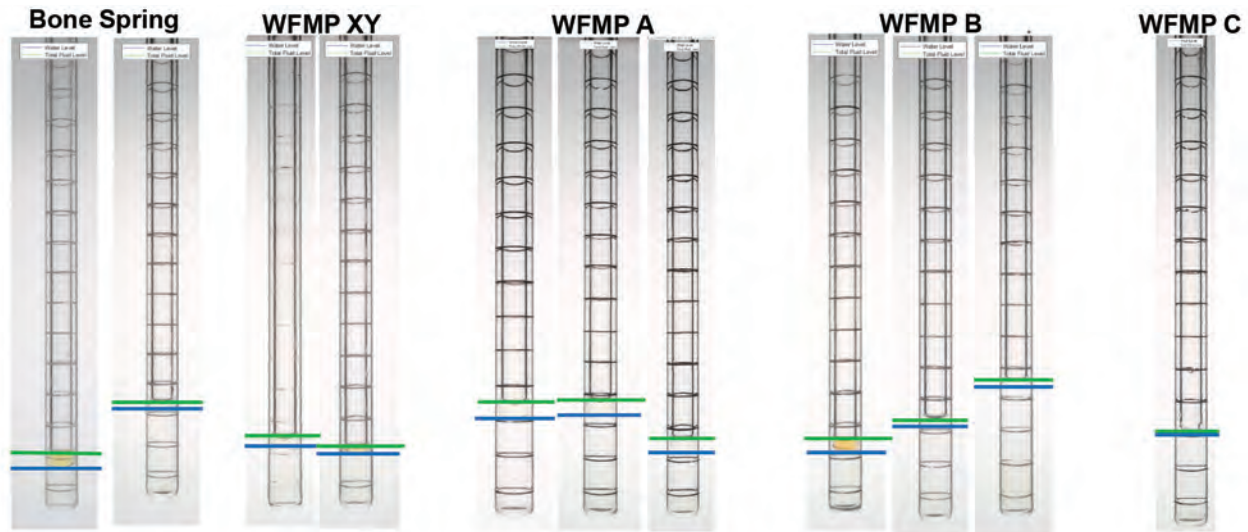


Fig. 13—Closed retort laboratory imagery for each stratigraphic zone in this study. The blue line on the glassware denotes where the top thermally liberated water (bulk volume water) is interpreted and can therefore be quantified. The green line that is located above the blue line represents the top of the hydrocarbon accumulated in the glassware. The difference between the volume of fluid up to the blue line vs. the volume of fluid up to the green line represents the total hydrocarbon extracted under the thermal experimental conditions. In samples where there is no hydrocarbon, the two lines overlap each other and cannot be differentiated. Note the very clear observation in the difference in thermally released oil color between the Bone Spring, WFMP XY (darker color) vs. the WFMP A (lighter color). Also, the increased total water level in the WFMP B-C vs. the shallower stratigraphy is easy to identify.

Given this relationship and interpretation of the liberated volatile fluids, the quantified closed retort oil volume can be defined as free oil under the given condition executed in the laboratory setting. Any remaining soluble or insoluble fraction in each sample can be defined as bound hydrocarbon and split into bitumen and kerogen fractions. In the case of organically lean stratigraphy, this could be waxy paraffinic vs. mobile fraction, etc. This important direct quantification of liberated hydrocarbons significantly advances crushed rock laboratory analysis,

which traditionally has been based on the quantification of measured water volumes only (Fig. 14), with a measured vs. remaining volume quantification based on assumed fluid densities. This correlation allows the expert to derive a wireline-log-based mobile hydrocarbon vs. bound hydrocarbon partitioned evaluation. Importantly, wireline-log-based total oil in place can then be corrected for (1) fluid loss related to laboratory crushing and (2) partitioning of mobile (free) vs. immobile (bound) hydrocarbon (Fig. 15).

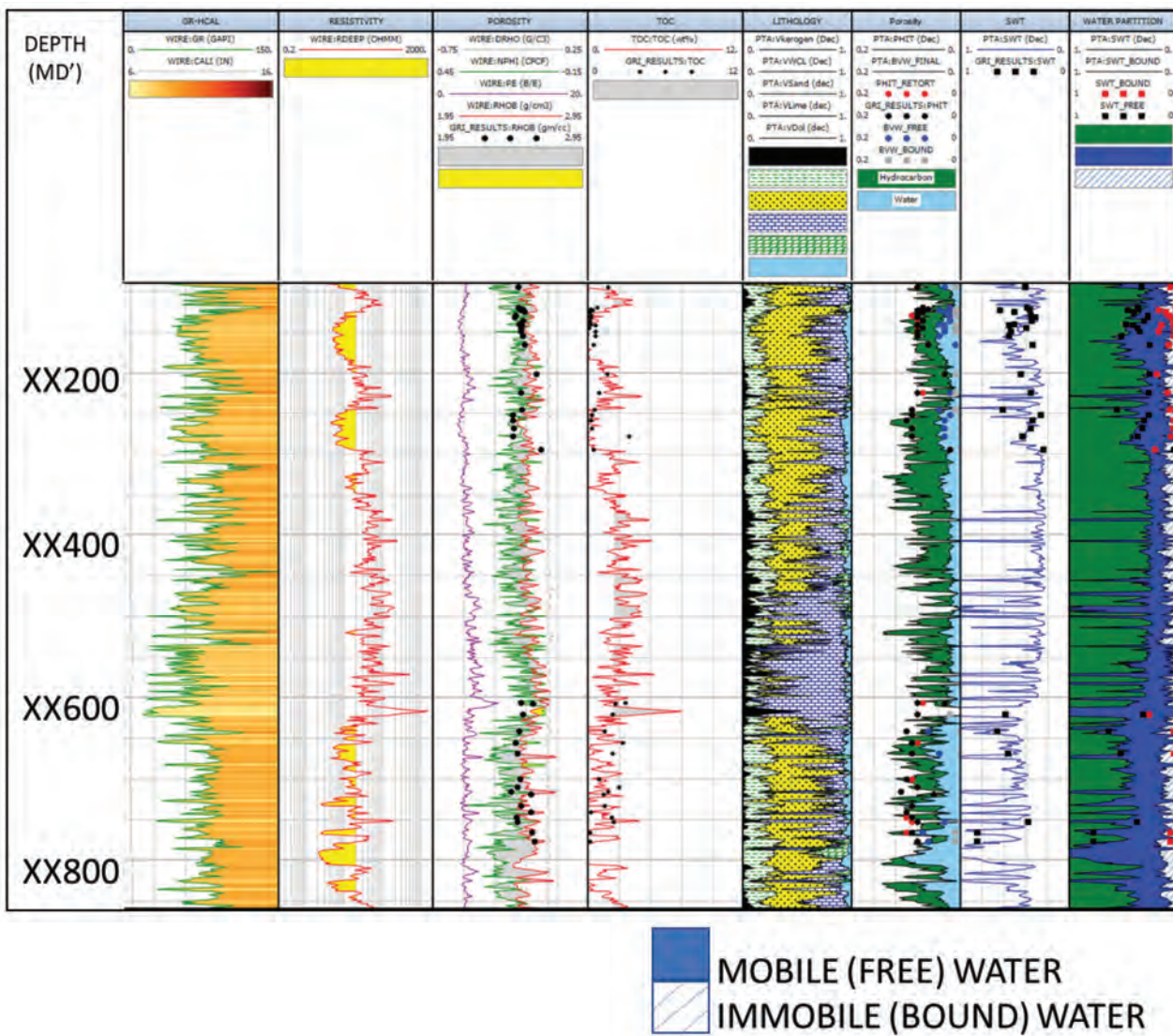


Fig. 14—Integrated petrophysical example of raw wireline, evaluated properties from wireline, and correlation to measurements in this study. The last track is where to focus where the correlation between the partitioned mobile vs. immobile water fraction from open retort analysis was used to develop a correlation with the volume of clay content. Then, the correlation equation was applied for a continuous representation of the amount of free vs. bound water in the stratigraphy. Observe the increase in free water content as the logs transition from Wolfcamp A into the Wolfcamp B stratigraphy. Potential related production WOR from wells that target the Wolfcamp A vs. the Wolfcamp B stratigraphy in the water-prone section differs from a 2:1 ratio up to a 10:1 ratio.

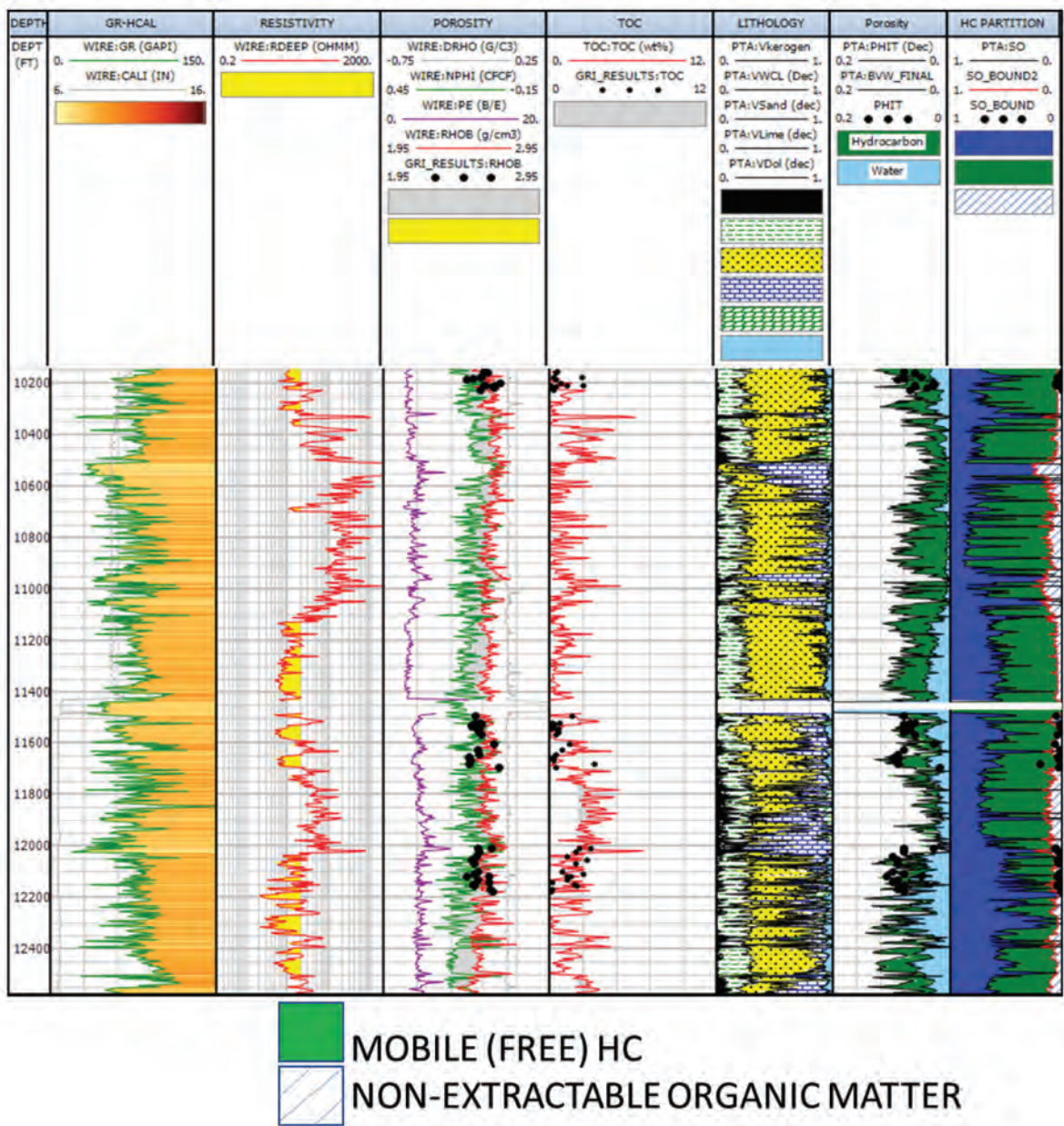


Fig. 15—Integrated petrophysical example of raw wireline, evaluated properties from wireline, and correlation to measurements in this study. The last track is where to focus where the correlation between the partitioned mobile vs. immobile hydrocarbon fraction from closed retort analysis and programmed pyrolysis was used to develop and apply the correlations presented in this study. Then, the correlation equation was applied for a continuous representation of the amount of free vs. bound hydrocarbon in the stratigraphy. Observe the increase in immobile hydrocarbon content in the more organically enriched shale zones (increased resistivity and lighter bulk density trends).

Based on this study, a five-well comparison of free vs. bound water and hydrocarbon fractions indicates that from a laboratory quantification, the southern Reeves, eastern Loving, and northern Reeves locations and stratigraphy have less movable water than the central Reeves area, particularly in the Wolfcamp B and C Formations. The southern Reeves Wolfcamp A has a decreased free vs.

bound oil volume in the Wolfcamp A compared against eastern and northern Loving. The impact of the individual measurements, here combined into a comprehensive workflow, provides crushed rock sample advancements and refinement in quantification from approaches previously conducted (Luffel and Guidry, 1992) in the oil and gas industry.

CONCLUSIONS AND RECOMMENDATIONS

We investigated and benchmarked rock and fluid quantitative results from an integrated workflow, including closed retort, open retort, geochemistry, and nuclear magnetic resonance data. Comparisons and observations spanning five well locations in the Delaware Basin were discussed relative to the stratigraphy tested and compared. Linking the geology to petrophysics and geochemistry is crucial in the Delaware Basin to understand where, when, and why the variations in fluid-filled storage characteristics change. Observations and lessons learned in terms of core property quantification upscaled to wireline-log interpretation were intended to aid the community regarding the application of workflows, reducing uncertainty, and demonstrating how the value of information could potentially impact exploration, appraisal, and development-related project objectives. Further investigation into the application of the closed retort methodology is recommended and suggested to span outside of the Delaware Basin context to test and share learnings from other basins and stratigraphy.

NOMENCLATURE

Abbreviations

- DRHO = density correction
DT/DTC = compressional sonic
GR = gamma ray
NMR = nuclear magnetic resonance
NPHI = neutron porosity
PE = photoelectric factor
RDEEP = resistivity
RHOB = bulk density
SNR = signal-to-noise ratio
TE = inter-echo
TOC = total organic carbon

REFERENCES

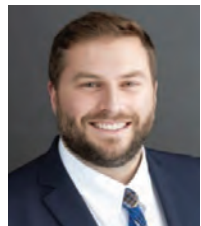
- Blount, A., Croft, T., Driskill, B., and Tepper, B., 2017, Lessons Learned in Permian Core Analysis: Comparison Between Retort, GRI, and Routine Methodologies, Paper SPWLA v58n5a5, *Petrophysics*, **58**(5), 517–527.
- Dembicki, H. Jr., 2009, Three Common Source Rock Evaluation Errors Made by Geologists During Prospect or Play Appraisals, *American Association of Petroleum Geologists Bulletin*, **93**(3), 341–356. DOI: 10.1306/10230808076.
- Durand, M., Nikitin, A., Blount, A., McMullen, A., Driskill, B., and Hows, A., 2019, Crushed Rock Analysis Workflow Based on Advanced Fluid Characterization for Improved Interpretation of Core Data, Paper SPWLA v60n6a4, *Petrophysics*, **60**(6), 755–769. DOI: 10.30632/PJV60N6-2019a4.
- Handwerger, D.A., Keller, J., and Vaughn, K., 2011, Improved Petrophysical Core Measurements on Tight Shale Reservoirs Using Retort and Crushed Samples, Paper SPE-147456 presented at the SPE Annual Technical Conference and Exhibition, Denver, Colorado, USA, 30 October–2 November. DOI: 10.2118/147456-MS.
- Jarvie, D.M., 2017, Perspectives on Shale Resource Plays, The Role of Organic Petrology in the Exploration of Conventional and Unconventional Hydrocarbon Systems, in Suarez-Ruiz, I., and Filho, J.G.M., editors, *Geology: Current and Future Developments*, Bentham Science Publishers, **1**, 316–343. DOI: 10.2174/97816810846331170101. ISBN: 978-1-68108-463-3.
- Luffel, D.L., and Guidry, F.K., 1992, New Core Analysis Methods for Measuring Reservoir Rock Properties of Devonian Shale, Paper SPE-20571, *Journal of Petroleum Technology*, **44**(11), 184–1190. DOI: 10.2118/20571-PA.
- Luffel, D.L., Hopkins, C.W., and Schettler, P.D. Jr., 1993, Matrix Permeability Measurement of Gas Productive Shales, Paper SPE-26633 presented at the SPE Annual Technical Conference and Exhibition, Houston, Texas, USA, 3–6 October. DOI: 10.2118/26633-MS.
- Luffel, D.L., Guidry, F.K., and Curtis, J.B., 1996, Development of Laboratory and Petrophysical Techniques for Evaluating Shale Reservoirs, Final Technical Report, October 1986–September 1993, *Gas Research Institute Technical Report*, GRI-95/0496.
- Schmoker, J.W., 1979, Determination of Organic Content of Appalachian Devonian Shales From Formation-Density Logs: GEOLOGIC NOTES, *AAPG Bulletin*, **63**(9), 1504–1509. DOI: 10.1306/2F9185D1-16CE-11D7-8645000102C1865D.
- Silver, B.A., and Todd, R.G., 1969, Permian Cyclic Strata, Northern Midland and Delaware Basins, West Texas and Southeastern New Mexico, *AAPG Bulletin*, **53**(11), 2223–2251. DOI: 10.1306/5D25C94D-16C1-11D7-8645000102C1865D.
- Spears, R.W., Dudus, D., Foulds, A., Passey, Q., Sinha, S., and Esch, W.L., 1992, Shale Gas Core Analysis: Strategies for Normalizing Between Laboratories and a Clear Need for Standard Materials, Paper A, SPWLA 52nd Annual Logging Symposium, Denver, Colorado, USA, 14–18 May.

ABOUT THE AUTHORS



Stephanie E. Perry is originally from upstate New York. She completed a dual BSc degree in geology and psychology (2004) at Union College, Schenectady, New York, an MSc degree in earth sciences (2006) at SUNY Albany, New York, and a PhD in geology (2014) at Syracuse University. Stephanie has

worked in the oil and gas industry for more than 12 years in exploration, development, and production. She has worked onshore and offshore opportunities spanning roles from a geologist to a geophysicist to a specialization in petrophysics. Stephanie formerly worked with operators, including ExxonMobil and Anadarko Petroleum Corporation. She currently works for GeoMark Research Ltd. as the chief petrophysical advisor.



J. Alex Zumberge has extensive lab experience in oil and rock extract analyses with an emphasis on correlation tools like bulk organic properties, lipid biomarkers, and carbon isotopes. He has over 9 years of experience in a lab environment doing experiments himself as well as overseeing general sample/project flow through each analysis phase. Alex recently finished his PhD in organic geochemistry at the University of California – Riverside, where he specialized in sterane/hopane relationships through time from the Precambrian to the present. Additionally, Alex has experience with traditional analytical techniques (LC, GC, GC-MS, GC-MS/MS), as well as new analytical approaches that allow access to the kerogen-bound biomarker pool within rock extracts via hydrogen pyrolysis, HyPy. Currently, Alex is executive vice president of operations at GeoMark Research and manages oil technical service projects as well as the new TruSat™ rock lab.



Kai Cheng is a TruSat™ scientist and rock analyst with GeoMark Research Ltd., focusing on laboratory rock measurements, TruSat™ data process and interpretation, and the development of unconventional rock analysis. He received a PhD degree in petroleum engineering (2019) from Texas A&M University in College Station, Texas. Kai has published eight peer-reviewed petrophysics papers in multiple

journals, including *Applied Clay Science*, *SPE Reservoir Evaluation & Engineering*, and *Petrophysics*. He received the Best Poster Paper Award in the 2015 SPWLA 55th Annual Logging Symposium. His research interests include petrophysics and formation evaluation of conventional and unconventional reservoirs, crushed/intact rock analysis, and NMR measurements and interpretations.

